ETP-KA/2024-5

Search for a dark Higgs boson produced in association with inelastic dark matter at the Belle II experiment

Zur Erlangung des akademischen Grades eines

DOKTORS DER NATURWISSENSCHAFTEN
(Dr. rer. nat.)

von der KIT-Fakultät für Physik des
Karlsruher Instituts für Technologie (KIT)

genehmigte

DISSERTATION

von

M.Sc. Patrick Ecker

aus Karlsruhe

Tag der mündlichen Prüfung: 25. Oktober 2024
Referent: Prof. Dr. Torben Ferber
Korreferent: Prof. Dr. Günter Quast

This document is licensed under a Creative Commons Attribution-NonCommercial 4.0 International License (CC BY-SA 4.0):
`https://creativecommons.org/licenses/by-sa/4.0/deed.en`

Disclaimer

Data analyses in high-energy physics such as the measurement presented in this doctoral thesis are a collaborative effort. The SuperKEKB particle accelerator which provides the particle beams essential for all studies at Belle II was built and is operated and maintained by the SuperKEKB accelerator group. The Belle II detector was built and is maintained and operated by the Belle II collaboration. The Belle II collaboration also creates the simulated and recorded datasets and maintains the computing infrastructure necessary to process them. The software environment necessary for studies with Belle II data plays an important role and was created and is maintained by the collaboration. The author of this thesis has been a part of the Belle II collaboration since 2018 and performed all studies detailed in this thesis except for the following:

- The development of the MadGraph5_aMC@NLO model used for the generation of the signal samples as described in Section 5.1
- The theoretical prediction of the cross sections and branching fractions of the signal process used throughout the thesis
- The determination of correction factors and the associated systematic uncertainties for:
    - Particle identification as described in Section 9.1
    - The efficiency correction for long-lived particles and prompt tracks as described in Sections 9.2 and 9.3
    - The derivation of the track monumentum scale factors in Section 9.4
    - The luminosity measurement and the associated uncertainty as described in Section 9.7

This thesis incorporates the use of Artificial Intelligence (AI) tools to help with grammatical or stylistic improvement of text, and program code creation.

Grammarly[*] is utilised throughout the thesis for spell and grammar checks, as well as for paraphrasing individual, selected sentences to improve clarity and precision in academic writing. I have approved all suggested changes.

ChatGPT[†] is used to aid the development of C++ and Python code, in particular code restructuring and optimisation that do not constitute the core scientific work of this thesis. I have approved and tested all suggestions to provide robust and reliable results.

---

[*] Grammarly: An AI writing assistant. See https://app.grammarly.com/ (Access Date: 2024-09-13).

[†] ChatGPT: A virtual AI assistant based on large language models. See https://openai.com/chatgpt/ (Access Date: 2024-09-13).

Contents

Chapter 1

Introduction

One of the biggest topics in modern particle physics is the hunt for unravelling the nature of dark matter (DM). Already in 1933, Fritz Zwicky proposed the concept of DM in studies of the Coma Cluster of galaxies [1, 2]. About 50 years later, in 1980, Vera Rubin and her collaborators found that the visible baryonic matter is not the only constituent of the universe by looking at the rotation curves of multiple galaxies [3]. Both observations showed that there has to be another contribution from invisible matter, so-called DM. As we know today, this DM is not covered in the Standard Model of particle physics (SM) [4–11], the commonly used theory to describe the interactions between fundamental particles in nature.

While many further measurements verified the existence of DM and the Planck collaboration observed that DM contributes with approximately 84% to the total matter density in the universe [12], up to today, about 90 years after Zwicky introduced the idea of DM, it is still unknown what it is made of. This includes the lack of knowledge if and how DM interacts with the constituents of the SM. Theorists developed a variety of models describing potential DM candidates, like weakly interactive massive particles (WIMPs), axions, and sterile neutrinos, just to name a few of them. None of them could yet be verified or fully ruled out by experimental collaborations. In addition, many models do not only predict DM alone, but additional mediator particles, forming a whole new dark sector.

If the DM interacts in some way non-gravitationally with the SM it can be produced directly at collider experiments like Belle II. Here the strength of the interaction has to be large enough to produce DM with a rate sufficient to be detected. In this thesis, I describe the search for a dark Higgs boson produced in association with inelastic DM, a model that contains two portals between the SM and the dark sector [13]. The interactions with the SM are realised by the mixing of a dark photon and the dark Higgs boson with their respective SM counterparts. While individual constraints on inelastic DM, the dark photon, and dark Higgs bosons exist, I present the first search for the combination of all three, making this search far more sensitive than the individual searches. The seven independent parameters of the model are causing this to be the first search within Belle II covering such a highly dimensional model parameter space. The model is of interest as it is consistent with both cosmological observations and with results from direct and indirect DM detection. At Belle II, the described model can manifest itself in a signature of up to two displaced vertices and additional missing energy. The very clean experimental environment of Belle II is an ideal place to search for such signatures.

A detailed introduction to the model and the signature within Belle II will be given in Chapter 2. Chapter 3 describes the experimental setup used for collecting the data that I analyse in this work. The analysis strategy is outlined in Chapter 4 and the datasets used during the development of the analysis are described in Chapter 5. In Chapter 6 I describe the reconstruction and the selection requirements used to distinguish the signal process of interest from SM background processes, together with the optimisation of the latter. Chapter 7 deals with the signal efficiency and in Chapter 8 I explain how the signal and SM background are paremetrized. The systematic uncertainties that are considered in this analysis are presented in Chapter 9. Possible discrepancies between the measured data and simulations are studied and discussed in Chapter 10. I explain the signal extraction and the statistical treatment of the results in Chapter 11. The results obtained with the data collected by the Belle II experiment between 2019 and 2022 are shown in Chapter 12. A conclusive summary and an outlook on future prospects are given in Chapter 13.

Chapter 2

Theoretical Foundations

In this chapter, I briefly explain the theoretical foundations behind dark Higgs bosons and inelastic DM, as well as the involved dark photon. This includes a discussion about constraints arising from observations of the DM relic density and the cosmic microwave background (CMB). Furthermore, I give an overview of existing limits in the model parameter region that is of interest in this thesis. Finally, I introduce the signature observable in Belle II that is used in this work for the search for dark Higgs bosons produced in association with inelastic DM.

2.1 The Dark Photon

To be able to produce DM in a collider experiment, the dark sector has to interact in some way non-gravitationally with the "visible" particles of the SM. There are many possibilities, so-called portals, how such an interaction could be realised in nature. One portal from the SM to the dark sector could be given by a new gauge boson that kinetically mixes with the SM photon. This new gauge boson is called dark photon A$'$ and can be either massless or massive. A detailed description of the two cases is given in [14]. The new gauge boson can, as done in [13, 15], be introduced via extending the SM with an additional $U(1)_X$ gauge group. The most general Lagrangian describing both the new $U(1)_X$ and the SM $U(1)_Y$ gauge group can be written as

$$\mathcal{L} = \mathcal{L}_{\mathrm{SM}} - \frac{1}{4}\hat{X}_{\mu\nu}\hat{X}^{\mu\nu} - \frac{\epsilon}{2\cos\theta_{\mathrm{W}}}\hat{X}_{\mu\nu}\hat{B}^{\mu\nu}, \tag{2.1}$$

where $\hat{X}_{\mu\nu}$ and $\hat{B}_{\mu\nu}$ are the (non-diagonalised) field strength tensors of the $U(1)_X$ and $U(1)_Y$ gauge group, respectively, and ϵ being the coupling strength normalised by the cosine of the Weinberg angle θ_{W}. The SM Lagrangian contains

$$\mathcal{L}_{\mathrm{SM}} \subset -\frac{1}{4}\left(B_{\mu\nu}B^{\mu\nu} + W^{a}_{\mu\nu}W^{a\mu\nu}\right), \tag{2.2}$$

with the additional field strength tensor of the $SU(2)_L$ gauge group $W_{\mu\nu}$.

As I am looking into the case where the dark photon is massive, an additional mechanism is needed to give mass to the dark photon. This can be realised either via the Stueckelberg mechanism [16], or similar to the SM via a dark Higgs mechanism with an additional scalar field, that will be described in Section 2.2. In the latter case Eq. (2.1) is expanded by additional terms from covariant derivatives of the scalar Lagrangian, which are up to linear order in the Higgs fields given by

$$\mathcal{L}_{\phi} \subset \frac{1}{2} m_{\hat{Z}}^2 \left(1 + \frac{2\hat{h}}{\nu_H}\right) \hat{Z}_{\mu}\hat{Z}^{\mu} + \frac{1}{2} m_{\hat{X}}^2 \left(1 + \frac{2\hat{h}'}{\nu_{\phi}}\right) \hat{X}_{\mu}\hat{X}^{\mu}, \tag{2.3}$$

with $\hat{Z}_{\mu} = \hat{W}_{\mu}^3$, the flavour eigenstates of the Higgs and dark Higgs field, $\hat{h}$ and $\hat{h}'$, and their corresponding vacuum expectation values acquired by symmetry breaking, ν_H and ν_{ϕ}, respectively. The diagonalisation is given by

$$\begin{pmatrix} \hat{Z}_{\mu} \\ \hat{B}_{\mu} \\ \hat{X}_{\mu} \end{pmatrix} = \begin{pmatrix} \cos\theta_{\mathrm{W}} & \sin\theta_{\mathrm{W}} & -\epsilon\sin\theta_{\mathrm{W}} \\ -\sin\theta_{\mathrm{W}} & \cos\theta_{\mathrm{W}} & -\epsilon\cos\theta_{\mathrm{W}} \\ \epsilon\tan\theta_{\mathrm{W}} & 0 & 1 \end{pmatrix} \begin{pmatrix} Z_{\mu} \\ A_{\mu} \\ A'_{\mu} \end{pmatrix}, \tag{2.4}$$

with the mass eigenstates Z_{μ} being the Z boson, A_{μ} the SM photon, and A'_{μ} the dark photon.

2.2 The Dark Higgs Boson

As already introduced in Section 2.1 to give mass to the dark photon, and explained in detail in [17], a dark Higgs field ϕ, that is a complex scalar field that is a singlet under the SM gauge group and carries charge under a new $U(1)_X$ gauge group, is introduced as an additional extension to the SM. The Lagrangian describing this field is in leading order of ϵ given by

$$\mathcal{L}_{\phi} = \left[\left(\partial^{\mu} + ig_{\mathrm{X}}q_{\phi}\mathrm{A}'^{\mu}\right)\phi\right]^{\dagger}\left[\left(\partial_{\mu} + ig_{\mathrm{X}}q_{\phi}\mathrm{A}'_{\mu}\right)\phi\right] - V(\phi, H), \tag{2.5}$$

where A' describes the dark photon, g_{X} the $U(1)_X$ gauge coupling, q_{ϕ} the charge of the dark Higgs field, and H the SM Higgs field. Similar to the SM Higgs field, the dark Higgs field acquires a vacuum expectation value ν_{ϕ} due to spontaneous symmetry breaking, giving mass to the gauge boson A'. The mass of the gauge boson is then given by

$$m(\mathrm{A}') = g_{\mathrm{X}}q_{\phi}\nu_{\phi}. \tag{2.6}$$

The resulting physical dark Higgs boson is denoted as h'.

The h' can decay either in SM or DM particles depending on the masses of the involved particles. One can realise the decay into SM particles via Higgs mixing. The potential before symmetry breaking contains the term

$$V(\phi, H) \subset \lambda_{\phi H} |H|^2 |\phi|^2. \tag{2.7}$$

After symmetry breaking the fields can be expressed via

$$\phi = \frac{\nu_\phi + \hat{h}'}{\sqrt{2}}, \tag{2.8}$$

$$H = \begin{pmatrix} 0 \\ \frac{\nu_h + \hat{h}}{\sqrt{2}} \end{pmatrix}, \tag{2.9}$$

with $\hat{h}$ and $\hat{h}'$ being the SM and dark Higgs flavour eigenstate (denoted by hats), respectively, and ν_h being the vacuum expectation value of the SM Higgs field. The mixing between the mass eigenstates is described by

$$\begin{pmatrix} \hat{h} \\ \hat{h}' \end{pmatrix} = \begin{pmatrix} \cos\theta & \sin\theta \\ -\sin\theta & \cos\theta \end{pmatrix} \begin{pmatrix} h \\ h' \end{pmatrix}, \tag{2.10}$$

with the mixing angle θ which is under the assumption $\theta \ll 1$ given by

$$\theta \approx \frac{\lambda_{\phi H} \nu_\phi \nu_h}{m(\mathrm{h}')^2 + m(\mathrm{h})^2}. \tag{2.11}$$

This mixing implies that the h' has the same decay modes as the SM Higgs boson, but the partial decay widths are suppressed by a factor of $\sin^2\theta$. Together with the mixing angle θ, the mass $m(\mathrm{h}')$ is needed to fully describe the dark Higgs boson.

The partial decay widths and the resulting branching fractions of the dark Higgs decays considered in this thesis are calculated and extensively discussed in [18]. The h' widths and branching fractions relevant in this thesis are shown in Fig. 2.1.

2.3 Inelastic Dark Matter

As of today, it is still unknown what DM consists of. One candidate is a stable Majorana fermion χ_1, as it is described in [13, 15]. The stable χ_1 can be excited to a state χ_2 via the absorption of a massive dark photon, that is described in Section 2.1. This is then called inelastic DM.

One can realise the inelastic DM by introducing, in addition to the additional spontaneously broken $U(1)_X$ symmetry and the scalar ϕ from Section 2.2, a Dirac fermion ψ. The corresponding Lagrangian of the Dirac fermion is then given by

$$\mathcal{L}_\psi = i\bar{\psi}\not{D}\psi - m_D\bar{\psi}\psi - f\phi\bar{\psi}^c\psi + \text{h.c.}, \tag{2.12}$$

where m_D is the mass of the Dirac fermion, $D_\mu = \partial_\mu - ig_\mathrm{X}\hat{X}_\mu$ the covariant derivative of

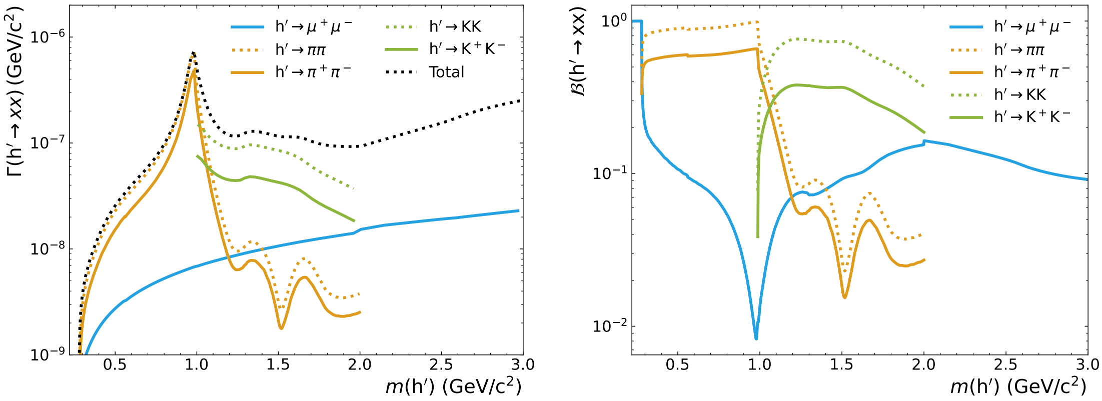

Figure 2.1: Partial decay widths of the dark Higgs boson (left) and branching fractions (right), taken from [18]. The solid lines show the theory predictions for the $\mathrm{h}' \to \mu^+\mu^-$ (cyan), $\mathrm{h}' \to \pi^+\pi^-$ (orange), and $\mathrm{h}' \to \mathrm{K}^+\mathrm{K}^-$ (light green) final state. The dashed lines show the corresponding widths/branching fractions including also the neutral hadrons. Above $m(\mathrm{h}') > 2\,\mathrm{GeV/c^2}$ no predictions for the $\mathrm{h}' \to \pi^+\pi^-$ and $\mathrm{h}' \to \mathrm{K}^+\mathrm{K}^-$ final state are available. While the branching fractions are independent of θ, for the calculation of the widths $\sin^2\theta$ is set to unity.

the $U(1)_X$ symmetry with the coupling constant g_X, and f being the coupling between DM and the scalar. To write this Lagrangian, the charges under the $U(1)_X$ symmetry of the Dirac fermion ψ and the scalar ϕ are chosen as 1 and 2, respectively. Note that in principle the charges can be chosen arbitrarily, as only the ratio between the charges is important. As described above, symmetry breaking causes the scalar field to acquire a vacuum expectation value ν_ϕ (see Eq. (2.8)), additionally ψ splits into two Majorana mass eigenstates:

$$\chi_1 = \frac{\psi - \psi^c}{\sqrt{2}}, \tag{2.13}$$

$$\chi_2 = \frac{\psi + \psi^c}{\sqrt{2}}. \tag{2.14}$$

This leads to the Lagrangian being written as

$$\begin{aligned}\mathcal{L} =& \frac{1}{2}\left(i\overline{\chi_1}\not\partial\chi_1 + i\overline{\chi_2}\not\partial\chi_2 - m(\chi_1)\overline{\chi_1}\chi_1 - m(\chi_2)\overline{\chi_2}\chi_2\right) \\ &+ \frac{i}{2}g_\mathrm{X}\hat{X}_\mu\left(\overline{\chi_2}\gamma^\mu\chi_1 - \overline{\chi_1}\gamma^\mu\chi_2\right) + \frac{f}{2}\hat{h}'\left(\overline{\chi_1}\chi_1 - \overline{\chi_2}\chi_2\right)\end{aligned}, \tag{2.15}$$

where the mass of the DM states is given by

$$m(\chi_1) = m_D - f\nu_\phi, \tag{2.16}$$

$$m(\chi_2) = m_D + f\nu_\phi. \tag{2.17}$$

From the Lagrangian in Eq. (2.15) one can directly see that only off-diagonal terms couple to the dark photon, resulting in the fact that besides the decay into SM only $\mathrm{A}' \rightarrow \chi_1\chi_2$ is allowed by the model. Furthermore, the χ_2 is always heavier than the χ_1. As already stated earlier, the transition between the DM states happens via a massive dark photon.

2.4 The Model

Combining the ingredients described in Sections 2.1 to 2.3, leads to a model that contains two independent portals between the dark and the visible sector. This is usually called a two-mediator model. The transition between the dark and visible part can either happen via the kinetic mixing of the dark photon with the SM photon, or via the mixing of the dark and the SM Higgs boson. Such a model has a rather rich phenomenology.

Seven independent model parameters are needed to fully describe the model. The dark photon is described by the mass $m(\mathrm{A}')$ and the kinetic mixing parameter ϵ. Hereby, ϵ controls both the production rate of the A' and its decay rate into SM particles. Consequently, ϵ controls additionally the lifetime of dark sector particles that decay into SM products via a dark photon. Similar to the dark photon, the dark Higgs boson is characterised by its mass $m(\mathrm{h}')$ and the mixing angle θ. Again the mixing controls both the production rate in SM interactions and the lifetime of the h', as the decay width scales with $\sin^2\theta$. Lastly, the dark matter fermions are described by the mass $m(\chi_1)$ of the ground state χ_1, the coupling to the dark photon defined as $\alpha_\mathrm{D} = g_\mathrm{X}^2/4\pi$, and the mass splitting Δm between the χ_1 and χ_2. This mass splitting directly controls the coupling between the dark matter fermions and the dark Higgs, as when using Eqs. (2.6), (2.16) and (2.17) the coupling f is given by

$$f = \frac{\Delta m g_\mathrm{X}}{m(\mathrm{A}')} \tag{2.18}$$

There are several constraints on the model parameters from both the DM relic abundance and observations of the CMB, that are discussed in detail in [13]. In order to be able to observe dark matter at collider experiments, the mixing parameters θ or ϵ have to be large enough to allow for a sizeable production. Such values cause a very large DM abundance in the early universe. Consequently, there has to be a mechanism that reduces the DM abundance at least to the size observed today. A possible scenario, that is discussed in [13], is given by DM annihilation. All possible annihilation channels, could in principle decay into SM particles and therefore alter the CMB. The precise observations from the CMB constrain the dark matter mass to be greater than $10\,\mathrm{GeV/c^2}$ when considering a thermal dark matter annihilation cross section [19]. As this is a scenario, not realisable within Belle II, the constraint has to be evaded, to make light DM possible. The annihilation channel $\chi_1\chi_1 \rightarrow \mathrm{A}'\mathrm{A}'$ will be kinematically closed at late times in the universe, where the DM carries a negligible amount of kinetic energy, if one requires

$$m(\chi_1) < m(\mathrm{A}'). \tag{2.19}$$

Additionally, the production of a DM bound state via the radiation of a h', $\chi_1\chi_1 \to \mathrm{h}'(\chi_1\chi_1)$, is also kinematically closed at late times if the mass of the h' is larger than the binding energy, so

$$\frac{1}{4}\alpha_\mathrm{f}^2 m(\chi_1) < m(\mathrm{h}') \tag{2.20}$$

[20], with $\alpha_\mathrm{f} = f^2/4\pi$. The annihilation rate via $\chi_1\chi_1 \to$ SM SM scales with $\alpha_\mathrm{f} y_\mathrm{SM}^2 \theta^2$, which is very small and can therefore be neglected. This leaves only the channels $\chi_1\chi_2 \to \mathrm{A}' \to$ SM SM and $\chi_1\chi_1 \to \mathrm{h}'\mathrm{h}'$. In order to reconstruct the decay products of the χ_2 decay in Belle II the mass splitting Δm, has to be sizeable. This causes the $\chi_1\chi_2 \to \mathrm{A}' \to$ SM SM channel to be suppressed, due to a suppressed abundance of χ_2. The remaining channel dominantly setting the annihilation cross section, $\chi_1\chi_1 \to \mathrm{h}'\mathrm{h}'$, can only be realised at late times if

$$m(\mathrm{h}') \lesssim m(\chi_1) \tag{2.21}$$

holds. Combining Eqs. (2.19) to (2.21) leads to a mass hierarchy that is crucial for the choice of model parameter configurations made in this thesis.

While there are constraints from direct detection experiments, they are not overly relevant for the inelastic DM model. The interaction of the DM (χ_1) with the target material can only be realised via the dark Higgs or dark photon mixing. The former is considered to be negligible due to the size of the involved couplings. As on tree-level, Eq. (2.15) allows the χ_1 only to interact with an A' via the production of a χ_2. At late times, the kinetic energy of the χ_1 is insufficient to overcome the mass splitting for mass splittings $\Delta m \geq 10^{-6}\, m(\chi_1)$ and therefore the inelastic scattering is forbidden. As discussed in [21], contributions from loop-induced elastic scattering are suppressed.

2.5 Existing Limits

As done extensively in [13, 15, 17], in this section, I will briefly discuss existing limits on the model parameters of the inelastic DM with a dark Higgs boson model.

In the scenario I cover in this thesis, the dark Higgs is the lightest dark sector state and therefore decays fully visible. Consequently, all searches for a scalar that mixes with the SM Higgs provide limits on the dark Higgs parameters I am looking for. Searching for the process $\mathrm{K}^\pm \to \pi^\pm \mathrm{h}'(\to \mathrm{inv})$, NA62 [22, 23] and E949 [24] excluded in the mass range $m(\mathrm{h}') < 250\,\mathrm{MeV/c^2}$ mixing angles down to $\theta \approx 10^{-4}$. The MicroBooNE experiment [25] used a similar process but with the h' decaying visibly into electrons and muons and excluded mixings down to 4×10^{-4} in the mass range below $m(\mathrm{h}') < 275\,\mathrm{MeV/c^2}$. Looking for a dark Higgs boson in the process $\mathrm{B} \to \mathrm{K}^{(*)}\mathrm{h}'$, with the h' decaying into multiple final states, Belle II was able to exclude mixings down to about 10^{-3} for the mass range relevant

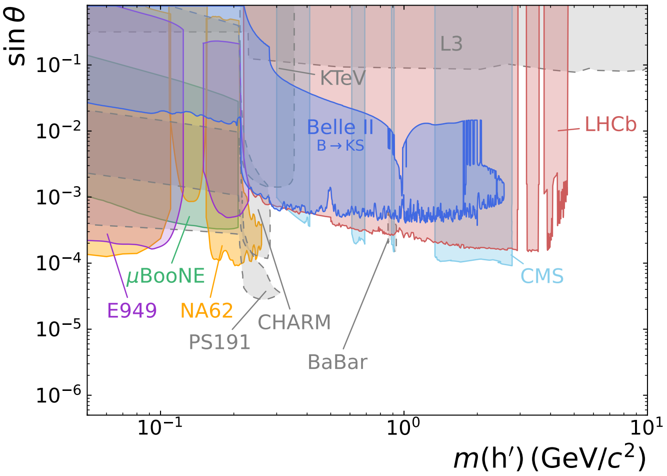

Figure 2.2: Existing constraints on the existence of a dark scalar in the plane of the dark Higgs mass $m(\mathrm{h}')$ and the sine of the mixing angle θ. The existing limits from Belle II, LHCb, CMS, CHARM, and MicroBooNE correspond to 95% CL, while KTeV, E949, PS191, NA62, BABAR, and L3 correspond to 90% CL. Constraints coloured in grey with a dashed outline are reinterpretations not performed by the experimental collaborations. Adapted from [17].

in [26]. Similarly, LHCb [27, 28] and CMS [29] also looked into b → s transitions (only covering the muon final state) and were able to exclude for most dark Higgs masses a slightly larger parameter space compared to the search from Belle II. All of these limits are shown in Fig. 2.2. Additionally, reinterpretations of results from CHARM [30], KTeV [31], PS191 [32], BABAR [33], and L3 [34] are presented there. All these constraints apply without any assumptions on the parameters constraining inelastic DM or the dark photon.

Constraints from generic dark photon searches do in general not apply for the presented scenario, as the A' neither decays fully visibly nor fully invisibly.

Parts of the inelastic DM parameter space are excluded by reinterpretations of results from CHARM [35] and NuCal [36, 37] that have been performed in [38]. Furthermore, reinterpretations of BaBar results [39] performed in [15] exclude further parts of the parameter space. These reinterpretations are shown in Fig. 2.3 for two example model parameter configurations. Note that these reinterpretations have been done only for some model parameter configurations covered in this thesis.

2.6 Signature in Belle II

The described model can manifest itself in many signatures within Belle II. As it gives access to all properties of the model, the process of interest in this thesis is given by $\mathrm{e}^+\mathrm{e}^- \rightarrow \mathrm{h}'(\rightarrow \mathrm{x}^+\mathrm{x}^-)\chi_1\chi_2(\rightarrow \chi_1\mathrm{x}^+\mathrm{x}^-)$. Fig. 2.4 shows the corresponding Feynman diagram of the process. Here the dark photon is used as the mediator in the production of the DM via its kinetic mixing.

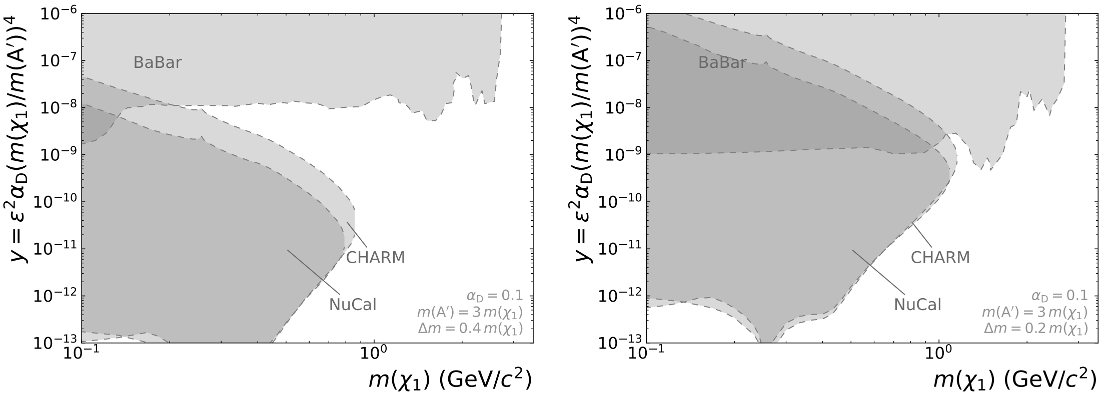

Figure 2.3: Existing constraints on inelastic DM in the plane of the DM mass $m(\chi_1)$ and the dimensionless variable $y = \epsilon^2\alpha_{\mathrm{D}}(m(\chi_1)/m(\mathrm{A}'))^4$ based on reinterpretations. The reinterpretations of the BaBar results [39] are taken from [15], while the ones reinterpreting results from CHARM [35] and NuCal [36, 37] are taken from [38]. The mass splitting between the χ_1 and χ_2 is set to $\Delta m = 0.4\,m(\chi_1)$ (left) and $\Delta m = 0.2\,m(\chi_1)$ (right). The two other parameters affecting these reinterpretations are set to $\alpha_{\mathrm{D}} = 0.1$ and $m(\mathrm{A}') = 3\,m(\chi_1)$. Reinterpretations for more model parameter configurations can be found in the references above.

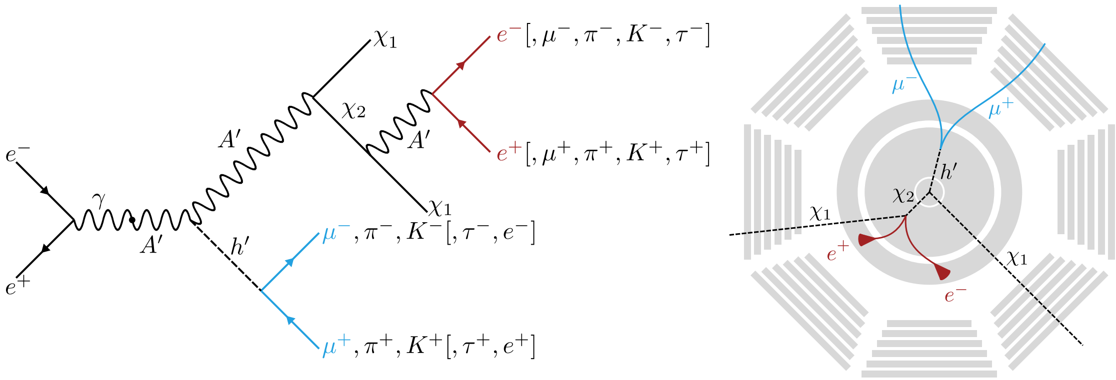

Figure 2.4: Left: Feynman graph of the dark Higgs produced in $\mathrm{e}^+\mathrm{e}^-$ collisions in association with inelastic DM process including all final states within the kinematic threshold of Belle II. All particles in the final state that are not considered in this thesis are shown in brackets. Right: Signature of the process in the Belle II detector (see Section 3.2). The sketch shows the $x - y$-plane. Plots adapted from [13].

The initial A' that is created in the process $\mathrm{e}^+\mathrm{e}^- \rightarrow \mathrm{h}'\mathrm{A}'$ can either be on- or off-shell depending on the mass of both the A' and h'. If the A' is produced on-shell, the $\mathrm{e}^+\mathrm{e}^- \rightarrow \mathrm{h}'\mathrm{A}'$ resembles a two-body decay, where the four-momentum of the h' and A' can be calculated via the center-of-mass energy. The situation gets more complicated if the dark photon cannot be produced on-shell. Then it is more convenient to express the production as $\mathrm{e}^+\mathrm{e}^- \rightarrow \mathrm{h}'\chi_1\chi_2$ showing the three-body decay structure that results in way more complicated kinematics.

The dark Higgs boson decays into a pair of SM particles via the mixing with the SM Higgs boson. Within the center-of-mass energy constraint of Belle II, the allowed final states in the decay $\mathrm{h}' \rightarrow \mathrm{x}^+\mathrm{x}^-$ are $x = \mathrm{e}, \mu, \pi, \mathrm{K}, \tau$. On the other side, the either on- or off-shell dark photon decays into inelastic DM, $\mathrm{A}' \rightarrow \chi_1\chi_2$. While the χ_1 is stable, the χ_2 decays into SM particles via the radiation of a dark photon. In this context, an additional stable χ_1 is produced. So the decay is given by $\chi_2 \rightarrow \chi_1\mathrm{x}^+\mathrm{x}^-$ with $x = \mathrm{e}, \mu, \pi, \mathrm{K}, \tau$. The kinematics of the additional pair of SM particles are mainly controlled by the mass splitting between the χ_1 and χ_2, Δm.

As Fig. 2.4 shows, the signature observable in the detector is given by two vertices, one from the dark Higgs decay and the other from the decay of the χ_2. Additionally, two stable χ_1 fermions, that do not interact with the detector, are produced, resulting in missing energy during the event reconstruction. Depending on the size of the mixings θ and ϵ and therefore the respective lifetime of the h' and χ_2, the two vertices can have a significant displacement. While both vertices are reconstructed from a pair of charged particles, they can be distinguished by their topology. The h' is fully reconstructed when combining the two particles, resulting in an alignment of the momentum and vertex vector. This is called a pointing vertex. On the other hand, when reconstructing the χ_2 out of two visible particles, one obtains the correct vertex position, but the four-momentum of the χ_2 can never be correctly reconstructed due to the escaping χ_1. This results in a misalignment between the reconstructed momentum and vertex vector – a non-pointing vertex.

Chapter 3

The Belle II Experiment

In this chapter, I describe the experimental setup used to collect the data that is analysed in this thesis. I give a brief overview of the SuperKEKB accelerator [40] and the Belle II detector [41].

3.1 The SuperKEKB Accelerator

The SuperKEKB accelerator is located at the High Energy Accelerator Research Organization (KEK) in Tsukuba, Japan. It provides the electron and positron beams that are collided within the Belle II experiment. Fig. 3.1 shows a schematic view of the accelerator with its different components.

While the electrons are emitted from a photocathode, the positrons are obtained by collisions of an electron beam with a tungsten target. The created bunches of electrons and positrons are then accelerated in a linear accelerator up to their desired energy of 7 GeV for electrons and 4 GeV for positrons. Afterwards, the electron bunches are injected into the High-Energy Ring (HER) and the positrons into the Low-Energy Ring (LER). The emittance of the positrons is damped in a damping ring beforehand. As all the acceleration happens in the linear accelerator, electron and positron bunches can continuously be injected into the storage rings. With one of the main physics focuses of the Belle II experiment in mind, the study of B mesons, the energy of the beams is chosen to reach a center-of-mass system (cms) energy of $\sqrt{s} \approx 10.58\,\text{GeV}$ in the collision. This energy allows for the resonant production of $\Upsilon(4S)$ mesons, which decay predominantly into a pair of B mesons. Nevertheless, the accelerator also runs on other beam energies to allow for studies of other Υ resonances or even off-resonance for calibration purposes. The asymmetric beam energies lead to a Lorentz boost of $\beta\gamma = 0.28$, boosting all produced particles in the direction of the electron beam.

As at SuperKEKB, unlike for example at the Large Hadron Collider (LHC), elementary particles collide, the knowledge about the exact energy in the collision is very powerful in analysis looking at signatures with missing energies, like the one I present in this thesis.

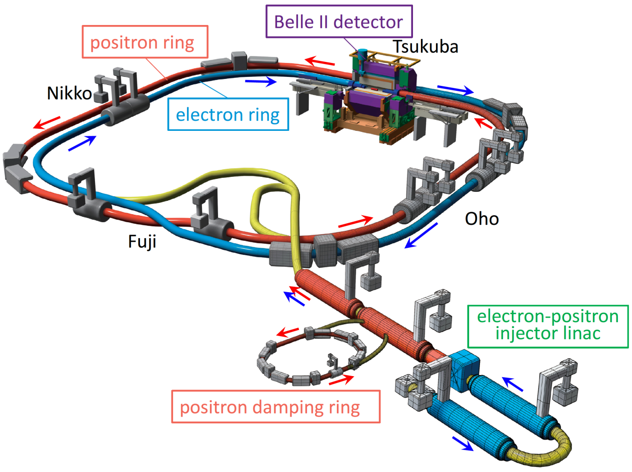

Figure 3.1: Schematic view on the SuperKEKB accelerator complex. Taken from [40].

To increase the amount of collected data, a large instantaneous luminosity is desirable. SuperKEKB reaches this goal with the use of the nano-beam scheme, resulting in a planned instantaneous luminosity of $L = 6 \times 10^{35}\,\mathrm{cm}^{-2}\mathrm{s}^{-1}$ [42][*], which is about a factor 30 larger than the instantaneous luminosity reached by its predecessor KEKB. While SuperKEKB currently runs on a much smaller instantaneous luminosity, it was able to reach the world record instantaneous luminosity of $L = 4.71 \times 10^{34}\,\mathrm{cm}^{-2}\mathrm{s}^{-1}$ in June 2022 [43].

3.2 The Belle II Detector

The Belle II detector is a general purpose 4π detector, arranged in a cylindrical way around the Interaction Point (IP). It consists of several subdetectors, that are used to reconstruct the particles produced in the $\mathrm{e}^+\mathrm{e}^-$-collisions. Each of these subdetectors serves a different purpose targeting the reconstruction and identification of different particle types. Fig. 3.2 shows a schematic view of the detector with all the relevant subdetectors.

Due to the asymmetry in the beam energies, the particles created in the collision are boosted in the forward direction, so in the direction of the electron beam. This asymmetry is reflected in an asymmetric detector design, to reach a better angular acceptance in the forward direction.

The Belle II coordinate system is defined with its origin at the nominal IP and the z-axis pointing approximately in the direction of the electron beam. Furthermore, the x-axis is defined horizontally pointing outward from the center of the storage ring and the y-axis points vertically to the top. The polar angle θ is defined in the range from 0 to π, where $\theta = 0$ describes the forward direction. The azimuthal angle ϕ is defined from $-\pi$ to π in the transverse x-y plane and $y = 0$ being $\phi = 0$.

---

[*] The initial target luminosity of SuperKEKB was $L = 8 \times 10^{35}\,\mathrm{cm}^{-2}\mathrm{s}^{-1}$, which was updated to the intermediate target of $L = 6 \times 10^{35}\,\mathrm{cm}^{-2}\mathrm{s}^{-1}$ after the start of the operation in 2019.

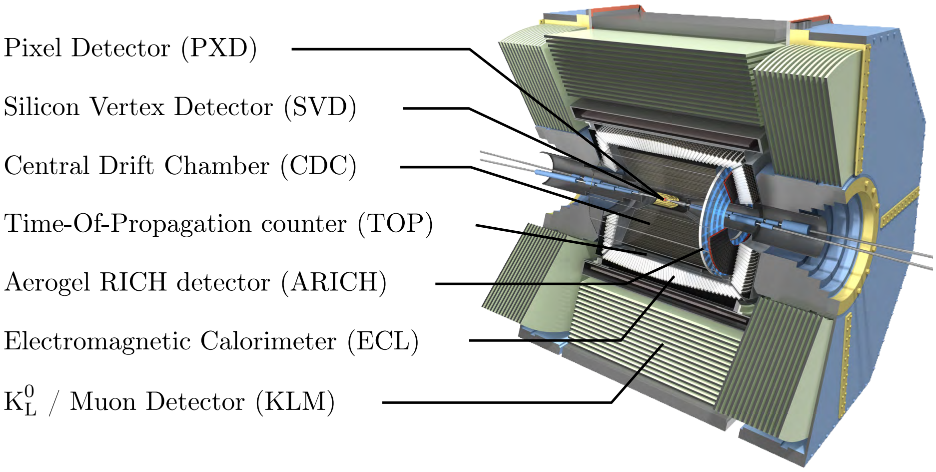

Figure 3.2: Schematic view on the Belle II detector with all subdetectors marked. Taken from [44].

In the following part, I give a short introduction to the several subdetectors. A detailed description can be found in [41].

3.2.1 Tracking Detectors

The tracking system of Belle II consists of three subdetectors that aim to measure the trajectory of charged particles and determine their momenta and vertex positions. This is done via the ionisation of the detector material by the transversing charged particle. The innermost part is covered by two vertex detectors, Pixel Detector (PXD) [45, 46] and Silicon Vertex Detector (SVD) [47], which have a high spatial resolution to improve the vertex resolution near the IP. This is followed by the Central Drift Chamber (CDC) [48, 49] which has less spatial resolution but due to its size provides a large lever arm for the measurement of the particle momentum.

The energy depositions in the detector material, usually referred to as hits, are combined by software algorithms to reconstruct the particle trajectories. These reconstructed charged particle candidates are often called tracks as they are reconstructed by their trajectory through the detector.

Pixel Detector Located directly outside of the beryllium beam pipe, which has a radius of 10 mm, the PXD is the detector closest to the IP. It is built from two pixelated silicon layers located at radii of 1.4 cm and 2.2 cm. To reduce the material budget the pixels are based on the Depleted Field Effect Transistor (DEPFET) technology, allowing for a thickness of just 75 μm. The pixel size ranges from $50\,\mu\text{m} \times 55\,\mu\text{m}$ to $50\,\mu\text{m} \times 85\,\mu\text{m}$.

In the data-taking period where the data analysed in this thesis was taken, only a sixth of the second PXD layer was installed.

Silicon Vertex Detector The other vertex detector that consists of four additional silicon layers is the SVD. The SVD is built from double-sided strip sensors, that are arranged cylindrical around the beam pipe at radii of 3.9 cm, 8.0 cm, 10.4 cm, and 13.5 cm. An angular acceptance of $17^\circ < \theta < 150^\circ$ is covered by the SVD. This is possible without increasing the number of layers, as the last three layers are slanted in the forward direction.

Central Drift Chamber The main tracking detector for measuring the particle momentum is the CDC, a gas-filled detector with a very low material budget to reduce the impact of multiple scattering on the transversing particles. Wires arranged in 56 layers around the beam axis in a radial range from 16.8 cm to 113 cm provide the long lever arm necessary to precisely measure the momentum. Transversing charged particles ionise the gas mixture, which is made up of 50% helium and 50% methane. The primary electrons created by the ionisation are accelerated to the wires due to a strong electric field resulting in an avalanche that is then detected at the wires. Three-dimensional information is gained by axial layers that are arranged along the z-axis and stereo layers that are tilted. Like the SVD, the CDC provides an angular acceptance of $17^\circ < \theta < 150^\circ$.

3.2.2 Particle Identification Detectors

While all subdetectors in Belle II besides the PXD contribute to the identification of the particle flavour, there are two that only serve this specific purpose: the Time-Of-Propagation counter (TOP) and Aerogel Ring-Imaging Cherenkov detector (ARICH) [50]. These focus mainly on the separation of charged pions and kaons as the other subdetectors are not well-suited to distinguish them.

Time-Of-Propagation Counter The TOP provides particle identification (PID) information in the barrel part of the detector using the Cherenkov effect. 16 quartz bars are arranged parallel to the z-axis around the IP. If a charged particle traverses one of the bars it emits Cherenkov photons under an angle that depends on its velocity. The Cherenkov photons are reflected within the quartz bar and collected at one side of the bar with photomultiplier tubes (on the other side a mirror reflects the photons). Measuring the time and position of the emitted photons allows for the reconstruction of the characteristic Cherenkov angle, which can then be used with momentum information provided by the tracking detectors to identify the particles. The TOP covers an angular region of $31^\circ < \theta < 128^\circ$.

Aerogel Ring-Imaging Cherenkov Detector Similar to the TOP, the ARICH uses the Cherenkov effect for the identification of particles in the forward direction. It is a proximity-focusing Ring-Imaging detector, consisting of two layers of aerogel that serve as a radiator. The emitted Cherenkov photons create characteristic rings whose radii depend on the velocity of the transversing particle. These are detected using hybrid avalanche photon detectors. The ARICH has an angular acceptance of 14° $< \theta <$ 30°.

3.2.3 Electromagnetic Calorimeter

The measurement of the energy of the particles is done with the Electromagnetic Calorimeter (ECL) [51]. This is especially relevant for neutral particles, explicitly photons and neutral hadrons, that are not measured by the tracking and PID detectors.. While the reconstruction of these particles is the main focus of the ECL, it also provides PID information for separating electrons from muons or charged hadrons. Electrons and photons nearly deposit their whole energy in the ECL, while for the other particle types often only a fraction is deposited.

The ECL can be divided into three parts, the barrel and two endcaps in forward and backward directions. In total it covers an angular acceptance of $12.4^\circ < \theta < 155.1^\circ$ with two small gaps between $31.4^\circ < \theta < 32.2^\circ$ and $128.7^\circ < \theta < 130.7^\circ$. The ECL consists of 8736 thallium-doped caesium iodide crystals, which provide, with their length of 30 cm, 16.1 radiation lengths. Particles are measured via the electromagnetic shower they create when hitting the ECL. The photons created in these showers are collected by photodiodes at the back of each crystal. The measured energy depositions are clustered by a software algorithm, creating so-called ECL clusters, that are later used in analyses to create particle candidates.

3.2.4 $\mathrm{K_L^0}$ and Muon Detector

The outermost sub-detector is the $\mathrm{K_L^0}$ and muon detector (KLM). As the name suggests, it serves to measure muons and long-lived neutral $\mathrm{K_L^0}$ that passed all previous subdetectors. The KLM consists of alternating layers of iron absorbers, that also serve as the magnetic flux return for the solenoid, and active material. The active material consists of either resistive plate chambers (RPCs) or scintillator strips coupled to silicon photomultipliers. The latter are used in the two innermost layers of the barrel and the two endcaps, as the dead time of the RPCs is too long to withstand the background rates in these detector regions.

The total angular acceptance of the KLM is $18^\circ < \theta < 155^\circ$. Due to its geometry, the KLM can be divided into five regions: A barrel, forward, and backward region and two overlap regions between the barrel and the endcaps.

3.2.5 Trigger System

SuperKEKB provides a bunch crossing rate of 250 MHz, but not all of these bunch crossings result in an actual collision of an $\mathrm{e^+e^-}$ pair. At the design luminosity of $L = 6\times10^{35}\,\mathrm{cm^{-2}s^{-1}}$ the $\mathrm{e^+e^-}$cross section is dominated by Bhabha scattering ($\mathrm{e^+e^-} \to \mathrm{e^+e^-}(\gamma)$), resulting in a collision rate greater than 40 kHz. Due to bandwidth restrictions, the storable rate must not exceed 10 kHz. Therefore, the rate has to be reduced, which is done in two steps. In the first step, a hardware-based trigger system, which is often referred to as Level 1 trigger (L1 trigger) is utilised. The L1 trigger reduces the rate to 30 kHz, the maximum input rate of the software-based trigger named High Level Trigger (HLT). Both trigger systems are designed with the aim of reducing the rate, e.g. rejecting most of the Bhabha scattering, while keeping all events that might be interesting for physics analyses, mainly focusing on $e^+e^- \to B\overline{B}$ and low multiplicity events like $e^+e^- \to \tau^+\tau^-(\gamma)$. As the physics program of Belle II is constantly extended, including for example dark sector analyses with extraordinary signatures, like the one I present in this thesis, and as the requirements for the trigger system might change during data taking, the trigger system is under constant development. Consequently, changes in the trigger system during data-taking have to be considered in the analysis.

Level 1 Trigger The L1 trigger is the first trigger step. Build from field-programmable gate arrays (FPGAs) the L1 trigger combines signals from several subdetectors (mainly from the CDC and ECL). The input signal passes the logic implemented on the FPGAs resulting in multiple bit-wise decisions per event. Several of these bits are combined in so-called trigger lines, that are evaluated by a global decision logic (GDL) to take the final decision for an event to pass or be rejected.

High Level Trigger The HLT is a software trigger operated on CPUs. It is running the Belle II reconstruction software to further reduce the event rate to the storable maximum. Thereby it takes information from all subdetectors besides the PXD into account. Similar to the L1 trigger, several trigger lines, that focus on different signatures of interest, are defined, and an event is rejected if none of these lines delivers positive feedback. To avoid biases from the PID, the HLT only uses information from two of the tracking detectors (SVD and CDC) and the ECL.

Chapter 4

Analysis Strategy

In this thesis, I search for a signature of inelastic DM produced in association with a dark Higgs boson in multiple final states of the dark Higgs decay.

The seven-dimensional model parameter space described in Section 2.4 is challenging in the sense that, to model the signal efficiency and shape of the reconstructed dark Higgs mass correctly, simulated samples have to be produced for each model parameter configuration. As this is computationally expensive, a seven-dimensional scan with an order of 100 points per model parameter is not possible, due to limitations in computing resources. With this in mind, I will discuss in the following part the choices to reduce the parameter space that is considered in this thesis.

When reconstructing the dark Higgs candidate, more explicitly its mass, due to its resonant structure with a very small nominal width[*], a very narrow peak in the reconstructed mass spectrum can be observed. Therefore, the analysis described in this thesis is designed as a bump-hunt in the reconstructed mass of the h'. This means I use the reconstructed h' mass to search for a signal-like excess over the SM background expectation. Besides the mass of the A' and the DM, which can alter the kinematics of the h' vertex for some model parameter configurations, the h' vertex is additionally described by its lifetime that is controlled by the mixing angle θ. Consequently, a natural plane to perform the scan is the $m(\mathrm{h}')$-θ-plane. Doing so I am also able to compare the results to existing constraints that have been placed on dark scalars (see Section 2.5). Note that all of these constraints do not make assumptions about a dark photon or even inelastic DM existing in nature. As already mentioned, these assumptions can, however, have an impact on the kinematics of the dark Higgs, and more importantly, they affect the efficiency with which I am able to reconstruct the signature of interest in this thesis. To see the effect these assumptions about the structure of the A' and the inelastic DM present in the model have on the limits I place on the h', the scan is done for variations of the five remaining model parameters.

Another interesting model parameter plane is given by the plane of the DM mass $m(\chi_1)$

---

[*] The assumed h' width is way smaller than the resolution of the Belle II detector, which then dominates the width of the reconstructed dark Higgs mass.

and the dimensionless variable

$$y = \epsilon^2 \alpha_\mathrm{D} \left(\frac{m(\chi_1)}{m(\mathrm{A}')} \right)^4 . \tag{4.1}$$

This choice is made as the DM annihilation cross section only depends on $m(\chi_1)$ and y [52]. When varying the χ_1 mass and the kinetic mixing parameter ϵ for the scan described above, I can also access this plane and place limits on the dark photon properties for several assumptions of the remaining model parameters, this time including the mass and lifetime (mixing) of the h'.

In both planes, I choose the variations of the parameters considering the sensitivity of Belle II and to allow for comparison with existing constraints that are available in the literature. I vary $m(\mathrm{A}') = \{3, 4\}\, m(\chi_1)$, $\Delta m = \{0.2, 0.4, 1.0\}\, m(\chi_1)$ and $\alpha_\mathrm{D} = \{0.1, 0.5\}$. For combinations of these, I generate events for h' masses between $0.22\,\mathrm{GeV/c^2}$ and $3.0\,\mathrm{GeV/c^2}$ in 45 steps of varying size and various lifetimes $0.1 < c\tau(\mathrm{h}') < 10000\,\mathrm{cm}$ in variable steps. Additionally, I generate events for $m(\chi_1)$ between $0.2\,\mathrm{GeV/c^2}$ and $3.0\,\mathrm{GeV/c^2}$ in 30 steps of $0.1\,\mathrm{GeV/c^2}$, and various lifetimes $0.01 < c\tau(\chi_2) < 1000\,\mathrm{cm}$ in variable steps. A full list of all model parameter configurations for the scans can be found in Tables A.1 and A.2 in the appendix.

To make the reinterpretation of the results easier, I produce them initially in terms of the h' lifetime $c\tau(\mathrm{h}')$ and χ_2 lifetime $c\tau(\chi_2)$ instead of the two mixing parameters θ and ϵ, respectively. This is possible as for the signature I am considering the mixing angle θ only controls the lifetime of the h', scaling with $c\tau(\mathrm{h}') \propto 1/\sin^2\theta$. For the kinetic mixing parameter the situation is similar, as ϵ controls the lifetime of the χ_2 (via $c\tau(\chi_2) \propto 1/\epsilon^2$), but in addition, also defines the production rate of DM via ϵ^2. Nevertheless, as the latter is only an additional factor in the calculation of the cross section, I can consider it only as a last step in the transition to fully model-dependent results. A detailed explanation on how to calculate θ and ϵ for fixed lifetimes will be given in Section 5.1.

Belle II collects data not only on the $\Upsilon(4\mathrm{S})$ resonance, but also accumulates smaller datasets on other center-of-mass energies. As the analysis presented here, does not involve B mesons, there is in principle no restriction on a specific center-of-mass energy. Nevertheless, to model the kinematics at the other center-of-mass energies correctly, I would need to perform simulations also at these energies. As already mentioned, the available computing resources are already limiting the model parameter space that can be accessed. I therefore concentrate the search to the $\Upsilon(4\mathrm{S})$ center-of-mass energy in this analysis to expand the reach to more model parameter variations. This comes with the price of a slightly smaller dataset with an integrated luminosity of $\int \mathcal{L}\mathrm{d}t = 364\,\mathrm{fb}^{-1}$ to analyse compared to the full dataset that has been collected by Belle II until June 2022 and has a size of $\int \mathcal{L}\mathrm{d}t = 427\,\mathrm{fb}^{-1}$ [53].

I perform the search in three different final states: $\mathrm{e}^+\mathrm{e}^- \to \mathrm{h}'\chi_1\chi_2(\to \chi_1\mathrm{e}^+\mathrm{e}^-)$ with the h' decaying into either a pair of muons, pions, or kaons. I do not consider the possible

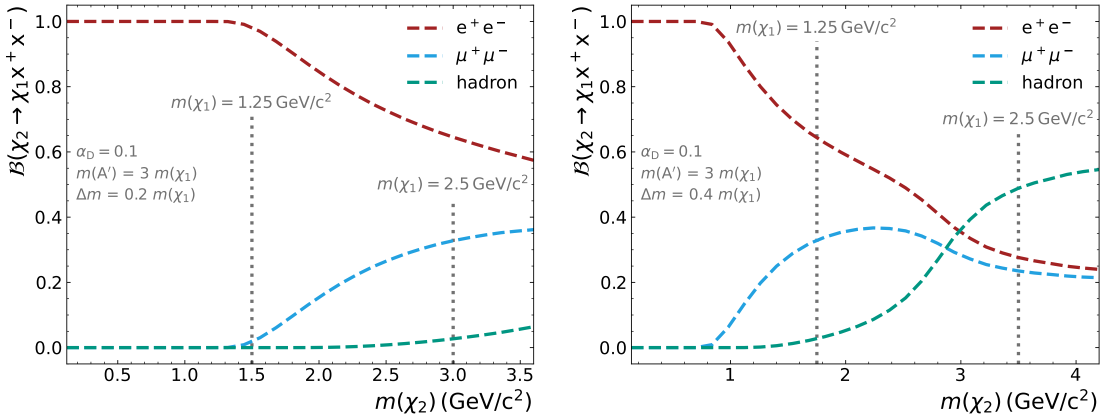

Figure 4.1: Branching fractions of the $\chi_2 \to \chi_1 \mathrm{x}^+\mathrm{x}^-$ decay, with x being e (red), μ (cyan), or inclusive hadrons (green), as a function of the χ_2 mass for $\alpha_\mathrm{D} = 0.1$. The left plot shows a mass splitting $\Delta m = 0.2\, m(\chi_1)$, while the right side shows $\Delta m = 0.4\, m(\chi_1)$. The vertical lines represent the $m(\chi_1)$ values used in the $m(\mathrm{h}')$-θ scans in this analysis. The mass of the dark photon is chosen to be three times larger than the mass of the χ_1.

decay $\mathrm{h}' \to \tau^+\tau^-$ for this analysis as the τ's would leave a more complicated signature in the detector due to them immediately decaying with several neutrinos in the final state. In general, the decay of the dark Higgs into a pair of electrons is possible but it is heavily suppressed above the di-muon threshold and therefore not considered in this analysis. Additionally, as can be seen in Fig. 2.2, the existing limits in the region below the di-muon threshold are quite strong so I do not expect to cover additional parameter space with the presented analysis in this region of parameter space. The limitation of considering only the electron final state in the χ_2 decay is motivated by studies of the trigger performance for the signal process that will be explained in more detail in Section 7.2.

For a rough estimation of how much of the phase space is lost by this restriction, Fig. 4.1 shows the branching fractions of the χ_2 decaying into electrons, muons, and hadrons with an additional χ_1. As can be seen there, even in the worst case (large mass splitting and large χ_1 mass), the electron final state covers more than 25 % of the total phase space. The $\chi_2 \to \chi_1 \mathrm{e}^+\mathrm{e}^-$ branching fraction gets larger the smaller the mass splitting and the smaller the mass of the χ_1 is chosen. Certainly, including the other final states would possibly improve the sensitivity of the analysis, but as worse efficiency due to the trigger performance is expected for these final states, I only consider the $\chi_2 \to \chi_1 \mathrm{e}^+\mathrm{e}^-$ final state in this work.

As described in detail in Chapter 6, after reconstructing two vertices according to the considered final states and performing a vertex fit on each of the vertices, I discriminate the signal from SM background processes in a cut-based selection approach. One key concept of this selection is requiring one of the two vertices to be significantly displaced, as this already suppresses large amounts of the SM background processes. In total the described selection delivers a nearly background-free scenario.

Because of the extremely low background level, when searching for a signal-like excess in the reconstructed h' mass spectrum, a counting experiment is conducted, and the outcomes are analysed using Bayesian techniques. I base the decision of whether a significant signal is found or not on the p-value of the background-only hypothesis. In the case that I observe no significant excess, I place upper limits on the product of the production cross section and the dark Higgs and χ_2 branching fractions for each of the three considered final states:

$$\sigma(\mathrm{e}^+\mathrm{e}^- \to \mathrm{h}'\chi_1\chi_2) \times \mathcal{B}(\chi_2 \to \chi_1\mathrm{e}^+\mathrm{e}^-) \times \mathcal{B}(\mathrm{h}' \to \mathrm{x}^+\mathrm{x}^-). \tag{4.2}$$

Additionally, when combining the three final states, I set a combined upper limit on the product of the production cross section $\sigma(\mathrm{e}^+\mathrm{e}^- \to \mathrm{h}'\chi_1\chi_2)$ and the branching fraction $\mathcal{B}(\chi_2 \to \chi_1\mathrm{e}^+\mathrm{e}^-)$. In the combination, the dark Higgs branching fractions $\mathcal{B}(\mathrm{h}' \to \mathrm{x}^+\mathrm{x}^-)$ are fixed to the theoretical predictions from [18].

Possible discrepancies between data and simulation are studied and corrected (see Chapter 9). The corresponding systematic uncertainties are, together with the statistical ones, incorporated as nuisance parameters in the Bayesian analysis.

The whole analysis is developed with the signal region blinded. This means that, to not bias the results in any direction by the analyst, the whole analysis pipeline is developed on simulated samples and additional checks are performed in specific signal-depleted control regions, described in Chapter 10. Only after the whole pipeline is set the measured data is analysed in the signal region.

Chapter 5

Datasets

In this analysis, simulated samples are used for three purposes: Both signal and background samples are used for the optimisation of the selection procedure whereas the signal samples are additionally used to derive the shape of the reconstructed dark Higgs mass as well as the signal efficiency. The generators used for the production of the signal and background processes are described below. For both signal and background the particle movement and the interaction with the detector material is simulated using GEANT4 [54] and the detector response is simulated with the Belle II Analysis Software Framework (basf2) [55, 56].

5.1 Signal Samples

The signal samples for the process $\mathrm{e}^+\mathrm{e}^- \to \mathrm{h}'(\to \mathrm{x}^+\mathrm{x}^-)\chi_1\chi_2(\to \chi_1\mathrm{e}^+\mathrm{e}^-)$, which are used to optimise the selection procedure, and derive the signal shape and efficiency, are generated with MadGraph5_aMC@NLO (MadGraph5) [57]. For the event generation of the purely leptonic final state ($\mathrm{h}' \to \mu^+\mu^-$) MadGraph5 is used exclusively, while for the final states where the dark Higgs decays hadronically, a combination of MadGraph5 and EvtGen [58] (used for decaying the h') is utilised.

Before generating the events with MadGraph5 the widths of the decaying dark sector particles, namely the widths of the A', h', and χ_2 have to be determined. While the partial decay width of the A' into dark matter scales with α_D, the partial width into SM particles scales with $\alpha_\mathrm{em}\epsilon^2$ [59]. As in the model parameter space studied in this thesis $\alpha_\mathrm{D} \gg \alpha_\mathrm{em}\epsilon^2$ holds, the width of the A' is dominated by the process $\mathrm{A}' \to \chi_1\chi_2$ and is calculated with MadGraph5. Fig. 5.1 shows the width and corresponding lifetime of the A' as a function of its mass for a typical model parameter configuration considered in this work. As can be seen there, the A' has a rather broad width and consequently a lifetime of the order of $c\tau(\mathrm{A}') \approx 10^{-12}$ cm for masses considered in this thesis. Therefore, the dark photons always decay promptly in the scenario described here. The decay of the A' into a pair of SM particles is still possible but heavily suppressed compared to the decay into dark matter. To give

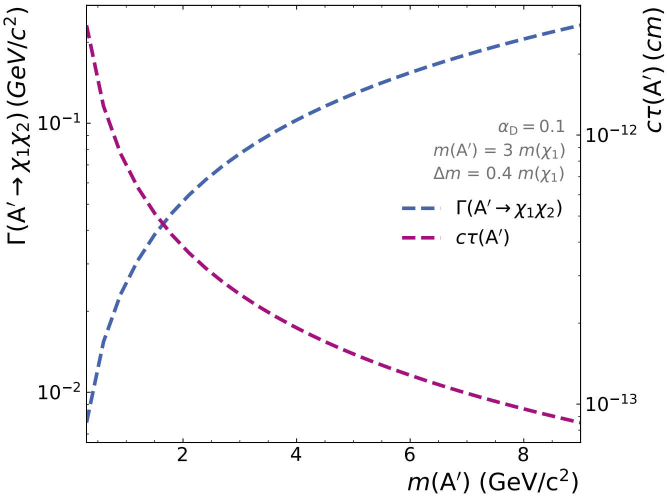

Figure 5.1: Decay width (blue) and corresponding lifetime (purple) of the dark photon as a function of the mass. The width is calculated via the process $A' \to \chi_1\chi_2$ which for small ϵ is the by far dominant contributor to the total width.

the reader a feeling on the size of the suppression, for a typical choice of model parameters considered in this analysis ($\alpha_D = 0.1, \epsilon = 10^{-3}, m(\chi_1) = 2.5\,\mathrm{GeV/c^2}, m(A') = 3\,m(\chi_1)$) the decay into SM particles is suppressed by a factor of 6×10^{-7} compared to the decay into DM. In this example, the choice of ϵ is motivated by the fact that much larger values for ϵ are already ruled out by other experiments [15]. Additionally, the widths of the h' and χ_2 are calculated via the chosen lifetime $c\tau$ with the formula

$$\Gamma = \frac{c \cdot \hbar}{c\tau}. \tag{5.1}$$

These widths are then used to calculate the corresponding mixing parameters θ and ϵ, respectively.

The partial decay rate of the χ_2 decaying into a χ_1 and an additional lepton pair can, following the derivation in [13], be written as

$$\Gamma(\chi_2 \to \chi_1 \ell^+ \ell^-) = -\epsilon^2 \alpha_{\mathrm{em}} \alpha_{\mathrm{D}} \int_{4m_\ell^2}^{\Delta m^2} \mathrm{d}s f(s), \tag{5.2}$$

with $f(s)$ being defined as

$$f(s) = \frac{|\mathbf{p}_{\chi_1}| \left(s - \Delta m^2\right) \left(2s + (2m(\chi_1) + \Delta m)^2\right) \left(s + 2m_\ell^2\right) \sqrt{s - 4m_\ell^2}}{6\pi m(\chi_2)^2 \sqrt{s^3} \left(s - m(A')^2\right)^2}, \tag{5.3}$$

where $|\mathbf{p}_{\chi_1}|$ is the momentum of the χ_1 in the rest frame of the χ_2 and is calculated via

$$|\mathbf{p}_{\chi_1}| = \sqrt{\left(\frac{s - m(\chi_1)^2 - m(\chi_2)^2}{2m(\chi_2)}\right)^2 - m(\chi_1)^2}. \tag{5.4}$$

Eq. (5.2) can directly be used to numerically calculate the partial decay width into the electron and muon final state. Furthermore, one can obtain the inclusive decay width into hadrons by setting $m_\ell = m_\mu$ and adding the experimentally obtained $R(s)$ ratio [4], defined as $R(s) = \sigma(\mathrm{e}^+\mathrm{e}^- \to \text{hadrons})/\sigma(\mathrm{e}^+\mathrm{e}^- \to \mu^+\mu^-)$, to the integrand. After summing all partial decay widths obtained with Eq. (5.2) to get the total width, I calculate ϵ for a given χ_2 lifetime using Eq. (5.1).

The partial and total decay widths of the $\mathrm{h}' \to \mathrm{x}^+\mathrm{x}^-$ decay are taken from [18]. As they scale with $\sin^2\theta$, for a given dark Higgs lifetime I derive the mixing angle θ with Eq. (5.1) and the known total decay width for the case $\sin\theta = 1$.

For the muon final states, the events are then generated with MadGraph5 using the decay chain $\mathrm{e}^+\mathrm{e}^- \to \mathrm{h}'(\to \mu^+\mu^-)\chi_1\chi_2(\to \chi_1\mathrm{e}^+\mathrm{e}^-)$. Since it is challenging to take care of the hadronization with MadGraph5, for the pion and kaon final state the h' is not decayed within MadGraph5, so the decay chain $\mathrm{e}^+\mathrm{e}^- \to \mathrm{h}'\chi_1\chi_2(\to \chi_1\mathrm{e}^+\mathrm{e}^-)$ is used. The h' is then decayed via EvtGen before running the detector simulation. Note that I assume the h' to be always on-shell because otherwise, one could not reconstruct a very narrow mass peak and consequently could not search for a narrow peak over the SM expectation.

After the event generation, the material interactions and the detector response are simulated using GEANT4 and basf2. The signal events are overlaid with beam background taken directly from data. A detailed description of the beam background sources in Belle II is given in [60, 61]. The beam background overlays are created from data by reading out the detector signals five revolutions after a Bhabha event was triggered by the L1 trigger. It can be seen later in Section 7.1 that the signal efficiency depends on the beam background conditions that vary within the whole data-taking period. To model this effect for each model parameter configuration, six different simulated samples are produced and overlaid with beam background from different data-taking periods with different conditions.

The event generation does not take Initial State Radiation (ISR) effects into account. A discussion on the possible impact of the ISR effects on the candidate selection based on missing energy is given in Section 6.5. The effect of the changing kinematics that would be caused by ISR effects is assumed to be negligible.

5.2 Background Samples

To study the background suppression and estimate the background level after the event selection, several SM background processes that occur in $\mathrm{e}^+\mathrm{e}^-$ collisions must be considered. As I am searching for a process with four tracks in the final state, all SM processes that can mimic a four-track signature have to be considered. The most natural SM processes here are the ones with four tracks in the final state, like for example $\mathrm{e}^+\mathrm{e}^- \to \mathrm{e}^+\mathrm{e}^-\mathrm{e}^+\mathrm{e}^-$ or $\mathrm{e}^+\mathrm{e}^- \to \mathrm{e}^+\mathrm{e}^-\mu^+\mu^-$. While at first glance the processes $\mathrm{e}^+\mathrm{e}^- \to \mathrm{e}^+\mathrm{e}^-(\gamma)$, $\mathrm{e}^+\mathrm{e}^- \to \mu^+\mu^-(\gamma)$, and $\mathrm{e}^+\mathrm{e}^- \to \tau^+\tau^-(\gamma)$ seem to be no relevant background for this analysis, they are due to several reasons. First of all, the decay products of the τ decays can leave multiple tracks in the detector. Additional photons created either by ISR or bremsstrahlung can leave additional tracks in the detector by doing pair conversion. These pair conversions are crucial as they leave a displaced vertex just like the signal I am searching for. Furthermore, there is always the possibility to get additional tracks from the different beam background sources that can be combined with the two tracks arising from these kinds of background processes. With the same reasoning $\mathrm{e}^+\mathrm{e}^- \to hh\gamma$ has to be included as well. This includes the process $\mathrm{e}^+\mathrm{e}^- \to \mathrm{K}^0_\mathrm{S}\mathrm{K}^0_\mathrm{L}\gamma$ which should be highlighted, as in the case the ISR photon does pair conversion it can mimic exactly the signal signature of up to two displaced vertices (K^0_S and $\gamma \to \mathrm{e}^+\mathrm{e}^-$) plus additional missing energy in case the K^0_L is not reconstructed. Being at a B factory the processes $\mathrm{e}^+\mathrm{e}^- \to \mathrm{B}\overline{\mathrm{B}}$ and $\mathrm{e}^+\mathrm{e}^- \to q\bar{q}(\gamma)$ play a role as well, as they contain decay channels with four tracks in the final state. Finally, the process $\mathrm{e}^+\mathrm{e}^- \to \gamma\gamma(\gamma)$, which has a rather large cross section, contributes as a potential background due to pair conversions, as described above.

A full list of the considered SM background processes and the integrated luminosity that is produced for these final states on the $\Upsilon(4\mathrm{S})$ resonance, can be found in Table 5.1. Depending on the final state a combination of the following generators is used: EvtGen, AAFH [62], Tauola [63], TREPS [64], KoralW [65], BabaYaga@NLO [66, 67], KKMC [68], PYTHIA8 [69], and PHOKHARA [70]. These samples are then scaled to the target integrated luminosity of this analysis of $\int \mathcal{L}\mathrm{d}t = 364\,\mathrm{fb}^{-1}$.

Note that, while present in the measured data, not for all of these simulated processes ISR effects are considered in the generator. As can be seen later on in Chapter 10 this can lead to differences when comparing the simulations to the measured data.

Table 5.1: Considered SM background processes and the generator used for the production together with available integrated luminosity. For processes where an additional γ is written, ISR effects are taken into account by the generator.

Process	Generator	Available Int. Luminosity
$\mathrm{e}^+\mathrm{e}^- \rightarrow \mathrm{e}^+\mathrm{e}^-\mathrm{e}^+\mathrm{e}^-$	AAFH	$361.0\,\mathrm{fb}^{-1}$
$\mathrm{e}^+\mathrm{e}^- \rightarrow \mathrm{e}^+\mathrm{e}^-\mu^+\mu^-$	AAFH	$361.0\,\mathrm{fb}^{-1}$
$\mathrm{e}^+\mathrm{e}^- \rightarrow \ell^+\ell^- XX$		$361.0\,\mathrm{fb}^{-1}$
$\mathrm{e}^+\mathrm{e}^- \rightarrow \mathrm{e}^+\mathrm{e}^-\tau^+\tau^-$	AAFH + Tauola	
$\mathrm{e}^+\mathrm{e}^- \rightarrow \mathrm{e}^+\mathrm{e}^-\pi^+\pi^-$	TREPS	
$\mathrm{e}^+\mathrm{e}^- \rightarrow \mathrm{e}^+\mathrm{e}^-\mathrm{K}^+\mathrm{K}^-$	TREPS	
$\mathrm{e}^+\mathrm{e}^- \rightarrow \mathrm{e}^+\mathrm{e}^-\overline{\mathrm{p}}\mathrm{p}$	TREPS	
$\mathrm{e}^+\mathrm{e}^- \rightarrow \mu^+\mu^-\mu^+\mu^-$	AAFH	
$\mathrm{e}^+\mathrm{e}^- \rightarrow \mu^+\mu^-\tau^+\tau^-$	AAFH + Tauola	
$\mathrm{e}^+\mathrm{e}^- \rightarrow \tau^+\tau^-\tau^+\tau^-$	KoralW + Tauola	
$\mathrm{e}^+\mathrm{e}^- \rightarrow \mathrm{e}^+\mathrm{e}^-(\gamma)$	BabaYaga@NLO	$36.1\,\mathrm{fb}^{-1}$
$\mathrm{e}^+\mathrm{e}^- \rightarrow \mu^+\mu^-(\gamma)$	KKMC	$361.0\,\mathrm{fb}^{-1}$
$\mathrm{e}^+\mathrm{e}^- \rightarrow \tau^+\tau^-(\gamma)$	KKMC + Tauola	$1444.0\,\mathrm{fb}^{-1}$
$\mathrm{e}^+\mathrm{e}^- \rightarrow \mathrm{B}\overline{\mathrm{B}}$	EvtGen + PYTHIA8	$1444.0\,\mathrm{fb}^{-1}$
$\mathrm{e}^+\mathrm{e}^- \rightarrow q\bar{q}(\gamma)$	KKMC + PYTHIA8	$1444.0\,\mathrm{fb}^{-1}$
$\mathrm{e}^+\mathrm{e}^- \rightarrow hh\gamma$		$361.0\,\mathrm{fb}^{-1}$
$\mathrm{e}^+\mathrm{e}^- \rightarrow \pi^+\pi^-\gamma$	PHOKHARA	
$\mathrm{e}^+\mathrm{e}^- \rightarrow \pi^+\pi^-\pi^0\gamma$	PHOKHARA	
$\mathrm{e}^+\mathrm{e}^- \rightarrow \mathrm{K}^+\mathrm{K}^-\gamma$	PHOKHARA	
$\mathrm{e}^+\mathrm{e}^- \rightarrow \mathrm{K}^0_\mathrm{S}\mathrm{K}^0_\mathrm{L}\gamma$	PHOKHARA	
$\mathrm{e}^+\mathrm{e}^- \rightarrow \gamma\gamma(\gamma)$	BabaYaga@NLO	$722.0\,\mathrm{fb}^{-1}$

Chapter 6

Reconstruction and Event Selection

In this section, I describe the reconstruction steps and the selections applied to the events to distinguish signal from SM background processes. Starting with the reconstruction of final state particles in Section 6.1, the chosen requirements on electrons, muons, pions, and kaons are described and I study the PID performance. Afterwards, the reconstruction of the two vertices (h' and χ_2) is explained in Section 6.2. To suppress pair conversion, in Section 6.3 selection requirements on the daughter opening angle between the tracks forming the h' and χ_2 candidates are described. Furthermore, Section 6.4 describes how the pointiness of the h' decay is exploited to further distinguish signal from background processes. Section 6.5 deals with the missing energy of the events and the reconstructed mass of the $\mathrm{e}^+\mathrm{e}^-$ pair. The rest-of-event (ROE) is studied in Section 6.6 and I use this to further separate signal from SM background processes. The contributions from background processes including K^0_S and Λ decays are studied in Section 6.7 and the mass veto to suppress these contributions is described there. Finally, a best candidate selection (BCS) is described in Section 6.8.

Table 6.1 provides a summary of the above-mentioned selection requirements that will be described throughout this chapter. All these criteria are developed by studies on the simulated samples described in Chapter 5. I derive additional requirements later on by studies of the control regions in recorded data. These are explained in detail in Chapter 10 and summarised in Table 6.2.

If not stated otherwise, the requirements derived in this section are optimised using the Punzi figure of merit (Punzi FOM) [71], which is defined as

$$\frac{\epsilon_{\mathrm{sig}}}{a/2 + \sqrt{N_{\mathrm{bkg}}}}, \tag{6.1}$$

with the signal efficiency ϵ_{sig} and the number of background events N_{bkg}. The parameter a is chosen to be 5 for this analysis as a corresponds to the number of standard deviations in a one-sided Gaussian test. The Punzi FOM is a powerful tool to estimate the sensitivity whenever the total number of signal events to expect is unknown and only the signal efficiency is available, as it is the case in the presented analysis. This optimisation is

Table 6.1: Summary of all selection requirements that are derived from studies on simulated signal and SM background samples. The requirements are split according to the reconstruction channel to which they are applied. The variables and the optimisation of the requirements are explained in detail throughout Chapter 6.

<table>
<tr><th colspan="3">Reconstruction Channel</th></tr>
<tr><th>$\mathrm{h}' \to \mu^+\mu^-$</th><th>$\mathrm{h}' \to \mathrm{K}^+\mathrm{K}^-$</th><th>$\mathrm{h}' \to \pi^+\pi^-$</th></tr>
<tr><td colspan="3">$N_{\mathrm{hits}}^{\mathrm{PXD}} + N_{\mathrm{hits}}^{\mathrm{SVD}} + N_{\mathrm{hits}}^{\mathrm{CDC}} > 20$</td></tr>
<tr><td colspan="3">$\mathrm{PID}_{\mathrm{BDT}}^{\mathrm{e}} > 0.5$</td></tr>
<tr><td>$\mathrm{PID}_{\mathrm{BDT}}^{\mu} > 0.5$</td><td>$\mathrm{PID}_{\mathrm{LH}}^{\mathrm{K}} > 0.5$</td><td>$\mathrm{PID}_{\mathrm{LH}}^{\pi} > 0.5$</td></tr>
<tr><td colspan="3">$\rho_{\mathrm{h}'} > 0.2\,\mathrm{cm}$ or $\rho_{\chi_2} > 0.2\,\mathrm{cm}$</td></tr>
<tr><td colspan="3">$\rho_{\mathrm{h}'} < 110\,\mathrm{cm}$ or $\rho_{\chi_2} < 110\,\mathrm{cm}$</td></tr>
<tr><td colspan="3">$\mathcal{P}_{\mathrm{vertex}}^{\mathrm{h}'} > 0.001$ and $\mathcal{P}_{\mathrm{vertex}}^{\chi 2} > 0.001$</td></tr>
<tr><td colspan="3">$37\,^{\circ} < \theta_{\mathrm{KLM}}^{\mathrm{ext}} < 122\,^{\circ}$ or $37\,^{\circ} < \theta_{\mathrm{KLM}}^{\mathrm{ext}} < 122\,^{\circ}$</td></tr>
<tr><td colspan="2"></td><td>$18\,^{\circ} < \theta_{\mathrm{KLM}}^{\mathrm{ext}} < 155\,^{\circ}$ for all tracks</td></tr>
<tr><td colspan="3">$\alpha_{\mathrm{xx}}^{\mathrm{h}'} > 0.1$ and $\alpha_{\mathrm{ee}}^{\chi 2} > 0.1$</td></tr>
<tr><td colspan="3">$-\log(1 - \cos(\Delta\alpha_{\mathbf{x},\mathbf{p}}^{\mathrm{h}'})) > 7.5$</td></tr>
<tr><td colspan="3">$E_{\mathrm{extra}}(\mathrm{neutral}) < 1\,\mathrm{GeV}$</td></tr>
<tr><td colspan="3">$N_{\mathrm{tracks}}^{\mathrm{ROE}} = 0$</td></tr>
<tr><td colspan="3">$E_{\mathrm{miss}} > 0.4\,\mathrm{GeV}$</td></tr>
<tr><td colspan="3">$M_{\mathrm{ee}}^{\chi 2} < 2.5\,\mathrm{GeV/c^2}$</td></tr>
<tr><td colspan="3">not $467.2\,\mathrm{MeV/c^2} \leq M_{\pi\pi}^{\mathrm{h}'} \leq 528.8\,\mathrm{MeV/c^2}$</td></tr>
<tr><td></td><td>not $1.06\,\mathrm{GeV/c^2} < M_{\mathrm{p}\pi}^{\mathrm{h}'} < 1.15\,\mathrm{GeV/c^2}$</td><td>not $0.977\,\mathrm{GeV/c^2} < M_{\mathrm{KK}}^{\mathrm{h}'} < 1.061\,\mathrm{GeV/c^2}$</td></tr>
</table>

Table 6.2: Summary of all selection requirements that are derived from studies on the data control regions described in Chapter 10. The requirements are split according to the reconstruction channel to which they are applied.

Reconstruction Channel		
$\mathrm{h}' \to \mu^+\mu^-$	$\mathrm{h}' \to \mathrm{K}^+\mathrm{K}^-$	$\mathrm{h}' \to \pi^+\pi^-$
$E_{\mathrm{hie}} > 1.5\,\mathrm{GeV}$		
$\Delta\alpha_{\mathrm{KLM}} > 0.5$		
$\alpha_{\mathrm{xx}}^{\mathrm{h}'} < 3.0$		
$E/p > 0.6$ for the electron tracks		
$0.4 < \theta_{\mathrm{miss}}^{\mathrm{lab}} < 2.6$		

done using an iterative approach. All selections are optimised with and without all other requirements from Tables 6.1 and 6.2 applied, using the at a given point during the optimisation current best value for all individual requirements. This procedure is repeated until the optimal values converge. In the presented work, I only show the result of the last iteration of this optimisation process. For some of the selection requirements, the optimal selection requirement depends on the choice of the model parameters. In that case, to avoid unnecessary complexity, some model parameter configurations are favored taking for example already existing limits on the signature of interest into account. Ultimately, this allows me to choose the requirements for the event selection independent of the model parameters.

6.1 Final State Particles

Every particle that typically does not decay within the Belle II detector is considered to be a Final State Particle (FSP). This list of particles can be separated into charged particles that are mainly reconstructed with the tracking detectors and neutral particles that are reconstructed via depositions in the ECL or KLM.

As the signature I am looking for consists of four charged particles in the final state the main focus is on tracks. Getting from depositions in the tracking detectors to reconstructed charged particles takes two steps: finding the tracks and then fitting the curvature to derive the particle momentum. In Belle II the track-finding is done using a Legendre transformation as described in detail in [72]. One of the main features of this algorithm is the assumption that the tracks originate from the IP. As I search for displaced vertices and therefore tracks that do not originate from the IP, this assumption does not hold and a significant efficiency drop can be observed for farther displaced decays of the h' and χ_2. Fig. 6.1 shows the effect for the h' decay products. In case a track is found the momentum of the particle is derived via fitting the curvature using a deterministic

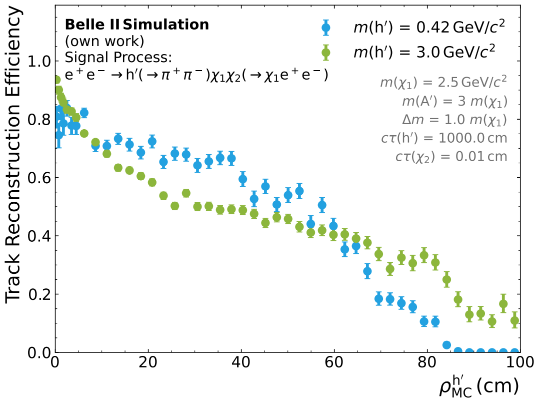

Figure 6.1: Track reconstruction efficiency of pion tracks as a function of the true transverse distance to the IP. The pions originate from a h' decay with a mass hypothesis of $m(\mathrm{h}') = 0.42\,\mathrm{GeV/c^2}$ (cyan) and $m(\mathrm{h}') = 3.0\,\mathrm{GeV/c^2}$ (light green). No selection has been applied on the tracks, to get an unbiased reconstruction efficiency.

annealing filter (DAF) within GenFit [73]. Not all tracks that are found and fitted by the tracking algorithms correspond to tracks that have been created by the primary interactions, but can also originate from secondary interactions with the detector material or beam background depositions. To reduce the amount of these contributions I select only tracks that have at least 20 associated tracking hits, i.e. the sum of PXD, SVD, and CDC hits.

The flavour of the FSP is not determined during the track reconstruction but by taking information of all subdetectors into account. Following the motivation about the included final states in Chapter 4, the FSPs considered in this analysis are $\mathrm{e}^\pm$, $\mu^\pm$, $\pi^\pm$, and $\mathrm{K}^\pm$. For the identification of electrons and muons, a Boosted Decision Tree (BDT)-based classifier is used. The respective classifier output score has to be greater than 0.5 for a track to be considered an electron or muon. Hadrons (pions and kaons) are selected with a likelihood-based PID. For a given particle flavour f the PID score is defined by taking the likelihood $\mathcal{L}$ of all particle hypotheses into account

$$\mathrm{PID_{LH}}(f) = \frac{\mathcal{L}_f}{\mathcal{L}_\mathrm{e} + \mathcal{L}_\mu + \mathcal{L}_\pi + \mathcal{L}_\mathrm{K} + \mathcal{L}_\mathrm{p} + \mathcal{L}_\mathrm{d}}, \tag{6.2}$$

where the indices denote electron, muon, pion, kaon, proton, or deuteron, respectively. I select pions with $\mathrm{PID_{LH}}(\pi) > 0.5$ and kaons with $\mathrm{PID_{LH}}(\mathrm{K}) > 0.5$. Additionally, I investigated the performance of classifying pions and kaons using a neural network (NN). While in both the $\mathrm{h}' \to \pi^+\pi^-$ and $\mathrm{h}' \to \mathrm{K}^+\mathrm{K}^-$ reconstruction channel the NN based PID classifier shows a very good performance separating pions from kaons, a large contribution from $\mathrm{e} \to \pi$ and $\mathrm{e} \to \mathrm{K}$ misidentification is observed (see Fig. 6.2). This means that when using the NN-based PID classifier, a lot of true electrons get the pion or kaon flavour (instead of the electron flavour) assigned by the reconstruction and are therefore misidentified. Additionally, the $\pi \to \mathrm{K}$ misidentification rate is also significantly larger for

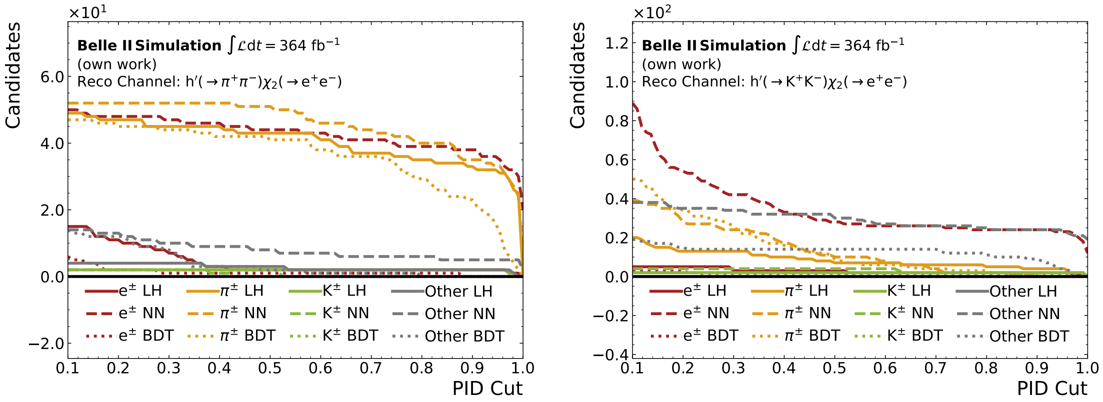

Figure 6.2: Number of candidates per truth-matched particle type as a function of the cut value on the pion PID (left) or kaon PID (right) applied to both daughters of the h′. The left side shows the pion reconstruction channel, while the right side shows the kaon reconstruction channel. The different line styles represent the three different PID classifiers: Likelihood (LH), neural network (NN), and boosted decision tree (BDT). Besides the PID requirement all other cuts have been applied beforehand. For a perfect identification in the left plot, all lines but the one for pions (orange) should be zero. Similar in the right plot, all lines but the one for kaons (green) should be zero if PID would work perfectly.

the NN-based PID classifier compared to the likelihood-based approach. This results in a higher background level that is visible when optimising the Punzi FOM in Figs. C.9 and C.10 where in the $h' \to K^+K^-$ reconstruction channel the likelihood-based PID outperforms both the NN and BDT-based PID algorithms for the identification of kaons. Furthermore, in the $h' \to \pi^+\pi^-$ reconstruction channel the likelihood-based PID outperforms the NN-based algorithm and shows similar performance as the BDT-based algorithm for the identification of pions.

6.1.1 PID Performance per Detector Region

After applying the respective PID requirements on the FSPs, one can observe a high $e \to \pi$ and $e \to K$ misidentification rate. As the PID takes information of nearly all subdetectors into account, to understand this misidentification rate it is of interest in which region of the detector the particles are located. I distinguish them by the position where the particles hit the KLM. As illustrated in Fig. 6.3, these positions are derived by extrapolating the track helices to the KLM boundary, which I assume to be cylindrical for this purpose. Afterwards, the extrapolated polar angle $\theta_{\mathrm{KLM}}^{\mathrm{ext}}$ describes the vector from the IP to this extrapolated position and can be compared with the KLM acceptance regions. This procedure is necessary as the usual polar angle θ is calculated with respect to the vertex position and therefore does depend on the latter, while $\theta_{\mathrm{KLM}}^{\mathrm{ext}}$ is not, which makes a comparison between different candidates possible.

Looking into where these misidentified electrons hit the KLM, it is observed that most

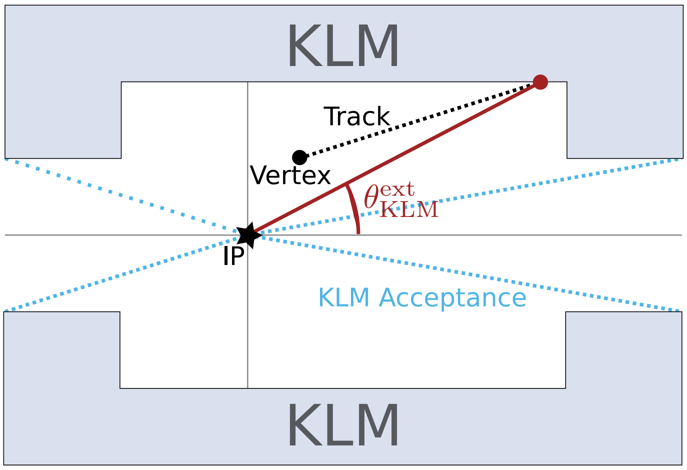

Figure 6.3: Illustration of the procedure to calculate the polar angle of the track extrapolated to the KLM. Using the helix parameters of the track the trajectory is extrapolated from the decay vertex (black circle) to the KLM boundary. The vector between the IP (black star) and this extrapolated position on the inner KLM surface (red circle) is illustrated with a red line. $\theta_{\mathrm{KLM}}^{\mathrm{ext}}$ describes the angle between this vector and the z-axis. The total angular acceptance of the KLM is shown with dashed lines in cyan.

of them either hit the endcaps of the KLM or do not hit the KLM at all (see Fig. 6.4). This leads to misidentification using the likelihood-based pion and kaon PID. While in the $\mathrm{h}' \to \mu^+\mu^-$ reconstruction channel the misidentification in these regions is not as big of a problem as for the other two reconstruction channels, one can still observe quite some $\pi \to \mu$ misidentification there.

The misidentification rate is lowered by requiring at least one of the two dark Higgs daughters to fulfil $\theta_{\mathrm{KLM}}^{\mathrm{ext}} > 37\,^{\circ}$, which describes the edge of the forward KLM endcap, and $\theta_{\mathrm{KLM}}^{\mathrm{ext}} < 122\,^{\circ}$, which is the edge of the backward KLM endcap. So at least one of the daughters is required to hit either the barrel or the overlap regions of the KLM.

Similar to the daughters of the h', the performance of the PID on the daughter electrons of the χ_2 is checked in Fig. 6.5. It can be seen that the selection on the BDT-based electron PID results in a very pure sample mainly reconstructing only true electrons. Nevertheless, in the case where the h' is reconstructed from two pions, there is a small contribution where true pions are reconstructed as electron candidates ($\pi \to \mathrm{e}$ misidentification).

6.1.2 PID Performance per Lifetime

Checking the PID performance as a function of the displacement of the dark Higgs decay shows that the performance of correctly identifying the particles gets worse the further displaced the dark Higgs decays are. As can be seen in Fig. 6.6, for larger lifetimes a larger fraction of events end up being reconstructed in the wrong reconstruction channel. This is caused by the impact of the TOP detector on the PID, which tends to assume heavier masses for the tracks depending on the lifetime of the mother particle. The issue

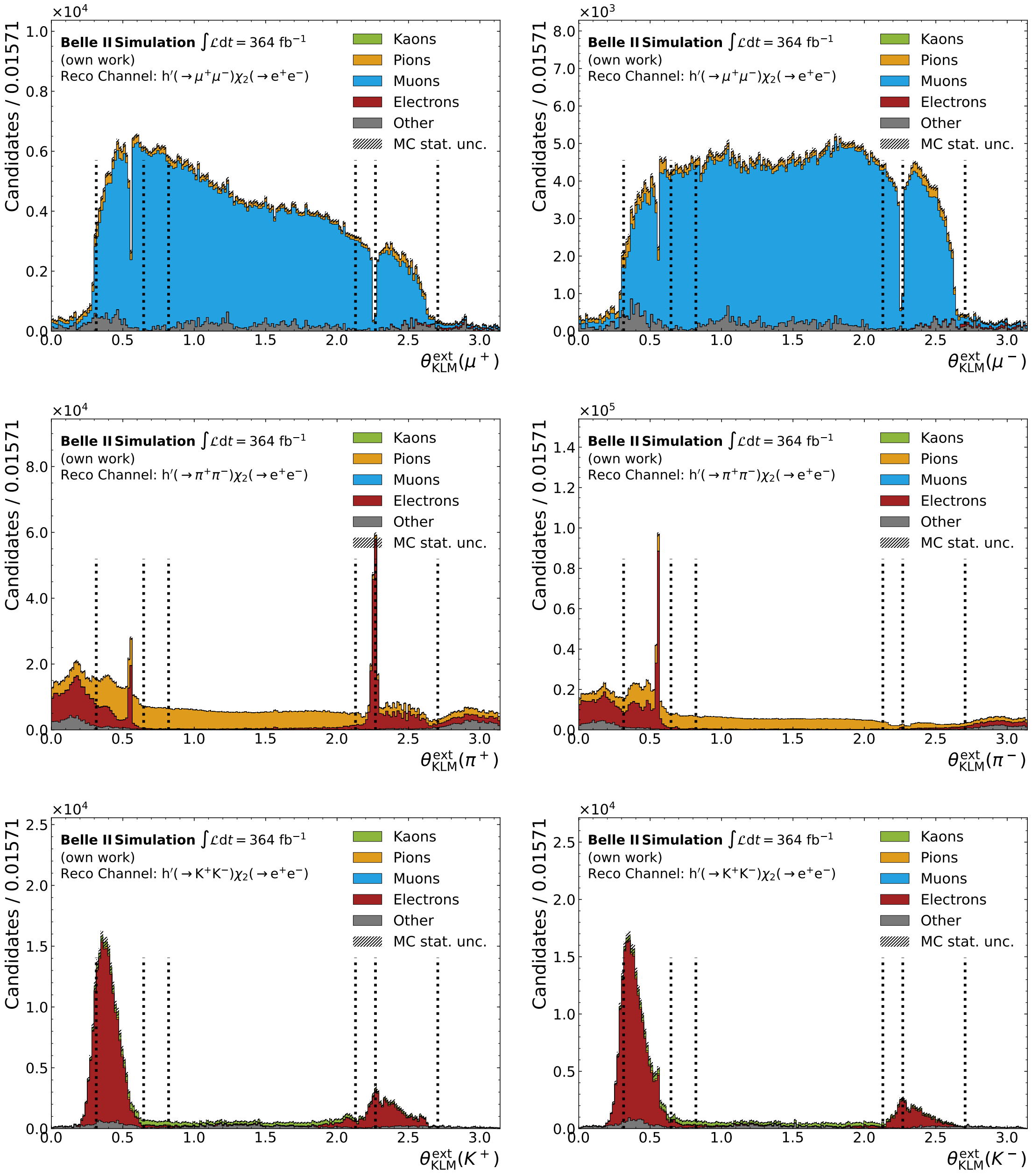

Figure 6.4: $\theta^{\text{ext}}_{\text{KLM}}$ for different truth-matched particles in the three different reconstruction channels $\text{h}' \to \mu^+\mu^-$, $\text{h}' \to \pi^+\pi^-$, and $\text{h}' \to \text{K}^+\text{K}^-$. The left side shows the polar angle of the track helix extrapolated the KLM of the positively charged daughter of the reconstructed h′, while the right side shows the negatively charged daughter. The black dashed vertical lines represent the borders of the klm regions. In these plots selections are only applied on the vertex position, number of tracking hits and the respective PID.

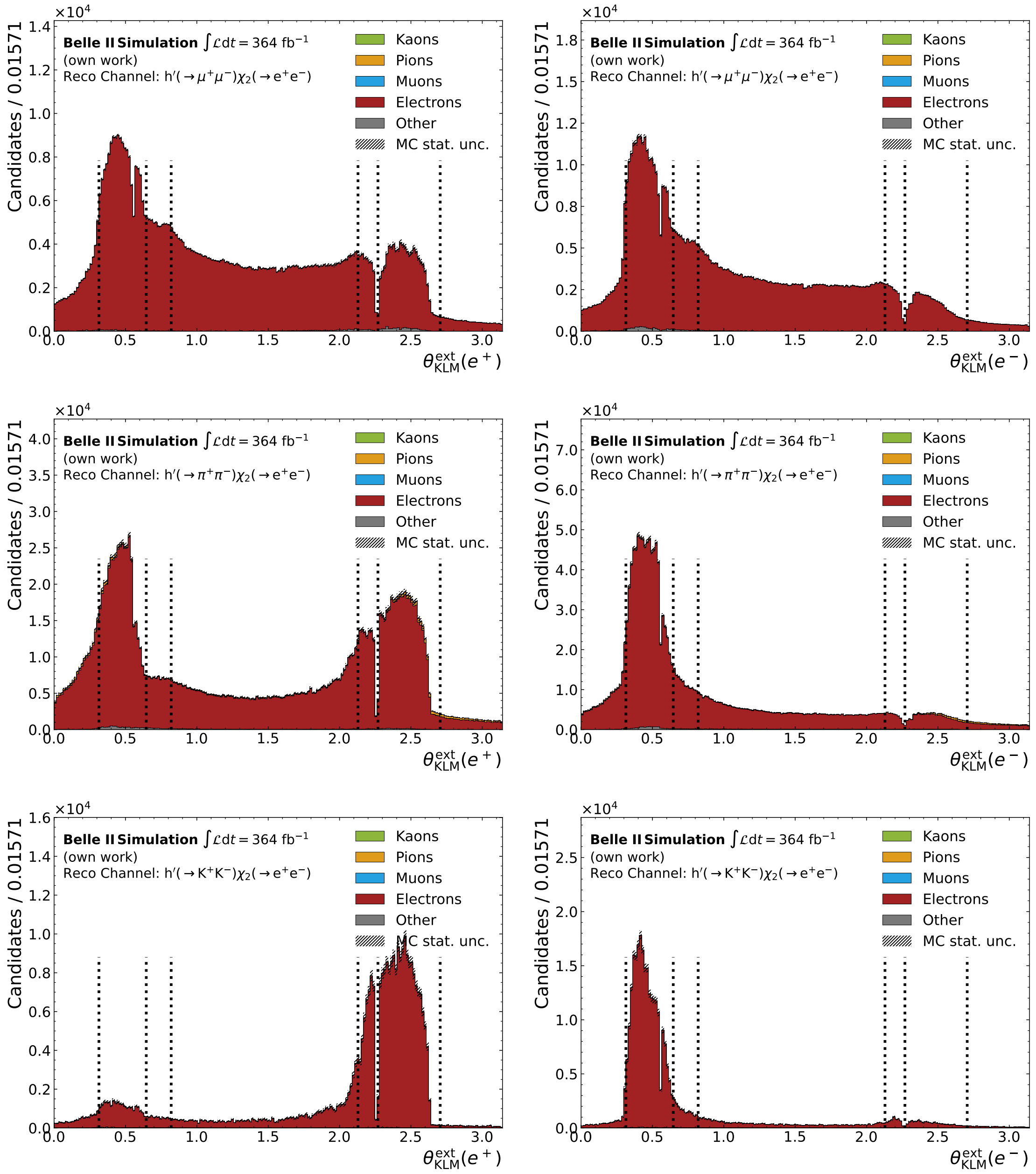

Figure 6.5: $\theta_{\mathrm{KLM}}^{\mathrm{ext}}$ for different truth-matched particles in the three different reconstruction channels ($\mathrm{h}' \rightarrow \mu^+\mu^-$, $\mathrm{h}' \rightarrow \pi^+\pi^-$, and $\mathrm{h}' \rightarrow \mathrm{K}^+\mathrm{K}^-$) with the χ_2 always being reconstructed from electrons. The left side shows the polar angle of the track helix extrapolated the KLM of the reconstructed positron, while the right side shows the reconstructed electron. The black dashed vertical lines represent the borders of the KLM regions. In these plots selections are only applied on the vertex position, number of tracking hits and the respective PID.

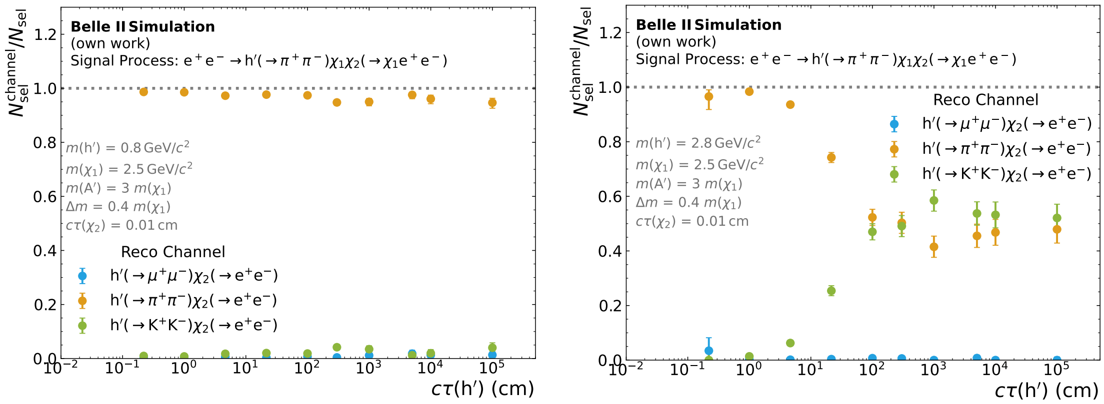

Figure 6.6: Fraction of $e^+e^- \to h'(\to \pi^+\pi^-)\chi_1\chi_2(\to \chi_1 e^+e^-)$ signal events reconstructed in the different reconstruction channels: $h' \to \mu^+\mu^-$ (cyan), $h' \to \pi^+\pi^-$ (orange), and $h' \to K^+K^-$ (light green). The fraction is shown as a function of the h' lifetime $c\tau(h')$. The left plot assumes a h' mass of $m(h') = 0.8\,\mathrm{GeV/c^2}$, while in the right plot, the dark Higgs is simulated with a mass of $m(h') = 2.8\,\mathrm{GeV/c^2}$. All other model parameters are fixed to the values given in the plots. The figures show the cross-feed of $h' \to \pi^+\pi^-$ signal events into the $h' \to K^+K^-$ reconstruction channel due to $\pi \to K$ misidentification for large dark Higgs boson masses and lifetimes.

is especially present for the $e^+e^- \to h'(\to \pi^+\pi^-)\chi_1\chi_2(\to \chi_1 e^+e^-)$ signal process. In the heavily displaced case, a significant fraction of these events are falsely reconstructed in the $h' \to K^+K^-$ reconstruction channel. The effect does not only depend on the lifetime of the dark Higgs boson but also on the mass. It can clearly be seen in Fig. 6.7 that for larger h' mass hypotheses the fraction of events that end up in the wrong reconstruction channel becomes larger. Nevertheless, besides lowering the reconstruction efficiency, this cross-feed from $\pi \to K$ misidentification is not a problem as long as the contributions from the different reconstruction channels do not overlap in the signal windows of the reconstructed mass. This requirement is fulfilled as can be seen in Fig. 6.7.

As the information from the TOP detector is causing this misidentification problem, in Fig. 6.8 I compare the performance of the likelihood-based PID when excluding the TOP to the other PID classifiers. It is observed that while the lifetime effect vanishes the overall performance is greatly diminished and therefore this variable is not used for the described analysis.

6.2 Vertex Reconstruction

The signature I am studying in this thesis contains two vertices, h' and χ_2, where the h' vertex is pointing back to the IP and the χ_2 vertex is non-pointing due to the χ_1 in the decay which cannot be reconstructed. As already mentioned in Chapter 4, for the h' I consider decays into an oppositely charged pair of muons, pions, or kaons in the reconstruction. To allow for the usage of ECL L1 trigger lines (see Section 7.2 for more details) the

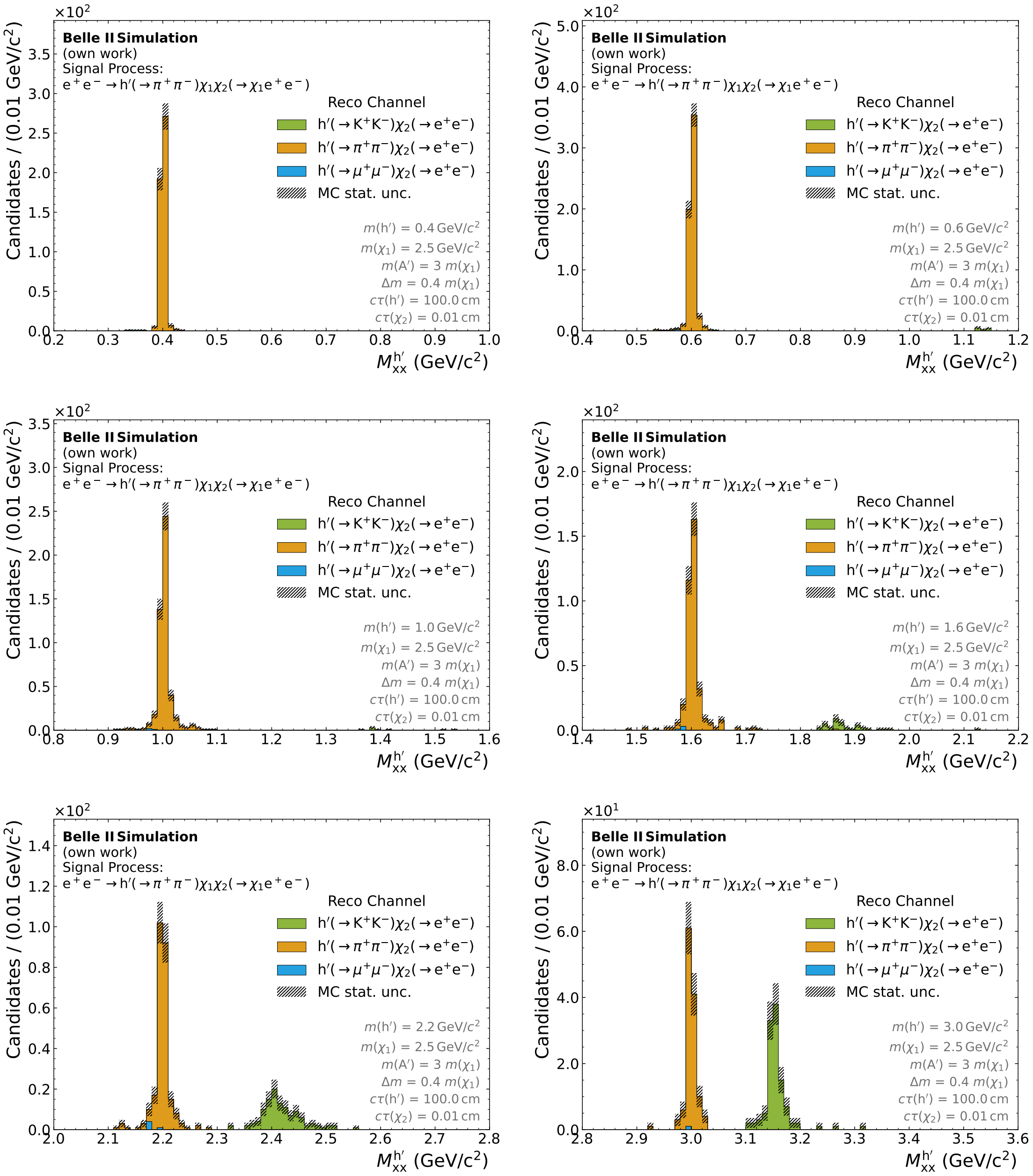

Figure 6.7: Reconstructed dark Higgs mass distributions for the reconstruction of $e^+e^- \to h'(\to \pi^+\pi^-)\chi_1\chi_2(\to \chi_1 e^+e^-)$ signal divided into the three reconstruction channels: $h' \to \mu^+\mu^-$ (cyan), $h' \to \pi^+\pi^-$ (orange), and $h' \to K^+K^-$ (light green). The plots show different mass hypotheses of the h', while the lifetime of the dark Higgs boson is fixed to $c\tau(h') = 100\,\text{cm}$.

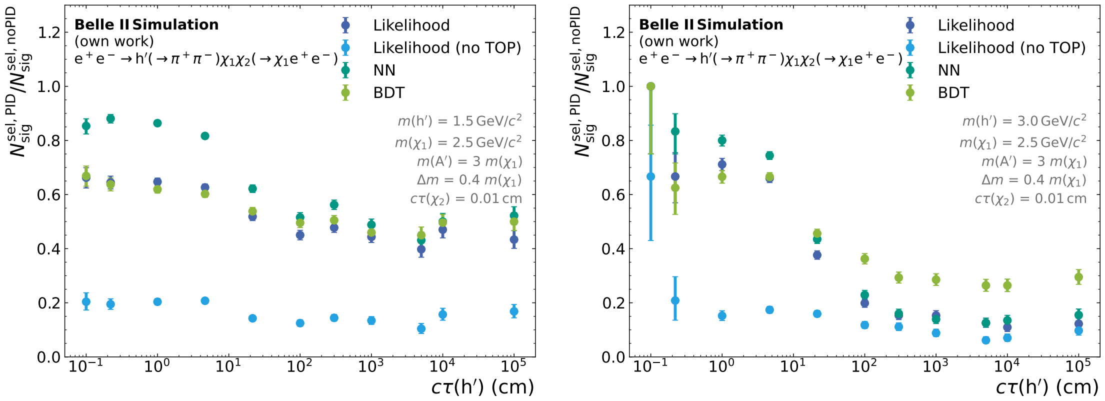

Figure 6.8: Efficiency of the PID requirement PID > 0.5 applied on both h' daughter tracks of the $\mathrm{h}' \rightarrow \pi^+\pi^-$ signal process in the $\mathrm{h}' \rightarrow \pi^+\pi^-$ reconstruction channel for different PID definitions. The left plot shows a dark Higgs mass hypothesis of $m(\mathrm{h}') = 1.5\,\mathrm{GeV/c^2}$, while in the right plot $m(\mathrm{h}') = 3.0\,\mathrm{GeV/c^2}$ is assumed. All other cuts described in Table 6.1 are applied.

second vertex (χ_2) is reconstructed from an electron-positron pair. I make this choice as electrons, contrary to the other FSPs, deposit nearly always their whole energy in the ECL which drastically increases the chances of an event being selected by the L1 trigger. After reconstructing the vertices, I perform a vertex fit [74] on both vertices to improve the vertex resolution. To suppress background contributions from randomly combined tracks both the fit on the h' and the χ_2 candidate are required to yield a probability score $\mathcal{P}_{\mathrm{vertex}}$ of above 0.001, otherwise the candidate is discarded. This requirement is motivated by looking at the signal distributions shown in Fig. 6.9 where one can see that this selection is located in the tail of the distribution and therefore does not reject a significant amount of signal.

Additionally, there is a selection performed on the position of the two reconstructed vertices. Since the region close to the IP is expected to be dominated by SM backgrounds, which can be seen in Fig. 6.10, at least one of the two vertices is required to decay with a sufficient displacement of $\rho > 0.2\,\mathrm{cm}$. Here ρ describes the transverse distance to the IP calculated via $\rho = \sqrt{x^2 + y^2}$, with x and y being the x and y-coordinates of the reconstructed vertex. This requirement is motivated by looking into the ρ distributions of a reconstructed pair of tracks from different SM background samples (see Fig. 6.10). As the aim is to suppress SM contributions, where nearly all tracks originate from the IP, for this specific study a requirement on the impact parameters $\rho_{\mathrm{track}} < 2\,\mathrm{cm}$ and $|z_{\mathrm{track}}| < 5\,\mathrm{cm}$, that are measured with respect to the tracks point of closest approach (POCA), is applied on the tracks[*]. It can be seen that the requirement of $\rho > 0.2\,\mathrm{cm}$ is above the peak of the contribution to ensure that a large amount of the SM contributions are removed

---

[*] These selections on the impact parameters of the track, $\rho_{\mathrm{track}} <$ and $|z_{\mathrm{track}}|$, are only applied to study the ρ distributions on simulated SM background samples. The requirements are not applied to tracks during the reconstruction process of the analysis described here.

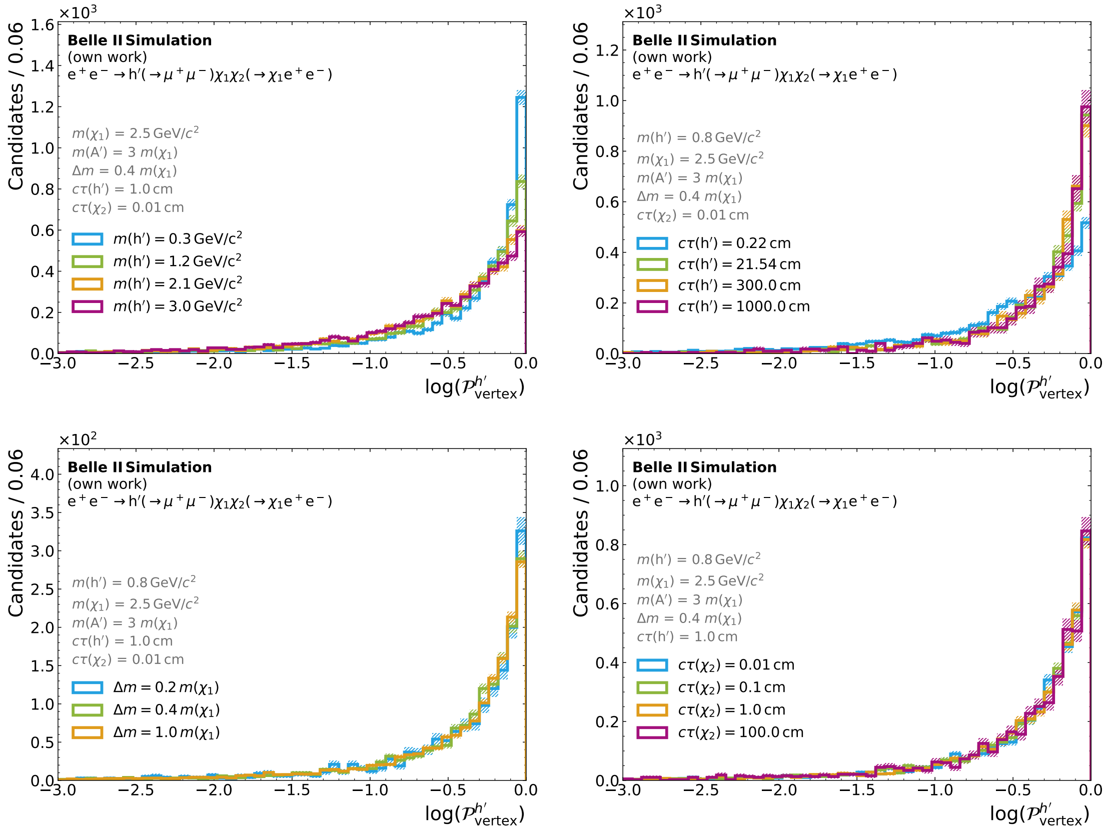

Figure 6.9: Signal distributions of the vertex fit probability $\mathcal{P}_{\text{vertex}}$ of the h' vertex for the $\mathrm{e}^+\mathrm{e}^- \to \mathrm{h}'(\to \mu^+\mu^-)\chi_1\chi_2(\to \chi_1\mathrm{e}^+\mathrm{e}^-)$ signal process. For better visualisation, the vertex fit probability is shown on a logarithmic scale. The selection is placed at $\log(\mathcal{P}_{\text{vertex}}) > -3$. The distributions are shown for different variations of the model parameters, h' mass (upper left), h' lifetime (upper right), mass splitting (lower left), and χ_2 lifetime (lower right). The corresponding distributions for the reconstructed χ_2 vertex can be found in Fig. B.1 in the appendix.

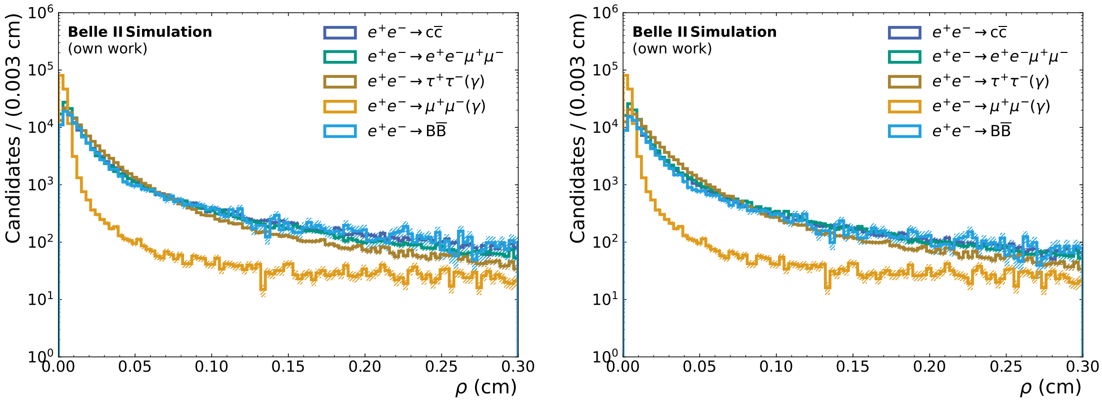

Figure 6.10: Transverse distance of the reconstructed vertex from the IP for different simulated SM background samples. The plots only show a subset of the samples in arbitrary units. In the left plot, the vertices are reconstructed from a pair of tracks with the requirement of $\rho_{\text{track}} < 2\,\text{cm}$ and $|z_{\text{track}}| < 5\,\text{cm}$ applied for both tracks, while these requirements are removed in the right plot. Additionally, a vertex fit is applied and the vertex fit probability $\mathcal{P}_{\text{vertex}}$ has to be above 0.001 (in both cases).

by this selection. As this requirement is chosen rather conservatively, the impact on the sensitivity of loosening the requirement to $\rho > 0.1\,\text{cm}$ is studied in Fig. 6.11. It can be seen that the loose requirement nearly has no impact on the sensitivity. Chosing a loose requirement here would increase the sensitivity to more prompt dark Higgs decays (larger mixing angles θ). As with the selection of $\rho > 0.2\,\text{cm}$ the full range up to the excluded region is already covered, there is no need to further loosen this requirement. Therefore, the loose selection is not considered in this analysis. Additionally, to suppress contributions from misreconstruction both vertices must be located within the CDC, so $\rho < 110\,\text{cm}$ for both vertices in addition to at least one of them being displaced with more than $\rho > 0.2\,\text{cm}$.

The required number of tracking hits from Section 6.1 implies an indirect selection on the maximal displacement that can be achieved in the vertex reconstruction. In the worst case, where the track is straight and in $\theta = 90^\circ$ direction, 20 CDC hits in the outer part correspond to a ρ of about 35 cm. So in that case the maximal displacement that could be achieved would be around 75 cm. This number increases for more shallow tracks and tracks with less momentum and therefore a larger curvature.

6.3 Suppressing Pair Conversions

One of the SM background processes that can mimic the signal signature is the conversion of a photon into an e^+e^- pair, as this process has the same signature as a particle that is invisible to tracking detectors and decays into a pair of charged tracks within the tracking geometry. This is especially relevant for the reconstructed χ_2 vertex, as I reconstruct the χ_2 candidate from an e^+e^- pair, where, unlike from the h$'$ vertex that is not reconstructed from

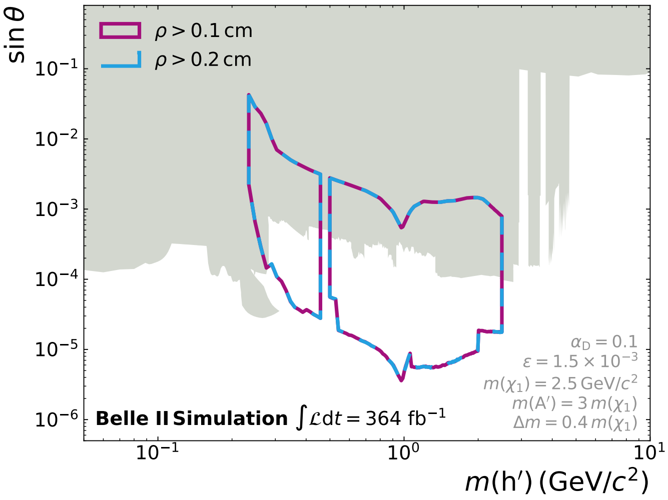

Figure 6.11: Expected sensitivity for an example model parameter configuration for the displacement selection used in this analysis, $\rho > 0.2\,\mathrm{cm}$ (cyan), and the looser requirement $\rho > 0.1\,\mathrm{cm}$ (purple). The already excluded parameter space (see Section 2.5) is shown in grey.

electrons, PID can not help to suppress the pair conversions. As the photon is massless, the e^+e^- pair created in the conversion mostly has a small opening angle α_{ee} between the electrons. Therefore, I use this opening angle to distinguish the pair conversions from signal vertices. Fig. 6.12 shows the opening angle distributions of the e^+e^- pair used to reconstruct the χ_2 candidate for both the signal process and SM background. These plots show that for signal the opening angle between the electrons only depends on the mass splitting Δm, as this controls the phase space available to the e^+e^- pair. The opening angle between the electrons indirectly depends on the mass of the χ_1, as in this thesis, the mass splitting is always chosen as multiples of the χ_1 mass. It can be seen that applying a minimal requirement on α_{ee} can suppress nearly all contributions of pair conversion backgrounds while preserving a very large fraction of the signal process over the whole model parameter space.

The selection is optimised using the Punzi FOM. As can be seen in Fig. C.1 in the appendix, the optimal selection depends on the mass splitting Δm between the χ_1 and χ_2, as this is the only model parameter the variable is sensitive to. Nevertheless, all the scans yield quite similar results. To simplify the analysis by not having different requirements for different model parameter configurations and as the Punzi FOM is not overly sensitive around this value, I choose a requirement of $\alpha_{ee}^{\chi 2} > 0.1$, independent of the model parameters. This value still yields the best discrimination even after applying all other selection criteria, as can be seen in Fig. C.2 in the appendix.

As pair conversions only happen in the presence of material, another option to suppress these contributions would be via the radial position of the vertex. The radial vertex position of the pair conversions is shown in Fig. B.4 in the appendix. One can clearly observe the

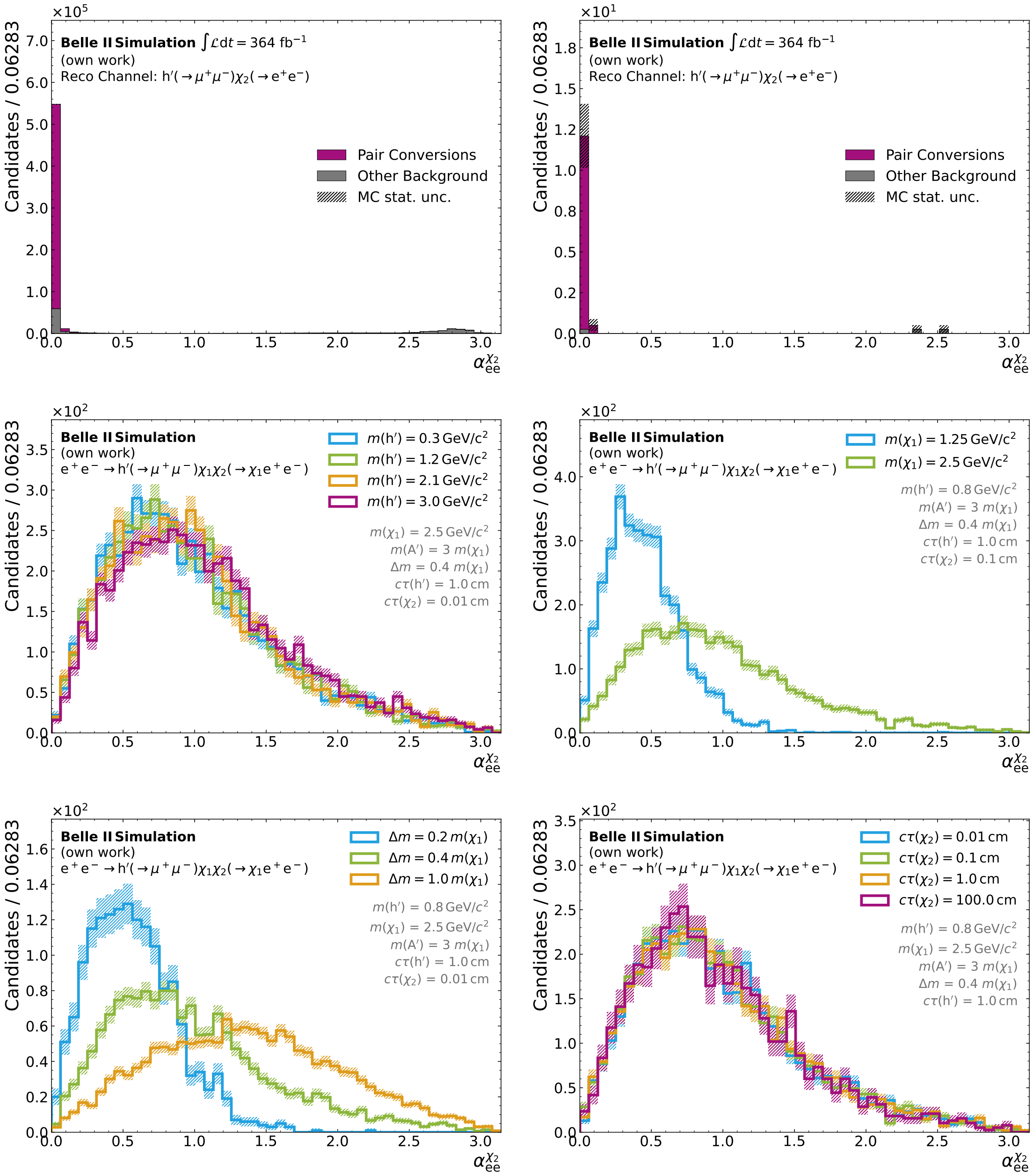

Figure 6.12: Background (top) and signal (center and bottom) distributions of the opening angle between the two reconstructed electrons of the χ_2 candidate. For the signal, the plots show only the $e^+e^- \to h'(\to \mu^+\mu^-)\chi_1\chi_2(\to \chi_1 e^+e^-)$ final state in the corresponding $h' \to \mu^+\mu^-$ reconstruction channel. The background distributions are also only shown in this reconstruction channel. Contributions from truth-matched pair conversions are shown in purple, while the other contributions are shown in grey. The upper left plot shows the background composition with a minimal set of selections applied, while in the right, plot all selections from Tables 6.1 and 6.2 besides the opening angle requirement are applied. For signal the plots show different variations of the model parameters: h' mass (center left), $\chi_1$mass (center right), mass splitting (lower left), and χ_2 lifetime (lower right). The lifetime of the h' has no influence on α_{ee} and is therefore not shown. The other two final states are shown in Figs. B.2 and B.3 in the appendix.

different detector layers from the PXD, SVD, and the beam pipe, but the distribution is smeared between the layers due to imprecisions in the vertex reconstruction and the material not being perfectly aligned in a cylindrical manner around the IP [47]. To catch all contributions of pair conversions, caused by this smearing, one would have to veto nearly the whole PXD and SVD region. As this would cause a non negligible efficiency drop, and the selection on the opening angle already shows an excellent performance in suppressing pair conversions, the radial vertex position is not considered as a selection variable in this analysis.

While the h' candidates are not reconstructed from electrons, backgrounds originating from pair conversions can still be observed if the electrons from the pair conversions are misidentified as one of the FSP flavours considered in the h' reconstruction. As seen in Fig. 6.13, this is especially a problem in the $\mathrm{h}' \to \mathrm{K}^+\mathrm{K}^-$ reconstruction channel, due to a significant amount of $\mathrm{e} \to \mathrm{K}$ misidentification. The contribution from pair conversion is suppressed similarly to the χ_2 case by applying a selection on the opening angle between the kaon candidates. In this case, as can be seen in Fig. 6.13, the model parameter sensitive to the h' daughter opening angle is the h' mass. Additionally, while the h' opening angle does not depend directly on the χ_1 mass, it does indirectly as the A' mass is chosen with respect to $m(\chi_1)$. The mass of the A' has an impact on the angle between the h' daughters, as in the production process $\mathrm{e}^+\mathrm{e}^- \to \mathrm{h}'\mathrm{A}'$ the mass of the A' alters the momentum distribution of the h' in the lab frame. The results of the Punzi FOM optimisation in all three final states are shown in the appendix as Fig. C.3 without other selection criteria and as Fig. C.4 with the other selections applied. The optimal requirement depends on the choice of the model parameters which affect the event kinematics, but with the same motivation as for α_{ee} the most conservative requirement of $\alpha_{\mathrm{xx}}^{\mathrm{h}'} > 0.1$ is chosen. This selection only shows a bad performance for parameter configurations where the h' mass is close to the kinematic threshold.

6.4 Pointing Angle Selection

I exploit the fact that the h' vertex is pointing back to the IP by having a requirement on the pointing angle $\Delta\alpha_{\mathbf{x},\mathbf{p}}^{\mathrm{h}'}$. As illustrated in Fig. 6.14, the pointing angle describes the angular distance between the momentum and position vector of a reconstructed vertex. For better visualisation, the pointiness is defined in terms of $-\log(1 - \cos(\Delta\alpha_{\mathbf{x},\mathbf{p}}^{\mathrm{h}'}))$, where high values correspond to a very pointing vertex. Selecting on this pointing angle is very powerful to reject candidates that are made up of random combinations of tracks, which also include vertices that have been reconstructed with at least one beam background track, as random combinations should not point back to the IP. Fig. 6.15 shows the pointing angle distributions of the h' candidates for signal and background in the $\mathrm{h}' \to \pi^+\pi^-$ reconstruction channel. One can see there that the pointiness of the dark Higgs depends on both its mass and lifetime. The lifetime dependence can be explained by the fact that the

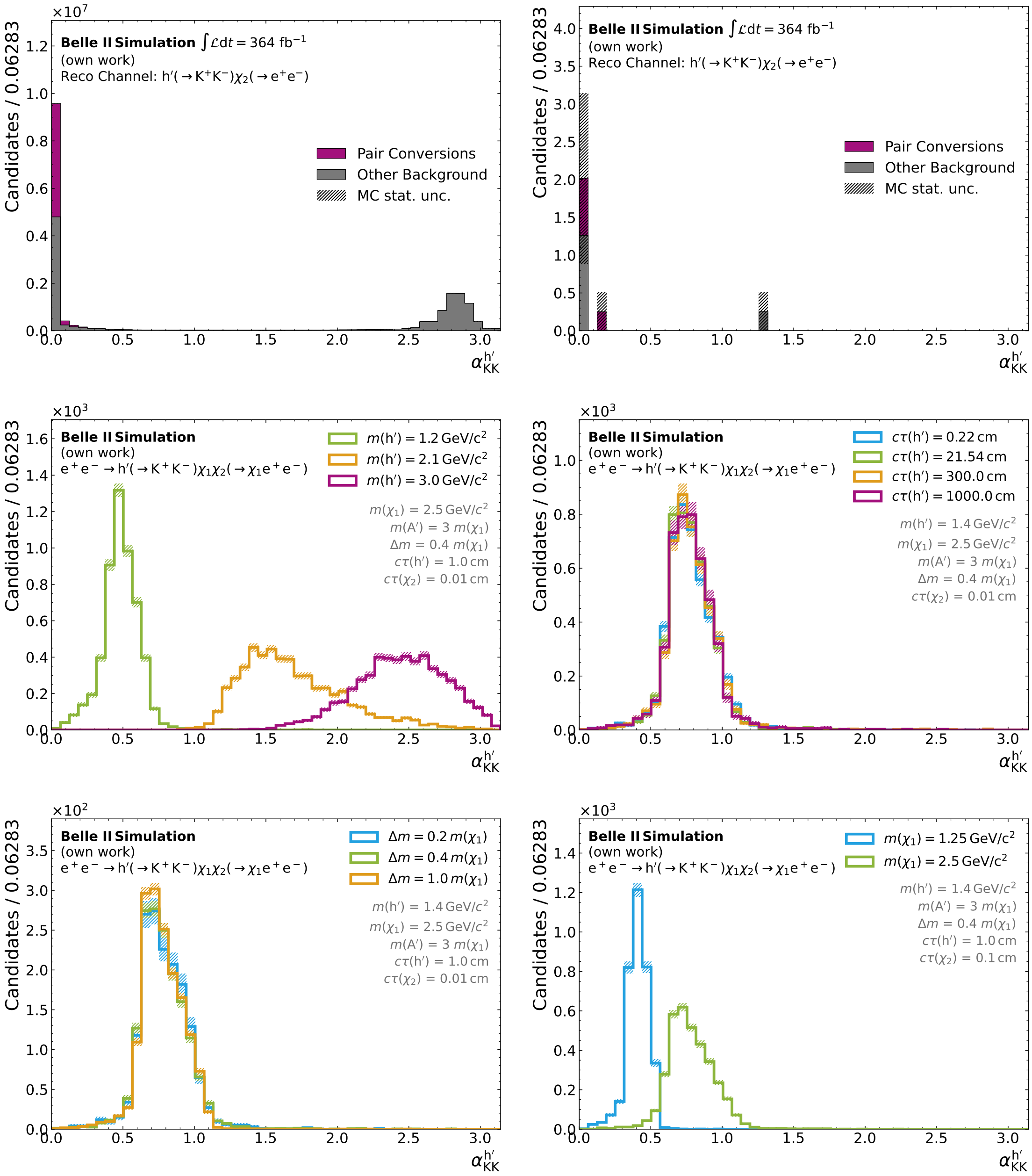

Figure 6.13: Background (top) and signal (center and bottom) distributions of the opening angle between the two reconstructed kaons of the h′ candidate. For the signal, the plots show only the $e^+e^- \to h'(\to K^+K^-)\chi_1\chi_2(\to \chi_1 e^+e^-)$ final state in the corresponding $h' \to K^+K^-$ reconstruction channel. The background distributions are also only shown in this reconstruction channel. Contributions from truth-matched pair conversions are shown in purple, while the other contributions are shown in grey. The upper left plot shows the background composition with a minimal set of selections applied, while in the right, plot all selections from Tables 6.1 and 6.2 besides the opening angle requirement are applied. For signal the plots show different variations of the model parameters: h′ mass (center left), h′ lifetime (center right), mass splitting (lower left), and χ_1 mass (lower right). The other two final states are shown in Figs. B.5 and B.6 in the appendix.

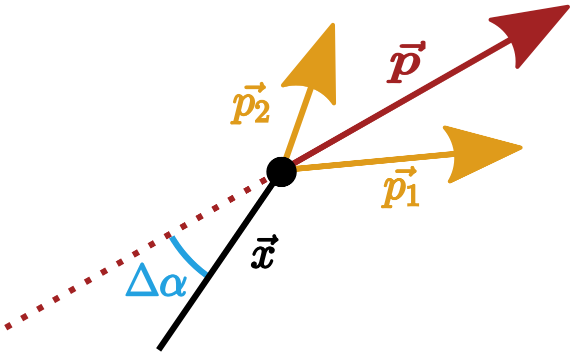

Figure 6.14: Sketch of the definition of the pointing angle. The pointing angle $\Delta\alpha$ (shown in cyan) describes the difference between the position vector of a vertex $\mathbf{x}$ and the momentum vector of this vertex $\mathbf{p}$ (shown in red). This momentum vector is calculated by the sum of the momenta of the daughter particles (both shown in orange): $\mathbf{p} = \mathbf{p_1} + \mathbf{p_2}$. For simplicity, this example shows only two daughter particles, but there could be more.

more displaced a particle decays the longer the lever arm to determine the position vector is. This results in a better resolution of the position vector which directly propagates to the pointing angle. The observed mass dependence is related to this. Given a fixed lifetime, lighter h' decay more displaced than heavier ones as they are more boosted. So in that case again the vertex position resolution is better for the lighter mass hypothesis.

Besides the expected behaviour of a pointing vertex for correctly reconstructed h' candidates, one can observe for low h' masses a peak at the lower end of the spectrum. This peak corresponds to candidates with $\Delta\alpha^{\mathrm{h}'}_{\mathbf{x},\mathbf{p}} = 180\,^{\circ}$, where the momentum and vertex vector point in opposite directions. In these cases, the vertex position determined from the vertex fit is set to the detector region opposite to the actual vertex position, where the track extrapolations meet again by chance. The effect is only present for rather low dark Higgs masses due to the kinematics in this case.

The requirement on the pointing angle is optimised using the Punzi FOM. Figs. C.5 and C.6 in the appendix show the results of this optimisation for all three final states with and without the other selection requirements applied. Based on the results of the optimisation with the other selections applied, I choose a requirement of $-\log(1 - \cos(\Delta\alpha^{\mathrm{h}'}_{\mathbf{x},\mathbf{p}})) > 7.5$. As can be seen in Fig. 6.15, this selection has a bigger impact on short-lived h' decays, as short-lived dark Higgs decays occur more non-pointing with the reason discussed above. Nevertheless, these short dark Higgs lifetimes correspond to larger mixing angles θ. As these large mixing angles are already excluded by previously performed analyses (see Section 2.5), in this work I focus on the long-lived case, where the selection is not problematic.

Contrary to the h' vertex, the reconstructed χ_2 vertex is not pointing back to the IP as the decay involves additional missing energy in the form of the χ_1. Selecting on the non-pointiness of this vertex could be used as an alternative for suppressing contributions from pair conversions that are described in Section 6.3, as they are pointing back to the IP. In Fig. C.11 the Punzi FOM when selecting on the χ_2 pointing angle is compared to the

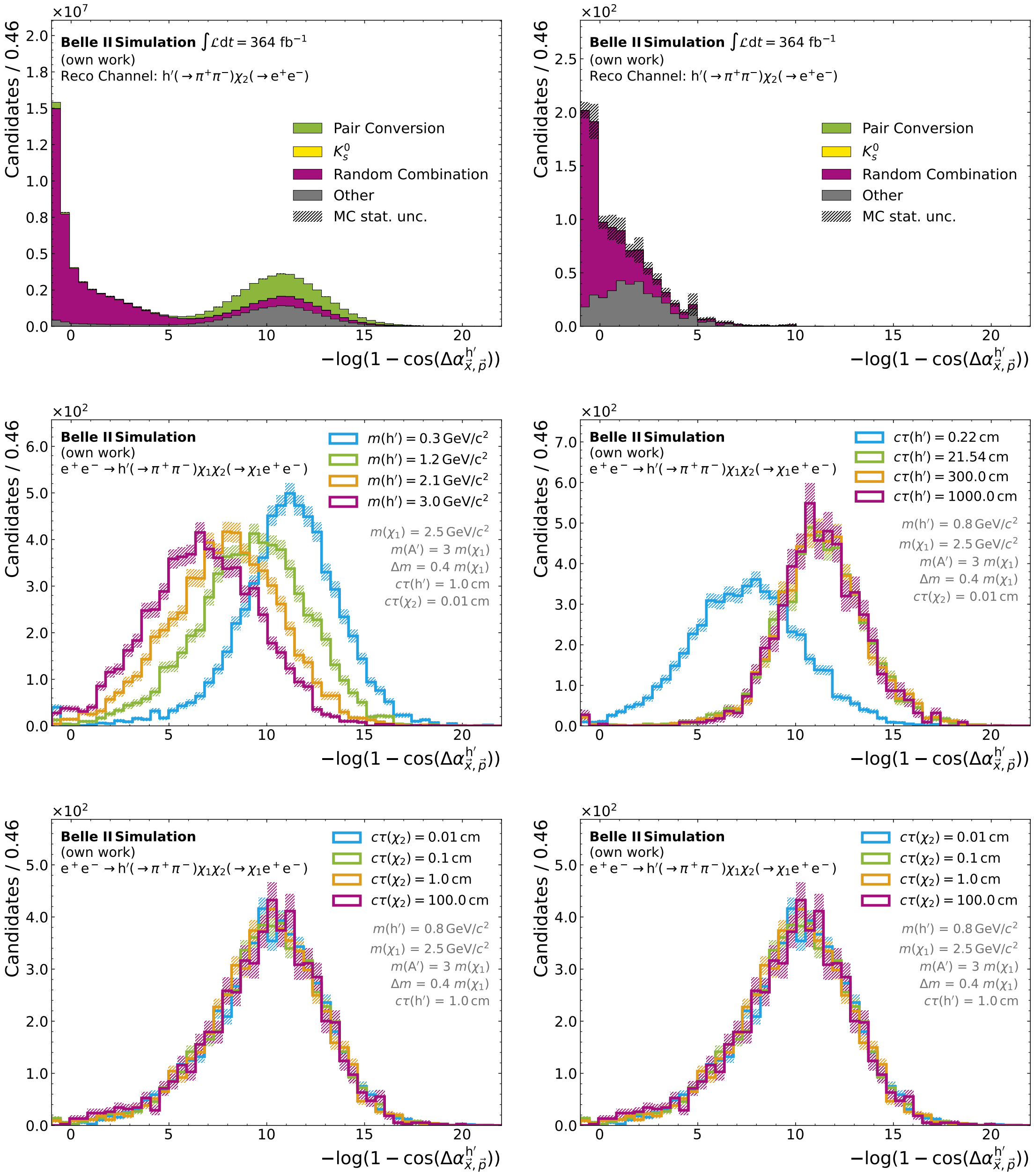

Figure 6.15: Background (top) and signal (center and bottom) distributions of the pointing angle $-\log(1-\cos(\Delta\alpha^{\mathrm{h}'}_{\mathbf{x},\mathbf{p}}))$ between momentum and vertex vector of the h′ candidate. For the signal, the plots show only the $\mathrm{e}^+\mathrm{e}^- \to \mathrm{h}'(\to \pi^+\pi^-)\chi_1\chi_2(\to \chi_1\mathrm{e}^+\mathrm{e}^-)$ final state in the corresponding $\mathrm{h}' \to \pi^+\pi^-$ reconstruction channel. The background distributions are also only shown in this reconstruction channel. Contributions from random track combinations are shown in purple, truth-matched pair conversions in light green and K^0_S decays in yellow, while the other contributions are shown in grey. The upper left plot shows the background composition with a minimal set of selections applied, while in the right plot, all selections from Tables 6.1 and 6.2 besides the pointing angle requirement are applied. For signal, the plots show different variations of the model parameters: h′ mass (center left), h′ lifetime (center right), mass splitting (lower left), and χ_2 lifetime (lower right). The other two final states are shown in Figs. B.7 and B.8 in the appendix.

performance of the selection on the opening angle from Section 6.3. The selection on the χ_2 pointiness shows similar performance as the selection on the opening angle for all tested model parameter configurations. As a result, I only use the opening angle to suppress pair conversion and do not apply an additional requirement on the non-pointiness of the χ_2 vertex.

6.5 Missing Energy and Reconstructed χ_2 Mass

The decay signature I am studying includes two χ_1 particles which cannot be reconstructed. This results in additional missing energy in the reconstruction process. I calculate the missing energy by subtracting the energies of the four reconstructed FSPs from the well-known beam energy: $E_{\text{miss}} = \sqrt{s} - \sum E_{\text{fsp}}$, where $\sqrt{s}$ is the cms energy and E_{fsp} the energy of the tracks in the cms frame.

Fig. 6.16 shows the missing energy distributions for both SM background and signal. The missing energy of the signal is heavily dependent on the mass of the χ_1 which defines the lower bound of the spectrum as $E_{\text{miss}}^{\text{min}} = 2\,m(\chi_1)$ (see Fig. 6.16). As in the model considered in this thesis, the χ_1 always has to be heavier than the dark Higgs and for this analysis, the minimal dark Higgs mass is given by the di-muon threshold, a requirement of $E_{\text{miss}} > 0.4\,\text{GeV}$ is chosen using the formula above.

As ISR effects are not considered during the event generation of the simulated signal samples, a potential impact of this on the selection using the missing energy needs to be discussed. The presence of ISR would increase the reconstructed missing energy as the available energy for the FSPs would be lowered. Given that the current selection of $E_{\text{miss}} > 0.4\,\text{GeV}$ retains all signal events the efficiency of this requirement would not be changed by taking ISR effects into account. Therefore, the absence of ISR effects in the event generation does not lead to a mismodelling of the selection efficiency.

Another variable that indirectly depends on the mass of the χ_1 is the reconstructed χ_2 mass $M_{\text{ee}}^{\chi_2}$, so the mass of the reconstructed e^+e^- pair. As the χ_2 vertex is reconstructed from a pair of electrons (and missing the χ_1) its mass spectrum has an upper bound at the mass splitting Δm between the χ_1 and χ_2 that defines the available phase space. This can be clearly seen in Fig. 6.17. As the maximal mass splitting that is considered in this analysis is $\Delta m = 1.0\,m(\chi_1)$ and I consider χ_1 masses up to $2.5\,\text{GeV/c}^2$, I apply the criterion $M_{\text{ee}}^{\chi_2} < 2.5\,\text{GeV/c}^2$. In Fig. 6.17 can be seen that this selection has an impact on further reducing the background, especially in the $\text{h}' \to \pi^+\pi^-$ reconstruction channel.

6.6 Rest-of-Event

Many final states in e^+e^- collisions contain more than four tracks or additional photons. So when reconstructing the two vertices out of four tracks, for these kinds of events there are unused tracks or ECL clusters present. These are summarised in the so-called ROE.

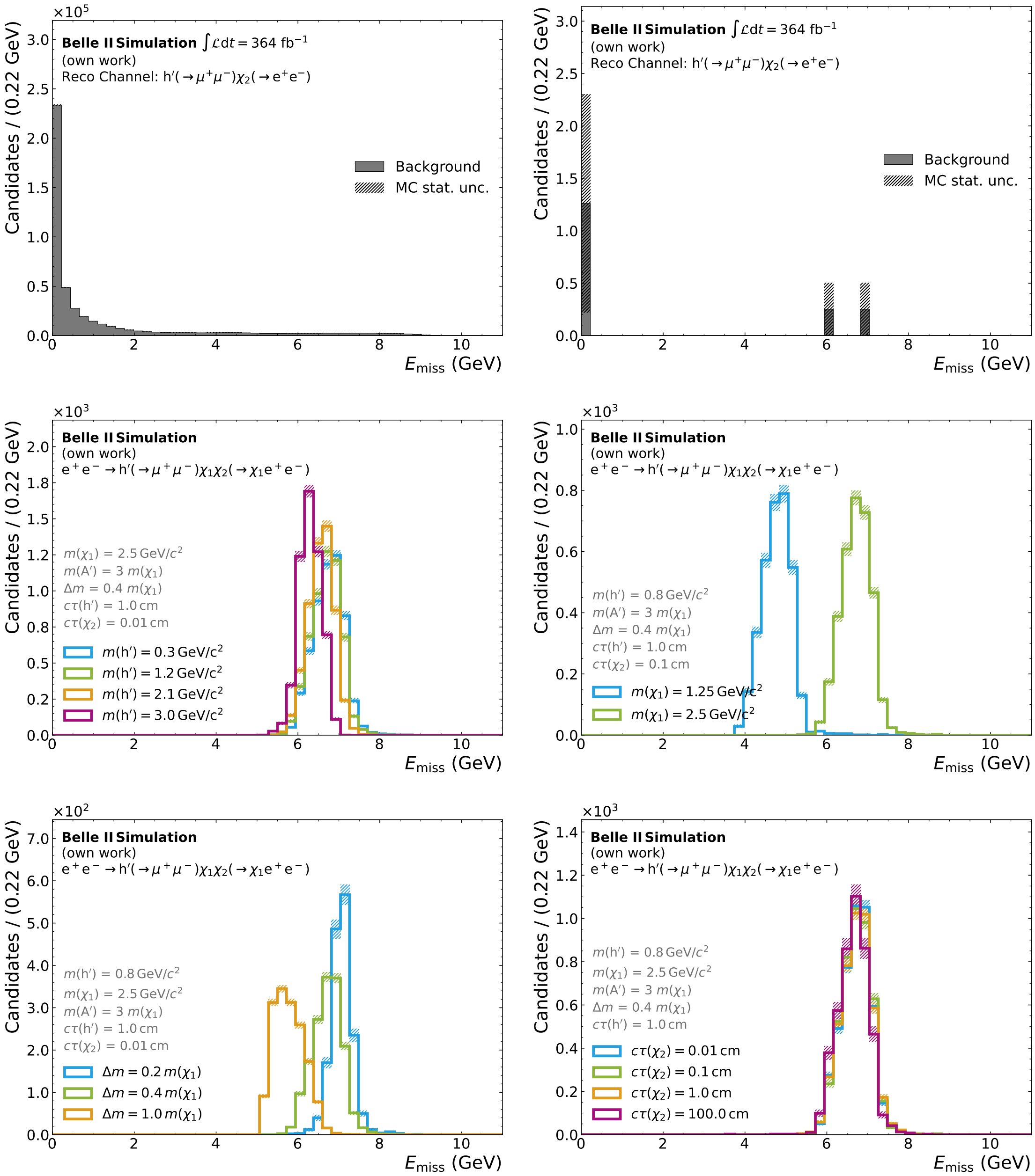

Figure 6.16: Background (top) and signal (center and bottom) distributions of the missing energy E_{miss} in the event. For the signal, the plots show only the $e^+e^- \to h'(\to \mu^+\mu^-)\chi_1\chi_2(\to \chi_1 e^+e^-)$ final state in the corresponding $h' \to \mu^+\mu^-$ reconstruction channel. The background distributions are also only shown in this reconstruction channel. The upper left plot shows the background composition with a minimal set of selections applied, while in the right plot all selections from Tables 6.1 and 6.2 besides the E_{miss} requirement are applied. For signal the plots show different variations of the model parameters: h' mass (center left), χ_1 mass (center right), mass splitting (lower left), and χ_2 lifetime (lower right). The other two final states are shown in Figs. B.9 and B.10 in the appendix.

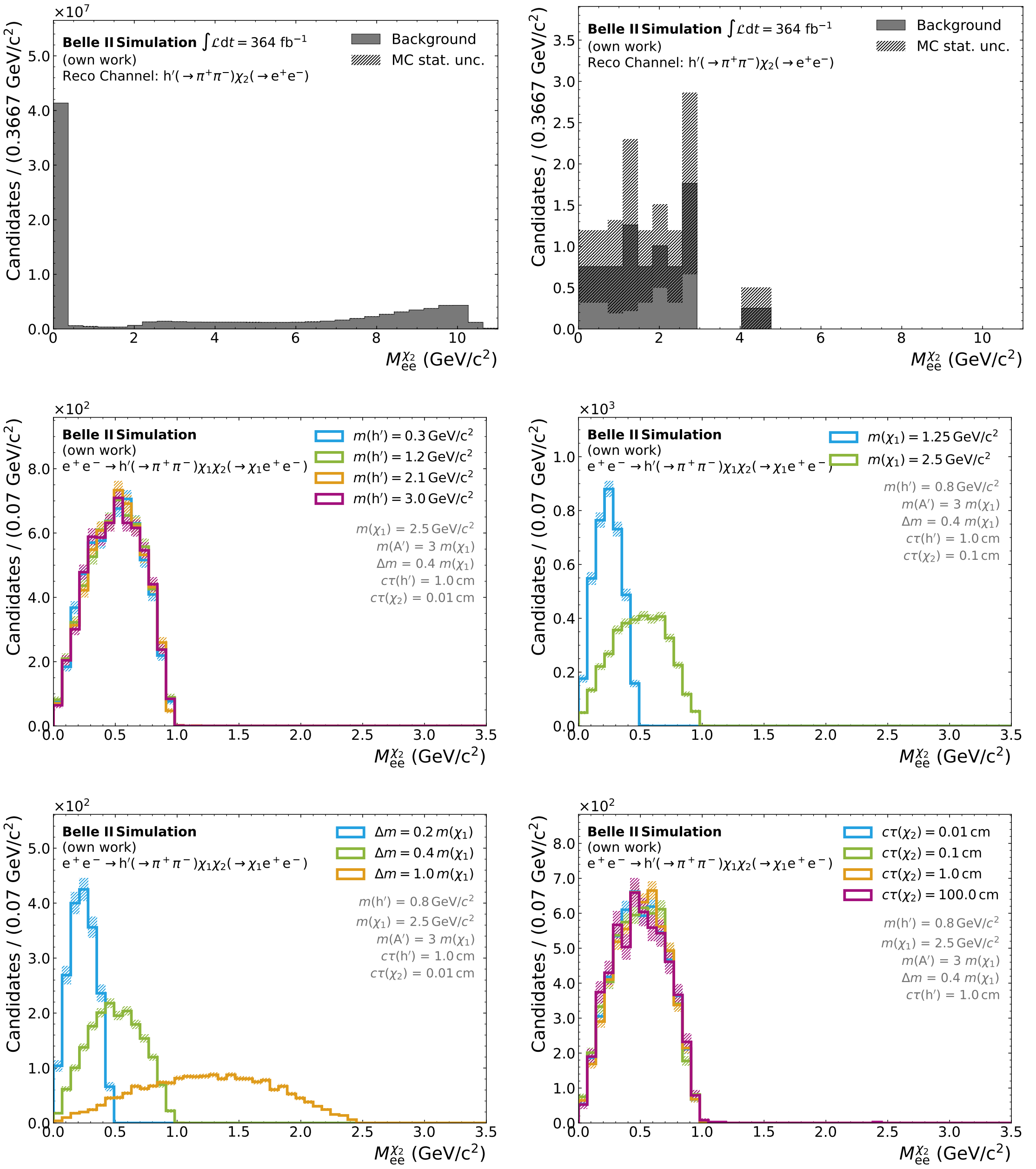

Figure 6.17: Background (top) and signal (center and bottom) distributions of the reconstructed mass that forms the χ_2 candidate. For the signal the plots show only the $e^+e^- \to h'(\to \pi^+\pi^-)\chi_1\chi_2(\to \chi_1 e^+e^-)$ final state in the corresponding $h' \to \pi^+\pi^-$ reconstruction channel. The background distributions are also only shown in this reconstruction channel. The upper left plot shows the background composition with a minimal set of selections applied, while in the right plot all selections from Tables 6.1 and 6.2 besides the $M_{ee}^{\chi_2}$ requirement are applied. For signal the plots show different variations of the model parameters: h' mass (center left), χ_1 mass (center right), mass splitting (lower left), and χ_2 lifetime (lower right). The other two final states are shown in Figs. B.11 and B.12 in the appendix.

As for the signal process of interest, the events are fully reconstructed, which means there are no additional tracks or deposited ECL energy expected in the ROE. Consequently, checking the ROE is a powerful tool to suppress the backgrounds mentioned above.

To reduce the number of tracks and ECL depositions in the ROE that are created by beam background, I place a few selections on the tracks and ECL clusters. As the selections on the ROE target SM processes which occur in most cases prompt, the ROE tracks are required to originate from the IP ($\rho_{\text{track}} < 0.5\,\text{cm}$ and $|z_{\text{track}}| < 2.0\,\text{cm}$) and have to be in the angular acceptance of the CDC. The ECL clusters that are considered in the ROE have to be located within the acceptance region of the CDC, and the weighted sum of assigned ECL crystals, which gives a rough estimate of the extent of a cluster, has to be above 1.5. While the ECL has a slightly bigger angular acceptance than the CDC, for the ROE I am only interested in neutral clusters where the energy deposition is not associated with a track (to not double count particles that created both a track and a cluster). As this requirement can only be checked in the area where tracks can be reconstructed the ECL ROE is restricted to the angular acceptance of the CDC. Additionally, there is a minimal energy requirement depending on the detector region (forward endcap: 80 MeV, barrel: 70 MeV, backward endcap: 100 MeV). To further suppress the amount of beam background clusters that are used in the ROE the time where the cluster was measured should be within 200 ns of the measured event t_0. I optimised this ROE definition such that the total extra energy deposited by neutral particles in the ECL $E_{\text{extra}}(\text{neutral})$ is stable across different beam background conditions while keeping the region-dependent energy thresholds as low as possible to ensure good separation power between signal events and SM backgrounds. Fig. 6.18 shows that if the energy thresholds are chosen too low a lot of beam background clusters are picked up which results in the $E_{\text{extra}}(\text{neutral})$ shape significantly varying with the different beam background conditions experienced during data-taking.

In Fig. 6.19 I show the signal and background distributions for the extra energy $E_{\text{extra}}(\text{neutral})$. The dip in the distribution between 0 GeV and 0.07 GeV is caused by the minimal energy thresholds in the ROE: If a cluster that fulfils the requirements is found, the minimal extra energy is given by the energy threshold in the barrel region of 70 MeV. For signal events, as I fully reconstruct the event there should be no additional energy being deposited in the ECL. The contributions that show up here are either from beam background or secondary processes within the Belle II detector. In contrast to that, for SM background processes one can expect significant amounts of extra energy due to, for example, processes that include photons or π^0 mesons that can be suppressed by looking into $E_{\text{extra}}(\text{neutral})$. For finding the optimal cut value on $E_{\text{extra}}(\text{neutral})$, I maximise the Punzi FOM and apply a requirement of $E_{\text{extra}}(\text{neutral}) < 1.0\,\text{GeV}$.

Similar to processes that have additional photons, there are many SM processes that leave more than four tracks in the detector. This can be seen in Fig. 6.20 and in contrast to signal events where more than four tracks are only visible in cases if there are additional

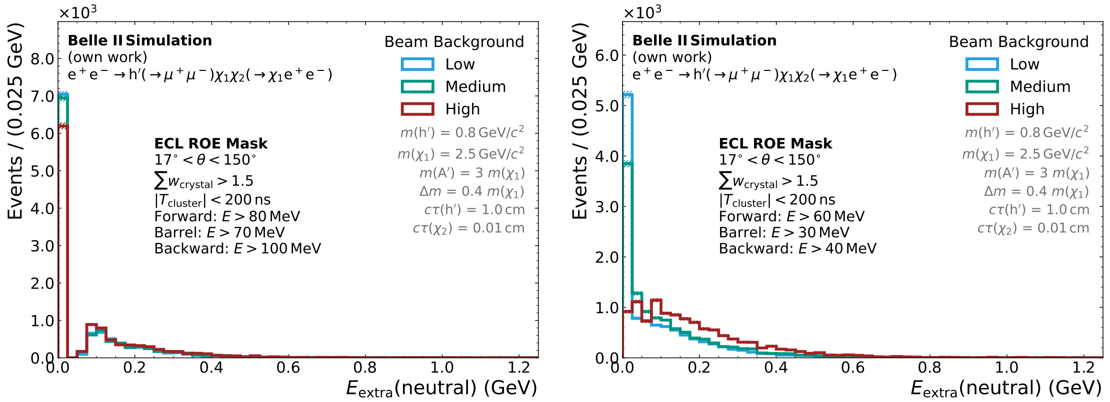

Figure 6.18: Total extra energy deposited in the ECL evaluated on $e^+e^- \to h'(\to \mu^+\mu^-)\chi_1\chi_2(\to \chi_1 e^+e^-)$ signal with fixed model parameters for different beam background conditions indicated with different colours: low (cyan), medium (light green), high (red). Only the ECL clusters that are not associated with a track are considered here. In the left plot, the detector region-dependent energy thresholds used in this analysis are shown while the right plot shows a ROE definition with smaller energy thresholds.

contributions from beam background tracks. Looking at the distributions makes it obvious that selecting on the absence of additional tracks in the ROE helps to suppress a large fraction of the remaining SM backgrounds while keeping nearly all of the signal events.

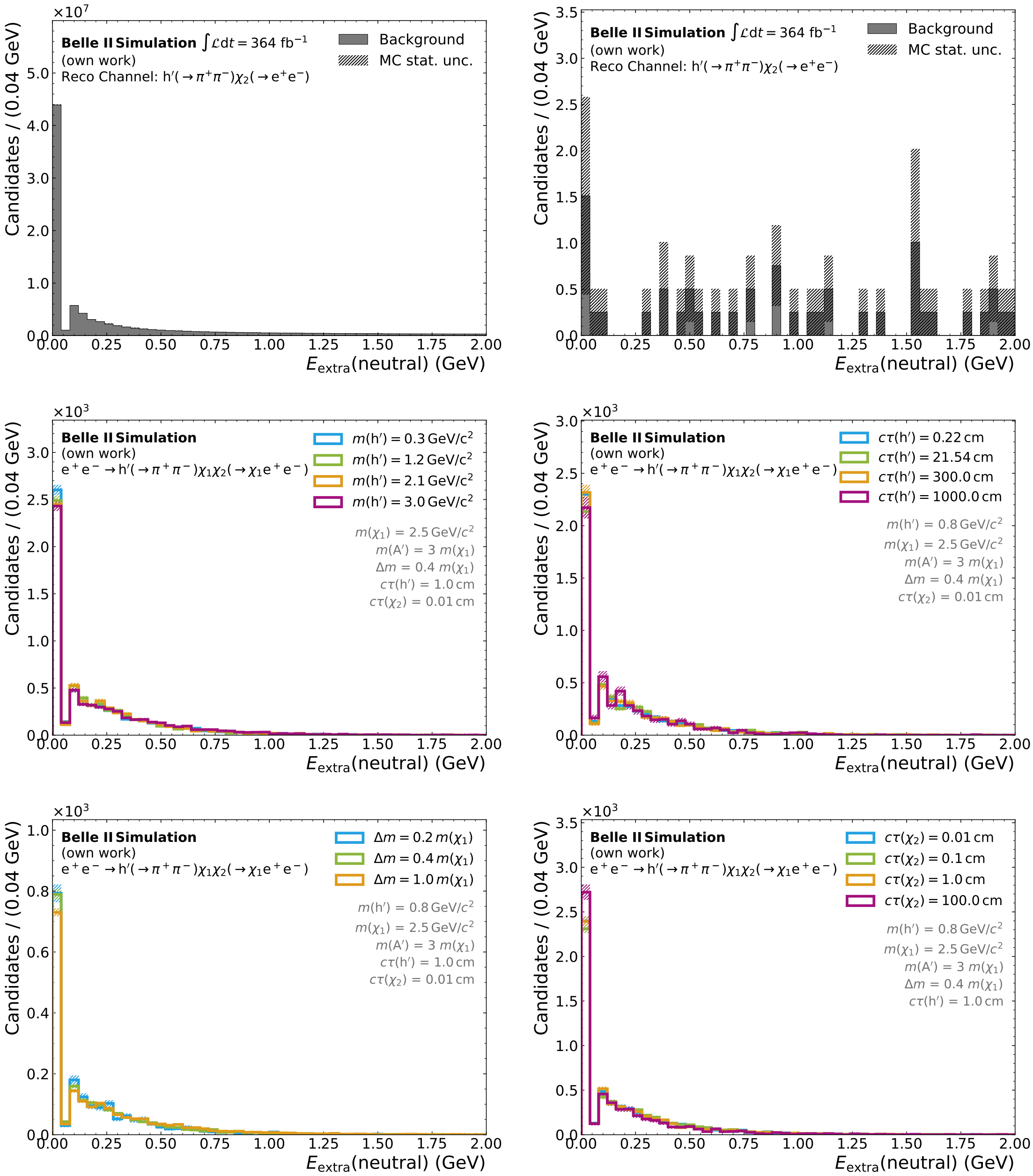

Figure 6.19: Background (top) and signal (center and bottom) distributions of the extra energy in the ECL. For the signal, the plots show only the $e^+e^- \rightarrow h'(\rightarrow \pi^+\pi^-)\chi_1\chi_2(\rightarrow \chi_1 e^+e^-)$ final state in the corresponding $h' \rightarrow \pi^+\pi^-$ reconstruction channel. The background distributions are also only shown in this reconstruction channel. The upper left plot shows the background composition with a minimal set of selections applied, while in the right plot, all selections from Tables 6.1 and 6.2 besides the E_{extra}(neutral) requirement are applied. For signal the plots show different variations of the model parameters: h′ mass (center left), h′ lifetime (center right), mass splitting (lower left), and χ_2 lifetime (lower right). The other two final states are shown in Figs. B.15 and B.16 in the appendix.

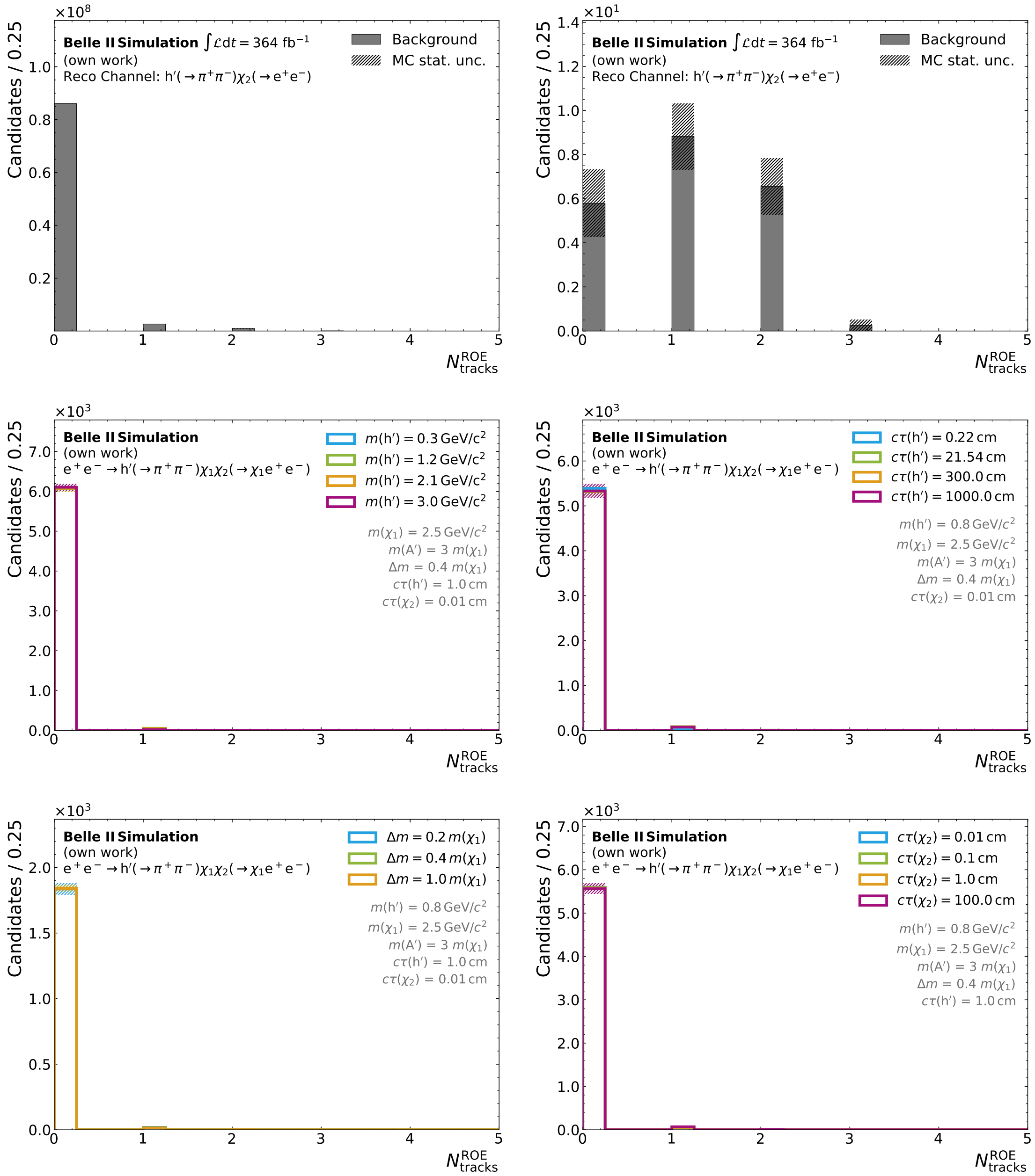

Figure 6.20: Background (top) and signal (center and bottom) distributions of the additional tracks in the ROE. For the signal, the plots show only the $e^+e^- \to h'(\to \pi^+\pi^-)\chi_1\chi_2(\to \chi_1 e^+e^-)$ final state in the corresponding $h' \to \pi^+\pi^-$ reconstruction channel. The background distributions are also only shown in this reconstruction channel. The upper left plot shows the background composition with a minimal set of selections applied, while in the right plot all selections from Tables 6.1 and 6.2 besides the $N_{\text{tracks}}^{\text{ROE}}$ requirement are applied. For signal the plots show different variations of the model parameters: h' mass (center left), h' lifetime (center right), mass splitting (lower left), and χ_2 lifetime (lower right). The other two final states are shown in Figs. B.13 and B.14 in the appendix.

6.7 Vetos

The studied signature allows for background contributions originating from irreducible backgrounds, namely $\mathrm{K_S^0}$ and Λ. As the $\mathrm{K_S^0}$ decays naturally into a pair of pions, it cannot be suppressed in the $\mathrm{h'} \to \pi^+\pi^-$ reconstruction channel. Contrary to that, the Λ, when decaying into a charged final state, decays mostly into a proton and pion. The contributions from the Λ could be suppressed if the PID would be perfect, which is unfortunately not the case. Another narrow resonance within the mass range covered by this analysis is the ϕ. While the ϕ does not decay displaced itself, it still has to be considered as the vertex selection from Section 6.2 allows for one prompt vertex.

In order to suppress the contributions from these sources, mass vetos are applied, which are described in the following.

$\mathrm{K_S^0}$ Veto

Due to the $\mathrm{K_S^0}$ decaying displaced and into a pair of charged pions in more than 69% of the cases [4], it mimics exactly the signature of the $\mathrm{h'}$ decaying into a pair of pions. Therefore there is no way of distinguishing the $\mathrm{K_S^0}$ from the studied signal decay, so the $\mathrm{K_S^0}$ mass region has to be vetoed in this analysis. As the $\mathrm{K_S^0}$ dominantly decays into a pair of pions, the variable to look at is the reconstructed mass of the $\mathrm{h'}$ assuming the pion hypothesis for the daughter tracks, denoted as $M_{\pi\pi}^{\mathrm{h'}}$. The corresponding distributions are shown in Fig. 6.21 for all reconstruction channels. While the $\mathrm{K_S^0}$ cannot decay into a pair of kaons and the decay into a pair of muons is very rare, one can still observe contributions of $\mathrm{K_S^0}$ mesons in the corresponding reconstruction channels. This is caused by the misidentification of the pions during the reconstruction.

I remove these contributions from $\mathrm{K_S^0}$ decays by vetoing the reconstructed mass region around the nominal $\mathrm{K_S^0}$ mass. Thereby, to cover also the detector resolution, I define the size of the veto region via fitting the $M_{\pi\pi}^{\mathrm{h'}}$ distributions of the simulated SM background samples with a Double Sided Crystal Ball (DSCB) function, which will be described in more detail in Section 8.1. The extracted width of the Gaussian core of the DSCB is then used to define the veto range. As the results in the muon and kaon final state are not sufficient to reach a conclusion due to the low statistics caused by the limited amount of simulated samples that are available, the width extracted in the pion reconstruction channel is used for the veto. Using the information of the fit, I exclude the region $\mu - 20\sigma \leq M_{\pi\pi}^{\mathrm{h'}} \leq \mu + 20\sigma$, where μ is the fitted mean and σ the fitted width of the Gaussian core of the DSCB. This range corresponds to $467.2\,\mathrm{MeV/c^2} \leq M_{\pi\pi}^{\mathrm{h'}} \leq 528.8\,\mathrm{MeV/c^2}$. It can be seen later that the overall background level in this search is quite low. Therefore, I choose this veto range very conservatively as already picking up very few $\mathrm{K_S^0}$ mesons from the tails of the distributions can lead to the observation of a significant signal that is not caused by actual signal but faked by contributions from $\mathrm{K_S^0}$ decays.

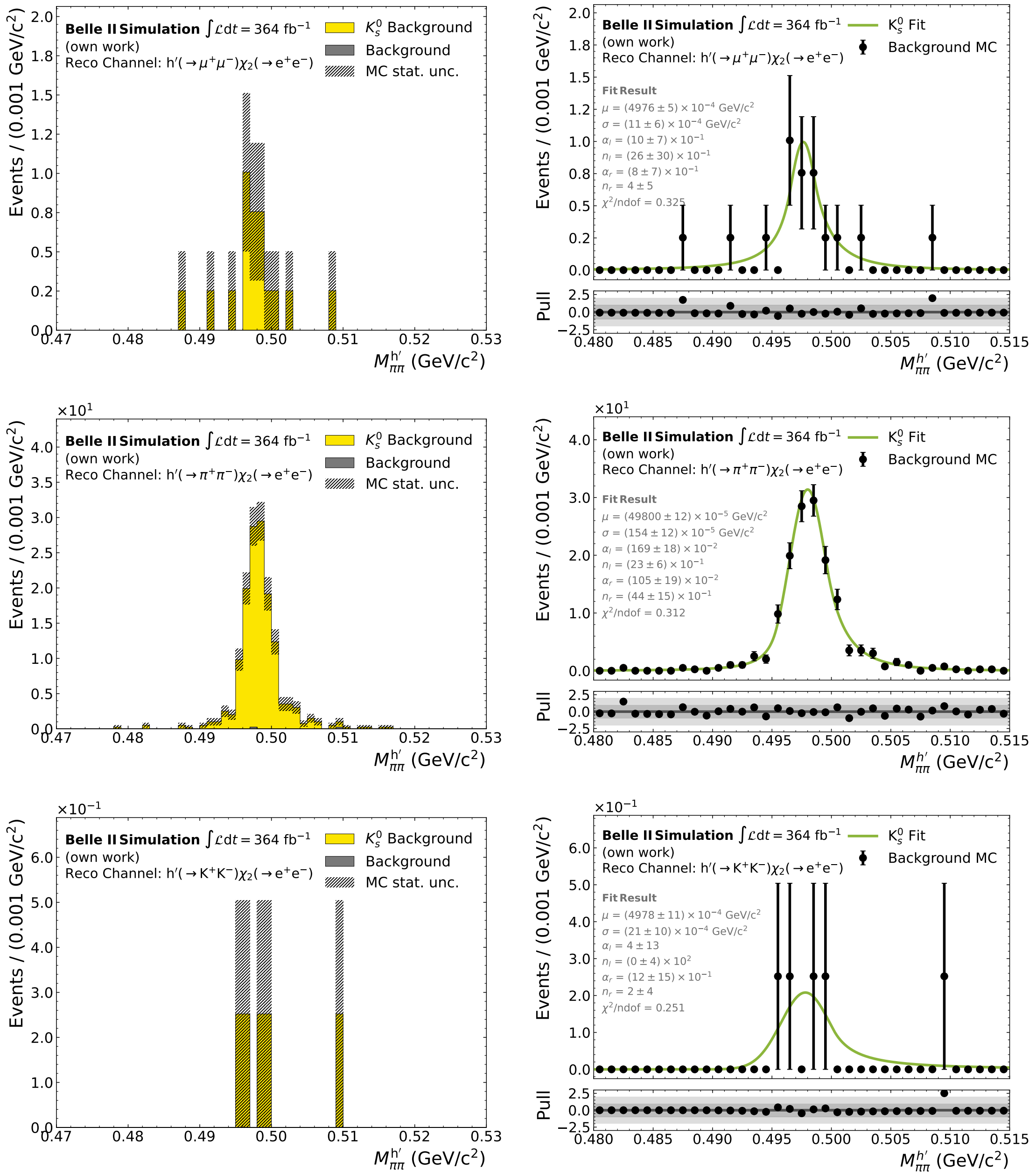

Figure 6.21: The reconstructed mass of the h' candidate with assuming the pion mass hypothesis for the two daughter tracks in the $h' \to \mu^+\mu^-$ (top), $h' \to \pi^+\pi^-$ (center), and $h' \to K^+K^-$ (bottom) reconstruction channel. The left plot shows the distributions on the background samples with true K_S^0 mesons marked in yellow. On the right side the DSCB fit used to extract the width for the veto is shown.

Λ Veto

Similar to the K_S^0, when misidentifying protons as pions leads to contributions from Λ mesons being reconstructed as signal candidates. To get rid of these I use a similar approach as for vetoing the K_S^0 mesons, with the only difference that the variable of interest is now the reconstructed mass with the proton-pion hypothesis $M_{p\pi}^{h'}$. As this decay involves two FSPs, I take both possible combinations into account and the combination closer to the nominal Λ mass is used to apply the veto.

Due to the low number of these events that pass the selection, one cannot fit the Λ shape to define a mass veto region, but still with the same argument as for the K_S^0, that already few reconstructed Λ candidates would lead to a falsely declared significant observation, they have to be vetoed. Therefore, the veto is chosen as $m_\Lambda - 20\sigma_\Lambda \leq M_{p\pi}^{h'} \leq m_\Lambda + 20\sigma_\Lambda$, with m_Λ being the nominal Λ mass and $\sigma_\Lambda = 2.5\,\mathrm{MeV/c^2}$ being approximately the nominal width. Using these values the veto range is given by $1.06\,\mathrm{GeV/c^2} < M_{p\pi}^{h'} < 1.15\,\mathrm{GeV/c^2}$. This veto is only applied in the $h' \to \pi^+\pi^-$ reconstruction channel, as contributions from misidentification in other reconstruction channels are negligible.

ϕ Veto

Another resonance that can cause a peaking structure in the reconstructed dark Higgs mass spectrum is the ϕ. The ϕ decays into a pair of kaons in approximately 83% of the cases and into charged kaons in nearly 50% of occasions, which makes it relevant in the $h' \to K^+K^-$ reconstruction channel [4]. While, unlike the K_S^0 and the Λ, the ϕ does not decay displaced itself, it can still enter the analysis as it can be produced in association with ISR photons. If one of the ISR photons does pair conversion and the pair conversion rejection described in Section 6.3 fails to reject the event, a peaking structure in the reconstructed dark Higgs mass can be observed. I expect that this happens very rarely. Nevertheless, as the expected background level is close to zero, a very low number of ϕ events would create a significant signal peak. Therefore, the mass region around the ϕ is vetoed ±10σ around to nominal mass, with σ being the nominal width of the ϕ taken from [4], so $0.977\,\mathrm{GeV/c^2} \leq M_{KK}^{h'} \leq 1.061\,\mathrm{GeV/c^2}$. This veto is only applied in the $h' \to K^+K^-$ reconstruction channel, as similar to the Λ veto contributions from misidentification in other reconstruction channels are negligible.

6.8 Best Candidate Selection

After applying all previously explained selection criteria there is the chance of having more than one candidate reconstructed per event. Fig. 6.22 shows the average candidate multiplicity per event for simulated signal events. One observes that this average multiplicity is in general very low, reaching up to 4% for the $e^+e^- \to h'(\to \mu^+\mu^-)\chi_1\chi_2(\to \chi_1 e^+e^-)$ final state in the mass range from 0.5 to $1.5\,\mathrm{GeV/c^2}$ when the dark Higgs decays sufficiently

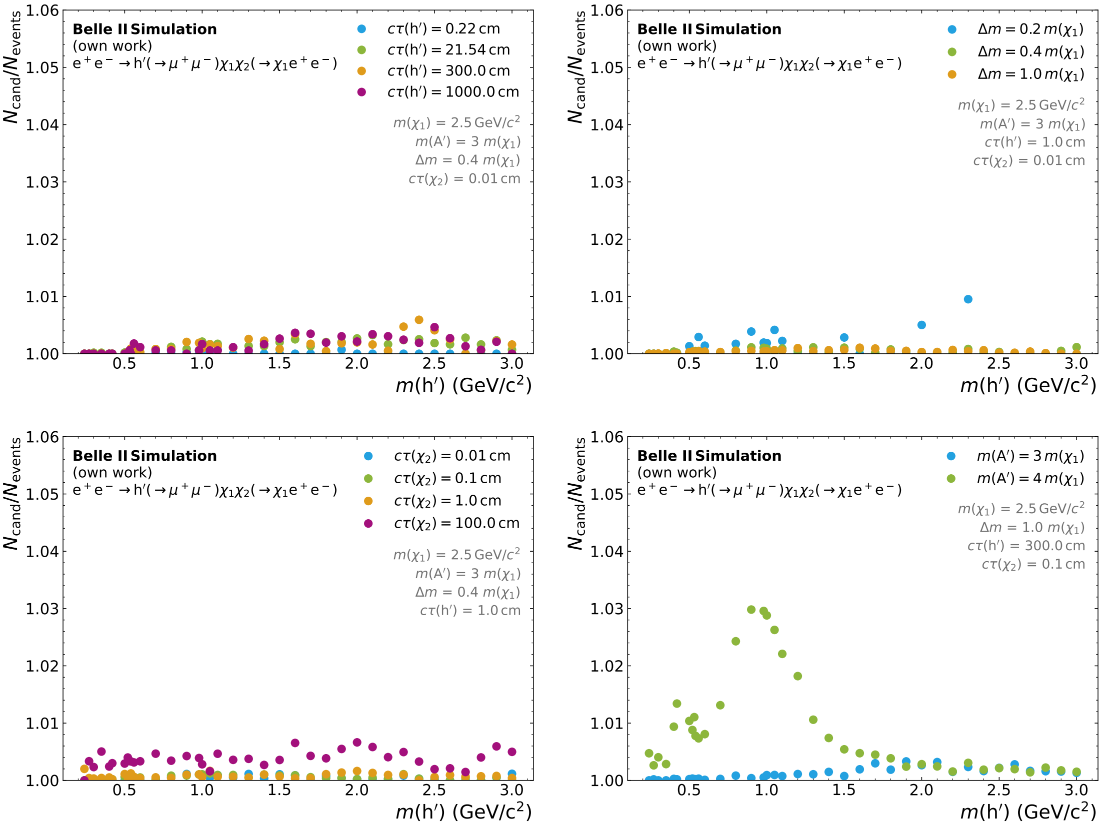

Figure 6.22: Average candidate multiplicity as a function of the h' mass for different variations of the model parameters $c\tau(\mathrm{h}')$ (upper left), mass splitting (upper right), $c\tau(\chi_2)$ (lower left), and $m(\mathrm{A}')$ (lower right). The plots are based on $\mathrm{e}^+\mathrm{e}^- \to \mathrm{h}'(\to \mu^+\mu^-)\chi_1\chi_2(\to \chi_1\mathrm{e}^+\mathrm{e}^-)$ signal and show the fraction of correctly reconstructed $\mathrm{h}' \to \mu^+\mu^-$ signal candidates in all three reconstruction channels with respect to the number of reconstructed events. Plots for the other two final states can be found as Figs. B.17 and B.18 in the appendix.

displaced. This is caused by the different PID methods that are used to identify muons and pions (see Section 6.1) as in this specific model parameter region the PID criteria allow the FSPs to be reconstructed in both the $\mathrm{h}' \to \mu^+\mu^-$ and $\mathrm{h}' \to \pi^+\pi^-$ reconstruction channels.

Given the low number of SM background events that survive the selection, the average multiplicity is one in all reconstruction channels.

For events that still yield more than one candidate after applying all selection criteria summarised in Tables 6.1 and 6.2, I apply a BCS. The remaining candidates are ranked according to the dark Higgs pointing angle (see Section 6.4) and I choose the most pointing candidate as the best candidate. It can happen very rarely that two candidates share the same pointing angle. As different PID methods are used to identify the FSPs, there is the chance of a pair of tracks being used in multiple reconstruction channels. The pointing angle is only calculated from the track properties, without taking the mass of the FSPs into account. Therefore, the two vertex candidates would share the same pointing angle, as they are reconstructed from the same pair of tracks. In this case, the candidate is chosen randomly.

Fig. 6.23 shows that the BCS keeps nearly all signal events that pass the selection criteria listed in Tables 6.1 and 6.2.

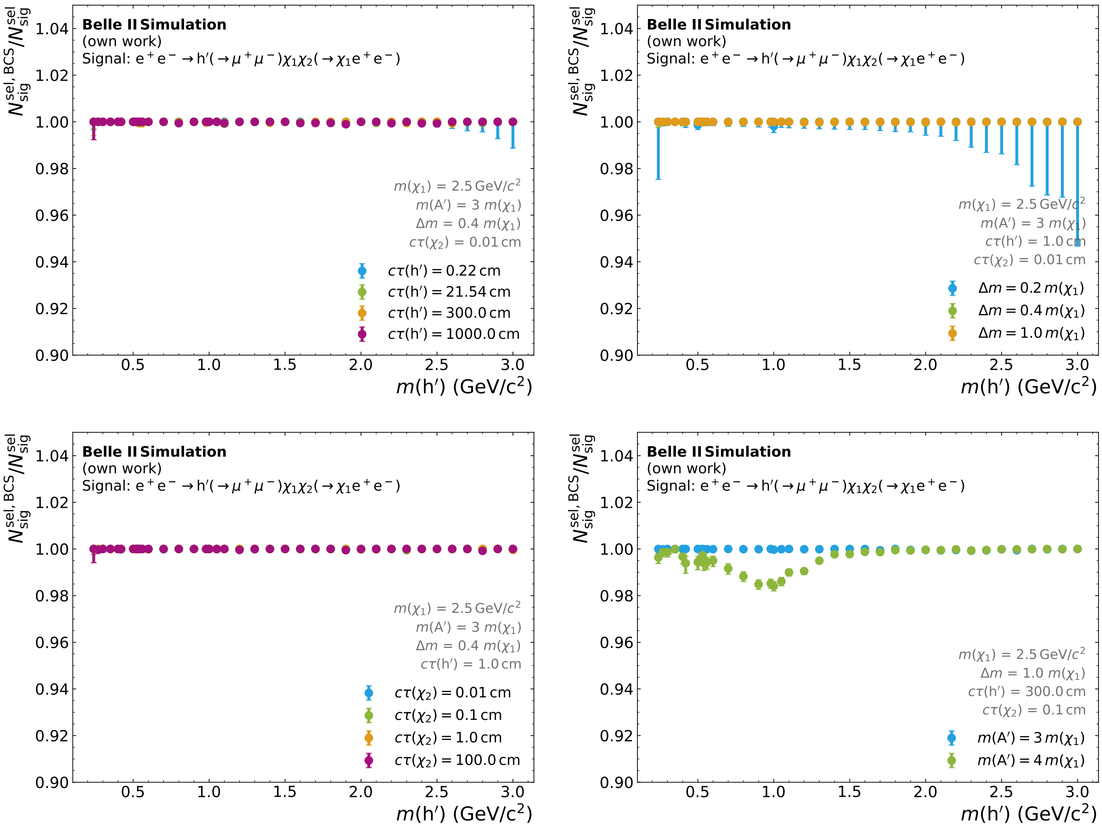

Figure 6.23: Performance of the BCS as a function of the h$'$ mass for different variations of the model parameters $c\tau(\mathrm{h}')$ (upper left), mass splitting (upper right), $c\tau(\chi_2)$ (lower left), and $m(\mathrm{A}')$ (lower right). The plots show the fraction of correctly reconstructed $\mathrm{e}^+\mathrm{e}^- \to \mathrm{h}'(\to \mu^+\mu^-)\chi_1\chi_2(\to \chi_1\mathrm{e}^+\mathrm{e}^-)$ signal events that are present after applying the BCS compared to the number of events that pass the selection criteria from Tables 6.1 and 6.2. Plots for the other two final states can be found in Figs. B.19 and B.20 in the appendix.

Chapter 7

Signal Efficiency

In this chapter I describe two studies related to the signal efficiency. First I discuss the impact of the beam background conditions on the efficiency for finding displaced vertices. Additionally, I study the trigger efficiency for the signature of interest.

7.1 Impact of Beam Background Conditions

In Fig. 7.1 I show the signal efficiency as a function of the dark Higgs lifetime for samples simulated with different beam background conditions. One can see there, that especially for larger h' lifetimes, the beam background conditions have a significant impact on the signal efficiency. This can be explained as track-finding becomes more complicated as more activity, which is not caused by the process of interest but by the different sources of beam background, is present in the detector. The fact that the effect becomes larger for larger lifetimes leads to the conclusion that the problem gets even more severe the more the assumption that tracks originate from the IP, that is made during the track-finding, is violated.

As the beam background conditions vary within the whole data-taking period, I need to derive the signal efficiency that corresponds to the beam background conditions that are present in the analysed data. The beam background conditions depend on various factors, for example, the instantaneous luminosity, which makes it complicated to measure the actual beam background conditions. Nevertheless, there are some observables that can give a good estimate of the beam background conditions. One of them is the number of hits in the CDC that are not associated with a track found by the track-finding algorithm. As illustrated in Fig. 7.2, the worse the beam background conditions are, the more of these extra CDC hits are present in an event. This can also be seen in Fig. 7.3, where the extra CDC hits are shown for samples that have been simulated with different beam background conditions according to the procedure described in Section 5.1. Another variable that can be used to describe the beam background conditions is the number of ECL crystals that have energy depositions that are out-of-time. These depositions are considered to be

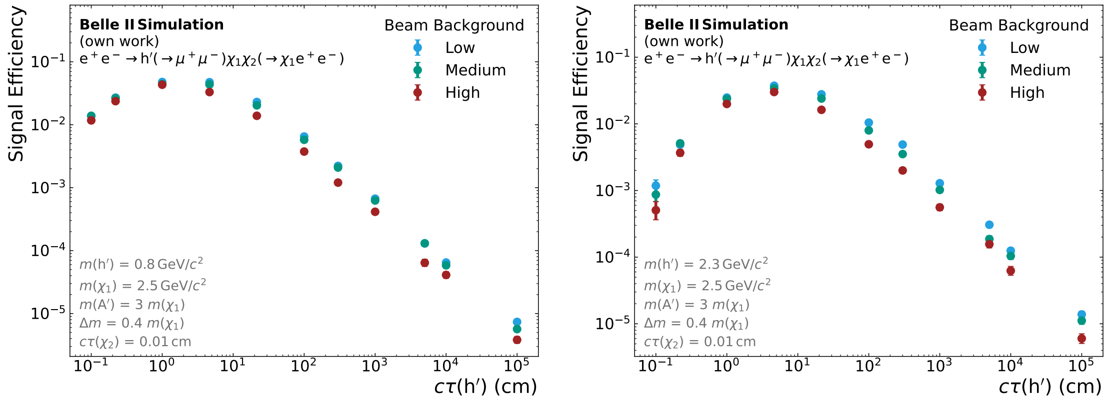

Figure 7.1: Signal efficiency as a function of the dark Higgs lifetime for events simulated with different beam background conditions. The cyan curve shows low beam background, while the green and red curves show medium and high beam background conditions, respectively. The efficiency is evaluated on $e^+e^- \to h'(\to \mu^+\mu^-)\chi_1\chi_2(\to \chi_1 e^+e^-)$ events.

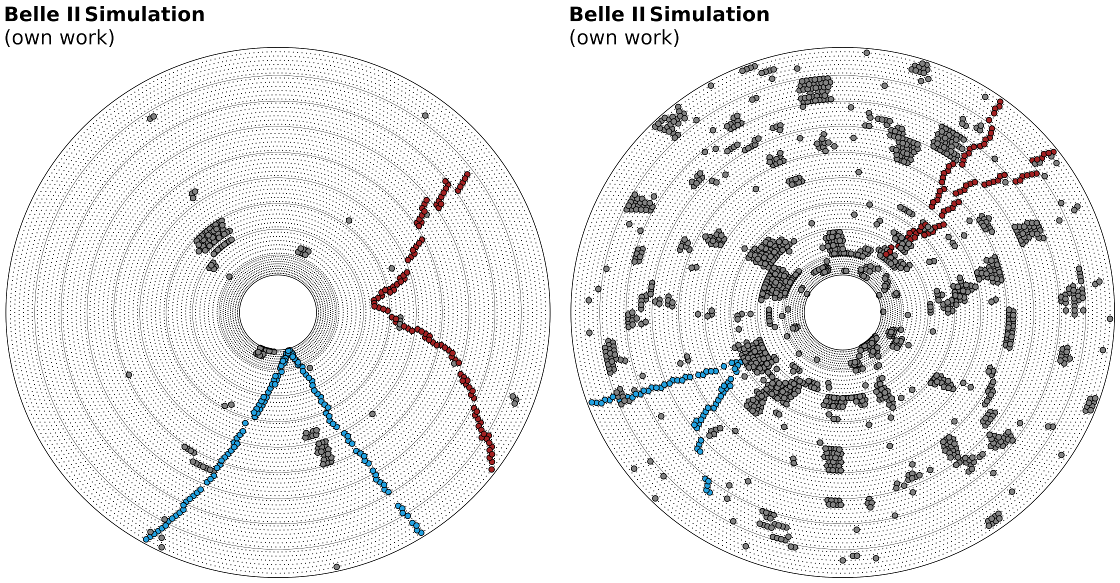

Figure 7.2: Simulated event displays for dark Higgs bosons produced in association with inelastic DM. The plots show the CDC in the x-y-plane. The left plot shows low beam background conditions, while the right plot was simulated with high beam background conditions. CDC hits marked in cyan represent the hits associated with the tracks originating from the h' decay and the red hits mark the tracks from the χ_2 decay. Grey hits are not associated with any track, and are therefore considered extra CDC hits. Plots adapted from L. Reuter.

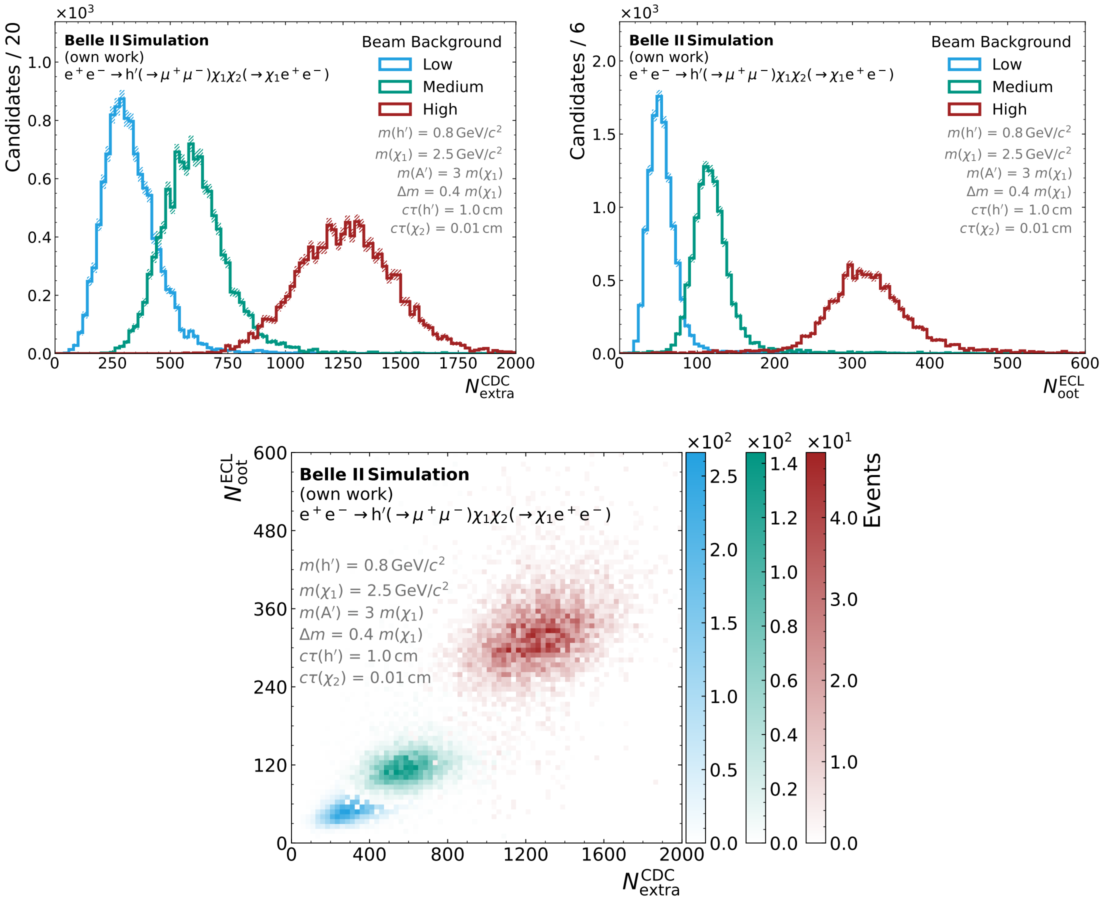

Figure 7.3: Upper left: Number of CDC hits that are not assigned to a reconstructed track. Upper right: Number of ECL crystals that have energy deposited more than 110 ns before or after the measured event t_0 (out-of-time). Bottom: Correlation between the two variables. The different colours represent $\mathrm{e}^+\mathrm{e}^- \to \mathrm{h}'(\to \mu^+\mu^-)\chi_1\chi_2(\to \chi_1\mathrm{e}^+\mathrm{e}^-)$ samples that have been simulated with different beam background conditions.

out-of-time if the deposition happens outside of a window of 110 ns around the measured event t_0. The distribution of the number of out-of-time crystals can be seen in Fig. 7.3. Additionally, one can see there that the number of additional CDC hits and the number of out-of-time crystals are highly correlated. As the two observables are measured by uncorrelated subdetectors, this is a strong indication that these observables can be used to describe the beam background conditions.

In principle, both of the described variables can be used as a proxy for the varying beam background conditions. Nevertheless, for the analysis described here, as it mostly relies on tracking, the number of extra CDC hits is the more natural observable. Fig. 7.4 shows the signal efficiency as a function of the average number of extra CDC hits, $N_{\text{extra}}^{\text{CDC}}$, that have been observed in the data-taking period the beam background overlays used for the simulation of the samples correspond to. One can see there that the worse the beam background conditions are (on average more $N_{\text{extra}}^{\text{CDC}}$) the worse the signal efficiency is. Furthermore, as one could already see in Fig. 7.1 the effect gets more pronounced for larger h' lifetimes where the h' decays on average more displaced. These observations verify that $N_{\text{extra}}^{\text{CDC}}$ serves as a good proxy to estimate the beam background conditions.

Fig. 7.4 shows that the efficiency loss depends linearly on $N_{\text{extra}}^{\text{CDC}}$. Therefore, for each simulated model parameter configuration I fit a linear function to extract the signal efficiency as a function of the extra CDC hits, $\epsilon_{\text{sig}}\left(N_{\text{extra}}^{\text{CDC}}\right)$. I use this function to get the signal efficiency for the full dataset, taking into account the average number of $N_{\text{extra}}^{\text{CDC}}$ of the data considered for this analysis.

To ensure that this efficiency drop is not caused by the selection described in Chapter 6, but by the track-finding efficiency for displaced vertices, I study the h' reconstruction on simulated samples without applying any selections. Fig. 7.5 shows the number of correctly reconstructed h' candidates with a lifetime of $c\tau(\mathrm{h}') = 300\,\text{cm}$. It can be clearly seen that the number of h' candidates drops in the same manner as the signal efficiency as the beam background conditions get worse (more $N_{\text{extra}}^{\text{CDC}}$). This check ensures that the efficiency drop is caused by the track-finding efficiency and is not induced by the selection.

7.2 Trigger Efficiency

In addition to the studies on the selection variables, I study the influence of the Belle II trigger system on the signal efficiency based on simulated samples. I do this for both the L1 trigger as well as for the HLT trigger level, which both are explained in Section 3.2.5.

On the L1 trigger several predefined trigger lines could be used to trigger a signature which includes four tracks in the final state. One of them is the single track trigger (STT), which triggers the presence of at least one track in the event. To reduce the amount of beam background events that are triggered by the STT, the track has to carry at least 0.7 GeV/c of momentum and the extrapolation of the track has to be close to the IP ($|z_{\text{track}}| < 15\,\text{cm}$). While a four-track final state should be effectively found by the STT the two additional

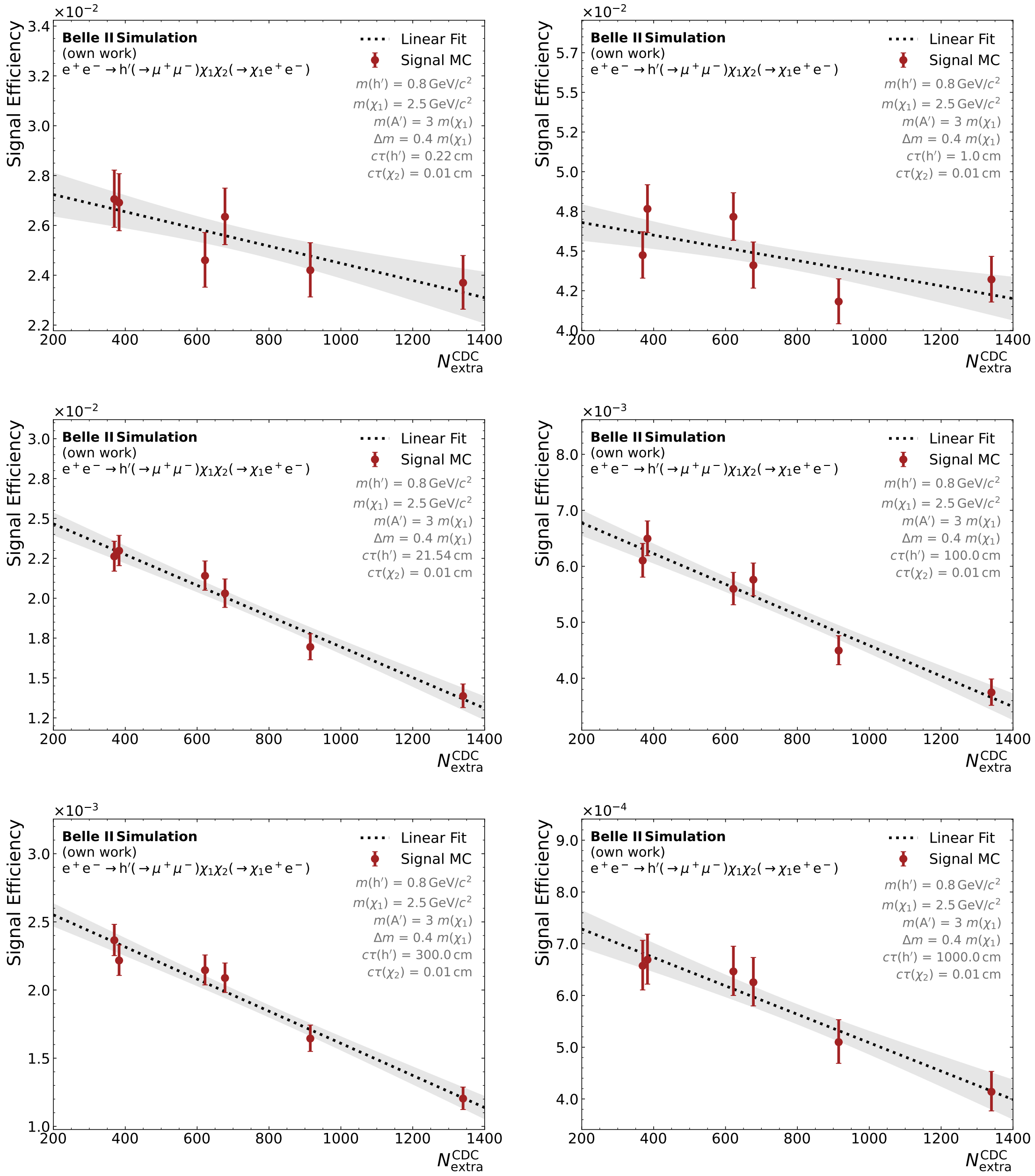

Figure 7.4: Signal efficiency as a function of the average number of extra CDC hits $N_{\text{extra}}^{\text{CDC}}$ for different lifetimes hypotheses of the h'. All other model parameters are fixed to the values in the plots. The plots show the $\mathrm{e}^+\mathrm{e}^- \to \mathrm{h}'(\to \mu^+\mu^-)\chi_1\chi_2(\to \chi_1\mathrm{e}^+\mathrm{e}^-)$ signal process as an example. Every data point (red) corresponds to a signal sample simulated with specific beam background conditions. The black dashed line represents a linear fit through the data points. The $\pm1\sigma$ uncertainty on the fit is marked with a grey band.

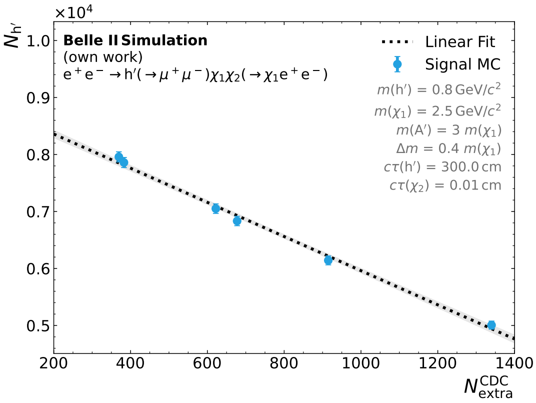

Figure 7.5: Number of correctly reconstructed h$'$ candidates as a function of the average number of extra CDC hits $N_{\text{extra}}^{\text{CDC}}$. The result is based on $e^+e^- \to h'(\to \mu^+\mu^-)\chi_1\chi_2(\to \chi_1 e^+e^-)$ signal with a fixed lifetime of $c\tau(h') = 300.0\,\text{cm}$. The h$'$ is reconstructed from a pair of muons. To show the pure reconstruction effect and not bias the result, no selections are applied on either the muons or the h$'$ candidates.

requirements make the situation more complicated for the studied signal signature. The performance drops for model parameter configurations where the tracks either do not carry enough momentum or are significantly displaced. Fig. 7.6 shows the STT performance for different choices of the model parameters. The results show exactly the expected behaviour that is described above. While the plots show that the STT performance depends on the lifetime of the dark Higgs candidates, it seems to be independent of the lifetime of the χ_2. This is only true for the model parameter configurations shown in these plots, as for the choice of model parameters shown here, most of the events are triggered by the muons from the h$'$ decay and therefore the displacement of the electron tracks has no impact on the performance. In addition to the performance loss for some parameter configurations, the STT was not active for the whole data-taking period where the dataset used in this analysis was collected. The integrated luminosity taken with the STT enabled corresponds only to $276\,\text{fb}^{-1}$ (of $364\,\text{fb}^{-1}$).

As long as the χ_2 is decaying into a pair of electrons, another class of L1 trigger lines that rely on the ECL can be considered. The most suitable line here is the HIE trigger line, which sums up the energy depositions in the barrel and part of the forward ECL ($19.23^\circ \leq \theta \leq 127.55^\circ$) and lets an event pass if the energy sum is above 1 GeV. Especially if the mass splitting between the $m(\chi_1)$ and $m(\chi_2)$ is large enough and the electrons consequently carry a lot of momentum, this line is expected to show good performance. The performance is shown in Fig. 7.6 and shows the expected behaviour of being independent of the h$'$ properties (lifetime and mass) and only losing efficiency for smaller mass splittings. Additionally, one can see that the performance of the HIE trigger line slightly improves for larger lifetimes of the χ_2. This effect is caused by the type of events that are selected and are used in the denominator to calculate the performance. If the lifetime of the χ_2 is larger

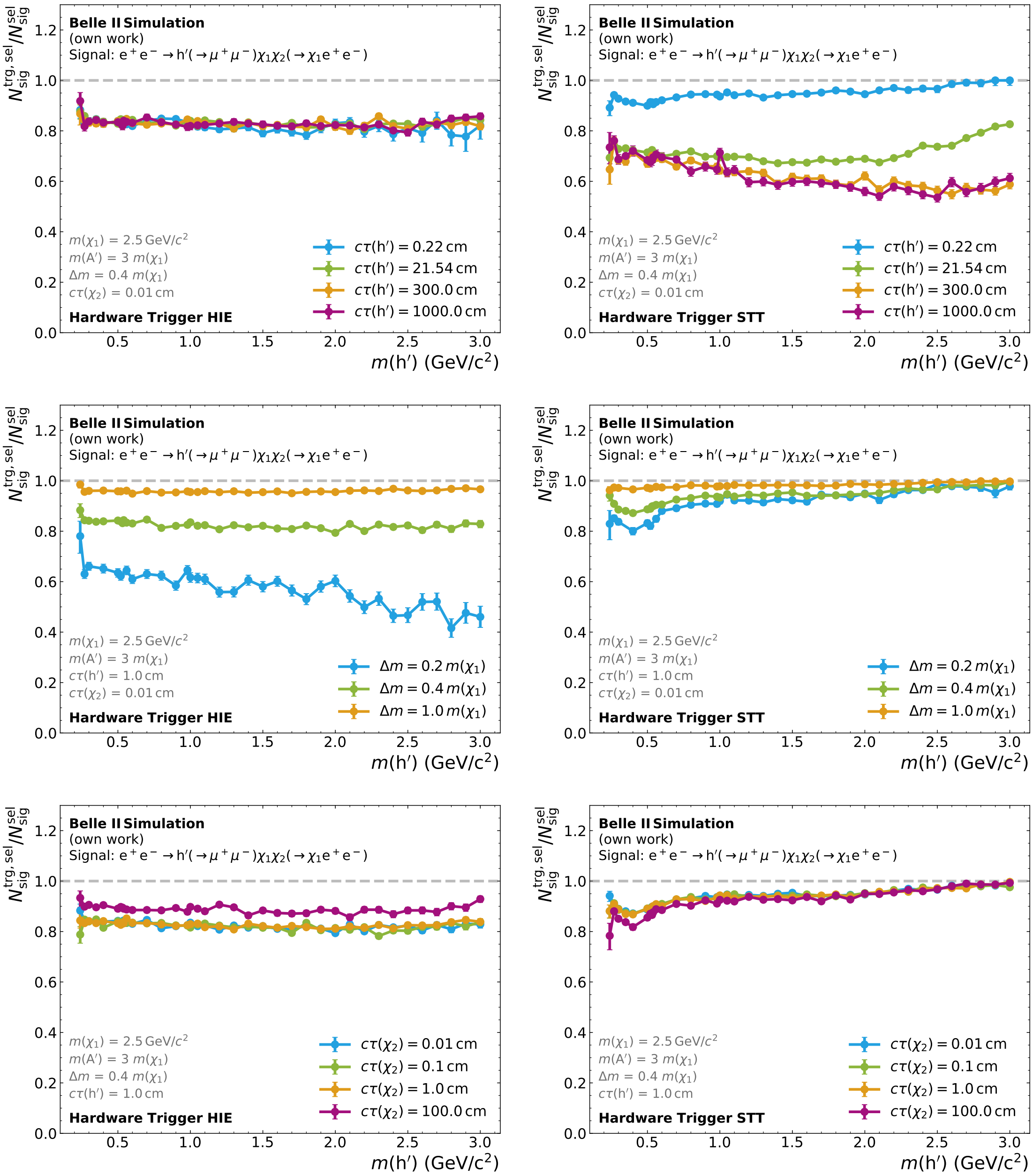

Figure 7.6: Fraction of events that are selected and triggered by the high energy (HIE) (left) and STT L1 trigger line (right) to all selected events. The selected events are selected with the selections from Tables 6.1 and 6.2 (excluding the selection on $E_{\rm hie}$). The performance is shown as a function of the dark Higgs mass for several variations of the other model parameters: $c\tau(\mathrm{h}')$ (top), Δm (center), and $c\tau(\chi_2)$ (bottom). Only the $\mathrm{e}^+\mathrm{e}^- \to \mathrm{h}'(\to \mu^+\mu^-)\chi_1\chi_2(\to \chi_1\mathrm{e}^+\mathrm{e}^-)$ signal is shown as an example and the plots for the other two final states can be found as Figs. D.1 and D.2 in the appendix. The linear interpolation between the points is added for better visualisation.

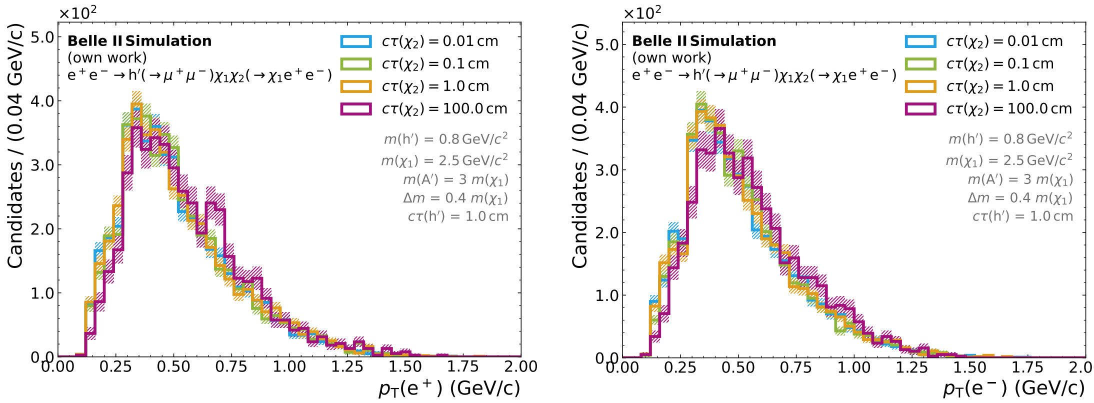

Figure 7.7: Transverse momentum of the reconstructed e^+ (left) and e^- (right) track for several variations of the χ_2 lifetime. The plots show the $e^+e^- \rightarrow h'(\rightarrow \mu^+\mu^-)\chi_1\chi_2(\rightarrow \chi_1 e^+e^-)$ final state.

the electrons are generated with more displacement. Tracks not originating from the IP can be easier reconstructed if they carry more transverse momentum as this results in a straighter track. While in general, the momentum distribution of the electrons from the χ_2 decay is independent of the χ_2 displacement, the reconstruction changes the momentum distribution favouring higher momentum tracks. This can be seen in Fig. 7.7. Consequently, as these tracks on average carry a higher momentum the energy deposited in the ECL is larger, resulting in a better HIE performance.

Especially as it is independent of the lifetime of the dark Higgs, the HIE trigger line shows overall better performance than the STT trigger line and as the former is available for the whole dataset used, I use the HIE trigger line for the analysis presented here.

I perform an additional check to ensure that the HIE performance does not depend significantly on the different beam background conditions observed during data taking. In Fig. 7.8 the HIE efficiency is shown for samples simulated with different beam background conditions and there are no significant differences observed in the HIE performance between them. On the contrary, the STT shows significant differences in the performance for the different beam background conditions. This is another reason why I do not use the STT line in this analysis, as the instability for different beam background conditions would introduce a systematic uncertainty on the signal efficiency that is complicated to estimate.

As the L1 trigger is only the first trigger step and is followed by the HLT I check the performance of the latter, as well. One observes that all events that pass the L1 trigger also pass the HLT, so there is no additional efficiency loss introduced by the HLT.

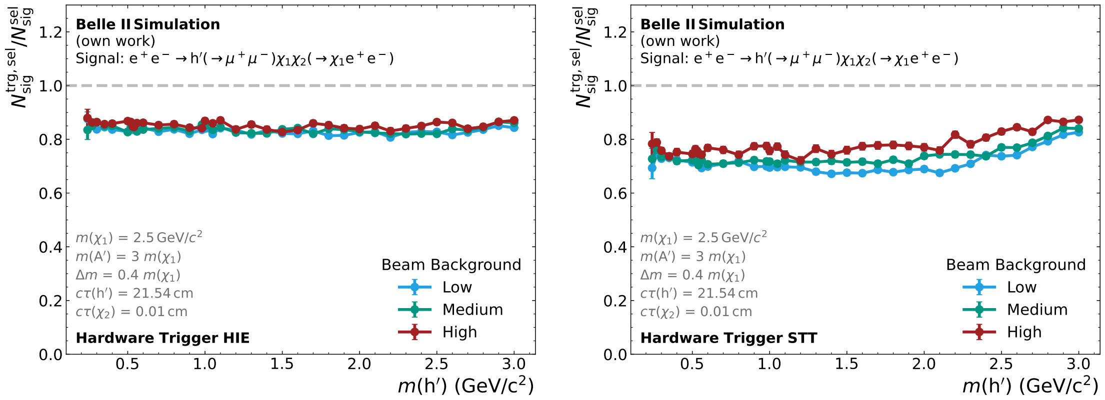

Figure 7.8: Fraction of events that are selected and triggered by the HIE L1 trigger (left) and STT L1 trigger line (right) to all selected events. The performance is shown as a function of the dark Higgs mass for different beam background conditions to check the stability of the trigger lines against these conditions. Only the process $e^+e^- \to h'(\to \mu^+\mu^-)\chi_1\chi_2(\to \chi_1 e^+e^-)$ is shown as an example, as the situation is similar in the other two considered final states. The linear interpolation between the points is added for better visualisation.

Chapter 8

Signal and Background Parametrization

To search for a signal-like excess over the SM expectation, I use the reconstructed mass of the h′, denoted as $M_{\mathrm{xx}}^{\mathrm{h}'}$. This is done via counting events in a given signal window and comparing the observed events with the expectation taken from the reconstructed mass sidebands on data[*]. The exact definition of the signal window and the sidebands will be given in Section 11.2. As the definition of the signal window includes the width of the reconstructed h′ mass, I obtain the signal width by fitting the signal shape using simulated signal samples. As a fitting framework zfit [75] is used.

8.1 Signal Parametrization

I describe the reconstructed signal h′ invariant mass distribution with a Double Sided Crystal Ball (DSCB) function [76, 77]. This function is defined as

$$f\left(x;\mathbf{\Theta}\right) = N \cdot \begin{cases} A_l\left(B_l - \frac{x-\mu}{\sigma}\right)^{-n_l} & \text{for } \frac{x-\mu}{\sigma} < -\alpha_l \\ \exp\left(-\frac{(x-\mu)^2}{2\sigma^2}\right) & \text{for } -\alpha_l \le \frac{x-\mu}{\sigma} \le \alpha_r \\ A_r\left(B_r - \frac{x-\mu}{\sigma}\right)^{-n_r} & \text{for } \frac{x-\mu}{\sigma} > \alpha_r \end{cases}, \tag{8.1}$$

with

$$\mathbf{\Theta} = \left(\mu, \sigma, \alpha_l, \alpha_r, n_l, n_r\right), \tag{8.2}$$

$$A_{l/r} = \left(\frac{n_{l/r}}{|\alpha_{l/r}|}\right)^{n_{l/r}} \exp\left(-\frac{|\alpha_{l/r}|^2}{2}\right), \tag{8.3}$$

$$B_{l/r} = \frac{n_{l/r}}{|\alpha_{l/r}|} - |\alpha_{l/r}|, \tag{8.4}$$

---

[*] As the signal region is blinded during the development and optimisation of the analysis, for the initial sensitivity studies the background expectation is derived from simulated SM background samples.

and the normalisation N. The function has a Gaussian core which is described by two parameters, the mean μ and the width σ and exponential tails on each side which are characterised by the $\alpha_{l/r}$ and $n_{l/r}$ parameters. Here, the parameters $\alpha_{l/r}$ describe the transition points from the Gaussian to the exponential functions and the exponential parts themselves are described by the $n_{l/r}$ parameters. Therefore, the signal is modelled with a probability density function (PDF) with six floating parameters.

The results of the signal shape fits are only used in a later step of the analysis to define the signal windows and not for fitting a potential signal peak in the measured data. Therefore, the normalisation N is only used for the visualisation of the shape fit results and not used later on during the analysis. Furthermore, there are no significant differences observed between the simulated signal samples produced with different beam background conditions. Therefore, to increase the statistics in the signal shape fits, I merge the signal samples produced with different beam background conditions. Fig. 8.1 shows six example signal shape fits for the $\mathrm{e}^+\mathrm{e}^- \to \mathrm{h}'(\to \mu^+\mu^-)\chi_1\chi_2(\to \chi_1\mathrm{e}^+\mathrm{e}^-)$ final state with three different h' masses and two lifetime hypotheses. Examples for the other two final states can be found in Figs. E.1 and E.2 in the appendix. The plots show that the DSCB describes the signal $M_{\mathrm{xx}}^{\mathrm{h}'}$ distribution very well for all tested masses and lifetimes. From now on, when speaking of the signal width, I refer to the width σ_{DSCB} of the Gaussian core of the DSCB PDF. Note that as the signal is described by a DSCB and not a simple Gaussian, this σ_{DSCB} does not correspond to the usual probability coverage one would obtain with a Gaussian PDF.

In Fig. 8.2 I show the extracted signal width of the DSCB for several variations of the model parameters. The fitted signal width is dominated by the detector resolution and not by the actual width of the dark Higgs which is, in the model parameter range covered in this thesis, significantly smaller than the resolution of Belle II. This manifests itself in the fact that the signal width mainly depends on both the mass and the lifetime of the dark Higgs candidates. The dependence on the mass is linear and can be explained by the fact that the relative uncertainty on the momentum measurement of the tracks directly propagates to a relative uncertainty on the di-particle mass. Under the assumption that the relative uncertainty does not depend on the mass itself, a constant relative uncertainty over the whole mass range results in a larger absolute uncertainty and consequently a broader signal peak for larger mass hypotheses. The dependence on the lifetime is caused by the on average shorter track length of more displaced particles. Less tracking hits result in a worse momentum resolution and therefore in a worse resolution of the reconstructed mass.

Another observable effect is the exponential decrease of the fitted signal width close to the kinematic threshold, where the h' mass is close to twice the mass of the FSPs it decays into. In these cases, the reconstructed h' mass is dominated by the mass of the FSPs, which are known with far higher precision than the momentum resolution of Belle II.

As simulated signal samples cannot be produced for all scanned mass hypotheses, the signal width has to be interpolated between the simulated mass hypotheses. This is done

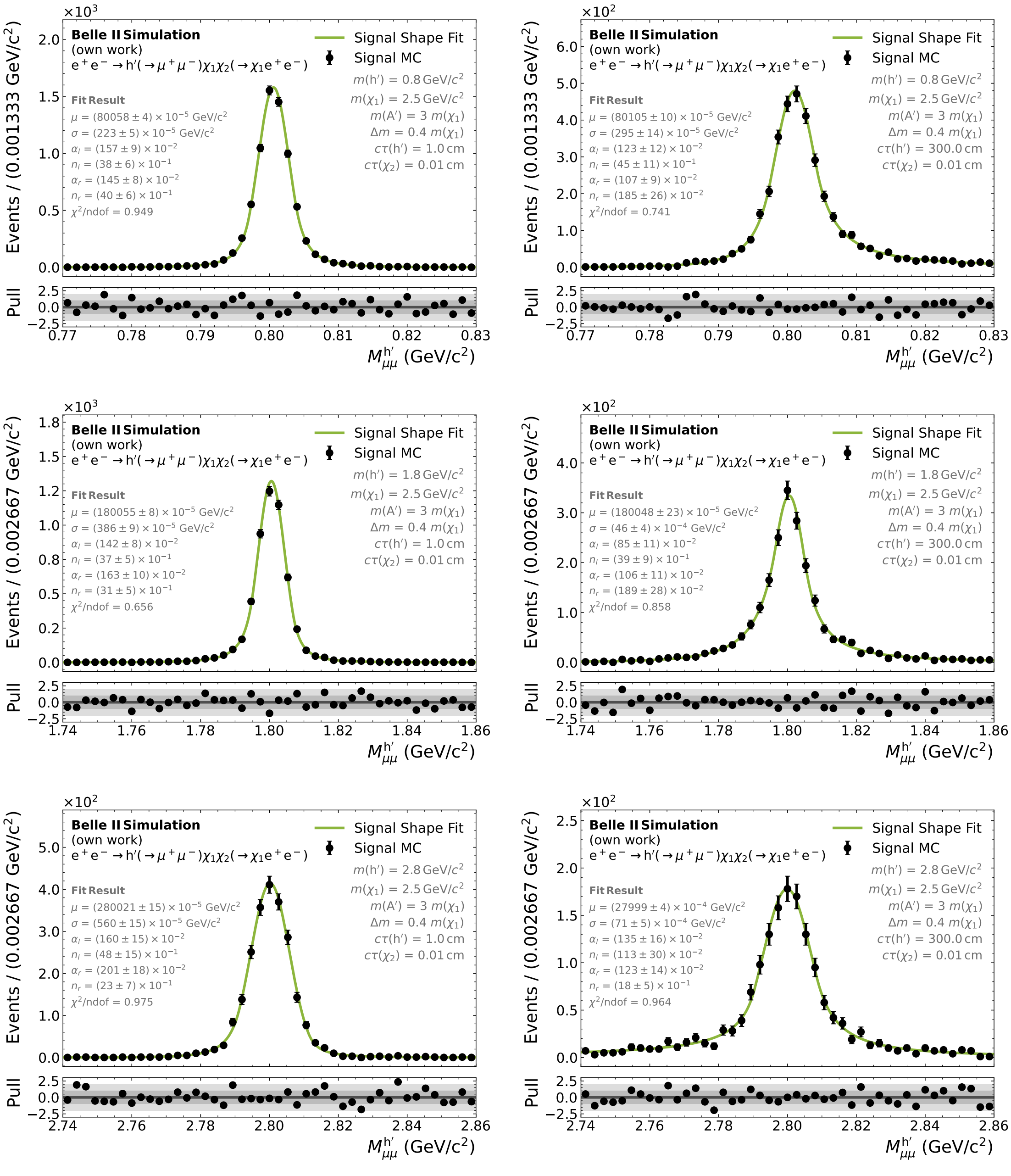

Figure 8.1: Signal shape fit examples for the $e^+e^- \to h'(\to \mu^+\mu^-)\chi_1\chi_2(\to \chi_1 e^+e^-)$ final state. The plots show fits on the reconstructed dark Higgs mass using a DSCB function. Plots on the left are produced with a dark Higgs lifetime set to $c\tau(h') = 1.0\,\mathrm{cm}$, while the plots on the right show the corresponding fits for $c\tau(h') = 300.0\,\mathrm{cm}$. The dark Higgs mass is choses as $m(h') = 0.8\,\mathrm{GeV/c^2}$ (top), $m(h') = 1.8\,\mathrm{GeV/c^2}$ (center), and $m(h') = 2.8\,\mathrm{GeV/c^2}$ (bottom). The values of all other model parameters are fixed to the values reported in the plots. The extracted fit parameters and their uncertainty are also shown for each fit in the corresponding plot. All selection requirements from Tables 6.1 and 6.2 are applied.

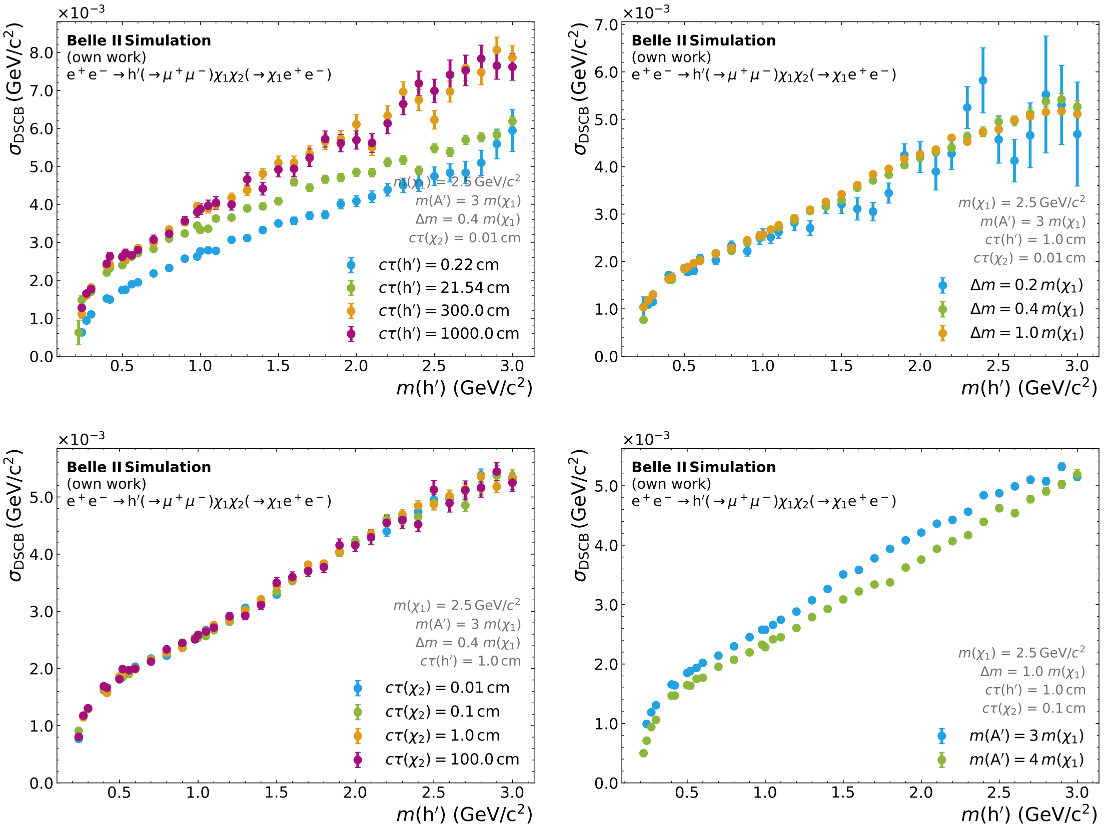

Figure 8.2: Extracted width σ_{DSCB} of the DSCB shape fit as a function of the dark Higgs mass. The plots show the $e^+e^- \to h'(\to \mu^+\mu^-)\chi_1\chi_2(\to \chi_1 e^+e^-)$ final state for several variations of the model parameters $c\tau(h')$ (upper left), mass splitting Δm (upper right), $c\tau(\chi_2)$ (lower left), and $m(A')$ (lower right).

with a linear fit on the extracted signal width parameter over the h' mass for each h' lifetime and the different variations of the remaining model parameters. As described above, close to the kinematic threshold the signal width does not follow a linear function but shows an exponential decrease. Therefore the mass points close to this threshold are excluded from the fit. This results in a slight overestimation of the signal width close to the respective threshold in the different final states. While this would be problematic if the signal width determined in this manner would be used to fit a signal peak on measured data, it is not problematic in the analysis described here as only the size of the signal window is slightly increased. The respective linear fits are shown for an exemplary selection of model parameter configurations in Figs. E.3 to E.5 in the appendix.

8.2 Background Parametrization

When looking into the reconstructed h' mass $M_{\mathrm{xx}}^{\mathrm{h}'}$ distribution of the remaining SM backgrounds after all selection criteria from Tables 6.1 and 6.2 are applied, no underlying peaking structure is observed in the simulated samples. The corresponding distributions for the different reconstruction channels are shown in Fig. 8.3. In the $\mathrm{h}' \to \mu^+\mu^-$ and $\mathrm{h}' \to \mathrm{K}^+\mathrm{K}^-$ reconstruction channel the expected background is close to zero, so I assume the background to be uniform across the whole $M_{\mathrm{xx}}^{\mathrm{h}'}$ range in these two channels. For the $\mathrm{h}' \to \pi^+\pi^-$ reconstruction channel the situation is a little bit different. While the general background level is very low as well, there are slightly more events visible there, which originate mainly from the $\mathrm{e}^+\mathrm{e}^- \to \tau^+\tau^-(\gamma)$ process. Furthermore, due to meson decays originating from this process, the low-mass region is more densely populated than the high-mass region. With the help of additional studies shown in Fig. 8.4 where the selection on the pointing angle is relaxed to increase the statistics, I set the point where the background level changes at $M_{\pi\pi}^{\mathrm{h}'} = 1.0\,\mathrm{GeV/c^2}$. I assume the background to be uniformly distributed above and below this threshold with different normalisations.

I use the normalisations obtained from the simulated samples only to get an estimate on the expected background level and the actual expected background level is derived from data in the $M_{\mathrm{xx}}^{\mathrm{h}'}$ sidebands which will be defined in Section 11.2. On data the $\mathrm{h}' \to \pi^+\pi^-$ reconstruction channel is split into two parts, as well, using the threshold derived from the studies on the simulated SM background samples.

In case there is no additional signal observed, I expect to observe 0.252 events in the $\mathrm{h}' \to \mu^+\mu^-$ reconstruction channel and 0.252 events in the $\mathrm{h}' \to \mathrm{K}^+\mathrm{K}^-$ reconstruction channel, based on SM background simulations. In the $\mathrm{h}' \to \pi^+\pi^-$ reconstruction channel there are in total 5.798 events expected, of which 4.537 events are expected below $1\,\mathrm{GeV/c^2}$ and 1.260 events above the threshold.

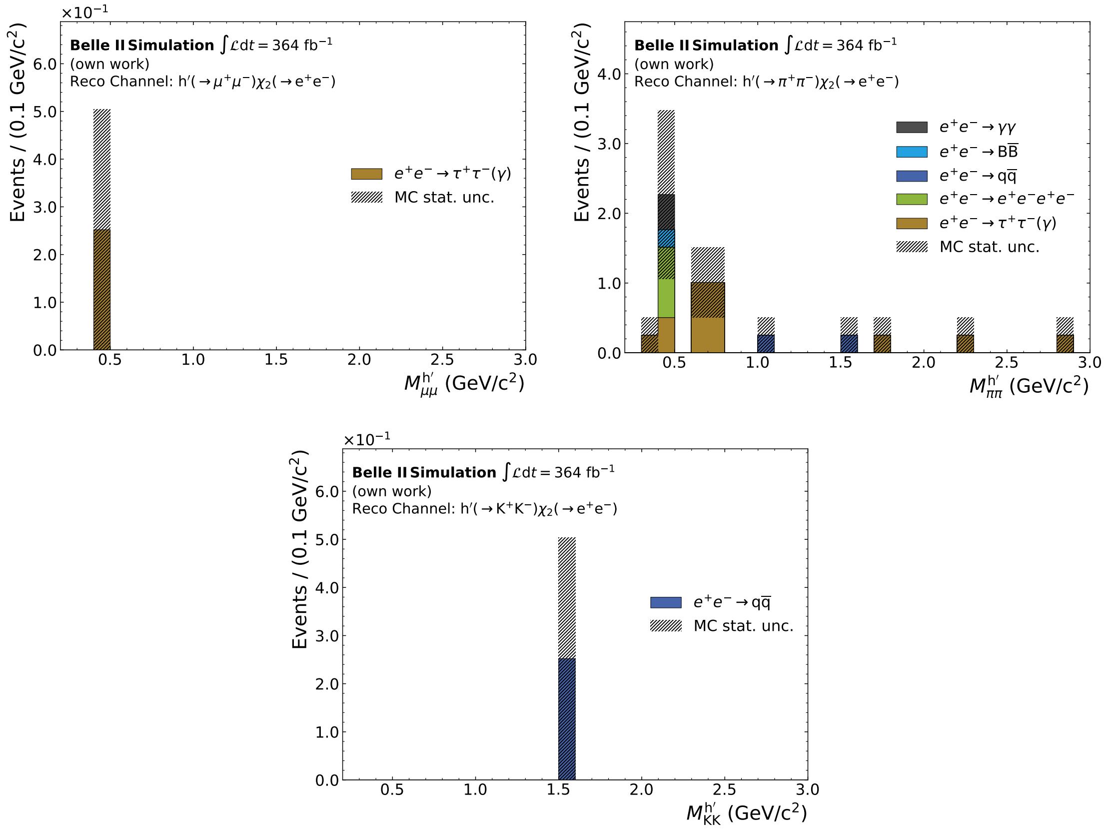

Figure 8.3: Reconstructed h$'$ mass in the three different reconstruction channels h$' \to \mu^+\mu^-$ (upper left), h$' \to \pi^+\pi^-$ (upper right) and h$' \to$ K$^+$K$^-$ (bottom) after applying all selections from Tables 6.1 and 6.2. All possible background sources described in Table 5.1 are considered, but only these that contribute after the selection are shown in the legend. Each component is scaled according to the produced number of events in each of the simulated samples to reach the target integrated luminosity of $\int \mathcal{L}\mathrm{d}t = 364\,\mathrm{fb}^{-1}$.

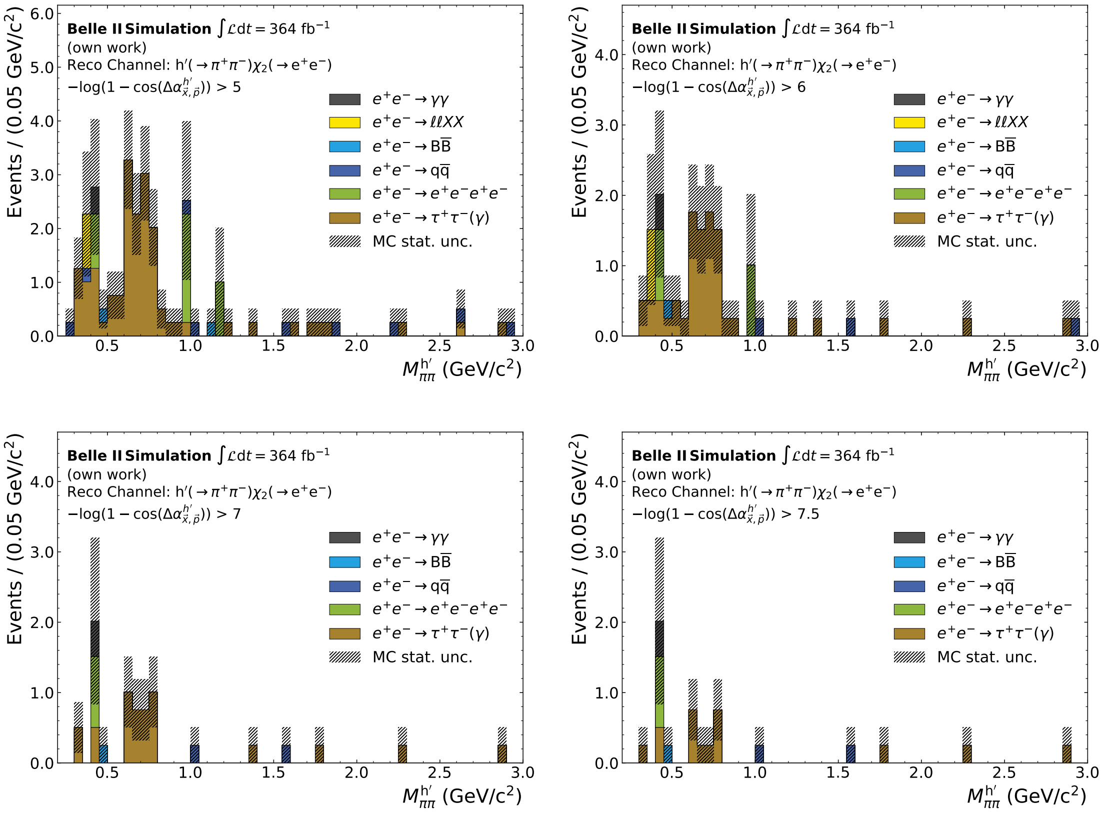

Figure 8.4: Reconstructed h′ mass in the $\mathrm{h}' \to \pi^+\pi^-$ reconstruction channel after applying all selections from Tables 6.1 and 6.2. The plots are created with different selections on the pointing angle of the dark Higgs candidate. All possible background sources described in Table 5.1 are considered, but only the ones that contribute after the selection are shown in the legend. Each component is scaled according to the produced number of events in each of the simulated samples to reach the target integrated luminosity.

Chapter 9

Corrections and Systematic Uncertainties

As the simulations are not perfectly reproducing the underlying physical models nor the detector response, differences between the observations on simulated samples and the data measured by Belle II are expected. Consequently, one has to correct the parameters (e.g. the signal efficiency and shape) derived from simulated samples to account for these discrepancies. I achieve this via control studies, that look into well-known processes that share similar kinematic properties as the signal process of interest. In this chapter, I describe the derivation of the corrections arising from different sources, such as the PID or the track-finding, and the associated systematic uncertainties introduced by these corrections. Additionally, I evaluate the systematic uncertainty due to the limited statistics available in the simulated samples. Furthermore, the uncertainty on the measurement of the integrated luminosity of the dataset is briefly discussed.

9.1 Particle Identification Corrections

The PID shows a different performance when applied to data or simulated samples. Therefore, a number of control channels are used to derive correction factors for both the efficiency and the fake rate. As the PID performance depends on the detector region and the momentum of the tracks, the corrections are given in bins of particle momentum p and polar angle θ. Furthermore, the performance depends on the particle type and is therefore studied for each particle type individually. I apply these correction factors on any track in the reconstructed event depending on the particle flavour.

The corrections are derived together with a statistical and a systematic uncertainty. Additionally, one has to take into account the correlation between the bins, in which the corrections are provided. While the statistical uncertainties are completely uncorrelated between the bins, the systematic part is fully correlated. To correctly propagate the uncertainties to the signal efficiency I perform a toy study. In each bin, 200 variations are drawn following a Gaussian distribution centered around the nominal correction and the width given by the uncertainty. These variations are then propagated to the correlation matrix using the sample covariance. In the end, I derive the systematic uncertainty on the signal efficiency via the width of the efficiency distribution obtained with these toys.

The PID corrections and their associated statistical and systematic uncertainty for the likelihood-based pion identification are derived via the SM process $\mathrm{K_S^0} \to \pi^+\pi^-$. Similarly, the corrections for kaons are derived with the process $\mathrm{D^{*+}} \to \mathrm{D^0}(\to \mathrm{K^-}\pi^+)\pi^+$. For the lepton corrections J/ψ decays are used, more explicit $\mathrm{J}/\psi \to \mathrm{e^+e^-}$ for electrons and $\mathrm{J}/\psi \to \mu^+\mu^-$ for muons. For all of these, I calculate the corrections with the use of the Systematic Corrections Framework*.

Fig. 9.1 shows the impact of the PID corrections on the signal efficiency for two example model parameter configurations in the $\mathrm{h}' \to \mu^+\mu^-$, $\mathrm{h}' \to \pi^+\pi^-$, and $\mathrm{h}' \to \mathrm{K^+K^-}$ final state. The associated systematic uncertainty on the correction is also shown there. The correction arising from the electron identification of the χ_2 daughter candidates is rather small with around 1 % over the whole mass range independent of the final state. With around $2 - 4$ % the systematic uncertainty associated with this correction is also rather small. While for the PID of the remaining FSPs the correction itself has a significant impact on the signal efficiency, reaching up to 15 % in the muon final state, 9 % in the pion final state, and around 5 % in the kaon final state, the systematic uncertainty arising from these sources is significantly smaller than the systematic uncertainty associated with the electron PID.

I do not explicitly consider a potential lifetime effect on the PID in this analysis. Nevertheless, corrections on the reconstruction efficiency for significantly displaced particles will be considered in Section 9.2.

9.2 Long-lived Particle Efficiency Correction

The finding efficiency for displaced $\mathrm{K_S^0}$ mesons shows significant discrepancies between data and simulation. As the $\mathrm{K_S^0}$ is a SM long-lived particle (LLP) which creates a pointing vertex it mimics exactly the signature of the displaced h' decay. Therefore, I can assume that the observed discrepancy between data and simulation is also applicable to the h'. While the χ_2 candidate is non-pointing, it is still expected that the correction can be applied to these candidates, as the driving factor for the discrepancy is the track-finding efficiency that is independent of a vertex being pointing or not. The discrepancy between data and simulation is studied in [78] and correction factors are derived in bins of the 3D-displacement r, momentum p, and polar angle θ of the $\mathrm{K_S^0}$. I apply these corrections to both the h' and the χ_2 candidate. The effect of this correction on the signal efficiency is shown in Fig. 9.2.

In addition to the correction itself, I derive the systematic uncertainty on the correction.

---

[*] https://syscorrfw.readthedocs.io (Access Date: 2024-09-16)

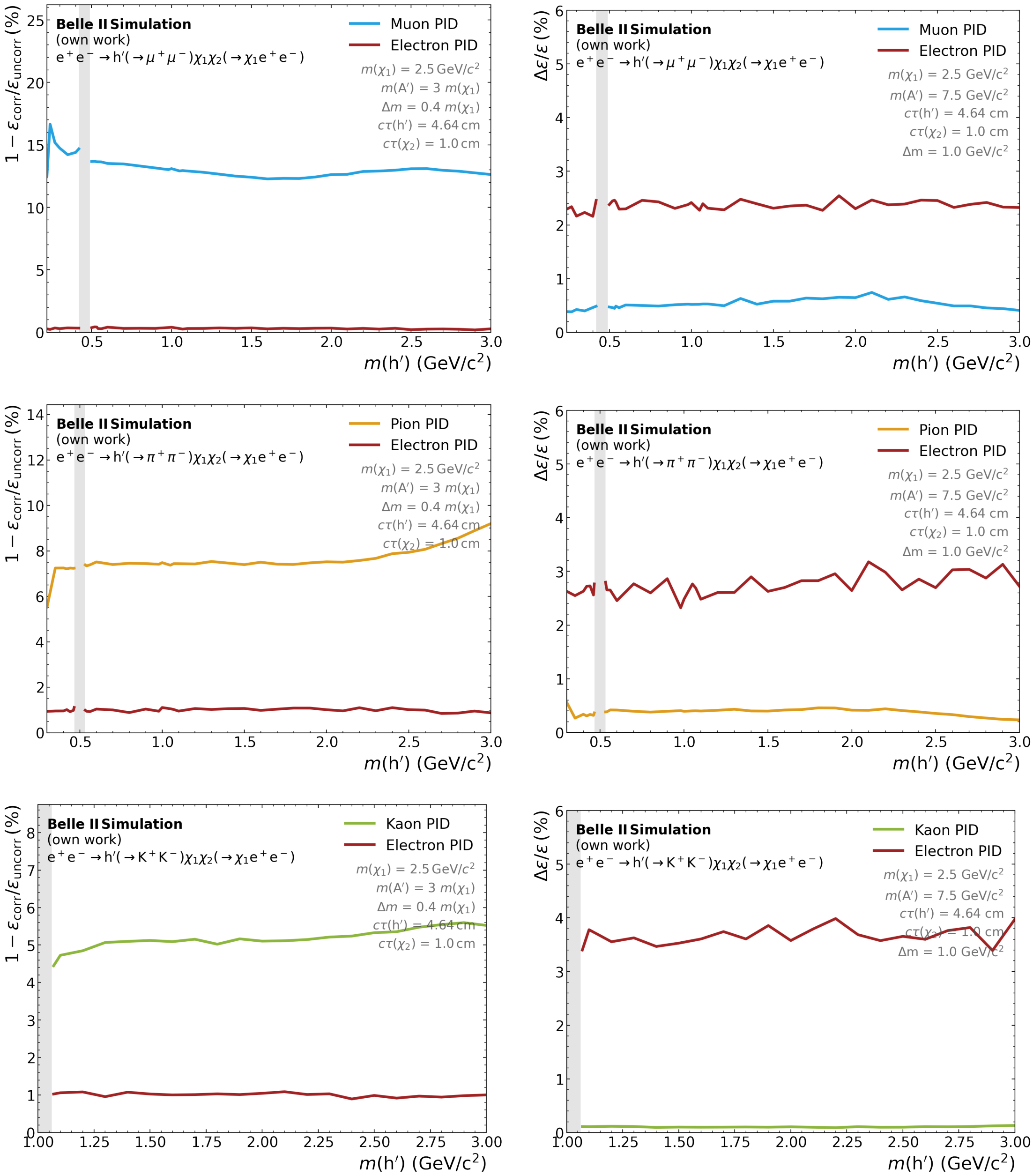

Figure 9.1: Correction on the signal efficiency (left) and associated relative systematic uncertainty (right) caused by the discrepancy in PID performance on data and simulated samples. The results are shown for the $e^+e^- \to h'(\to \mu^+\mu^-)\chi_1\chi_2(\to \chi_1 e^+e^-)$ (top), $e^+e^- \to h'(\to \pi^+\pi^-)\chi_1\chi_2(\to \chi_1 e^+e^-)$ (center), and $e^+e^- \to h'(\to K^+K^-)\chi_1\chi_2(\to \chi_1 e^+e^-)$ (bottom) final state as a function of the dark Higgs mass. The remaining model parameters are fixed to $m(\chi_1) = 2.5\,\mathrm{GeV/c^2}$, $m(A') = 3\,m(\chi_1)$, $\Delta m = 0.4\,m(\chi_1)$, $c\tau(h') = 4.64\,\mathrm{cm}$, and $c\tau(\chi_2) = 1.0\,\mathrm{cm}$. In the $h' \to \mu^+\mu^-$ and $h' \to \pi^+\pi^-$ final state the region corresponding to the K_S^0 veto is shown as a grey band. Similarly, in the $h' \to K^+K^-$ final state the region corresponding to the ϕ veto is marked with a grey band.

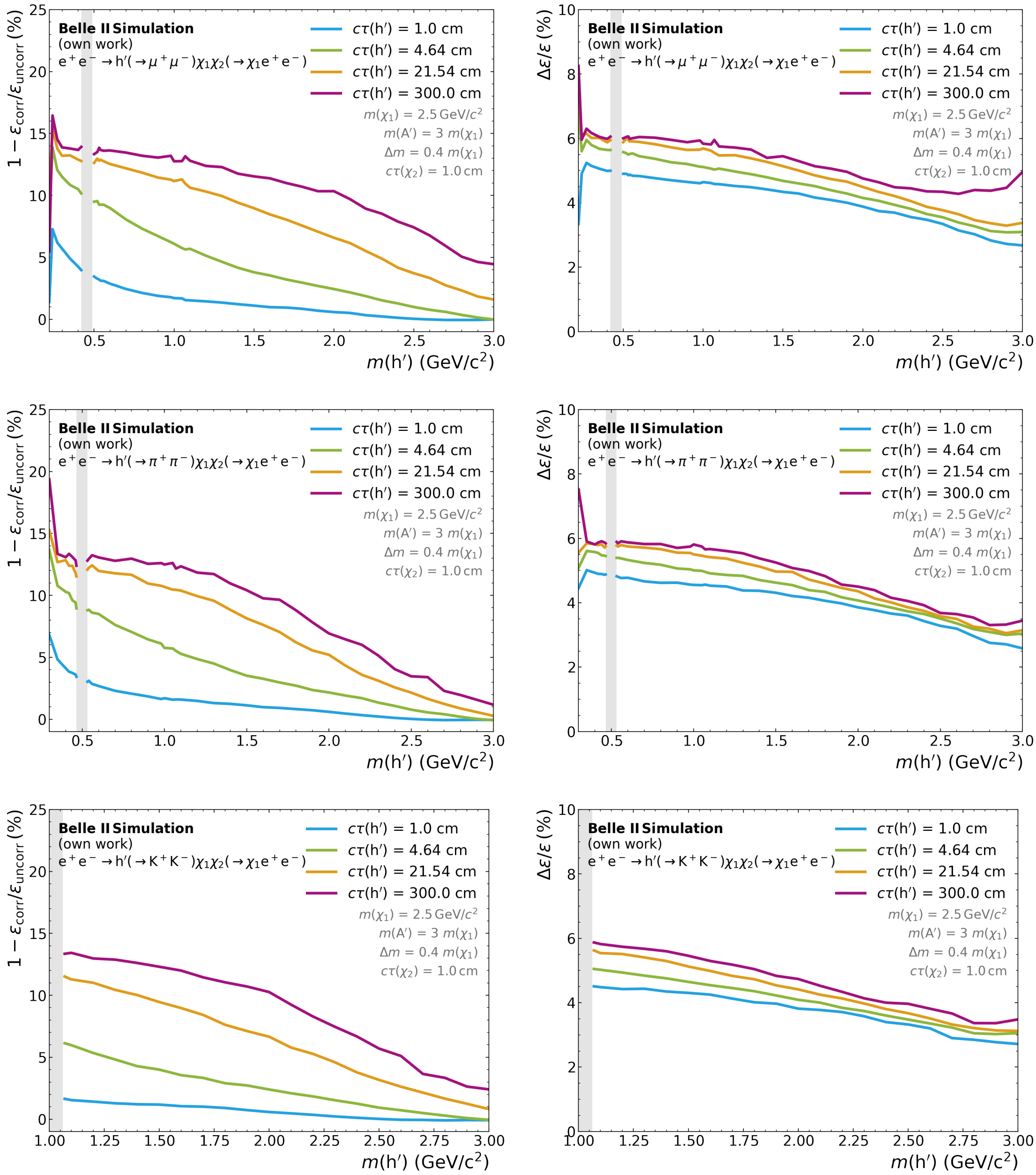

Figure 9.2: Impact of the LLP efficiency correction on the signal efficiency (left) and associated systematic uncertainty (right) in the $e^+e^- \to h'(\to \mu^+\mu^-)\chi_1\chi_2(\to \chi_1 e^+e^-)$ (top), $e^+e^- \to h'(\to \pi^+\pi^-)\chi_1\chi_2(\to \chi_1 e^+e^-)$ (center), and $e^+e^- \to h'(\to K^+K^-)\chi_1\chi_2(\to \chi_1 e^+e^-)$ final state as a function of the dark Higgs mass for different $c\tau(h')$. The remaining model parameters are fixed to $m(\chi_1) = 2.5\,\text{GeV}/c^2$, $m(A') = 3\,m(\chi_1)$, $\Delta m = 0.4\,m(\chi_1)$, and $c\tau(\chi_2) = 1.0\,\text{cm}$. In the $h' \to \mu^+\mu^-$ and $h' \to \pi^+\pi^-$ final state the region corresponding to the K_S^0 veto is shown as a grey band. Similarly, in the $h' \to K^+K^-$ final state the region corresponding to the ϕ veto is marked with a grey band.

This is done separately for the statistical and systematic components which are later added in quadrature. The statistical part is calculated by drawing 200 variations of the weights according to a Gaussian distribution with mean r_i^k and width σ_i^k, where σ_i^k is the statistical uncertainty on the respective weight r_i^k. For these 200 variations the varied signal efficiency $\epsilon_{\text{sig}}^{\text{corr}}$ is calculated according to the procedure described in Chapter 7 (taking into account the effect of the different beam background conditions) and the statistical uncertainty σ_{stat} is derived from the standard deviation of the resulting distribution of the 200 $\epsilon_{\text{sig}}^{\text{corr}}$ values. As the correction on the h' and χ_2 candidates are correlated the same variation is applied to both vertices at the same time. I estimate the systematic part by creating an up and down variation of the corrected efficiency by varying all weights at once with $r_i^k \pm \Delta_i^k$, where Δ_i^k is the systematic uncertainty on the weight r_i^k. Using these $\epsilon_{\text{sig}}^{\text{corr,up}}$ and $\epsilon_{\text{sig}}^{\text{corr,down}}$ variations, the systematic uncertainty Δ_{sys} can be estimated as the maximum deviation from the nominal corrected efficiency, $\max\left(|\epsilon_{\text{sig}}^{\text{corr,up}} - \epsilon_{\text{sig}}^{\text{corr}}|, |\epsilon_{\text{sig}}^{\text{corr,down}} - \epsilon_{\text{sig}}^{\text{corr}}|\right)$. Combining these two uncertainties one gets the total uncertainty on the LLP efficiency correction via

$$\Delta\epsilon = \sqrt{\sigma_{\text{stat}}^2 + \Delta_{\text{sys}}^2} \tag{9.1}$$

The resulting total uncertainty is shown in Fig. 9.2.

Both the correction and the associated relative uncertainty on the signal efficiency show the expected behaviour. The discrepancy between data and simulation of the LLP finding efficiency is larger for vertices with a larger displacement. Consequently, the correction has a bigger impact if the dark Higgs (or χ_2) lifetime is larger, reaching up to 15% for very large displacements. This also explains the effect that for a fixed lifetime the correction is larger for light h' candidates, as they decay on average further displaced than heavier dark Higgs candidates caused by the boost of SuperKEKB. The relative systematic uncertainty on the signal efficiency induced by this correction is between 3 and 7%. Here, the same effect as for the correction itself is visible: The uncertainty is larger for lighter and more displaced dark Higgs candidates. This is caused by the smaller statistics available to derive the corrections for vertices with a larger displacement, as less $\mathrm{K_S^0}$ mesons decay with such a large displacement and also the track-finding efficiency for tracks originating from such displaced vertices is very low (see Section 6.1).

9.3 Near-IP Tracking Efficiency

In addition to the track finding efficiency correction for LLPs (see Section 9.2) the systematic uncertainty on the track finding efficiency for prompt vertices ($r < 0.5\,\text{cm}$) has to be considered. This uncertainty depends on the track momentum and the associated correction factors and their uncertainties are listed in Table 9.1. The systematic uncertainty on the signal efficiency that arises due to this correction is estimated by varying all weights up and down and taking the maximum deviation from the nominal value as uncertainty. It

Table 9.1: Tracking efficiency correction and associated uncertainty of prompt vertices ($r < 0.5\,\mathrm{cm}$) in different track momentum regions.

Track momentum	Correction with uncertainty
$0.05\,\mathrm{GeV/c} < p \leq 0.12\,\mathrm{GeV/c}$	0.947 ± 0.020
$0.12\,\mathrm{GeV/c} < p \leq 0.16\,\mathrm{GeV/c}$	0.985 ± 0.017
$0.16\,\mathrm{GeV/c} < p \leq 0.2\,\mathrm{GeV/c}$	0.983 ± 0.019
$p > 0.2\,\mathrm{GeV/c}$	1.0000 ± 0.0027

has to be noted that this is a rather conservative approach, but as the contribution of this correction to the total systematic uncertainty is very small a potential overestimation of this uncertainty is not problematic.

9.4 Track Momentum Scaling

The magnetic field within Belle II is not known with perfect precision. This leads to the problem that the track momentum cannot be determined with high accuracy for recorded data, as the calculation of the momentum from the track curvature requires knowledge of the magnetic field. In [79] the effect is measured using D mesons and the extracted scaling factors are applied to the recorded data in this analysis.

On simulation the track momentum scaling is not required, as for the simulation and reconstruction of the events the same magnetic field map is used.

The systematic uncertainty from the correction affects the signal efficiency as a wrong momentum calculation could lead to migration of events in or out of the signal window. As found in other measurements, e.g. [80], the resulting uncertainty is very small and therefore can be neglected in this analysis.

9.5 Trigger Efficiency Correction

As described in Section 7.2, I use the HIE hardware trigger line for this analysis. To account for possible discrepancies in the performance on measured data and simulated samples, I study the performance in control regions.

I investigate the performance as a function of the deposited energy in the ECL to account for possible discrepancies in the event kinematics between the signal and the data from the control regions. The deposited energy is calculated by summing up all reconstructed ECL clusters that are within the HIE acceptance given by $4 \leq \theta_{\mathrm{ID}} \leq 58$, which corresponds to an acceptance of $19.23^\circ \leq \theta \leq 127.55^\circ$. This is measured at the center of the outermost included ECL crystals, thus the actual angular acceptance is slightly larger. Additionally, as the ECL hardware trigger only considers trigger cells that

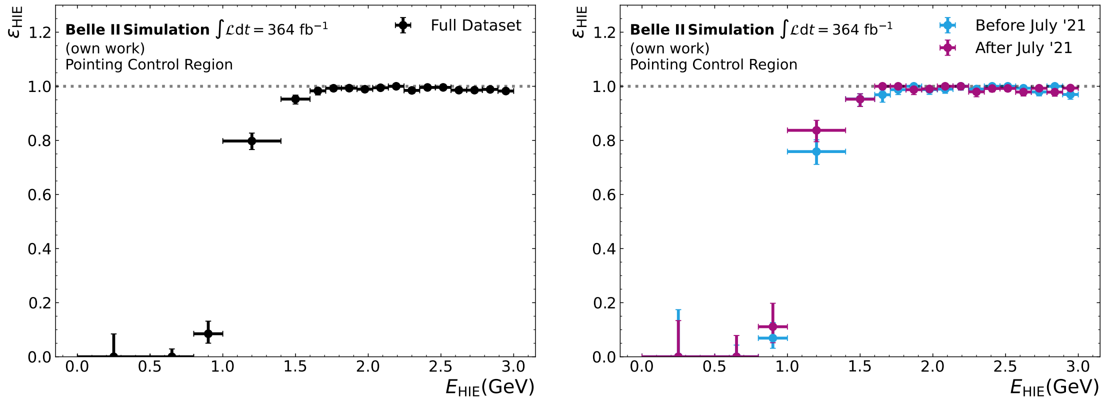

Figure 9.3: Performance of the HIE L1 trigger line as a function of the deposited ECL energy in the HIE acceptance as defined in Eq. (9.3). The results are based on the simulated SM background samples in the pointing angle control region. The left side shows the whole data-taking period, while on the right side, the sample is split into different data-taking periods with different beam background conditions.

contain at least 100 MeV of energy, only clusters with at least $E > 100\,\mathrm{MeV}$ are considered to calculate the deposited energy. Furthermore, the energy is calculated without taking the leakage correction into account as this gives a better approximation of the energy the trigger has seen. Summarising these conditions, the deposited energy E_{HIE} is given by

$$E_{\mathrm{HIE}} = \sum_i E_i^{\mathrm{cluster}}, \tag{9.2}$$

$$\text{with} \quad E_i^{\mathrm{cluster}} = \begin{cases} E_i^{\mathrm{cluster}} & \text{if } 4 \leq \theta_{\mathrm{ID},i} \leq 58 \text{ and } E_i^{\mathrm{cluster}} > 100\,\mathrm{MeV} \\ 0 & \text{else} \end{cases}. \tag{9.3}$$

It has to be noted that E_{HIE} is only an approximation of the energy that is used in the decision by the L1 trigger, as the low-level information used by the L1 trigger is not available at this stage of the analysis.

The performance is analysed on orthogonal trigger lines, e.g. the efficiency is calculated with respect to events that are triggered by CDC triggers that use information from an uncorrelated subdetector. The HIE efficiency is defined as

$$\epsilon_{\mathrm{HIE}} = \frac{N(\mathrm{sel\&CDC\&HIE})}{N(\mathrm{sel\&CDC})}, \tag{9.4}$$

where I use trigger lines that select events containing at least a pair of tracks with an opening angle of at least 30° for the CDC trigger.

The HIE efficiency in the pointing angle control region (see Section 10.2) is shown in Fig. 9.3 based on the simulated SM background samples. The performance shows the expected behaviour with nearly no events being triggered below $E_{\mathrm{hie}} = 1\,\mathrm{GeV}$, which corresponds to the energy threshold for the HIE trigger line. At $E_{\mathrm{HIE}} = 1\,\mathrm{GeV}$ a rapid

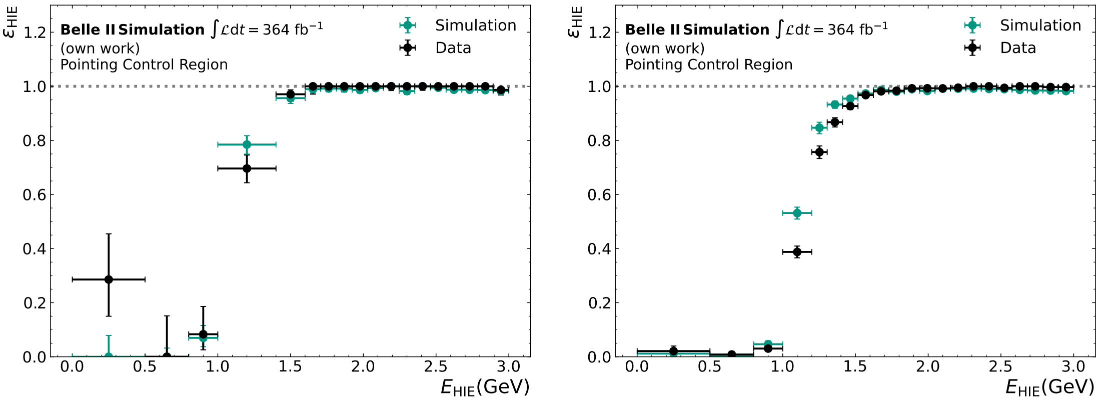

Figure 9.4: Performance of the HIE L1 trigger line as a function of the deposited ECL energy in HIE acceptance as defined in Eq. (9.3). The results are shown for simulated samples (green) and measured data (black) in the pointing angle control region. On the left side, all selections from Tables 6.1 and 6.2 are applied, while on the right side only the selections from Table 6.1 are applied to enrich the available statistics.

increase is observed ending up in nearly perfect efficiency for larger deposited energy values. A possible impact of the different beam background conditions on the HIE performance is checked by splitting the performance study into different data-taking periods. As can be seen on the right side of Fig. 9.3 the data-taking period and therefore the beam background conditions have no significant impact on the HIE performance.

Fig. 9.4 shows the comparison of data with simulation in the pointing angle control region. Especially when enriching the available statistics by only applying the selections from Table 6.1 (and not applying the data-driven selections from Table 6.2), below $E_{\mathrm{HIE}} < 1.5\,\mathrm{GeV}$ a significant discrepancy in the HIE performance between data and simulation is visible. There are two ways to address this problem: One can either calibrate the effect by applying correction factors based on the observed deviations, or one can restrict the analysis to the region where the agreement between data and simulation is good. As the former would introduce a non-negligible systematic uncertainty, I restrict the analysis to the region with good agreement, $E_{\mathrm{HIE}} > 1.5\,\mathrm{GeV}$. For most of the model parameter space, this restriction has no significant impact on the sensitivity of this analysis.

9.6 Signal Sample Size

The limited amount of events that are generated for each signal configuration gives rise to another systematic uncertainty on the signal efficiency. This uncertainty is directly extracted from the uncertainty on the linear fit used to derive the signal efficiency depending on the beam background conditions, as described in Section 7.1.

For some model parameter configurations, the systematic uncertainty in the signal efficiency caused by the limited statistics is quite large. More specifically, this is the case, whenever either the number of correctly reconstructed events and consequently the signal efficiency is very small, or for very large lifetimes where many of the decay vertices are outside of the reach of the Belle II detector. This problem could in principle be resolved by producing larger signal samples. As already stated in the analysis outline in Chapter 4, the computing resources required to cover the huge model parameter space is one of the limiting factors of the analysis. Therefore, I concentrate the resource usage on covering a larger variety of model parameter configurations, with the trade-off of a higher systematic uncertainty arising from the sample size in some regions of model parameter space.

A discussion on the size of the effect caused by the statistics and corresponding plots will be given in Section 9.9.

9.7 Luminosity Uncertainty

The integrated luminosity of the dataset recorded at the $\Upsilon(4\mathrm{S})$ that is considered in this thesis is measured as

$$\int \mathcal{L}\mathrm{d}t = (364.49 \pm 1.64)\,\mathrm{fb}^{-1} \tag{9.5}$$

[53]. This results in a relative uncertainty on the integrated luminosity of

$$\Delta_{\mathcal{L}} = \frac{\sigma_{\mathcal{L}}}{\int \mathcal{L}\mathrm{d}t} = 0.45\,\%. \tag{9.6}$$

This uncertainty is very small compared to the other systematic uncertainties I report in this chapter. Nevertheless, it still is considered as an additional nuisance parameter in the signal extraction.

9.8 Uncertainty on the Background Expectation

As described in Section 8.2, for the background determination the $\mathrm{h}' \to \pi^+\pi^-$ reconstruction channel is split into two regions at $M_{\pi\pi}^{\mathrm{h}'} = 1.0\,\mathrm{GeV/c}^2$ with different background levels on each side. I estimate the systematic uncertainty arising from this choice by varying the point where the sample is split and evaluating the impact on the background level. The split point is varied to $M_{\pi\pi}^{\mathrm{h}'} = 0.9\,\mathrm{GeV/c}^2$ and $M_{\pi\pi}^{\mathrm{h}'} = 1.2\,\mathrm{GeV/c}^2$, and the maximum deviation from the nominal background level is taken as a systematic uncertainty on the background expectation. Based on the simulated SM background samples, this relative uncertainty on the background expectation is determined as $\Delta_{\mathrm{bkg}} = 17\%$.

9.9 Summary of Systematic Uncertainties

The different sources of systematic uncertainty on the signal efficiency that are described in Chapter 9 are summarised in Fig. 9.5. Here, the total systematic uncertainty is determined by adding the individual sources in quadrature. One can observe that for most model parameter configurations the uncertainty on the finding efficiency of displaced vertices (Section 9.2) is the dominant source of systematic uncertainty. This is especially pronounced for cases where the dark Higgs has a large lifetime. For model parameter configurations where the signal efficiency is very low, the limited statistics of the simulated samples play a dominant role. Overall the total systematic uncertainty on the signal efficiency varies between 5 and 20% depending on the choice of the model parameters[*]. Therefore, the systematic uncertainty on the signal efficiency is significantly larger than the uncertainty on the luminosity measurement (see Section 9.7), causing the impact of the latter to be negligible.

To estimate the impact of the systematic uncertainty on the final sensitivity I perform a study calculating 95% CL upper limits with and without considering the systematic uncertainties. The calculation of the upper limits will be described in detail in Section 11.5 and the procedure to estimate the sensitivity is explained in Section 11.6. The result of this study is visualised in Fig. 9.6. It can be seen that the impact of the systematic uncertainties is rather small, increasing the upper limits by around 1% over nearly the full model parameter space. For large h' masses combined with very small h' lifetimes, the impact is slightly larger as the upper limits are weakened by up to 3% for these model parameter configurations.

---

[*] For mass points very close to the respective kinematic threshold, the systematic uncertainty on the signal efficiency can exceed this value due to the efficiency being close to zero and therefore the limited statistics playing a dominant role. As for these mass points the sensitivity is already very poor, due to the low efficiency, the large systematic uncertainty is negligible.

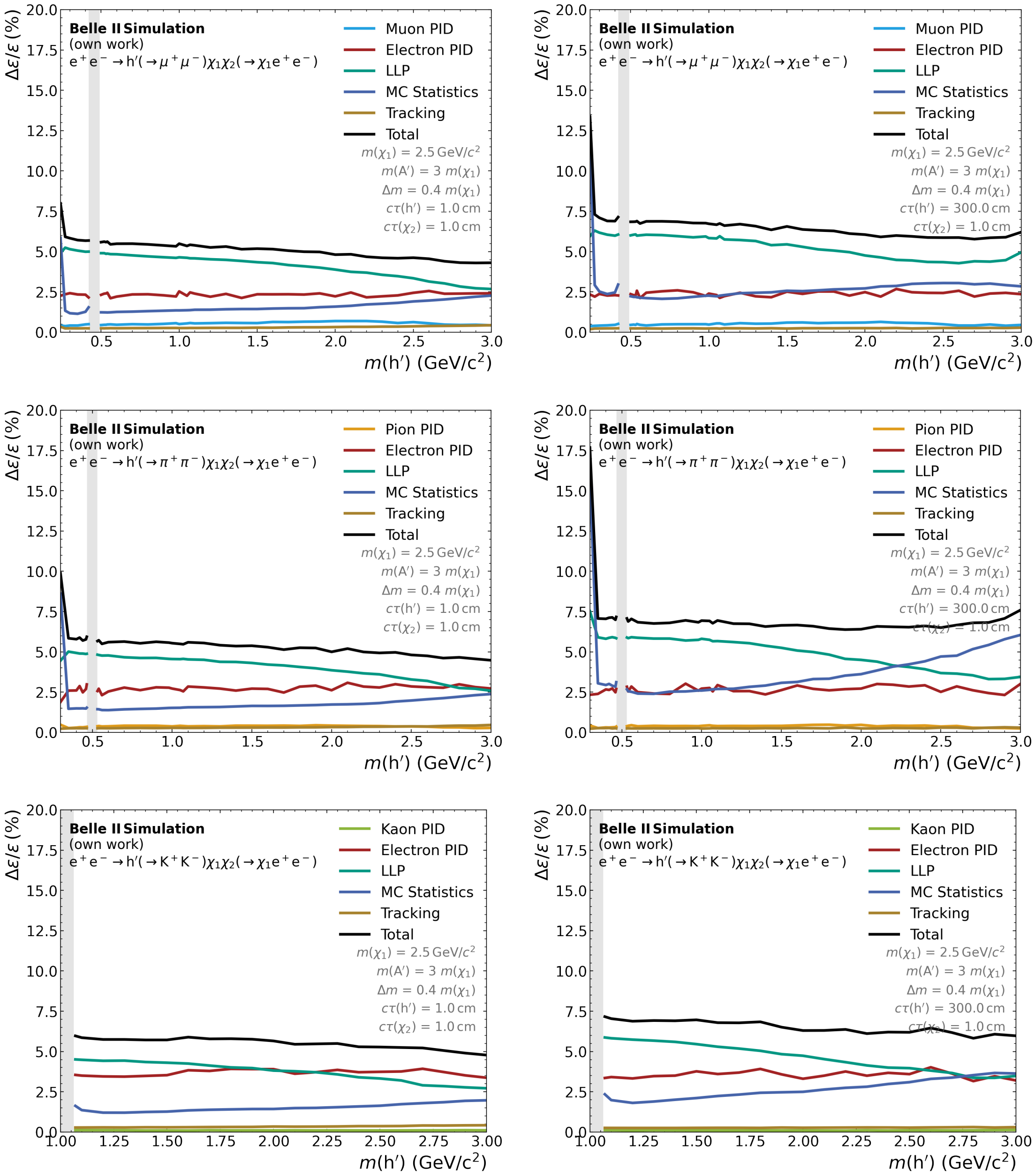

Figure 9.5: Summary of the different sources of systematic uncertainties described in Chapter 9. The plots show the relative systematic uncertainty on the signal efficiency as a function of the dark Higgs mass. The results are shown for the $\mathrm{e^+e^-} \rightarrow \mathrm{h}'(\rightarrow \mu^+\mu^-)\chi_1\chi_2(\rightarrow \chi_1\mathrm{e^+e^-})$ (top), $\mathrm{e^+e^-} \rightarrow \mathrm{h}'(\rightarrow \pi^+\pi^-)\chi_1\chi_2(\rightarrow \chi_1\mathrm{e^+e^-})$ (center), and $\mathrm{e^+e^-} \rightarrow \mathrm{h}'(\rightarrow \mathrm{K^+K^-})\chi_1\chi_2(\rightarrow \chi_1\mathrm{e^+e^-})$ (bottom) final state. The lifetime hypothesis of the h' is set to $c\tau(\mathrm{h}') = 4.64\,\mathrm{cm}$ (left) and $c\tau(\mathrm{h}') = 100.0\,\mathrm{cm}$ (right). The remaining model parameters are fixed to $m(\chi_1) = 2.5\,\mathrm{GeV/c^2}$, $m(\mathrm{A}') = 3\,m(\chi_1)$, $\Delta m = 0.4\,m(\chi_1)$, and $c\tau(\chi_2) = 1.0\,\mathrm{cm}$. In the $\mathrm{h}' \rightarrow \mu^+\mu^-$ and $\mathrm{h}' \rightarrow \pi^+\pi^-$ final states the region corresponding to the $\mathrm{K^0_S}$ veto is shown as a grey band. Similarly, in the $\mathrm{h}' \rightarrow \mathrm{K^+K^-}$ final state the region corresponding to the ϕ veto is marked with a grey band.

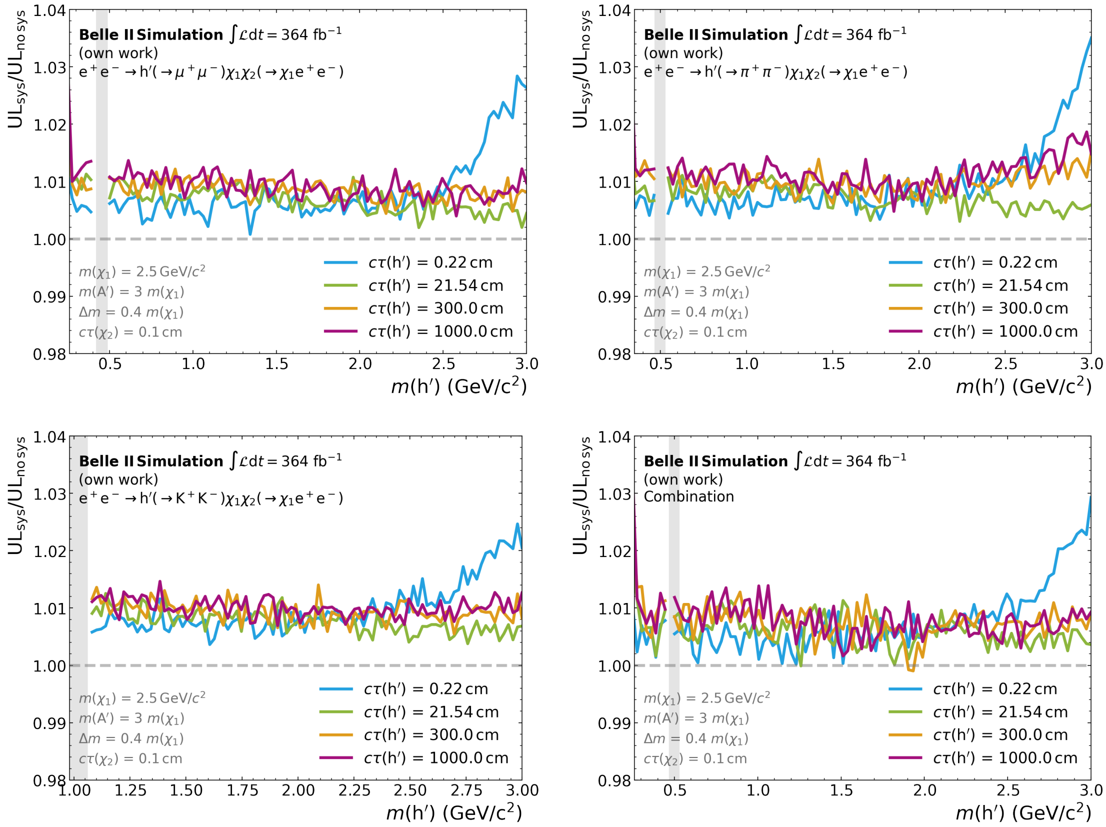

Figure 9.6: Impact of the systematic uncertainties on the expected sensitivity in the $e^+e^- \rightarrow h'(\rightarrow \mu^+\mu^-)\chi_1\chi_2(\rightarrow \chi_1 e^+e^-)$ (upper left), $e^+e^- \rightarrow h'(\rightarrow \pi^+\pi^-)\chi_1\chi_2(\rightarrow \chi_1 e^+e^-)$ (upper right), and $e^+e^- \rightarrow h'(\rightarrow K^+K^-)\chi_1\chi_2(\rightarrow \chi_1 e^+e^-)$ (lower left) final state, and for the combination of all three (lower right). The sensitivity is estimated according to the procedure that will be described in Section 11.6. The impact is shown as a function of the dark Higgs mass for several h' lifetime hypotheses. The remaining model parameters are set to $m(\chi_1) = 2.5\,\text{GeV/c}^2$, $m(A') = 3\,m(\chi_1)$, $\Delta m = 0.4\,m(\chi_1)$, and $c\tau(\chi_2) = 0.1\,\text{cm}$. The linear interpolation between the points is added for better visualisation.

Chapter 10

Control Regions

Up to now, the whole analysis that I describe has been developed on simulated samples. To test the quality of the simulation, without directly looking into the measured data in the signal region, the measured data is compared to the simulation in various control regions. These signal-depleted control regions are defined by the inversion of selection criteria from Table 6.1.

10.1 $\mathrm{K_S^0}$ Control Region

The most natural control region for this analysis is the reconstructed h' mass region around the $\mathrm{K_S^0}$ which is vetoed (see Section 6.7). One advantage of this region is that the $\mathrm{K_S^0}$ decay mimics the h' signal decay as it also creates a displaced vertex that is pointing back to the IP. $\mathrm{K_S^0}$ mesons are already used in Section 9.2 to derive correction factors for the track-finding efficiency of displaced tracks. Besides the efficiency, the shape of the reconstructed di-particle mass plays a role in this analysis as I use the signal shape (Section 8.1) for the definition of the signal window in the signal extraction. Therefore, I fit the reconstructed $\mathrm{K_S^0}$ mass shape both on simulation and measured data with a DSCB to compare the widths of the Gaussian cores of the distributions. Doing so, a ratio between the two fitted widths can be defined as

$$r_{\text{shape}} = \frac{\sigma_{\text{DSCB}}^{\text{data}}}{\sigma_{\text{DSCB}}^{\text{MC}}}. \tag{10.1}$$

If this ratio is significantly different from one it can be used to scale the signal width that is extracted from signal simulations. This scaling would then propagate to the signal window.

Before performing the fits, I use the $\mathrm{K_S^0}$ control region to compare the distributions of several observables between data and simulation to check their agreement. Fig. 10.1 shows that the missing energy E_{miss} distributions differ a lot, which also leads to a noticeable difference in the amount of $\mathrm{K_S^0}$ candidates observed in the reconstructed mass distribution. The data shows a peak at $E_{\text{miss}} \approx 2.5\,\text{GeV}$ that is not visible in the simulated

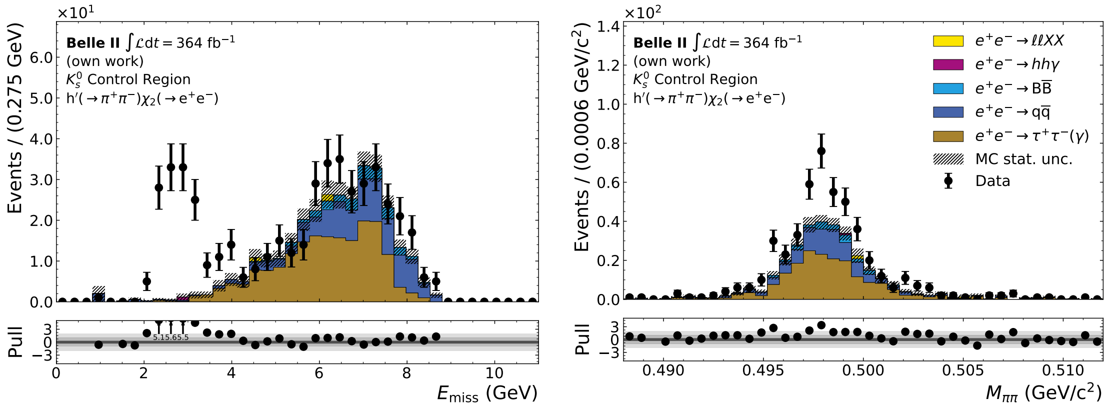

Figure 10.1: Left: Missing energy distributions for data and simulation in the K_S^0 control region. Right: Reconstructed mass of the h′ candidate in the K_S^0 control region for both data and simulation. The different simulated SM background components are scaled to the integrated luminosity of $\int \mathcal{L}\mathrm{d}t = 364\,\mathrm{fb}^{-1}$.

samples. One process that can cause such a peak in the missing energy distribution is the process $e^+e^- \to e^+e^-\phi(\to K_S^0 K_L^0)$ which is missing in the simulated samples as no reliable generator is available. In this case, both the electron pair and the K_S^0 have been correctly reconstructed. Additionally, the missing energy corresponds to the K_L^0 whose decay vertex is too far displaced to be reconstructed via its decay products. Nevertheless, for reconstructing K_L^0 mesons Belle II can make use of the KLM subdetector (and the ECL). To verify that the missing energy can be attributed to K_L^0 candidates that have been missed in the reconstruction, all KLM clusters that start at least at the 8-th KLM layer and have an associated timing of $-15\,\mathrm{ns} < t - t_0 < 30\,\mathrm{ns}$ are taken into consideration. I place these requirements on the KLM clusters to reject cluster candidates that have been produced by beam background depositions, as these are not of interest here. Using all these clusters, I derive the angle $\Delta\alpha_{\mathrm{KLM}}$ between the missing momentum vector and the closest KLM cluster. Fig. 10.2 shows the corresponding distributions from which one can see that the peak in the missing energy is caused by K_L^0 mesons that created clusters in the KLM as for nearly all events in the peak region of E_{miss} a KLM cluster close to the missing momentum vector is found. To remove contributions from K_L^0 mesons in the analysis, I place an additional requirement of $\Delta\alpha_{\mathrm{KLM}} > 0.5$ (see Table 6.2). Fig. 10.3 shows that this additional requirement removes the peaking disagreement in the missing energy distributions and leads to a reasonable agreement between data and simulation in the reconstructed K_S^0 mass.

After applying the additional $\Delta\alpha_{\mathrm{KLM}}$ selection together with the other selections from Tables 6.1 and 6.2, the K_S^0 shape is fitted in both data and simulation using a DSCB function to derive the shape correction from Eq. (10.1). The fit results for both data and simulation are displayed in Fig. 10.4. As only the width σ_{DSCB} of the Gaussian core of the DSCB is of interest, in the fit on data the values for the $n_{l/r}$ and $\alpha_{l/r}$ parameters are fixed

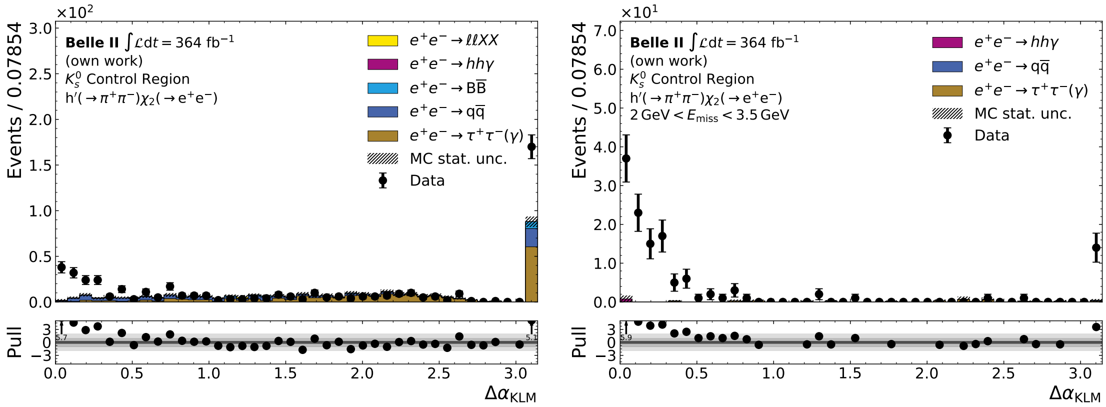

Figure 10.2: Minimal angle between the missing momentum vector and KLM cluster position $\Delta\alpha_{\mathrm{KLM}}$. The left plot shows the full $\mathrm{K_S^0}$ control region, while the right plot is restricted to the peak position from Fig. 10.1. The events where no KLM cluster was found are included in the last bin at $\Delta\alpha_{\mathrm{KLM}} = \pi$. The different simulated SM background components are scaled to the integrated luminosity of $\int \mathcal{L}\mathrm{d}t = 364\,\mathrm{fb}^{-1}$.

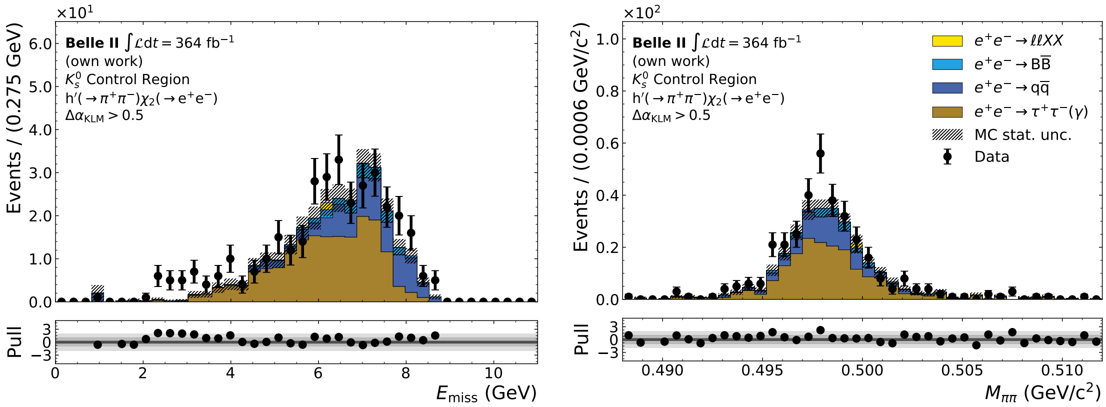

Figure 10.3: Left: Missing energy distributions for data and simulation in the $\mathrm{K_S^0}$ control region. Right: Reconstructed mass of the $\mathrm{h'}$ candidate in the $\mathrm{K_S^0}$ control region for both data and simulation. For both distributions, an additional requirement of $\Delta\alpha_{\mathrm{KLM}} > 0.5$ is applied to remove contributions from $\mathrm{K_L^0}$ mesons. The different simulated SM background components are scaled to the integrated luminosity of $\int \mathcal{L}\mathrm{d}t = 364\,\mathrm{fb}^{-1}$.

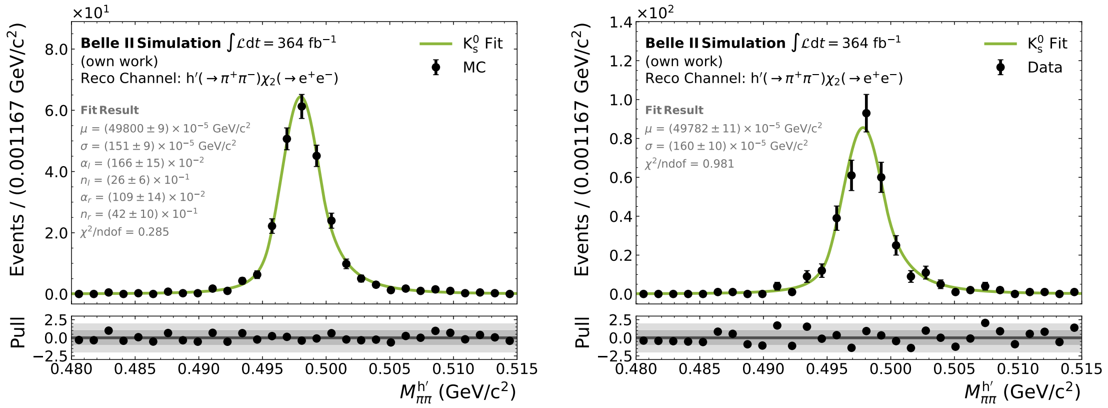

Figure 10.4: $\mathrm{K_S^0}$ shape fit in the $\mathrm{K_S^0}$ control region performed on simulation (left) and data (right). For the fit on data, the $n_{l/r}$ and $\alpha_{l/r}$ parameters are fixed to the values obtained from the simulation.

to the values obtained from simulation, as all the parameters are highly correlated. With the results obtained from the fits the ratio between the widths is

$$r_{\text{shape}} = 1.06 \pm 0.08, \tag{10.2}$$

which is within its uncertainty in agreement with one. Therefore I do not apply a correction on the signal width.

10.2 Pointing Angle Control Region

Another useful control region is obtained by inverting the requirement on the angle between the momentum and vertex vector of the h′ vertex that is described in Section 6.4. I define the pointing angle control region as $-\log(1-\cos(\Delta\alpha^{\mathrm{h}'}_{\mathbf{x},\mathbf{p}})) < 4.5$, which selects a large fraction of the exponentially decreasing SM background contributions. For some model parameter configurations, a small contribution from signal events is selected by this requirement (see Fig. 6.15). However, this signal contribution is negligible compared to the large number of SM background events in the defined control region. I use this control region to check for reasonable agreement between the measured data and the simulation and to ensure that there are no processes missing in the simulated samples that are observed on data.

Fig. 10.5 shows the comparison between data and simulation in the reconstructed mass distributions for the three considered reconstruction channels. Especially in the $\mathrm{h}' \to \mu^+\mu^-$ and $\mathrm{h}' \to \pi^+\pi^-$ reconstruction channels a large discrepancy between data and the simulation is observable. Part of this discrepancy is caused by selections on the $\mathrm{e^+e^-}/\mu^+\mu^-$ mass on generator level of at least 0.5 GeV/c²[*] in the $\mathrm{e^+e^-} \to \mathrm{e^+e^-e^+e^-}$ and

---

[*] https://github.com/belle2/basf2/blob/release/06-00/generators/scripts/generators.py#L89 contains the selections that are applied during the event generation.

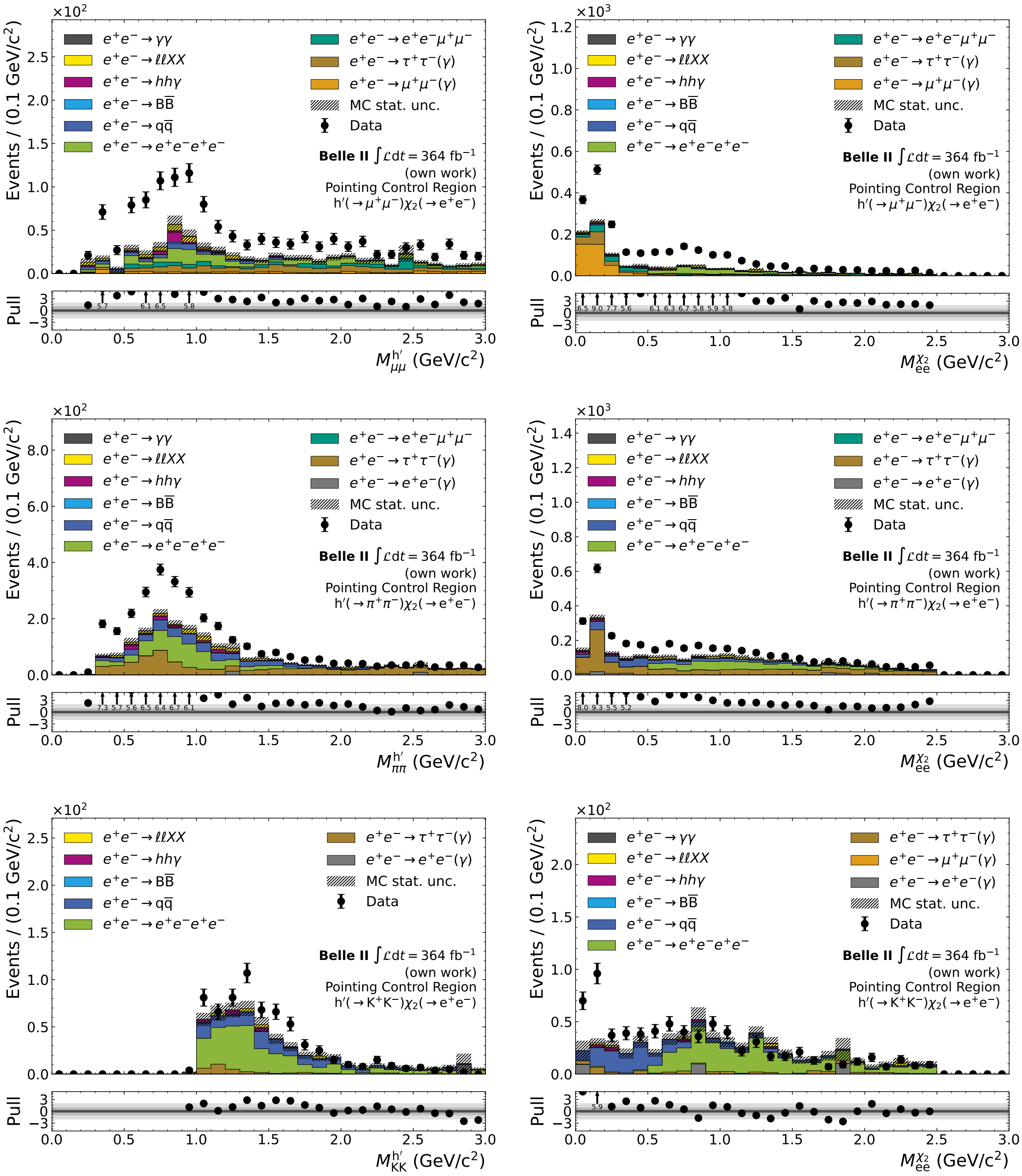

Figure 10.5: Reconstructed h' mass (left) and χ_2 mass (right) in the pointing control region for both simulated SM background samples and measured data. The plots show the $\mathrm{h}' \to \mu^+\mu^-$ (top), $\mathrm{h}' \to \pi^+\pi^-$ (center), and $\mathrm{h}' \to \mathrm{K}^+\mathrm{K}^-$ (bottom) reconstruction channel. All selections from Table 6.1 are applied. The different simulated SM background components are scaled to the integrated luminosity of $\int \mathcal{L}dt = 364\,\mathrm{fb}^{-1}$.

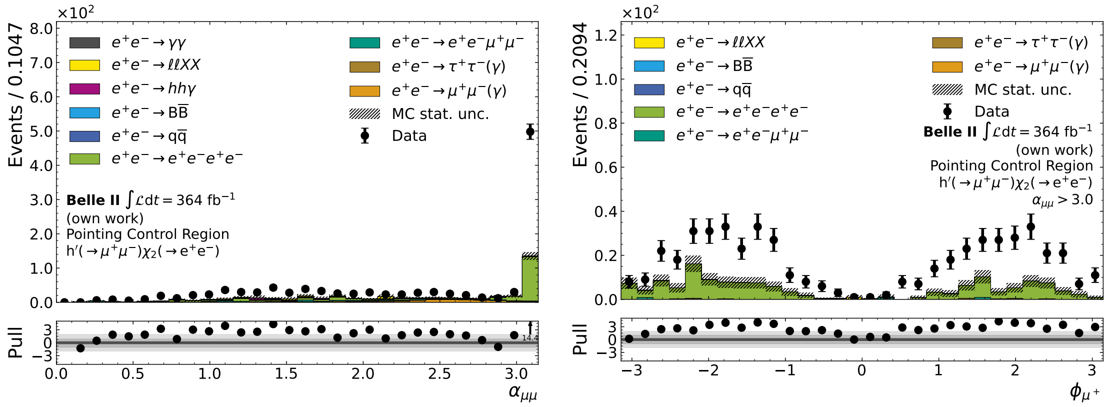

Figure 10.6: Left: Comparison between data and simulation of the opening angle between the two muon tracks from the h' candidate in the pointing control region. Right: Azimuthal angle ϕ of the μ^+ track. In both plots, additional selections on the reconstructed mass of the two lepton pairs $M_{\ell\ell} > 0.5\,\mathrm{GeV/c^2}$ are applied. The right plot is additionally restricted to the area with $\alpha_{\mu\mu} > 0.5$. Only the $\mathrm{h}' \to \mu^+\mu^-$ reconstruction channel is shown. The corresponding ϕ distribution of the μ^- track is shown in Fig. F.1 in the appendix.

$\mathrm{e^+e^-} \to \mathrm{e^+e^-}\mu^+\mu^-$ processes. These selections are clearly visible in the reconstructed mass distributions in Fig. 10.5, hence I consider only the region $M_{\mathrm{ee}}^{\chi_2} > 0.5\,\mathrm{GeV/c^2}$ in all reconstruction channels for further studies in this control region. Furthermore, the requirement $M_{\mu\mu}^{\mathrm{h}'} > 0.5\,\mathrm{GeV/c^2}$ is applied in the $\mathrm{h}' \to \mu^+\mu^-$ reconstruction channel for the studies in this control region. These selections on the reconstructed masses are only placed for the studies described in this section and are not applied in the general selection of the analysis.

In the $\mathrm{h}' \to \mu^+\mu^-$ reconstruction channel another discrepancy can be observed when looking into the opening angle of the two reconstructed muons in the lab frame (see Fig. 10.6). For very large opening angles $\alpha_{\mu\mu} > 3.0$ the number of events observed in data is significantly larger than the expectation obtained from simulation. Checking the ϕ distributions of the μ^- and μ^+ in this region (see Fig. 10.6) shows that the particles pass the detector from top to bottom or vice versa. Consequently, it can be assumed that these are cosmic muons and their contribution is heavily underestimated in the simulated samples. Further investigation of the momenta of the two muon candidates shows that the momenta are highly correlated (see Fig. F.2 in the appendix). This leads to the conclusion that one cosmic muon passes the detector and the track-finding algorithm creates two tracks with opposite charges and a vertex in the middle. These two tracks then have exactly the observed opening angle of 180° in the lab frame. Independent from the discrepancy, the contribution from cosmic muons needs to be suppressed in the analysis by placing an additional selection of $\alpha_{\mathrm{xx}}^{\mathrm{h}'} < 3.0$ in all three reconstruction channels.

Fig. 10.7 shows the E/p distributions for the electron candidates used in the reconstruction of the χ_2 vertex. Here p is the reconstructed momentum obtained from the track fit and

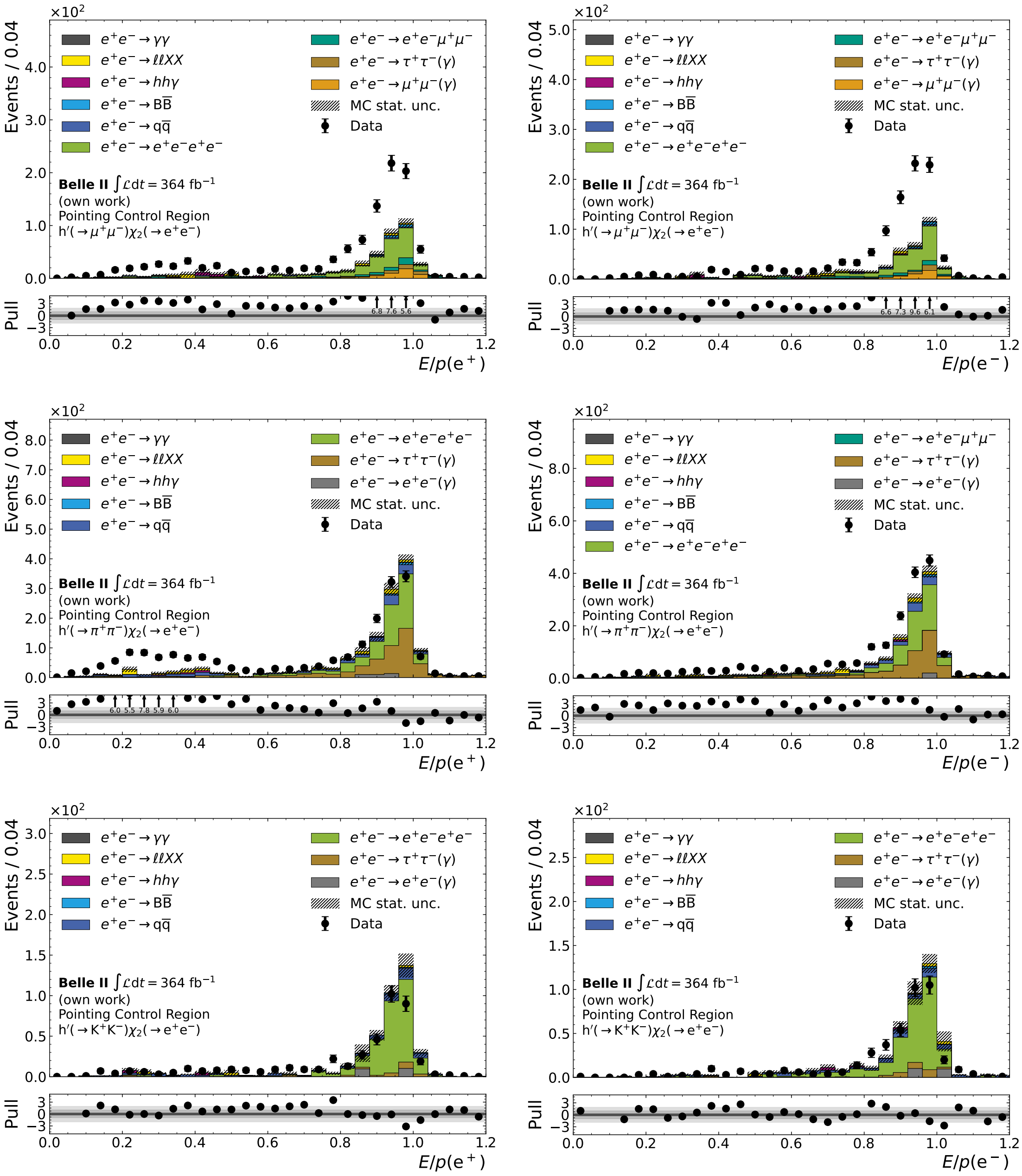

Figure 10.7: E/p for the positron (left) and electron track (right) in the pointing control region. p is the momentum derived from the track fit and E is the energy of the associated ECL cluster. The plots show the $\mathrm{h}' \to \mu^+\mu^-$ (top), $\mathrm{h}' \to \pi^+\pi^-$ (center), and $\mathrm{h}' \to \mathrm{K}^+\mathrm{K}^-$ (bottom) reconstruction channel. The different simulated SM background components are scaled to the integrated luminosity of $\int \mathcal{L}dt = 364\,\mathrm{fb}^{-1}$.

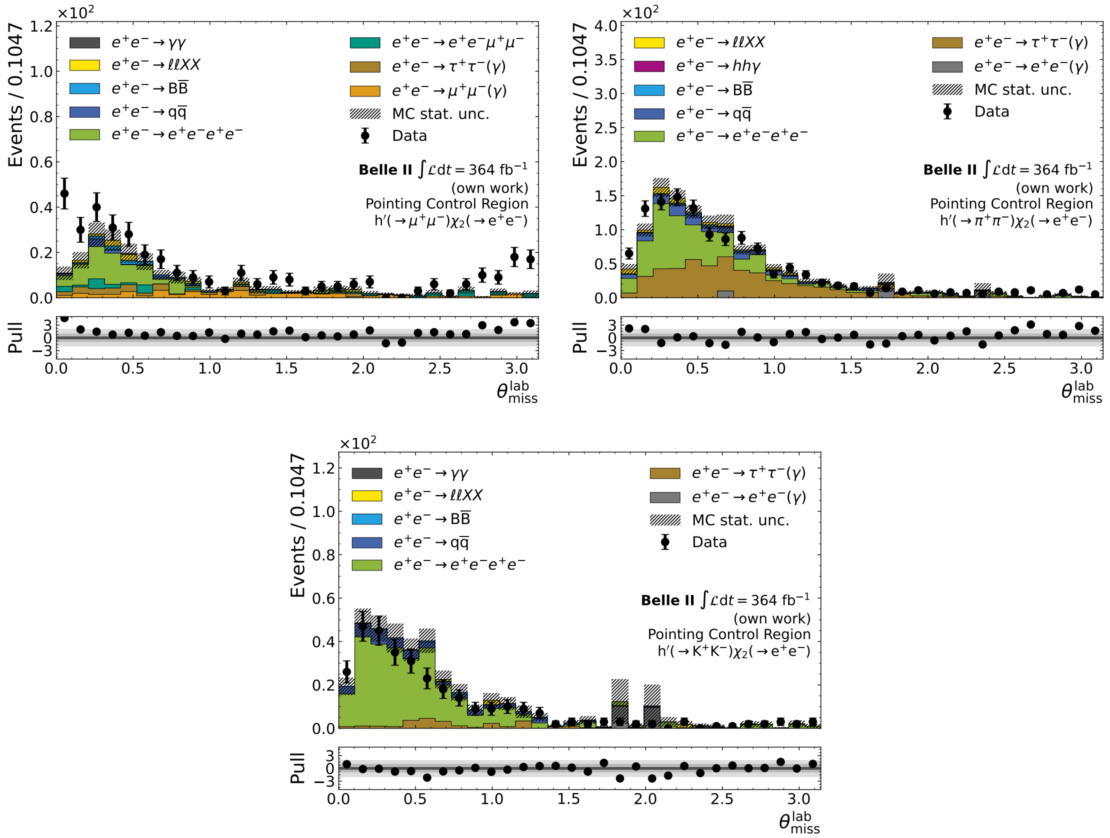

Figure 10.8: Polar angle $\theta^{\mathrm{lab}}_{\mathrm{miss}}$ of the missing momentum vector in the lab frame. The plots show the comparison between data and simulation in the $\mathrm{h}' \to \mu^+\mu^-$ (top left), $\mathrm{h}' \to \pi^+\pi^-$ (top right), and $\mathrm{h}' \to \mathrm{K}^+\mathrm{K}^-$ (bottom) reconstruction channel. Besides the selection on $\theta^{\mathrm{lab}}_{\mathrm{miss}}$ itself, all selections from Tables 6.1 and 6.2 are applied. The different simulated SM background components are scaled to the integrated luminosity of $\int \mathcal{L}\mathrm{d}t = 364\,\mathrm{fb}^{-1}$.

E is the ECL cluster energy associated with the track. For correctly identified electrons this ratio should be one, as electrons deposit nearly all their energy in the ECL. From the plots, a clear discrepancy between data and simulation is visible in the low E/p region. This region mostly contains electron candidates that are misidentified. To suppress these contributions, a selection of $E/p > 0.6$ is applied to the electron and positron candidates. The remaining discrepancy in the $\mathrm{h}' \to \mu^+\mu^-$ reconstruction channel for larger values of E/p can be attributed to another source that is described below.

After applying all previously mentioned additional selections, another difference between data and simulation is visible in the direction of the missing momentum vector shown in Fig. 10.8. There are more events observed in data in the regions where the missing momentum points in the direction of the beam axis. This can have multiple reasons: A background component not considered in the simulated samples, ISR effects not covered for some of the background processes, angular acceptance requirements on generator level for some of the components, to name a few of them. Since this discrepancy cannot be attributed to one specific cause, the missing momentum vector is required to point into the acceptance region of the detector ($0.4 < \theta_{\mathrm{miss}}^{\mathrm{lab}} < 2.6$). Otherwise, one cannot ensure that the missing energy is caused by an actual non-detectable particle or by for example a track being outside of the detector acceptance.

As can be seen in Fig. 10.9, when applying all previously mentioned additional selection criteria, that are summarised in Table 6.2, the distributions of data and simulation show a reasonable agreement. This order of agreement is sufficient as the actual background level will be derived from data in the reconstructed mass sidebands and is not taken from simulated samples.

10.3 E_{extra}(neutral) Control Region

Similar to the pointing angle control region, the E_{extra}(neutral) control region is used to check if the expected background level on data is similar to the expectation obtained from the simulated samples. While the signal region is defined in Section 6.6 as $E_{\mathrm{extra}}(\mathrm{neutral}) < 1\,\mathrm{GeV}$, the control region is defined as $1\,\mathrm{GeV} < E_{\mathrm{extra}}(\mathrm{neutral}) < 2\,\mathrm{GeV}$. For the studies in this control region all selection criteria from Tables 6.1 and 6.2 are applied.

Fig. 10.10 shows that the observed number of events is low in both data and in the simulated SM background samples. This underlines the assumption of the background level being low in the signal region, as well.

10.4 $\mathrm{e}^{+}\,\mu^{-}$ Control Region

Another control region that is beneficial for checking how well the background expectation obtained from the simulated samples represents the measured data can be created when looking into the non-physical case where the h' is reconstructed from an electron and muon track. For the studies in this control region all selection criteria from Tables 6.1 and 6.2 that are applied in the $\mathrm{h}' \to \mu^{+}\mu^{-}$ reconstruction channel are applied*. This is especially powerful for checking the impact of randomly combined tracks on data.

Fig. 10.11 shows that the number of events in this nonphysical reconstruction channel agrees between data and the simulated samples and is in general very low. Together with the observations from Section 10.3, this check verifies the background modelling which is expected to translate into a good modelling of the background expectation in the signal region.

---

*Electrons and muons are selected via their respective BDT-based PID classifier.

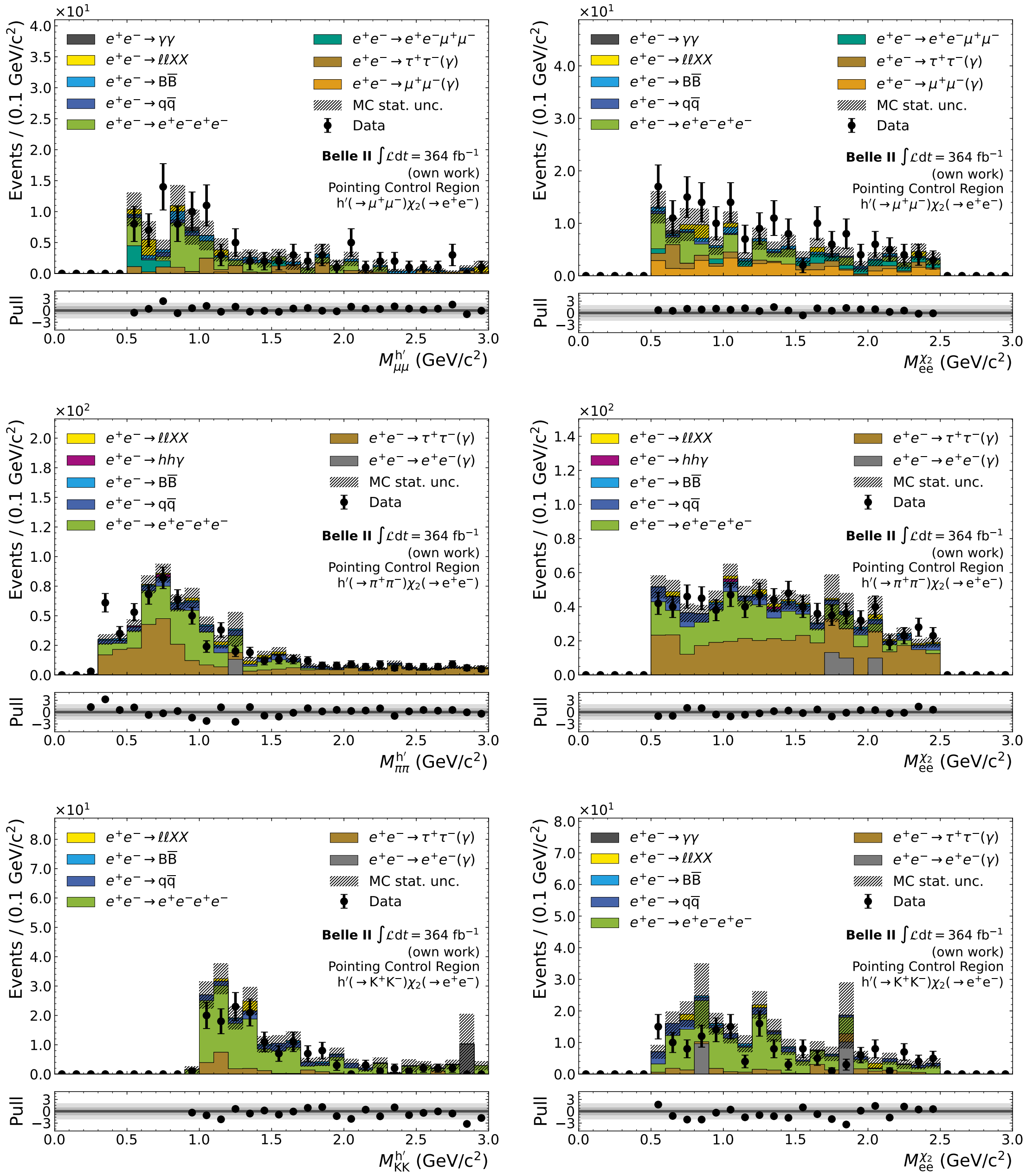

Figure 10.9: Reconstructed h$'$ (left) and χ_2 (right) mass in the pointing control region. The plots show the h$' \to \mu^+\mu^-$ (top), h$' \to \pi^+\pi^-$ (center), and h$' \to$ K$^+$K$^-$ (bottom) reconstruction channel after applying all selections from Table 6.1 and additional selection criteria described in Section 10.2 and summarised in Table 6.2. The different simulated SM background components are scaled to the integrated luminosity of $\int \mathcal{L}dt = 364\,\text{fb}^{-1}$.

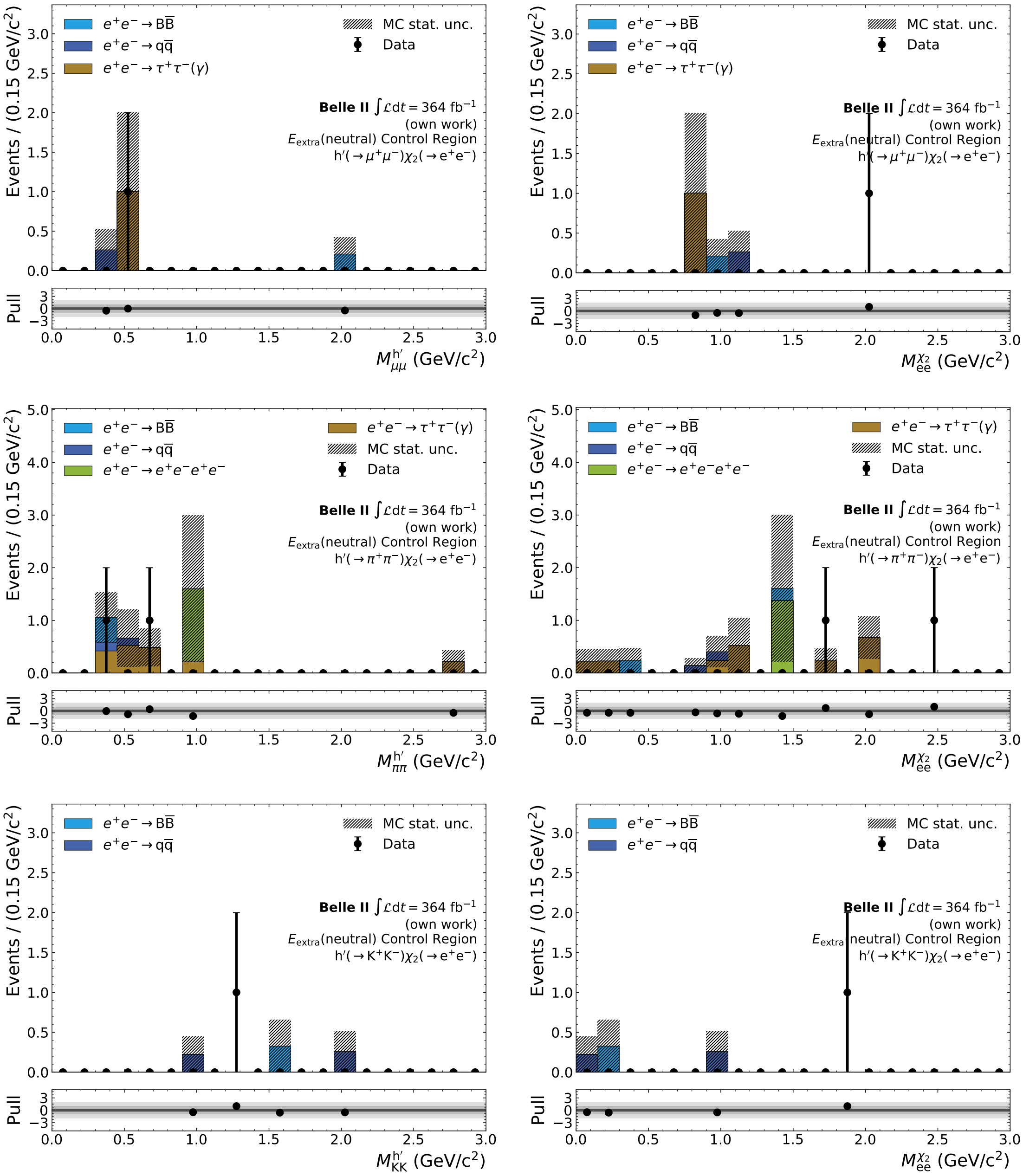

Figure 10.10: Reconstructed h$'$ (left) and χ_2 (right) mass in the E_{extra}(neutral) control region. The plots show the $h' \to \mu^+\mu^-$ (top), $h' \to \pi^+\pi^-$ (center), and $h' \to K^+K^-$ (bottom) reconstruction channel. Besides the requirement on E_{extra}(neutral) (which is inverted) all cuts from Tables 6.1 and 6.2 are applied. The different simulated SM background components are scaled to the integrated luminosity of $\int \mathcal{L}\mathrm{d}t = 364\,\mathrm{fb}^{-1}$.

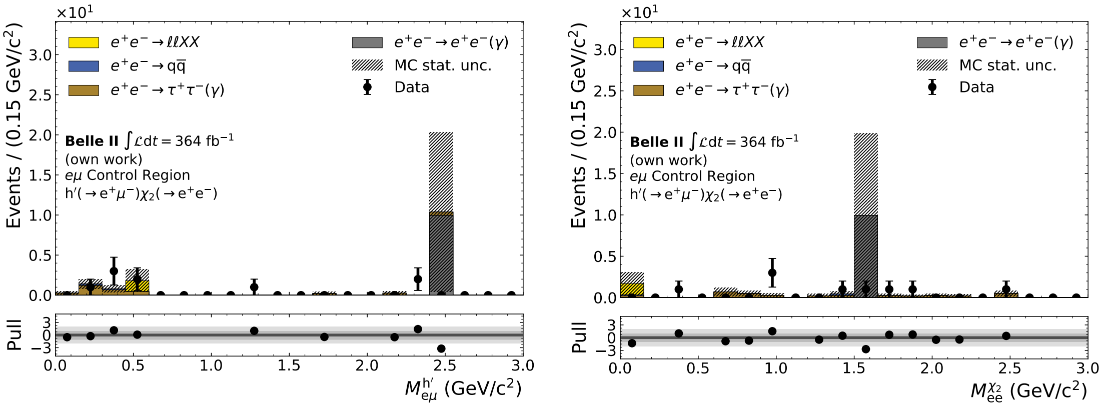

Figure 10.11: Reconstructed h' (left) and χ_2 (right) mass in the e^+ μ^- control region. Besides the requirement on E_{extra}(neutral) (which is inverted) all cuts from Tables 6.1 and 6.2 are applied. The different simulated SM background components are scaled to the integrated luminosity of $\int \mathcal{L}\mathrm{d}t = 364\,\mathrm{fb}^{-1}$.

Chapter 11

Signal Extraction

I search for a signal as a peaking excess in the reconstructed h$'$ mass $M_{\mathrm{xx}}^{\mathrm{h}'}$ over the SM background. I do this in steps of the $M_{\mathrm{xx}}^{\mathrm{h}'}$ where the stepsize is taken as half of the signal width derived from the simulated signal samples. Hereby, the signal width is derived as described in Section 8.1. Due to the low expected background level, I perform a counting experiment, where the number of observed events in a given signal window is compared with the number of expected events, which is taken from the $M_{\mathrm{xx}}^{\mathrm{h}'}$ sidebands on data. First, I determine the significance using the p-value as described in Section 11.3. In the case that no significant signal is observed, the results are used to set upper limits on the cross section of the signal process (see Section 11.5), using Bayesian techniques. To do so the Bayesian Analysis Toolkit [81] is used. Both the calculation of the p-value and the limit setting are done for the three individual final states considered in this thesis and the combination of all three final states.

Extracting the individual cross sections has the advantage that no assumptions about the branching fractions $\mathcal{B}(\mathrm{h}' \to \mathrm{x}^+\mathrm{x}^-)$ of the h$'$ decays are made, which in the end yields more model-independent results. Nevertheless, for the mass range below $M_{\mathrm{xx}}^{\mathrm{h}'} < 2.0\,\mathrm{GeV/c^2}$*, the combination of the individual final states, where each final state is weighted according to the branching fraction prediction from theory [18], yields stronger results in the end. This has the disadvantage that the results are no longer independent from the inelastic DM with a dark Higgs model.

11.1 Bayesian Analysis

Data analysis with a Bayesian approach is based on Bayes theorem

$$p(\lambda|x) = \frac{p(x|\lambda)p(\lambda)}{p(x)}. \tag{11.1}$$

---

*As no reliable branching fraction calculations are available for the $\mathrm{h}' \to \pi^+\pi^-$ and $\mathrm{h}' \to \mathrm{K}^+\mathrm{K}^-$ final state above $2.0\,\mathrm{GeV/c^2}$, only the $\mathrm{h}' \to \mu^+\mu^-$ final state contributes to the combination in this mass region.

It relates the posterior probability $p(\lambda|x)$ of λ being the true parameter given measured data x with the probability of measuring x given a specific λ, $p(x|\lambda)$, the likelihood function often denoted as $\mathcal{L}$. $p(\lambda)$ describes the prior probability, or in other words the current knowledge, about the parameter λ. The denominator $p(x)$ describes the probability of measuring the data x and can in many analyses be neglected as it only serves as an additional normalisation. One can also interpret Bayes theorem as a learning rule, as it describes how the prior knowledge about a parameter is updated by a measurement, taking into account the probability of measuring the data for a given value of the parameter, resulting in the posterior knowledge.

The posterior probability can be used to set upper limits on the parameter of interest λ. For a given Bayesian credibility level[*] α the upper limit on a parameter λ_{ul} is defined via

$$\alpha = \int_{\lambda_{\mathrm{min}}}^{\lambda_{\mathrm{up}}} p(\lambda|x)\mathrm{d}\lambda, \tag{11.2}$$

with λ_{min} being the minimal possible value the parameter λ can take. Using this definition, one can obtain the upper limit when solving for λ_{up}, which is typically not trivial if the likelihood function cannot be integrated analytically.

The situation gets a little bit more complicated when λ is not the only free parameter but there are additional ones, denoted as $\mathbf{\Theta}$. This is for example the case if there are systematic uncertainties present as they would enter as nuisance parameters in $\mathbf{\Theta}$. Nevertheless, these nuisance parameters are not of intrinsic interest, and if one is only interested in λ one can construct the corresponding posterior probability via marginalisation:

$$p(\lambda|x) = \int_{\mathbf{\Theta}_{\mathrm{min}}}^{\mathbf{\Theta}_{\mathrm{max}}} p(\lambda, \mathbf{\Theta}|x)\mathrm{d}\mathbf{\Theta} = \int_{\mathbf{\Theta}_{\mathrm{min}}}^{\mathbf{\Theta}_{\mathrm{max}}} p(x|\lambda, \mathbf{\Theta})p(x|\Theta)\mathrm{d}\mathbf{\Theta}. \tag{11.3}$$

The upper limit on the parameter λ is then calculated using this marginalised posterior pdf.

11.2 Bayesian Model

To extract the signal cross-section σ_{sig}, the number of observed events N_{obs} is compared to the number of expected events n_{bkg}, where the following formula holds

$$N_{\mathrm{obs}} = n_{\mathrm{sig}} + n_{\mathrm{bkg}} = \sigma_{\mathrm{sig}} \cdot L \cdot \epsilon_{\mathrm{sig}} + n_{\mathrm{bkg}}, \tag{11.4}$$

where L is the integrated luminosity and ϵ_{sig} the signal efficiency.

The signal window, in which the number of observed events are counted, is derived from the signal shape fits (see Section 8.1) and chosen as $m_{\mathrm{h}'} \pm 2\sigma$. This was optimised to achieve the lowest upper limit when determining the sensitivity on simulated samples while

---

[*] The credibility level is the Bayesian equivalent to the confidence level in the Frequentist interpretation.

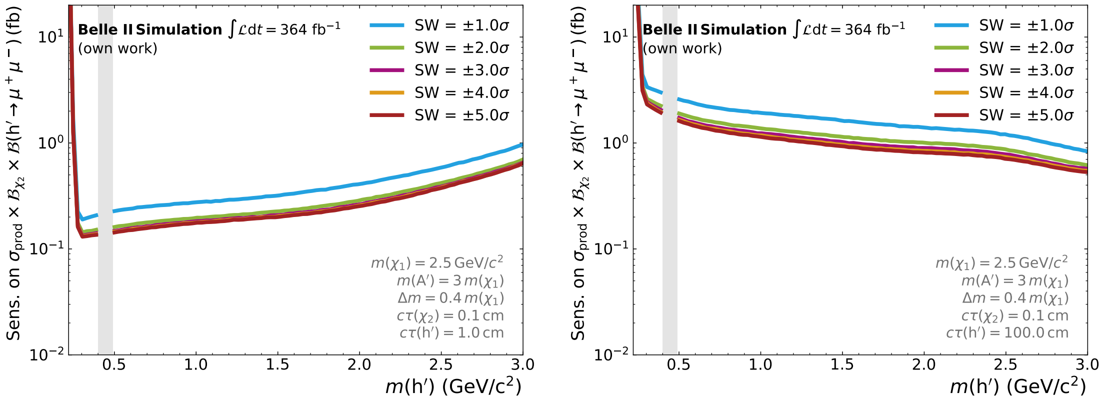

Figure 11.1: Sensitivity on the product of the production cross section $\sigma(\mathrm{e}^+\mathrm{e}^- \to \mathrm{h}'\chi_1\chi_2)$ and the product of the branching fractions $\mathcal{B}(\chi_2 \to \chi_1\mathrm{e}^+\mathrm{e}^-) \times \mathcal{B}(\mathrm{h}' \to \mu^+\mu^-)$ as a function of the mass of the h'. The sensitivity is derived by calculating 95% CL upper limits as described in Section 11.5 based on simulated samples. Different sizes of the signal windows (SW) chosen as multiples of the signal width are shown with different colours. The h' lifetime is set to $c\tau(\mathrm{h}') = 1.0\,\mathrm{cm}$ (left) and $c\tau(\mathrm{h}') = 100.0\,\mathrm{cm}$ (right). The remaining model parameters are chosen as $m(\chi_1) = 2.5\,\mathrm{GeV/c}^2$, $m(\mathrm{A}') = 3\,m(\chi_1)$, $\Delta m = 0.4\,m(\chi_1)$, and $c\tau(\chi_2) = 0.1\,\mathrm{cm}$. The region corresponding to the K^0_S veto is marked with a grey band.

keeping the size of the signal window rather small to not be prone to statistical fluctuations of the SM background. The corresponding plots are shown in Fig. 11.1. The number of expected events is taken from the mass sidebands in data via counting the number of events $N_{\mathrm{obs}}^{\mathrm{SB}}$ within the mass sideband. Hereby in each reconstruction channel the mass sidebands are defined as $m \in (2m_f, m_{\mathrm{max}})$ excluding the signal window and the vetoed mass regions. Here m_f is the mass of the FSP and m_{max} is chosen for each final state to ensure that the last scan point is fully included. As the last scan point is at $m = 3\,\mathrm{GeV}$ for a given final state $m_{\mathrm{max}} = m + 2\sigma(m)|_{m=3.0\,\mathrm{GeV/c}^2}$, with σ being the width associated with the last scan point. To account for the fact that the SM background expectation from simulations shows that in the $\mathrm{h}' \to \pi^+\pi^-$ reconstruction channel the background is not flat (see Fig. 8.3), in this final state the sideband range is split into two parts. The two ranges are chosen as $m \in (2m_\pi, 1.0\,\mathrm{GeV/c}^2)$ and $m \in (1.0\,\mathrm{GeV/c}^2, m_{\mathrm{max}})$ depending on the scanned mass point m. With the knowledge of the size of the signal window and the sideband, the number of expected background events in the signal window can be calculated via

$$n_{\mathrm{bkg}} = \frac{N_{\mathrm{obs}}^{\mathrm{SB}}}{w}, \tag{11.5}$$

where w is the ratio between the sizes of the sideband and the signal window.

The number of observed events is expected to follow a Poisson distribution and therefore in each signal window and for each final state, one can define the Poissonian likelihood function for measuring n events as

$$\mathcal{L}(n) = \frac{\left(n_{\text{sig}} + n_{\text{bkg}}\right)^n}{n!} e^{-\left(n_{\text{sig}} + n_{\text{bkg}}\right)}, \tag{11.6}$$

with the definitions of n_{sig} and n_{bkg} as given above. For the calculations, the logarithmic form of this, the so-called log-likelihood function is used. When combining the individual final states the total log-likelihood is given as the sum of the individual ones:

$$\log\mathcal{L}_{\text{total}} = \sum_{f=\mu,\pi,K} \log\mathcal{L}_f. \tag{11.7}$$

Thereby, for each final state, the number of signal events n_{sig} is derived from the total cross section by multiplying the latter with the respective efficiencies and branching fractions

$$n_{\text{sig},f} = \sigma_{\text{tot}} \cdot \epsilon_f \cdot \mathcal{B}_f \cdot L, \tag{11.8}$$

with $f = \mu, \pi, \mathrm{K}$.

The systematic uncertainties on the parameters are included as nuisance parameters and will be explained in the following chapters.

11.3 p-Value

I determine the significance by deriving the p-value p_0 of the background-only hypothesis. The p-value, which describes the probability of observing N_{obs} or more events given a background expectation, is for a single final state calculated via

$$p_0 = \sum_{n=N_{\text{obs}}}^{\infty} \mathcal{L}(n) \tag{11.9}$$

[82], where $\mathcal{L}(n)$ is the likelihood of observing n events as defined in Eq. (11.6) with $n_{\text{sig}} = 0$. For the combination of the final states, the combined p-value is given by the product of the p-values of the individual final states. To incorporate the systematic uncertainty associated with the background expectation obtained from the sideband, I use a hybrid approach where the likelihood for the p-value calculation is defined with Bayesian ansatz. The likelihood of observing n events in the signal window is implemented as

$$\mathcal{L}(n, \mu) = \frac{\left(\mu/w\right)^n}{n} e^{-\mu/w} \cdot \frac{\mu^{N_{\text{obs}}^{\text{SB}}}}{N_{\text{obs}}^{\text{SB}}!} e^{-\mu} \tag{11.10}$$

[83], with the floating background expectation μ that is constrained by a Poisson prior given the number of observed events in the sideband $N_{\text{obs}}^{\text{SB}}$ and w being the ratio between the size of the sideband and the signal window. Here μ is a nuisance parameter addressing the uncertainty arising from the background estimation from the mass sideband. I obtain

the marginalised likelihood depending only on the parameter n via the marginalisation described in Section 11.1:

$$\mathcal{L}(n) = \int_0^\infty \mathrm{d}\mu \frac{(\mu/w)^n}{n} e^{-\mu/w} \cdot \frac{\mu^{N_{\mathrm{obs}}^{\mathrm{SB}}}}{N_{\mathrm{obs}}^{\mathrm{SB}}!} e^{-\mu}. \tag{11.11}$$

This marginalised likelihood is then used in Eq. (11.9) to calculate the p-value. While this is the complete likelihood to calculate the p-value in the $\mathrm{h}' \to \mu^+\mu^-$ and $\mathrm{h}' \to \mathrm{K}^+\mathrm{K}^-$ reconstruction channel, in the $\mathrm{h}' \to \pi^+\pi^-$ reconstruction channel the uncertainty on the background estimation Δ_{bkg}, arising from splitting the $M_{\pi\pi}^{\mathrm{h}'}$ spectrum into two parts, has to be considered. I do this by adding an additional nuisance parameter, which is then marginalised, to the likelihood,

$$\mathcal{L}_{\pi\pi}(n) = \int_0^\infty \mathrm{d}\mu \int_{-\infty}^\infty \mathrm{d}x \frac{(\mu/w(1+x\Delta_{\mathrm{bkg}}))^n}{n} e^{-(\mu/w(1+x\Delta_{\mathrm{bkg}}))} \cdot \frac{\mu^{N_{\mathrm{obs}}^{\mathrm{SB}}}}{N_{\mathrm{obs}}^{\mathrm{SB}}!} e^{-\mu} \cdot \frac{e^{\frac{1}{2}x^2}}{\sqrt{2\pi}}. \tag{11.12}$$

The additional nuisance parameter x is constrained by a Gaussian prior. During the marginalisation, the background expectation in the signal window $\mu/w(1 + x\Delta_{\mathrm{bkg}})$ is restricted to be positive.

The p-value can be translated into the significance via

$$S = \Phi^{-1}(1 - p_0), \tag{11.13}$$

where Φ^{-1} is the quantile of the standard Gaussian [84].

I test this approach with the use of a toy dataset to ensure that the procedure does not bias the results. To generate a toy dataset I draw for each reconstruction channel n_f events, where n_f is taken from a Poisson distribution with mean N_f. Here N_f is the number of expected background events taken from the SM background simulations shown in Fig. 8.3. In the $\mathrm{h}' \to \mu^+\mu^-$ and $\mathrm{h}' \to \mathrm{K}^+\mathrm{K}^-$ reconstruction channel I draw the events from a uniform distribution in the range $M_{\mathrm{xx}}^{\mathrm{h}'} \in [2\,m_f, 3.0\,\mathrm{GeV/c^2}]$, with m_f being the mass of the corresponding FSP. To incorpoarate the non-flatness of the background in the $\mathrm{h}' \to \pi^+\pi^-$ reconstruction channel (see Section 8.2), for this reconstruction channel the $n_{\leq 1}$ events are drawn from a uniform distribution in the range $M(\pi\pi) \in [2\,m_\pi, 1.0\,\mathrm{GeV/c^2}]$ and $n_{>1}$ events in the range $M(\pi\pi) \in (1.0\,\mathrm{GeV/c^2}, 3.0\,\mathrm{GeV/c^2}]$. The different background levels in these ranges are considered in $n_{\leq 1}$ and $n_{>1}$. In total, I draw 100,000 toy datasets and evaluate them at two arbitrary mass points, with the restriction that one is above and one below the splitting point of the pion reconstruction channel. Fig. 11.2 shows the outcome of the toy study for the lower mass point. The distributions show the expected behaviour of being approximately flat. The discrete structure of the p-value that is observable is caused by the low background level, as the number of combinations the values for N_{obs} and $N_{\mathrm{obs}}^{\mathrm{SB}}$ can take is limited. This is also visible in the toy study evaluated at a mass point above the threshold (see Fig. 11.3). Due to the even lower background level in the $\mathrm{h}' \to \pi^+\pi^-$

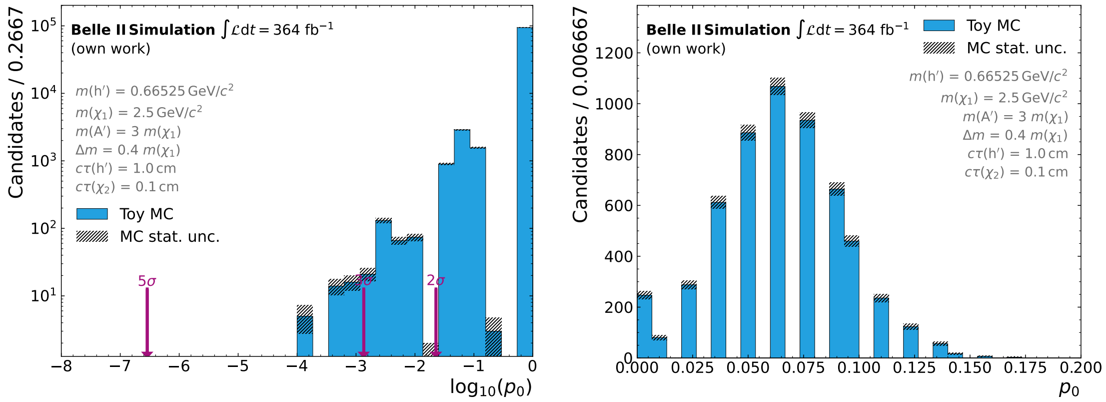

Figure 11.2: p-value evaluated on 100,000 toy samples for a fixed model parameter configuration with a fixed mass at $m(\mathrm{h}') = 0.665\,25\,\mathrm{GeV/c^2}$. While the left side shows the p-value on a logarithmic scale with the 2, 3, and 5σ significances marked in purple, the right side shows the result on a non-logarithmic scale with the bin at $p_0 = 1.0$ excluded for better visualisation.

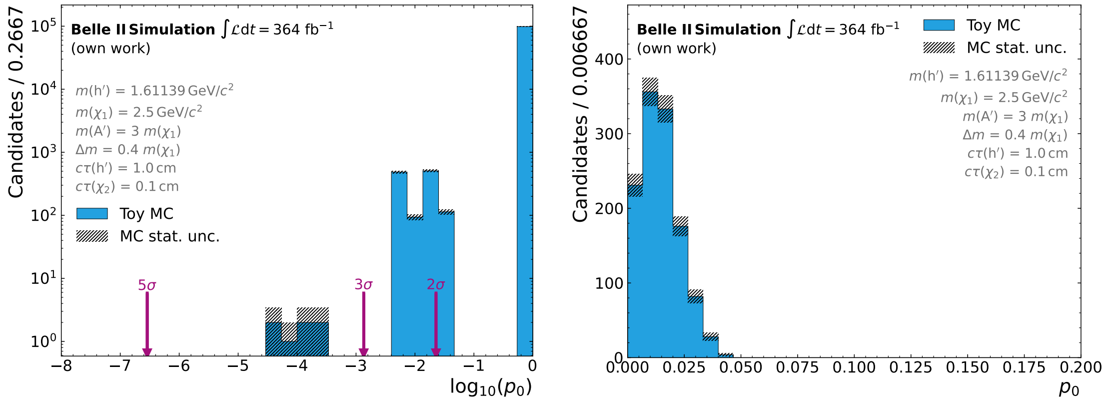

Figure 11.3: p-value evaluated on 100,000 toy samples for a fixed model parameter configuration with a fixed mass at $m(\mathrm{h}') = 1.611\,39\,\mathrm{GeV/c^2}$. While the left side shows the p-value on a logarithmic scale with the 2, 3, and 5σ significances marked in purple, the right side shows the result on a non-logarithmic scale with the bin at $p_0 = 1.0$ excluded for better visualisation.

reconstruction channel there, the distribution is more discrete and yields lower p-values whenever at least one event is observed in the signal window.

11.4 Look-elsewhere Effect

As I search in this thesis for a possible signal at many mass points along the reconstructed dark Higgs mass, the look-elsewhere effect has to be considered. This effect deals with the fact that the probability of observing a significant excess that is caused by a statistical fluctuation of the background scales with the number of scan points. Therefore, the extracted local p-value, which is independent of all other experiments, has to be corrected to determine the global p-value. This global p-value is determined by weighting the local p-value with a trial factor up to a higher, less significant, global p-value. The trial factor was proposed by Gross and Vitells in [85].

Given an extracted local p-value p_{local} and the related significance S_{local} (see Eq. (11.13)) the trial factor N_{trial} is given by

$$N_{\text{trial}} = 1 + \frac{1}{p_{\text{local}}} < N_{\text{up}}(S_{\text{test}}) > e^{\frac{S_{\text{test}}^2 - S_{\text{local}}^2}{2}}, \tag{11.14}$$

where $N_{\text{up}}(S_{\text{test}})$ describes the number of times in the scan the extracted significance exceeds a chosen threshold S_{test}. The effect of the overlapping signal windows, which are not uncorrelated, is accounted for by only counting the number of up-crossings. The average number of up-crossings $< N_{\text{up}}(S_{\text{test}}) >$ for a given threshold is determined with a toy study based on the simulated SM background samples.

While the calculation of the p-value only relies on the background hypothesis the information about the signal is still used for defining the signal windows via the signal width. As the signal width is slightly dependent on the model parameter configuration the number of scan points varies between the different model parameter configurations. Furthermore, as the different final states cover different mass ranges, the number of scan points depends additionally on the final state or if the p-value is derived for the combination of the three final states. To incorporate this effect, the look-elsewhere effect is considered for each model parameter configuration separately and is calculated for all three final states and the combination individually. Nevertheless, the differences between the different model parameter configurations turn out to be negligible for the size of the look-elsewhere effect. Here I only show the outcome for one model parameter configuration as an example.

I create the toy datasets used to derive the impact of the look-elsewhere effect with the procedure explained in Section 11.3. Using these toy datasets, I extract the significance for each of the mass points in the scan. The whole procedure is repeated 2000 times. The outcomes of two of the toy experiments are shown in Fig. 11.4 as examples. The number of up-crossings for all toy experiments can be found in Fig. 11.5 for different choices of S_{test}. A truncated Gaussian function is fitted to each of the distributions to determine

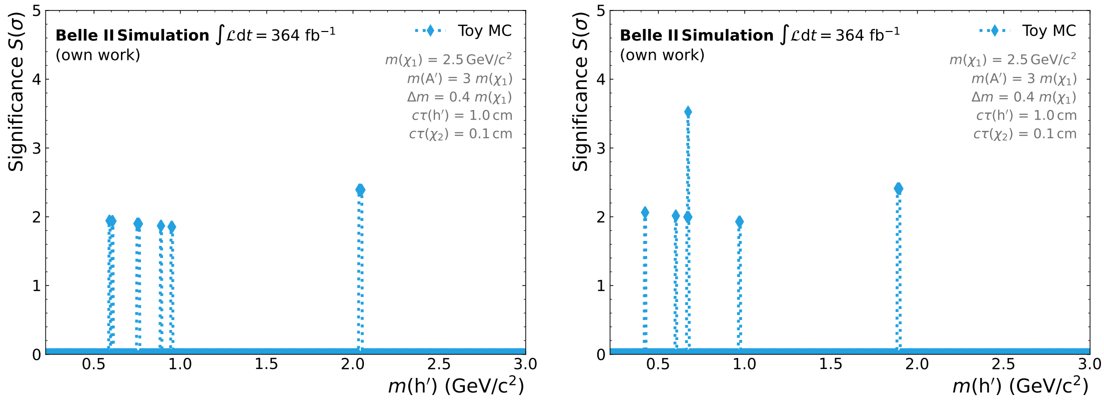

Figure 11.4: Extracted significances on two example toy datasets for a mass scan assuming a lifetime of $c\tau(\mathrm{h}') = 1.0\,\mathrm{cm}$. All other parameters are fixed to the values shown in the plot.

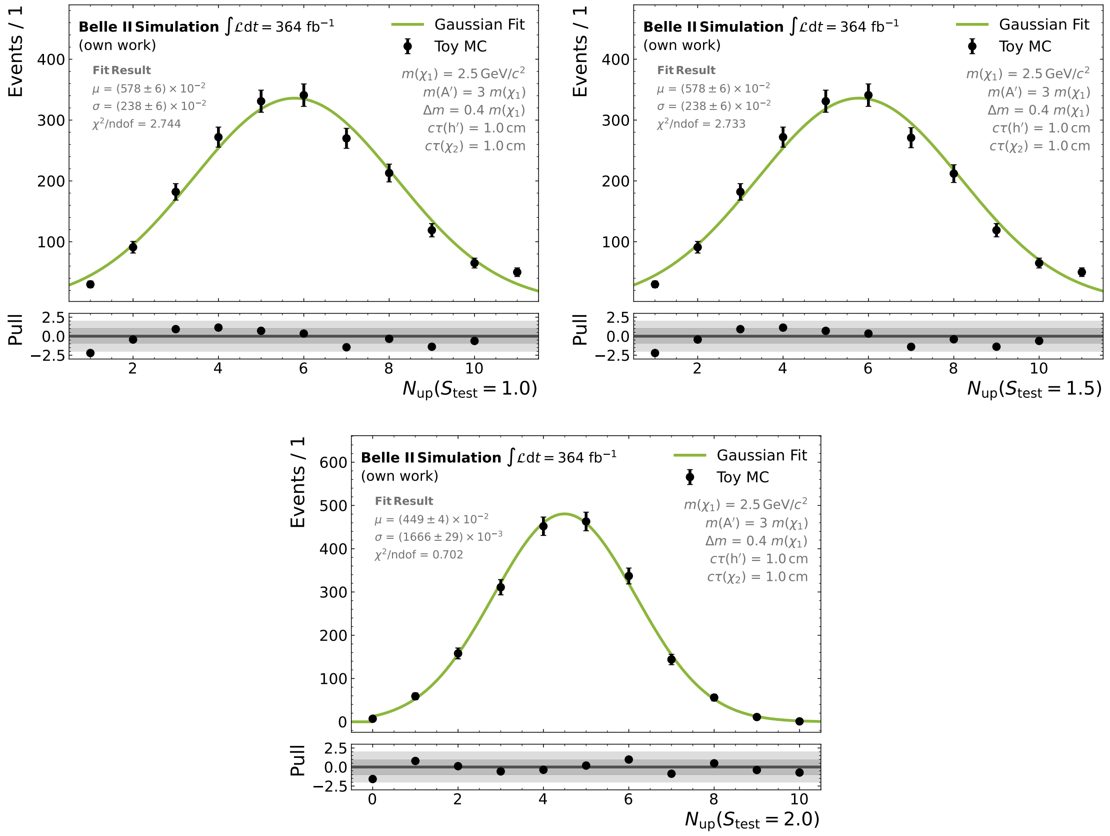

Figure 11.5: Number of up-crossings N_{up} for 2000 toy mass scans with a lifetime hypothesis of $c\tau(\mathrm{h}') = 1.0\,\mathrm{cm}$. The different plots correspond to different thresholds of S_{test}. All other parameters are fixed to the values shown in the plot. A truncated Gaussian distribution is fitted to the data to extract the mean μ ($=< N_{\mathrm{up}}(S_{\mathrm{test}}) >$).

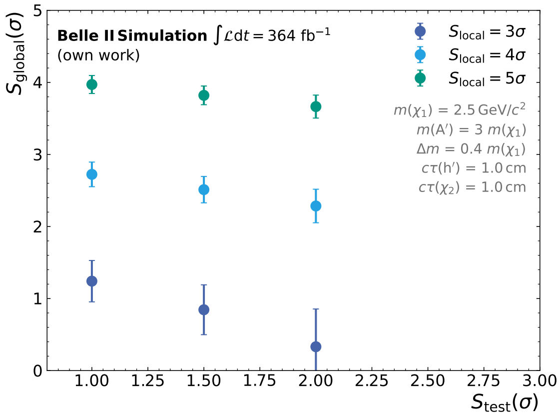

Figure 11.6: Calculated global significances S_{global} assuming different S_{local}. The calculation is performed for different choices of the threshold S_{test}. For the mass scan a lifetime of $c\tau(\mathrm{h}') = 1.0\,\mathrm{cm}$ is assumed. All other parameters are fixed to the values shown in the plot.

the mean μ which is equivalent to $< N_{\mathrm{up}}(S_{\mathrm{test}}) >$. One can see that the average number of up-crossings does not change between $S_{\mathrm{test}} = 1$ and $S_{\mathrm{test}} = 1.5$. This is again caused by the very low background level where a minimal fluctuation of the background already results in a local significance $S_{\mathrm{local}} > 1.5$. With this, the trial factor from Eq. (11.14) can be calculated and propagated to the calculation of the global p-value

$$p_{\mathrm{global}} = p_{\mathrm{local}} \cdot N_{\mathrm{trial}} \tag{11.15}$$

$$= p_{\mathrm{local}} + < N_{\mathrm{up}}(S_{\mathrm{test}}) > e^{\frac{S_{\mathrm{test}}^2 - S_{\mathrm{local}}^2}{2}}, \tag{11.16}$$

which then can be translated into the global significance S_{total}. For hypothetical local significances of $S_{\mathrm{local}} = \{3, 4, 5\}\,\sigma$ the resulting global significance is shown in Fig. 11.6 with the use of the different S_{test}. As the choice of the threshold significance S_{test} has no significant impact on the trial factor $S_{\mathrm{test}} = 1.0\,\sigma$ is chosen.

11.5 Upper Limit Setting

In case no significant signal is observed with the methods described in Sections 11.3 and 11.4, I set upper limits on the product on the production cross section $\sigma(\mathrm{e}^+\mathrm{e}^- \to \mathrm{h}'\chi_1\chi_2)$ with the product of the branching fractions $\mathcal{B}(\mathrm{h}' \to \mathrm{x}^+\mathrm{x}^-) \times \mathcal{B}(\chi_2 \to \chi_1\mathrm{e}^+\mathrm{e}^-)$. Additionally, when combing all three considered final states, I set upper limits on the product of the production cross section and the branching fraction $\mathcal{B}(\chi_2 \to \chi_1\mathrm{e}^+\mathrm{e}^-)$. To increase the readability of the equations these products of cross section and branching fraction(s) are denoted as σ_{sig}. I set these upper limits using the Bayesian approach described in Section 11.1 with the Bayesian Analysis Toolkit. The confidence level is set to the community standard of $\alpha = 0.05$, so 95% CL upper limits are reported.

While the likelihood for the calculation of the p-value (Eq. (11.10)) only takes the background expectation into account, for setting the upper limits also the information about this signal has to be included. The full likelihood is given by

$$\mathcal{L}(n_{\mathrm{sig}}, \mu, x, y) = \frac{(n_{\mathrm{sig}} + \mu/w)^{N_{\mathrm{obs}}}}{N_{\mathrm{obs}}!} e^{-(n_{\mathrm{sig}}+\mu/w)} \cdot \frac{\mu^{N_{\mathrm{obs}}^{\mathrm{SB}}}}{N_{\mathrm{obs}}^{\mathrm{SB}}!} e^{-\mu} \cdot \frac{1}{2\pi} e^{-\frac{1}{2}(x^2+y^2)}, \tag{11.17}$$

with

$$n_{\mathrm{sig}} = \sigma_{\mathrm{sig}} \cdot (\epsilon + x\Delta_\epsilon) \cdot \mathcal{B}(\mathrm{h}' \to \mathrm{x}^+\mathrm{x}^-) \cdot (L + y\Delta_L). \tag{11.18}$$

Here σ_{sig} is the signal cross section, ϵ the signal efficiency with the associated systematic uncertainty Δ_ϵ, the dark Higgs branching fraction $\mathcal{B}(\mathrm{h}' \to \mathrm{x}^+\mathrm{x}^-)$, and L being the integrated luminosity with the uncertainty Δ_L. The last term in Eq. (11.17) describes the two Gaussian priors that constrain the variation of the signal efficiency and integrated luminosity. So the likelihood depends on the parameter of interest σ_{sig} and three nuisance parameters: μ, x, and y. Again I obtain the marginalised likelihood that depends only on the parameter of interest via integration over the full parameter space of the nuisance parameters

$$\mathcal{L}(\sigma_{\mathrm{sig}}) = \int_0^\infty \mathrm{d}\mu \int_{-\infty}^\infty \mathrm{d}x \int_{-\infty}^\infty \mathrm{d}y \mathcal{L}(\sigma_{\mathrm{sig}}, \mu, x, y). \tag{11.19}$$

I then use this marginalised likelihood in Eq. (11.2) to calculate the upper limits on the cross sections. Note that similar to the calculation of the p-value in Section 11.3, the marginalised likelihood in the $\mathrm{h}' \to \pi^+\pi^-$ final state contains the additional term arising from the uncertainty on the background expectation with an additional integration (see Eq. (11.12)). To keep the equations readable, the additional term is not written here again but is still considered in the calculation of the upper limits.

11.6 Sensitivity

To estimate the sensitivity of the analysis, I use the information of both the signal simulations and the simulations of the SM backgrounds to calculate Bayesian upper limits (see Section 11.5). As the expected background level is very low, I expect to observe zero events in most of the signal windows when performing the scan on data. Therefore, I estimate the sensitivity with $N_{\mathrm{obs}} = 0$. This is done for all three considered final states individually, as well as for the combination of the latter.

Fig. 11.7 shows the sensitivity in the $\mathrm{e}^+\mathrm{e}^- \to \mathrm{h}'(\to \mu^+\mu^-)\chi_1\chi_2(\to \chi_1\mathrm{e}^+\mathrm{e}^-)$ final state for several variations of the model parameters. First of all, one can observe that the sensitivity close to the kinematic threshold is quite bad because of the low signal efficiency in this region. Furthermore, one can see that the sensitivity heavily depends on the lifetime of the dark Higgs. The best sensitivity is achieved for intermediate $c\tau(\mathrm{h}')$, as the lifetime is sufficiently long to pass the minimal displacement requirement and still the dark Higgs

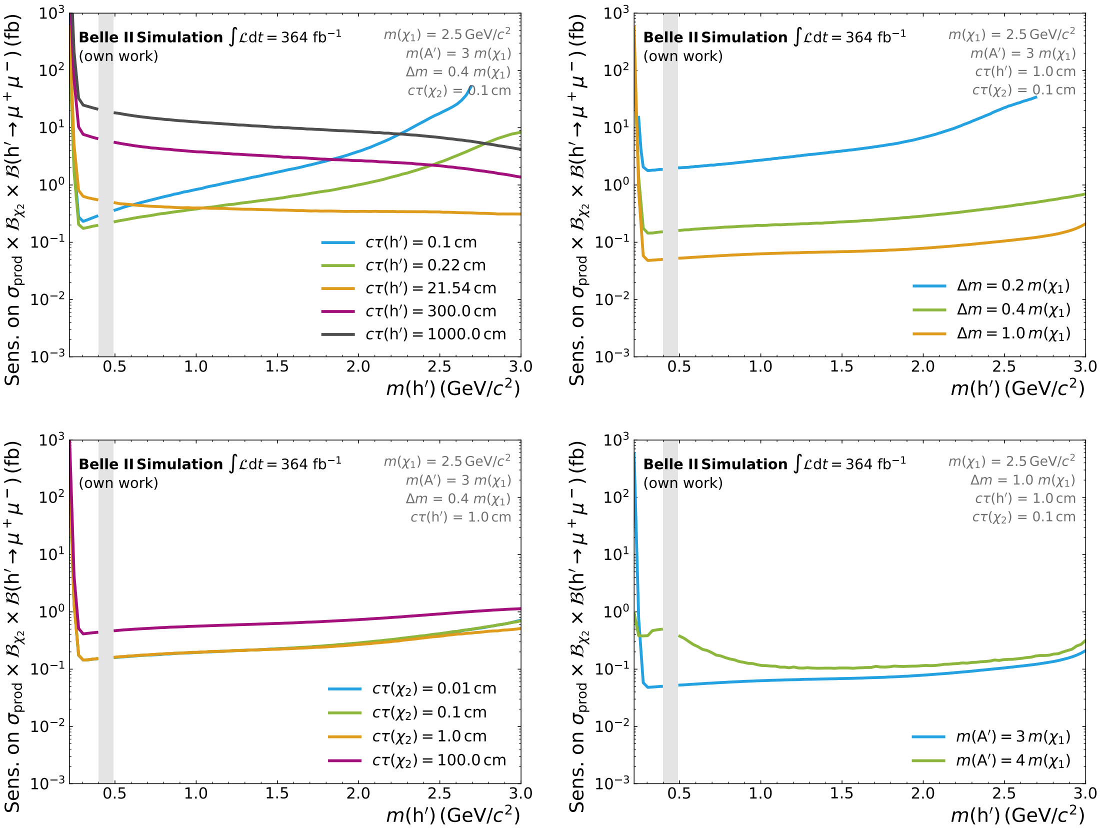

Figure 11.7: Expected sensitivity on the product of the production cross section $\sigma(e^+e^- \to h'\chi_1\chi_2)$ (denoted as σ_{prod}) and the branching fractions $\mathcal{B}(\chi_2 \to \chi_1 e^+e^-)$ (denoted as $\mathcal{B}_{\chi_2}$) and $\mathcal{B}(h' \to \mu^+\mu^-)$ as a function of the h′ mass. The plots show different variations of the model parameters $c\tau(h')$ (upper left), Δm (upper right), $c\tau(\chi_2)$ (lower left), and $m(A')$ (lower right). All other model parameters are fixed to the values reported in the plots. The sensitivity is estimated by calculating 95% CL Bayesian upper limits assuming $N_{\text{obs}} = 0$ with the background expectation taken from SM background simulations. The fully-vetoed K^0_S region is marked in grey.

decays not too far away from the IP where the bad track reconstruction efficiency for displaced vertices plays a role. For very large lifetimes a huge amount of h' bosons decays outside of the Belle II detector, leading to worse efficiency and therefore worse sensitivity. For a fixed lifetime the sensitivity additionally depends on the mass of the dark Higgs. This dependence is related to the lifetime dependence, as for short lifetimes, the sensitivity is better the lighter the dark Higgs is, as the h' are then more boosted leading to a higher chance of passing the minimal displacement requirement. For larger lifetimes the boost has the opposite effect, lighter h' decay farther away from the IP and therefore suffer more from the bad reconstruction efficiency for displaced vertices. The sensitivity also depends on the mass splitting Δm. The smaller the mass splitting, the less energy is carried by the electrons from the χ_2 decay. Consequently, the events are less likely triggered by the HIE L1 trigger. This effect is even enhanced by the selection requirement on the deposited energy in the ECL that is needed to ensure good agreement of the HIE performance between data and simulations. The decay products of the h' also deposit some energy in the ECL which makes the dependence on the mass splitting most pronounced in the $\mathrm{h}' \to \mu^+\mu^-$ final state as muons only deposit on average around 200 MeV in the Belle II ECL and pion and kaons can deposit a larger fraction of their energy. The lifetime of the χ_2 affects the sensitivity similar to the h' lifetime leading to a weaker sensitivity if the χ_2 lifetime increases. Lastly, the mass of the A' has a slight effect on the sensitivity as it changes the kinematics of the decay products and consequently alters the reconstruction efficiency. All of these arguments apply to the $\mathrm{e}^+\mathrm{e}^- \to \mathrm{h}'(\to \pi^+\pi^-)\chi_1\chi_2(\to \chi_1\mathrm{e}^+\mathrm{e}^-)$ and $\mathrm{e}^+\mathrm{e}^- \to \mathrm{h}'(\to \mathrm{K}^+\mathrm{K}^-)\chi_1\chi_2(\to \chi_1\mathrm{e}^+\mathrm{e}^-)$ final state, as well, and they are therefore not shown explicitly.

In Fig. 11.8 I show the sensitivity of the combination of the three final states, where each final state is weighted according to the branching fraction prediction from theory. In general, the sensitivity shows the same dependence on the model parameters as the sensitivity of the individual final states described above. Nevertheless, there are a few additional features arising from the combination of the final states. In the region below the di-pion threshold, the sensitivity is purely given by the $\mathrm{h}' \to \mu^+\mu^-$ final state, which covers nearly the full dark Higgs branching fraction. Above $m(\mathrm{h}') > 2\,\mathrm{GeV/c^2}$ the $\mathrm{h}' \to \mu^+\mu^-$ final state is also the only one contributing as no reliable branching fraction predictions are available for the other two final states. As these have a non-negligible branching fraction above this threshold, this results in a sensitivity drop. Other sensitivity drops are observable at the di-pion and di-kaon thresholds, respectively, as the additional final states start to contribute there to the total branching fraction but enter with bad efficiency. In the $\mathrm{h}' \to \mathrm{K}^+\mathrm{K}^-$ final state this bad efficiency is caused by the ϕ veto from Section 6.7. Another sensitivity drop can be seen around the $\mathrm{K^0_S}$ veto (see Section 6.7), as in the first part only the $\mathrm{h}' \to \pi^+\pi^-$ final state and then only the $\mathrm{h}' \to \mu^+\mu^-$ final state contributes. The region where the veto ranges of both final states overlap is completely excluded from the analysis.

Furthermore, I study the sensitivity as a function of the χ_1 mass in Fig. 11.9 for

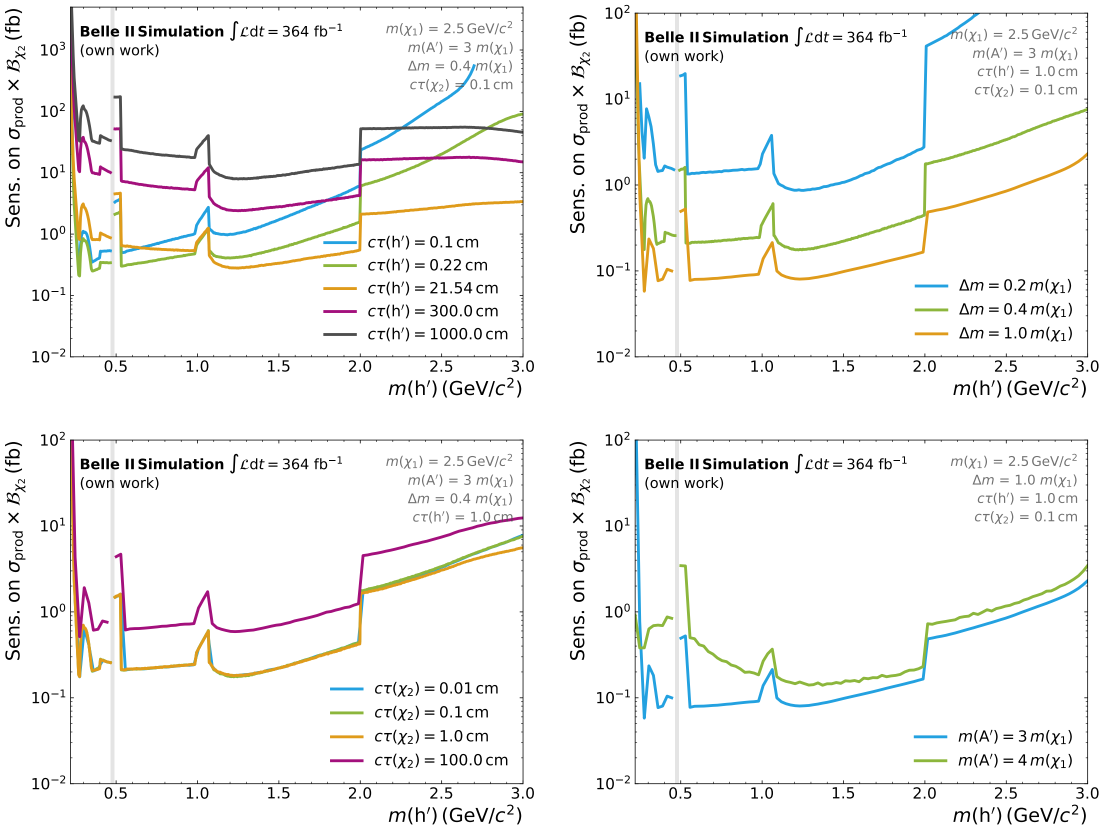

Figure 11.8: Expected sensitivity on the product of the production cross section $\sigma(e^+e^- \to h'\chi_1\chi_2)$ (denoted as σ_{prod}) and the branching fraction $\mathcal{B}(\chi_2 \to \chi_1 e^+e^-)$ (denoted as $\mathcal{B}_{\chi_2}$) as a function of the h$'$ mass. The plots show different variations of the model parameters $c\tau(h')$ (upper left), Δm (upper right), $c\tau(\chi_2)$ (lower left), and $m(A')$ (lower right). All other model parameters are fixed to the values reported in the plots. The sensitivity is estimated by calculating 95% CL Bayesian upper limits assuming $N_{\text{obs}} = 0$ with the background expectation taken from SM background simulations. The fully-vetoed K^0_S region is marked in grey.

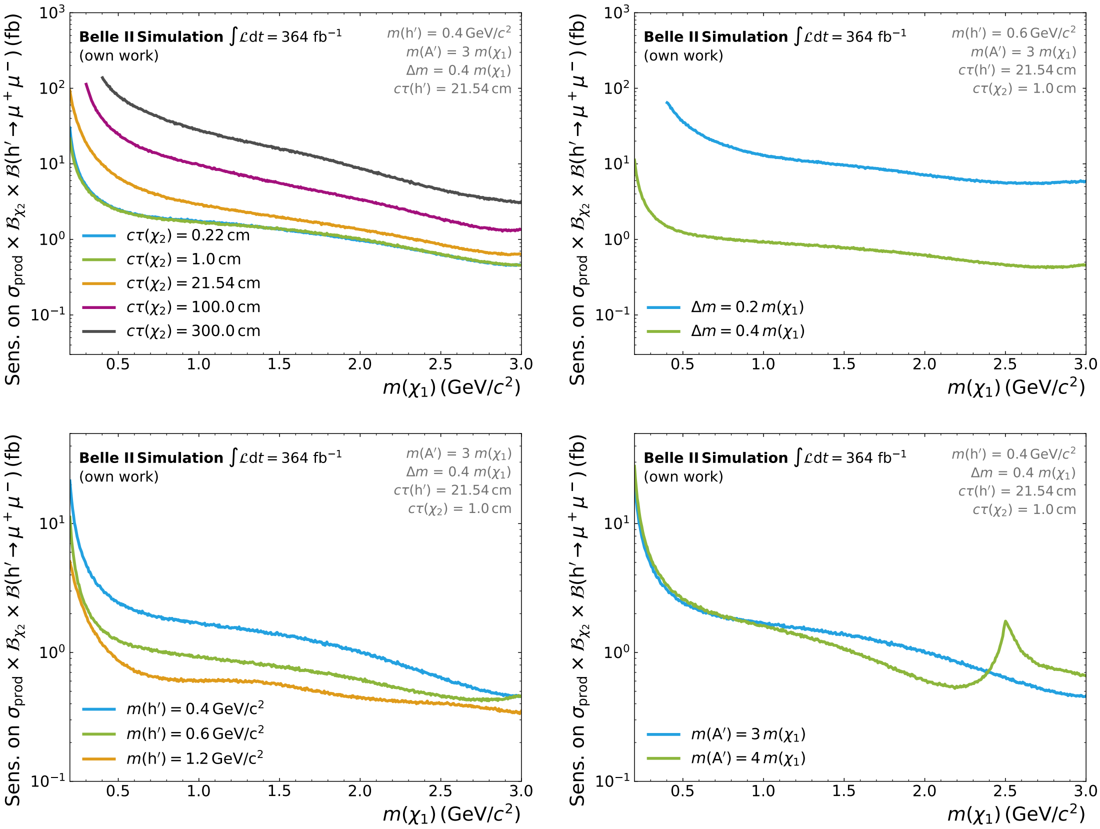

Figure 11.9: Expected sensitivity on the product of the production cross section $\sigma(e^+e^- \to h'\chi_1\chi_2)$ (denoted as σ_{prod}) and the branching fractions $\mathcal{B}(\chi_2 \to \chi_1 e^+e^-)$ (denoted as $\mathcal{B}_{\chi_2}$) and $\mathcal{B}(h' \to \mu^+\mu^-)$ as a function of the χ_1 mass. The plots show different variations of the model parameters $c\tau(\chi_2)$ (upper left), Δm (upper right), $m(h')$ (lower left), and $m(A')$ (lower right). All other model parameters are fixed to the values reported in the plots. The sensitivity is estimated by calculating 95% CL Bayesian upper limits assuming $N_{\mathrm{obs}} = 0$ with the background expectation taken from SM background simulations.

variations of the other model parameters. Overall one can observe that the sensitivity improves for larger values of the χ_1 mass. One reason for this is that the mass splitting is chosen as multiples of the χ_1 mass and a higher mass splitting leads to a better trigger efficiency. Besides the dependencies that already have been discussed above, there is another feature visible for large dark photon masses. The sensitivity drops at the point where the dark photon in the subprocess $e^+e^- \to h'A'$ cannot be produced on-shell anymore. In the lower right plot of Fig. 11.9 this can be seen around a χ_1 mass of $m(\chi_1) = 2.5\,\mathrm{GeV}/c^2$ which roughly marks this threshold if the h' mass is set to $0.4\,\mathrm{GeV}/c^2$.

As the weighting for the combination of the final states does only depend on the mass of the h' and not on the χ_1 mass, qualitatively the sensitivity as a function of the χ_1 mass for the combination is identical to the one for the individual final states and is therefore not shown explicitly.

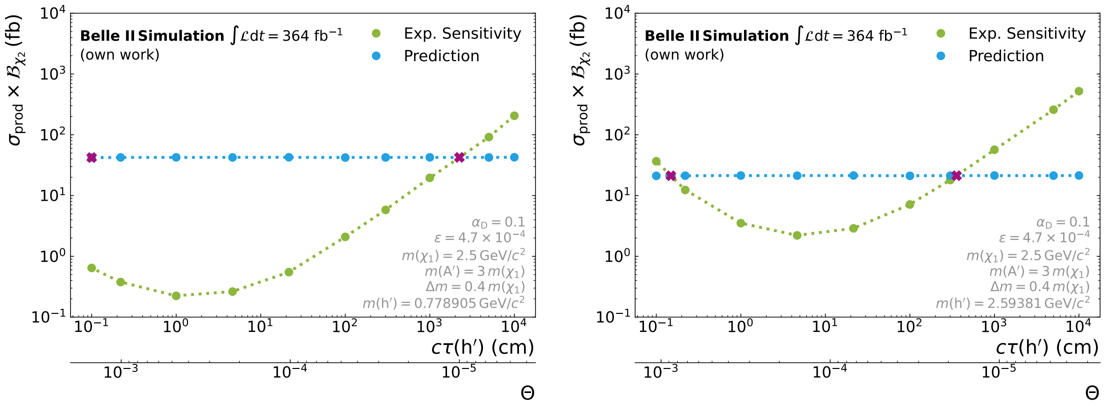

Figure 11.10: Comparison of the expected sensitivities on the product of the production cross section $\sigma(\mathrm{e}^+\mathrm{e}^- \to \mathrm{h}'\chi_1\chi_2)$ (denoted as σ_{prod}) and the branching fraction $\mathcal{B}(\chi_2 \to \chi_1\mathrm{e}^+\mathrm{e}^-)$ (denoted as $\mathcal{B}_{\chi_2}$) (light green) with the theoretical prediction (cyan) as a function of the h$'$ lifetime $c\tau(\mathrm{h}')$/mixing angle θ. The plots show different test masses of the h$'$. The dashed lines show the interpolations between the tested $c\tau(\mathrm{h}')/\theta$. The purple crosses indicate the derived intersections between the expected sensitivity and predicted cross sections. For the given test mass, the parameter space in θ between these intersections is considered to be excluded.

11.7 Translation into Model Parameters

To obtain model-dependent limits on the mixing parameters θ and ϵ, I compare the extracted upper limits on the product of the production cross section $\sigma(\mathrm{e}^+\mathrm{e}^- \to \mathrm{h}'\chi_1\chi_2)$ and the branching fraction $\mathcal{B}(\chi_2 \to \chi_1\mathrm{e}^+\mathrm{e}^-)$ with the theoretical prediction. Before doing so, the model-independent lifetimes of the h$'$ and χ_2 are translated into the mixing parameters θ and ϵ, respectively. This is done via the procedure described in Section 5.1. With the knowledge about the mixing parameters, I calculate the predicted cross section for each tested model parameter configuration and compare it with the extracted upper limit. Model parameter configurations, where the extracted upper limit is lower than the theoretical prediction are considered to be excluded for the dark Higgs in association with inelastic DM model.

As illustrated in Fig. 11.10, I apply this procedure for variations of the h$'$ mass and lifetime to obtain exclusions in the $m(\mathrm{h}')$-θ plane for fixed values of the remaining five model parameters. The expected sensitivity of Belle II in this plane is shown in Fig. 11.11 for two example model parameter configurations. Depending on the model parameters, I expect to improve existing limits on $\sin\theta$ by two orders of magnitude. In general, the sensitivity for $\sin\theta$ as a function of the h$'$ mass follows the model-independent results from Section 11.6, with the $\mathrm{K}^0_{\mathrm{S}}$ and the ϕ veto clearly visible in the plots. Additionally, the sensitivity drop at $m(\mathrm{h}') > 2\,\mathrm{GeV/c}^2$, where only the $\mathrm{h}' \to \mu^+\mu^-$ final state contributes, is also visible here. Furthermore, there is an increased sensitivity observable just below $m(\mathrm{h}') = 1\,\mathrm{GeV/c}^2$. The sensitivity of Belle II does depend on the h$'$ lifetime and due to the

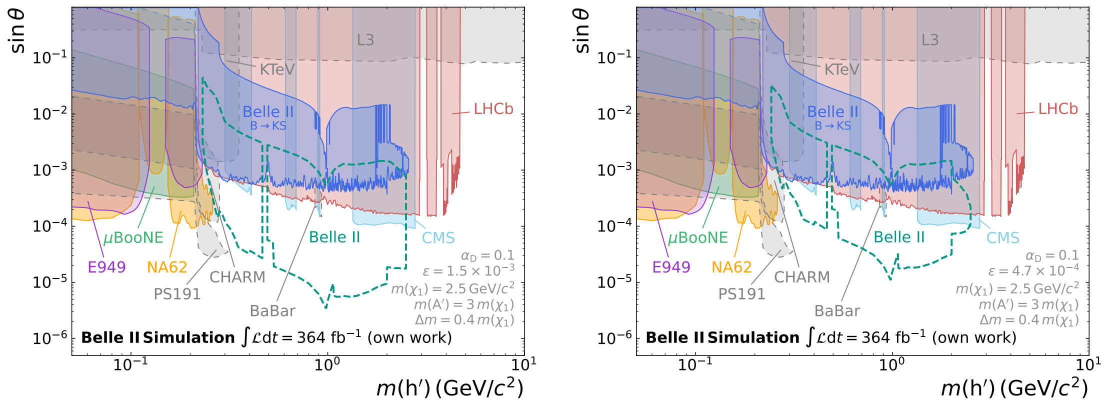

Figure 11.11: Expected sensitivity of Belle II (green) in the plane of the dark Higgs mass $m(\mathrm{h}')$ and the sine of the mixing angle θ compared to existing constraints that have been described in Section 2.5. The remaining model parameters are fixed to $\alpha_\mathrm{D} = 0.1$, $m(\chi_1) = 2.5\,\mathrm{GeV/c^2}$, $m(\mathrm{A}') = 3\,m(\chi_1)$, and $\Delta m = 0.4\,m(\chi_1)$. The mixing between the dark photon and the SM photon is set to $\epsilon = 1.5 \times 10^{-3}$ (left) and $\epsilon = 4.7 \times 10^{-4}$ (right). All other constraints do not depend on the presence of a dark photon or inelastic DM and do consequently not depend on these model parameters.

increased h$'$ width around $1\,\mathrm{GeV/c^2}$ (see Fig. 2.1), smaller values of θ can be probed. As the production cross section $\sigma(\mathrm{e}^+\mathrm{e}^- \to \mathrm{h}'\chi_1\chi_2)$ scales with ϵ the model-dependent limits are stronger for larger mixings ϵ.

Additionally, as exclusions in the $m(\chi_1)$-ϵ are also of interest, the procedure is repeated for variations of the χ_1 mass and the χ_2 lifetime, thereby with the mass and lifetime of the h$'$ fixed (see Fig. 11.12). The resulting sensitivity for two example model parameter configurations is shown in Fig. 11.13. As already discussed in Chapter 4, the limits are visualised in the plane of the DM mass ($m(\chi_1)$) and the dimensionless variable $y = \epsilon^2\alpha_\mathrm{D}(m(\chi_1)/m(\mathrm{A}'))^4$. In general, the sensitivity gets better for larger masses of the χ_1.

The results of these scans on measured data will be shown and discussed in Chapter 12.

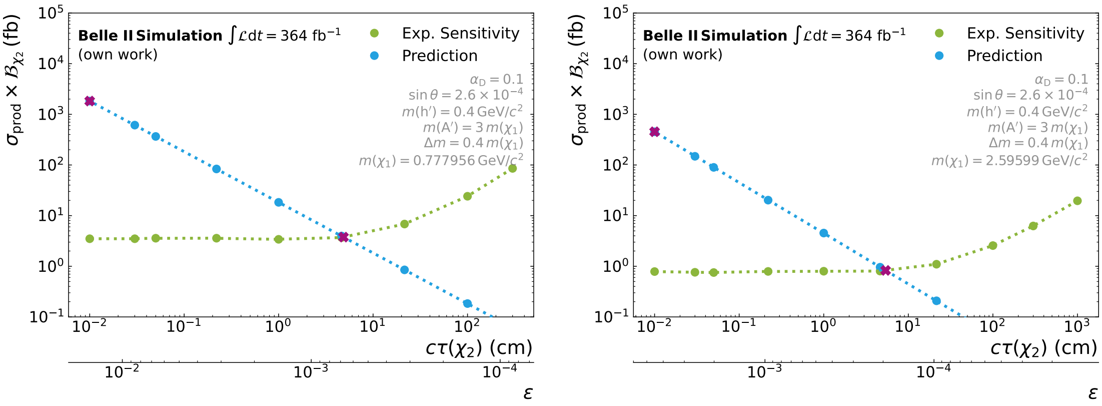

Figure 11.12: Comparison of the expected sensitivities on the product of the production cross section $\sigma(e^+e^- \to h'\chi_1\chi_2)$ (denoted as σ_{prod}) and the branching fraction $\mathcal{B}(\chi_2 \to \chi_1 e^+e^-)$ (denoted as $\mathcal{B}_{\chi_2}$) (light green) with the theoretical prediction (cyan) as a function of the χ_2 lifetime $c\tau(\chi_2)$/mixing parameter ϵ. The plots show different test masses of the χ_1. The dashed lines show the interpolations between the tested $c\tau(\chi_2)/\epsilon$. The purple crosses indicate the derived intersections between the expected sensitivity and predicted cross sections. For the given test mass, the parameter space in ϵ between these intersections is considered to be excluded.

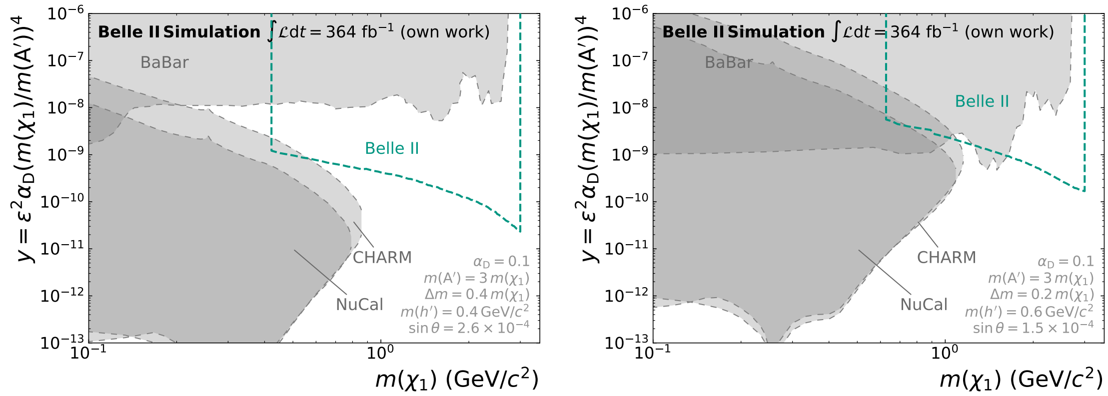

Figure 11.13: Expected sensitivity of Belle II (green) in the plane of the DM mass $m(\chi_1)$ and the dimensionless variable $y = \epsilon^2\alpha_D(m(\chi_1)/m(A'))^4$ compared to existing constraints from [15, 35–39]. The left plot assumes $m(h') = 0.4\,\mathrm{GeV/c^2}$, $\sin\theta = 2.6 \times 10^{-4}$, and $\Delta m = 0.4\,m(\chi_1)$. In the right plot these parameters are chosen as $m(h') = 0.6\,\mathrm{GeV/c^2}$, $\sin\theta = 1.5 \times 10^{-4}$, and $\Delta m = 0.2\,m(\chi_1)$. The remaining model parameters are fixed to $\alpha_D = 0.1$ and $m(A') = 3\,m(\chi_1)$. All other constraints do not depend on the presence of a dark Higgs boson and the model parameters that describe it.

Chapter 12

Results

In this chapter, I present the results obtained with the dataset collected by Belle II between 2019 and 2022, corresponding to an integrated luminosity of $\int \mathcal{L} \mathrm{d}t = 364\,\mathrm{fb}^{-1}$. To not bias the results in any direction, they are derived from the measured data after the full analysis pipeline described throughout this thesis has been fixed.

12.1 Reconstructed Mass Distributions

First I compare the reconstructed dark Higgs mass $M_{\mathrm{xx}}^{\mathrm{h}'}$ distributions in all three considered reconstruction channels with the expectation from the SM simulation. The results are shown in Fig. 12.1. While the limited statistics make it hard to compare the actual shape of the distributions there are still some comparisons that can be made. First of all the overall number of observed events is in good agreement with the expectation from the simulation in all three reconstruction channels. Furthermore, in the $\mathrm{h}' \to \pi^+\pi^-$ reconstruction channel one can additionally observe the expected non-uniformity of the background, which was already described in Section 8.2. This further confirms the necessity to split the mass region into two parts in this reconstruction channel.

12.2 Model-independent Results

To get the model-independent results I scan the reconstructed h' mass with a step size of half the signal width. I count events in each signal window and compare the number of observed events to the expectation derived from the mass sidebands as described throughout Chapter 11. Initially, this is done for each individual final state. As a first step, for each model parameter configuration and each scanned mass point I calculate the p-value and the corresponding local significance according to the procedure defined in Section 11.3. The highest local significance in the $\mathrm{h}' \to \pi^+\pi^-$ final state is found as $2.9\,\sigma$ for a dark Higgs mass of $0.531\,\mathrm{GeV}/\mathrm{c}^2$ and a dark Higgs lifetime of $1.0\,\mathrm{cm}$. The corresponding global significance after considering the look-elsewhere effect (Section 11.4) for this final state

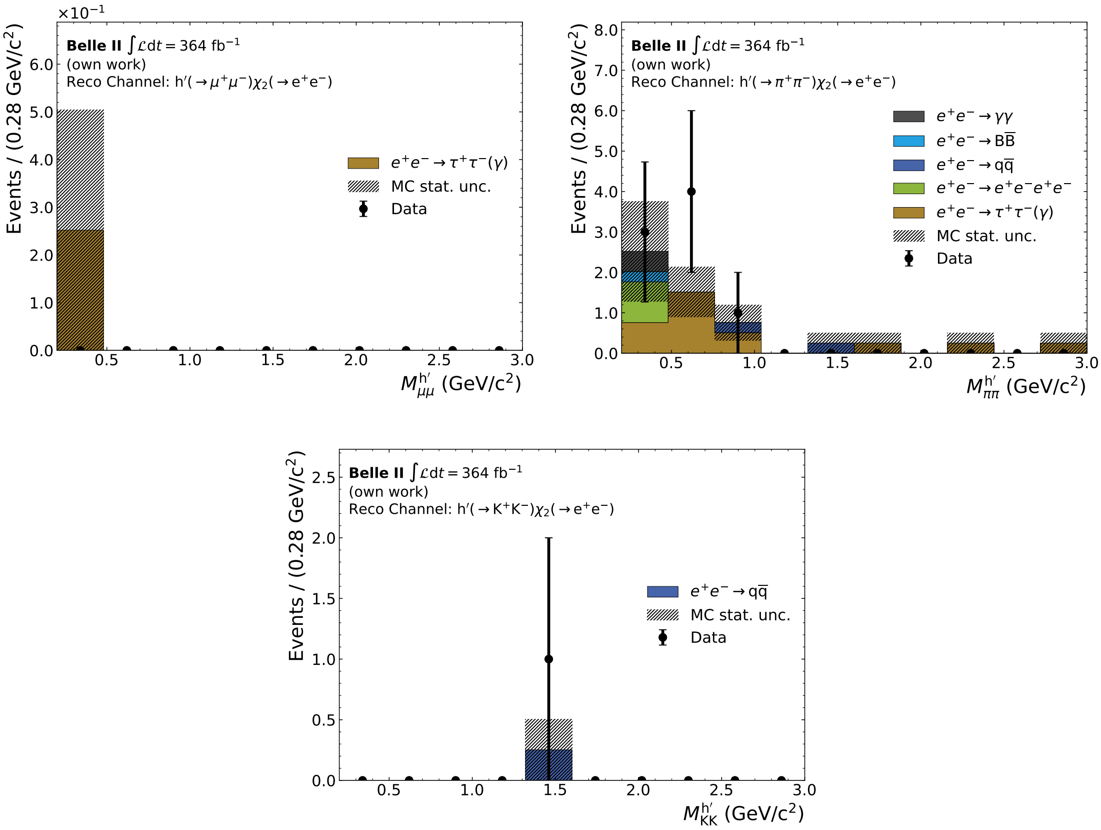

Figure 12.1: Reconstructed h′ mass in the three different reconstruction channels $h' \to \mu^+\mu^-$ (upper left), $h' \to \pi^+\pi^-$ (upper right) and $h' \to K^+K^-$ (bottom) after applying all selections from Tables 6.1 and 6.2. The coloured histograms show the expectation from the SM simulations considering all possible background sources described in Table 5.1. Each component is scaled according to the produced number of events in each of the simulated samples to reach the target integrated luminosity of $\int \mathcal{L}dt = 364\,\text{fb}^{-1}$. The data collected by the Belle II experiment is shown with black dots.

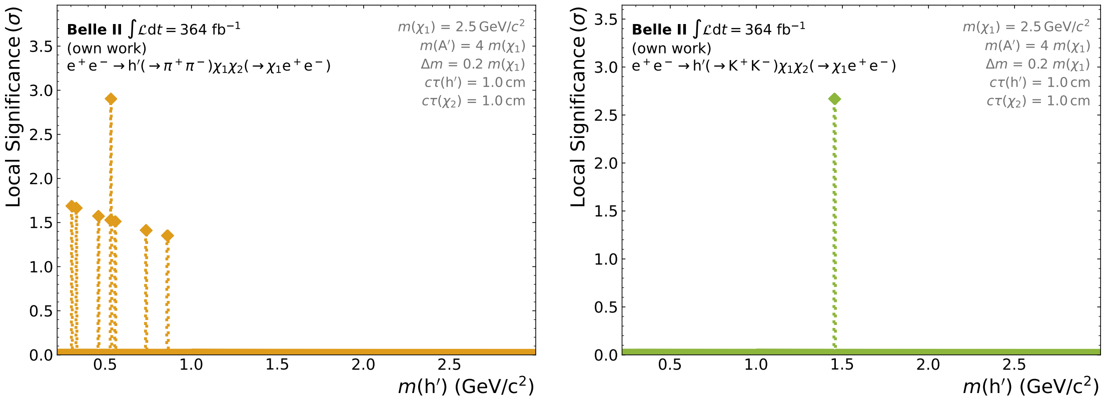

Figure 12.2: Observed local significances as a function of the dark Higgs mass in the $\mathrm{h}' \to \pi^+\pi^-$ (left) and $\mathrm{h}' \to \mathrm{K}^+\mathrm{K}^-$ (right) final state. The values of the remaining model parameters are fixed to $c\tau(\mathrm{h}') = 1.0\,\mathrm{cm}$, $c\tau(\chi_2) = 0.1\,\mathrm{cm}$, $m(\chi_1) = 2.5\,\mathrm{GeV/c^2}$, $m(\mathrm{A}') = 4\,m(\chi_1)$, and $\Delta m = 0.2\,m(\chi_1)$.

is determined to $1.1\,\sigma$. At a dark Higgs mass of $1.452\,\mathrm{GeV/c^2}$ and a dark Higgs lifetime of 1.0 cm the $\mathrm{h}' \to \mathrm{K}^+\mathrm{K}^-$ final state shows the highest local significance of $2.7\,\sigma$. The look-elsewhere effect in the $\mathrm{h}' \to \mathrm{K}^+\mathrm{K}^-$ final state is much smaller due to the smaller amount of scan points together with the lower background expectation, leading to a global significance of $2.2\,\sigma$ in this final state. Fig. 12.2 shows the observed significances as a function of the h' mass for the model parameter configuration for which the highest local significance is observed. Note that as no events are observed in the $\mathrm{h}' \to \mu^+\mu^-$ final state I do not report significances for this individual final state as the p-value equals one over the whole mass range. As the signal hypothesis enters the calculation of the p-value only in the definition of the signal windows via the signal width and the signal width only depends slightly on the choice of model parameters, the differences in p-values for the different tested model parameter configurations are found to be very small. Therefore the shown model parameter configuration is a good representation for all scans performed with different variations of the model parameters.

As I do not find a significant excess over the SM expectation, I calculate 95% CL upper limits on the product of the production cross section $\sigma(\mathrm{e}^+\mathrm{e}^- \to \mathrm{h}'\chi_1\chi_2)$ and the branching fractions $\mathcal{B}(\chi_2 \to \chi_1\mathrm{e}^+\mathrm{e}^-) \times \mathcal{B}(\mathrm{h}' \to \mathrm{x}^+\mathrm{x}^-)$ for each final state. The calculation of the upper limits involves the signal efficiency, which depends on the average beam background conditions, as described in 7.1. To derive the average beam background conditions, I use the average number of additional CDC hits in the whole dataset, which I measure as $< N_{\mathrm{extra}}^{\mathrm{CDC}} >= 635.98$. Using this number, I calculate the signal efficiency for each model parameter configuration with the procedure described in Section 7.1. The upper limits for two model parameter configurations are shown in Fig. 12.3. Dependent on the dark Higgs lifetime, the observed upper limits are within the range of $10^{-1}\,\mathrm{fb}$ to $10\,\mathrm{fb}$ over nearly the full scanned mass range, reaching to higher values close to the kinematic thresholds of the

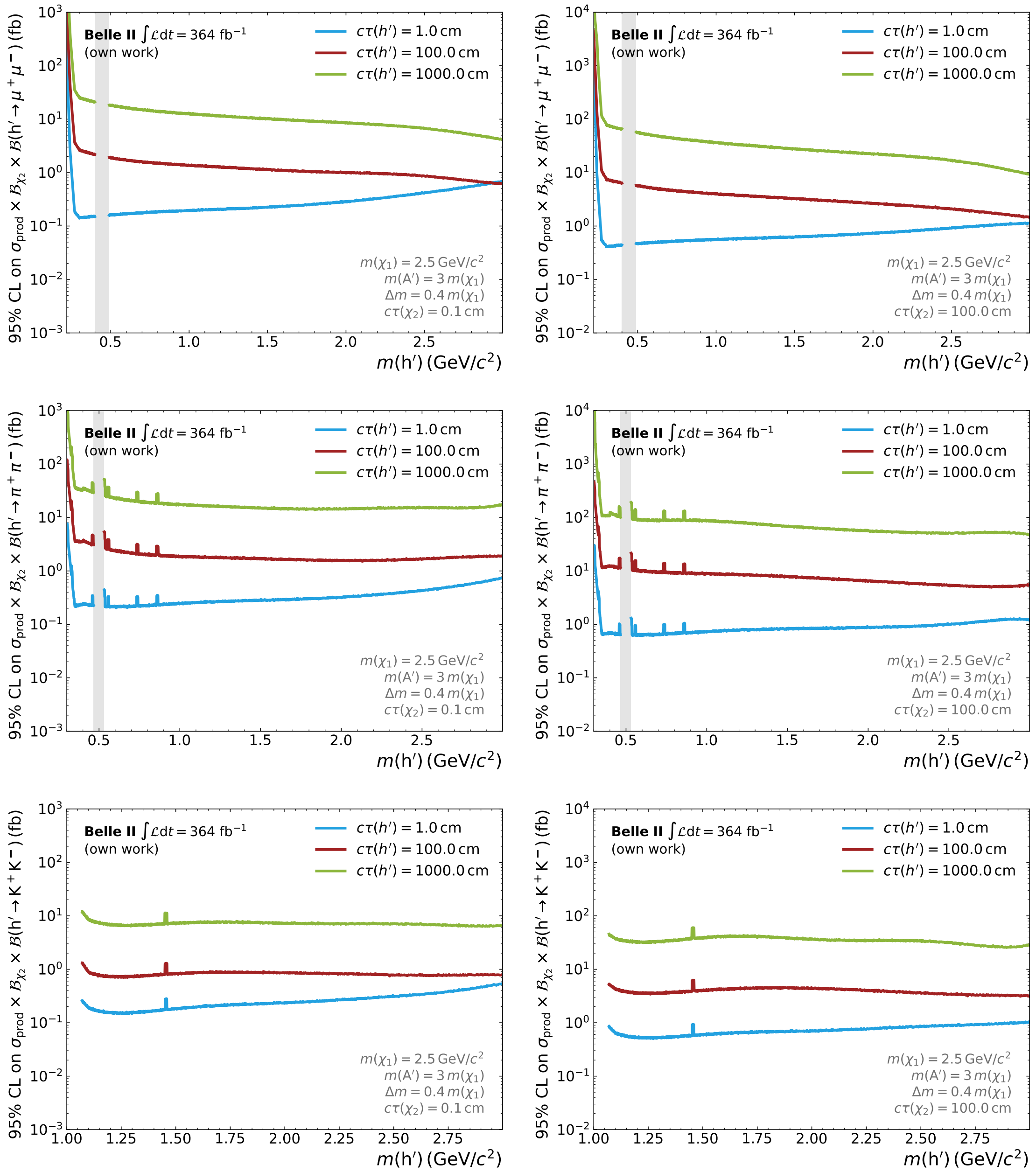

Figure 12.3: 95% CL upper limits on the product of the production cross section $\sigma(e^+e^- \to h'\chi_1\chi_2)$ and the branching fractions $\mathcal{B}(\chi_2 \to \chi_1 e^+e^-) \times \mathcal{B}(h' \to x^+x^-)$ for the different final states $e^+e^- \to h'(\to \mu^+\mu^-)\chi_1\chi_2(\to \chi_1 e^+e^-)$ (top), $e^+e^- \to h'(\to \pi^+\pi^-)\chi_1\chi_2(\to \chi_1 e^+e^-)$ (center), and $e^+e^- \to h'(\to K^+K^-)\chi_1\chi_2(\to \chi_1 e^+e^-)$ (bottom). The left side shows a χ_2 lifetime hypothesis of $c\tau(\chi_2) = 0.1\,\text{cm}$ and the right $c\tau(\chi_2) = 100.0\,\text{cm}$. Different lifetime hypothesis of the h' are indicated with different colours: $c\tau(h') = 1.0\,\text{cm}$ (cyan), $c\tau(h') = 100.0\,\text{cm}$ (red), and $c\tau(h') = 1000.0\,\text{cm}$ (light green). The remaining model parameters are fixed to $m(\chi_1) = 2.5\,\text{GeV/c}^2$, $m(A') = 3\,m(\chi_1)$, and $\Delta m = 0.4\,m(\chi_1)$. The fully vetoed K^0_S region is marked with a grey band.

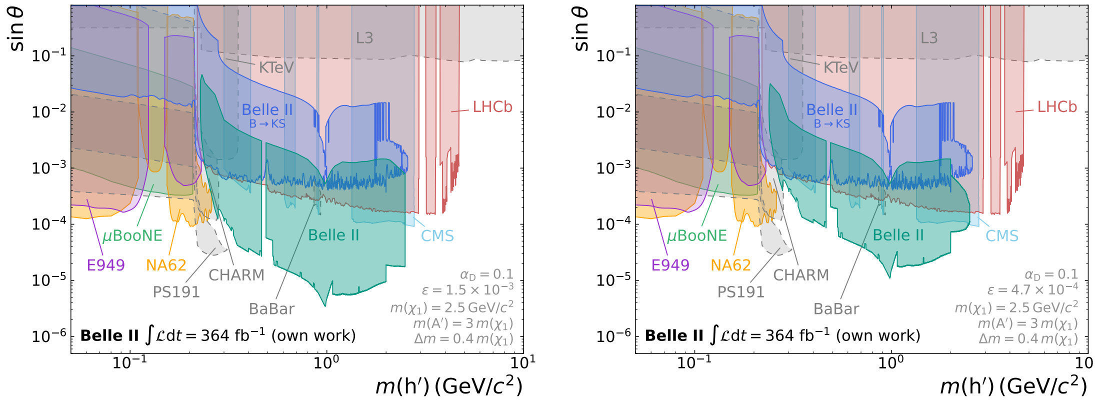

Figure 12.4: Exclusions at 95% CL in the plane of the dark Higgs mass $m(\mathrm{h}')$ and the sine of the mixing angle θ of this work (green) together with existing constraints that have been described in Section 2.5. The remaining model parameters are fixed to $\alpha_\mathrm{D} = 0.1$, $m(\chi_1) = 2.5\,\mathrm{GeV/c^2}$, $m(\mathrm{A}') = 3\,m(\chi_1)$, and $\Delta m = 0.4\,m(\chi_1)$. The mixing between the dark photon and the SM photon is set to $\epsilon = 1.5 \times 10^{-3}$ (left) and $\epsilon = 4.7 \times 10^{-4}$ (right). All other constraints do not depend on the presence of a dark photon or inelastic DM and do consequently not depend on these model parameters.

respective final states. Plots showing the model-independent upper limits for all tested model parameter configurations can be found in Chapter G in the appendix.

12.3 Model-dependent Results

While in Section 12.2 each final state was considered individually, in this section the information of all final states is combined. For this combination, each final state is weighted with the $\mathcal{B}(\mathrm{h}' \to \mathrm{x}^+\mathrm{x}^-)$ predictions from [18] making the results fully dependent on the inelastic DM in association with a dark Higgs boson model. As the p-values for the combination are calculated by the multiplication of the p-values of the individual final states and I do not observe events in the same signal window in different final states, the highest local significance observed is identical to the model-independent one measured in the $\mathrm{h}' \to \pi^+\pi^-$ final state. Therefore, when combining the final states, still no significant excess over the SM expectation is found. Consequently, I calculate 95% CL upper limits on the product of the production cross section and the χ_2 branching fraction, $\sigma(\mathrm{e}^+\mathrm{e}^- \to \mathrm{h}'\chi_1\chi_2) \times \mathcal{B}(\chi_2 \to \chi_1\mathrm{e}^+\mathrm{e}^-)$. To derive the upper limits on the mixing angle θ, for each h' mass point I derive the value of θ so that the observed 95% CL upper limits match the theoretical predictions as it is described in Section 11.7. Here the theoretical prediction on $\sigma(\mathrm{e}^+\mathrm{e}^- \to \mathrm{h}'\chi_1\chi_2) \times \mathcal{B}(\chi_2 \to \chi_1\mathrm{e}^+\mathrm{e}^-)$ is taken from [13]. Fig. 12.4 shows the observed upper limits on $\sin\theta$ for two example model parameter configurations. It has to be stressed again that the existing constraints do not depend on the existence of a dark photon or inelastic DM being realised in nature and therefore not on the model parameters describing them, while the model-dependent results of this thesis do. Nevertheless, the

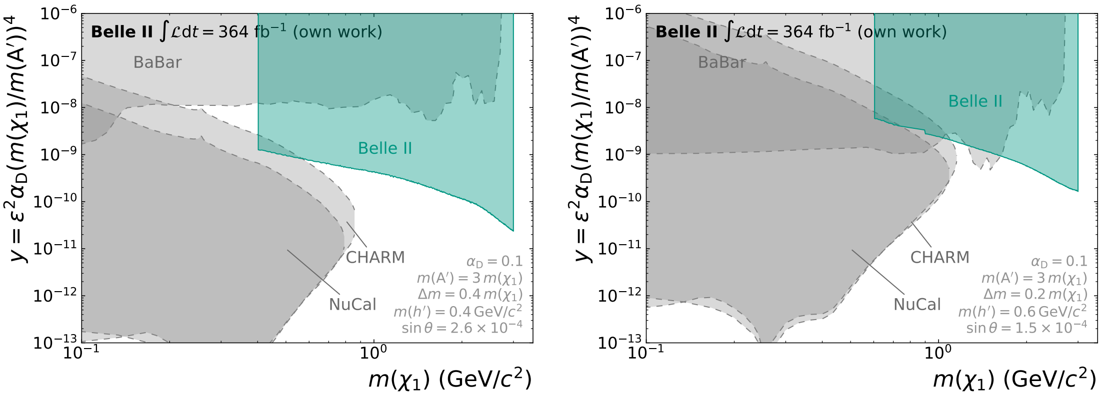

Figure 12.5: Exclusions at 95% CL in the plane of the DM mass $m(\chi_1)$ and the dimensionless variable $y = \epsilon^2\alpha_\mathrm{D}(m(\chi_1)/m(\mathrm{A}'))^4$ of this work (green) together with existing constraints from [15, 35–39]. The left plot assumes $m(\mathrm{h}') = 0.4\,\mathrm{GeV/c}^2$, $\sin\theta = 2.6 \times 10^{-4}$, and $\Delta m = 0.4\,m(\chi_1)$. In the right plot these parameters are chosen as $m(\mathrm{h}') = 0.6\,\mathrm{GeV/c}^2$, $\sin\theta = 1.5 \times 10^{-4}$, and $\Delta m = 0.2\,m(\chi_1)$. The remaining model parameters are fixed to $\alpha_\mathrm{D} = 0.1$ and $m(\mathrm{A}') = 3\,m(\chi_1)$. All other constraints do not depend on the presence of a dark Higgs boson and the model parameters that describe it.

closer ϵ is chosen to the maximal value not already excluded, the upper limits on θ improve by up to two orders of magnitude over the existing ones. For some model parameter configurations, there is a sharp cut-off at the upper end of the $m(\mathrm{h}')$ spectrum. This is caused by the mass hierarchy $m(\mathrm{h}') \lesssim m(\chi_1)$ that is discussed in Section 2.4 and required to realise the thermal relic density with the dark Higgs in association with inelastic DM model.

I repeat the procedure to derive additional upper limits on the mixing parameter ϵ for values of the χ_1 mass. Inspired by existing limits and [52], I present the upper limits on ϵ in terms of the dimensionless variable $y = \epsilon^2\alpha_\mathrm{D}(m(\chi_1)/m(\mathrm{A}'))^4$. The observed upper limits on y for two example model parameter configurations are shown in Fig. 12.5. In this plane the lower limit on the minimal excluded χ_1 mass is again given by the assumption made on the h' mass taking into account the mass hierarchy between the χ_1 and h'.

The exclusions for all tested model parameter configurations can be found in Chapter G in the appendix.

Chapter 13

Conclusion

In this thesis, I present the first search for a dark Higgs boson produced in association with inelastic DM, a model containing seven independent model parameters. The search is performed on a dataset of $\int \mathcal{L}\mathrm{d}t = 364\,\mathrm{fb}^{-1}$, collected by the Belle II experiment between 2019 and 2022. I do not find evidence for the signal process of interest and therefore I place both model-independent and model-dependent upper limits on the product of the production cross section and the χ_2 and h' branching fractions, $\sigma(\mathrm{e}^+\mathrm{e}^- \to \mathrm{h}'\chi_1\chi_2) \times \mathcal{B}(\chi_2 \to \chi_1\mathrm{e}^+\mathrm{e}^-) \times \mathcal{B}(\mathrm{h}' \to \mathrm{x}^+\mathrm{x}^-)$, with $x = \{\mu, \pi, \mathrm{K}\}$. While there are existing limits constraining either the dark Higgs or inelastic DM individually, this is the first search combining both. This makes the model more complex but also increases the sensitivity resulting in stronger limits compared to the individual searches. Depending on the choice of model parameters, the limits improve by up to two orders of magnitude over existing ones. Therefore the presented search is another step towards unravelling the mystery of the nature of DM.

The search does not only give strong limits on a dark Higgs boson produced in association with inelastic DM but the model-independent limits can be used additionally to constrain other dark sector models with a signature of up to two displaced vertices and additional missing energy in the final state, such as [86].

The analysed dataset is still a small fraction of the final expected dataset of $50\,\mathrm{ab}^{-1}$ Belle II plans to collect. As the search is limited by the available statistics the larger dataset would help to further improve the limits. Neglecting systematics, one expects an improvement in sensitivity of about one order of magnitude on the mixing parameters. While at some point the systematic uncertainties will have a larger impact, the larger dataset will help to reduce their size as well, as the statistics also play a large role in the determination of the respective corrections, for example, the LLP efficiency correction.

There are several aspects at the reconstruction level where improvements can be highly beneficial for the analysis. First of all, with the current track-finding algorithms used in Belle II, the reconstruction efficiency drops heavily for more displaced vertices. Improving the track-finding, to be more independent of the displacement, would give a huge gain in signal efficiency and consequently a better sensitivity. There is currently ongoing development using graph neural networks (GNNs) for track-finding, which shows already promising results for displaced vertices. This also applies to the trigger system of Belle II, where work is ongoing to improve the trigger to cover the novel signatures as for example described in [87]. Improvements on the trigger are especially crucial as, contrary to the track-finding where the events can be reanalysed once new algorithms are available, events lost at this stage are lost forever.

Currently, the track-finding efficiency for displaced vertices depends significantly on the beam background conditions. Having in mind that the beam background conditions are expected to get even worse in the upcoming data-taking periods this will even further reduce the signal efficiency if no more robust track-finding algorithms become available. The analysis I present here is the first in Belle II that corrects for this effect but with the cost of having to produce more simulations for each model parameter configuration. This and the computing time needed for the simulation and reconstruction of these samples limits the model parameter space that can be covered. Improving the reconstruction and making both the reconstruction and simulation significantly faster would drastically increase the model parameter space in which the search can be performed.

Another field of improvement is PID. Especially for pions, the current PID algorithms suffer from a large misidentification rate whenever the particles are created far from the IP. Further improvement of these algorithms can help to increase the sensitivity reach of the presented analysis.

One of the more obvious approaches to extend the reach of the search is the inclusion of additional final states that have not been considered in this thesis. The inclusion of the additional χ_2 decay channels that have not been covered due to restrictions of the trigger and limitations on the computing resources that have been available is straightforward, especially in case new trigger algorithms become available. Including the $\mathrm{h}' \to \tau^+\tau^-$ final state in the kinematically allowed region is more challenging. As the τ decays include additional neutrinos the reconstructed h' vertex would not point back to the IP anymore. With the pointiness being one of the most powerful selection variables this would make the background suppression more challenging.

While there is always room for improvement, in this thesis, I already show the possibilities of the Belle II experiment in the detection of events with multiple displaced vertices in the final state and additional missing energy, improving existing limits by two orders of magnitude in parts of the model parameter space. The analysis techniques that are developed and studied in the context of the presented analysis are expected to further extend the reach of Belle II into the unknown dark sector.

To summarise, in this thesis, I present world-leading limits on dark Higgs bosons produced in association with inelastic DM and the first search at Belle II with two displaced vertices.

Danksagung

An dieser Stelle möchte ich den Menschen danken, die maßgeblich zum Gelingen der Promotion beigetragen haben.

Zunächst möchte ich mich herzlich bei meinem Referenten Prof. Dr. Torben Ferber bedanken. Ich habe mich während der gesamten Promotion stets ausgezeichnet betreut und wertgeschätzt gefühlt und die zahlreichen Diskussionen im Rahmen dieser Arbeit sehr genossen. Er wusste immer Rat, falls ich in der Analyse auf Probleme gestoßen bin und hat mir hierbei den Freiraum gelassen, die Arbeit nach meinen Vorstellungen zu gestalten, wodurch ich nie den Spaß an der Teilchenphysik verloren habe.

Zudem möchte ich Prof. Dr. Günter Quast dafür danken, dass er das Korreferat für die Promotion übernommen hat sowie immer ein offenes Ohr für Fragen jeglicher Art hatte.

Ein weiterer Dank gilt Dr. Pablo Goldenzweig, der sowohl die Masterarbeit bei Belle II sowie zu Beginn diese Promotion ermöglicht hat.

Die Promotion wäre sicherlich nicht möglich gewesen ohne die Hilfe meiner Kolleg:innen am ETP und in der Belle II Kollaboration, die eine Atmosphäre geschaffen haben, in der ich mich sehr wohl gefühlt habe und auch in stressigen Zeiten eine Menge Spaß hatte. Dr. Felix Metzner und Dr. Moritz Bauer, mit denen ich über Jahre hinweg das Büro geteilt habe, haben mir sehr geholfen, neue Sichtweisen zu entwickeln und mit ihrem gründlichen Korrekturlesen sehr zum Gelingen dieser Arbeit beigetragen. Ein besonderer Dank gilt Dr. Giacomo De Pietro, der mir zu jeder Zeit mit Rat und Tat zu Seite stand, und mir in stressigen Situationen sehr geholfen hat, nicht die Nerven zu verlieren. Dieser besondere Dank gilt auch Isabel Haide für die inhaltlichen und stilistischen Vorschläge zur Dissertation und dem Promotionsvortrag, sowie die aufbauenden Worte in den Wochen vor der Doktorprüfung. Ich möchte die Liste von Menschen, denen ich sehr dankbar bin, erweitern um Alexander Heidelbach, Jonas Eppelt, Lea Reuter und Dr. Slavomira Stefkova, die große Teile dieser Arbeit Korrektur gelesen haben, sowie Dr. Matthias Schnepf, der mir bei sämtlichen Computingfragen zur Seite stand.

Abseits des beruflichen Umfelds möchte ich mich bei all meinen Freund:innen bedanken, die es mir ermöglicht haben, auch einmal abzuschalten und damit den nötigen Ausgleich zu schaffen, ohne den diese Promotion sicherlich nicht möglich gewesen wäre.

Der größte Dank gilt meiner Familie, allen voran meinen Eltern Gabi und Ralf, sowie meiner Partnerin Lara, die mich jederzeit bedingungslos unterstützt und mich auch in schwierigeren Phasen immer motiviert haben.

Acknowledgement

The author of this work acknowledges support by the state of Baden-Württemberg through bwHPC and the German Research Foundation (DFG) through grant no INST 39/963-1 FUGG (bwForCluster NEMO).

Bibliography

[1] F. Zwicky. “Die Rotverschiebung von extragalaktischen Nebeln”. In: *Helvetica Physica Acta* 6 (1933), pp. 110–127.

[2] F. Zwicky. “Republication of: The redshift of extragalactic nebulae”. In: *Gen. Relativ. Gravit.* 41 (2009), pp. 207–224. DOI: `10.1007/s10714-008-0707-4`.

[3] V. C. Rubin, W. K. Ford Jr., and N. Thonnard. “Rotational properties of 21 SC galaxies with a large range of luminosities and radii, from NGC 4605 (R=4kpc) to UGC 2885 (R=122kpc).” In: *Astrophys. J.* 238 (1980), pp. 471–487. DOI: `10.1086/158003`.

[4] **Particle Data Group**, S. Navas et al. “Review of Particle Physics”. In: *Phys. Rev. D* 110 (2024), p. 030001. DOI: `10.1103/PhysRevD.110.030001`.

[5] S. L. Glashow. “Partial-symmetries of weak interactions”. In: *Nuclear Physics* 22 (1961), pp. 579–588. DOI: `10.1016/0029-5582(61)90469-2`.

[6] S. Weinberg. “A Model of Leptons”. In: *Phys. Rev. Lett.* 19 (1967), pp. 1264–1266. DOI: `10.1103/PhysRevLett.19.1264`.

[7] A. Salam and J. C. Ward. “Weak and electromagnetic interactions”. In: *Nuovo Cimento* 11 (1959), pp. 568–577. DOI: `10.1007/BF02726525`.

[8] S. L. Glashow, J. Iliopoulos, and L. Maiani. “Weak Interactions with Lepton-Hadron Symmetry”. In: *Phys. Rev. D* 2 (1970), pp. 1285–1292. DOI: `10.1103/PhysRevD.2.1285`.

[9] F. Englert and R. Brout. “Broken Symmetry and the Mass of Gauge Vector Mesons”. In: *Phys. Rev. Lett.* 13 (1964), pp. 321–323. DOI: `10.1103/PhysRevLett.13.321`.

[10] P. W. Higgs. “Spontaneous Symmetry Breakdown without Massless Bosons”. In: *Phys. Rev.* 145 (1966), pp. 1156–1163. DOI: `10.1103/PhysRev.145.1156`.

[11] G. S. Guralnik, C. R. Hagen, and T. W. B. Kibble. “Global Conservation Laws and Massless Particles”. In: *Phys. Rev. Lett.* 13 (1964), pp. 585–587. DOI: `10.1103/PhysRevLett.13.585`.

[12] N. Aghanim et al. “Planck 2018 results - VI. Cosmological parameters”. In: *Astron. Astrophys.* 641 (2020), A6. DOI: `10.1051/0004-6361/201833910`. arXiv: `1807.06209 [astro-ph.CO]`.

[13] M. Duerr et al. “Long-Lived Dark Higgs and Inelastic Dark Matter at Belle II”. In: *J. High Energy Phys.* 2021 (2021), p. 146. DOI: `10.1007/JHEP04(2021)146`. arXiv: `2012.08595 [hep-ph]`.

[14] M. Fabbrichesi, E. Gabrielli, and G. Lanfranchi. “Introduction”. In: *The Physics of the Dark Photon: A Primer*. Ed. by M. Fabbrichesi, E. Gabrielli, and G. Lanfranchi. Cham: Springer International Publishing, 2021, pp. 1–19. DOI: `10.1007/978-3-030-62519-1_1`. arXiv: `2005.01515 [hep-ph]`.

[15] M. Duerr et al. “Invisible and Displaced Dark Matter Signatures at Belle II”. In: *J. High Energy Phys.* 2020 (2020), p. 39. DOI: `10.1007/JHEP02(2020)039`. arXiv: `1911.03176 [hep-ph]`.

[16] H. Ruegg and M. Ruiz-Altaba. “The Stueckelberg Field”. In: *Int. J. Mod. Phys. A* 19 (2004), pp. 3265–3347. DOI: `10.1142/S0217751X04019755`. arXiv: `hep-th/0304245 [hep-th]`.

[17] T. Ferber, A. Grohsjean, and F. Kahlhoefer. “Dark Higgs Bosons at Colliders”. In: *Progress in Particle and Nuclear Physics* 136 (2024), p. 104105. DOI: `10.1016/j.ppnp.2024.104105`. arXiv: `2305.16169 [hep-ph]`.

[18] M. W. Winkler. “Decay and Detection of a Light Scalar Boson Mixing with the Higgs Boson”. In: *Phys. Rev. D* 99 (2019), p. 015018. DOI: `10.1103/PhysRevD.99.015018`. arXiv: `1809.01876 [hep-ph]`.

[19] P. a. R. Ade et al. “Planck 2015 results - XIII. Cosmological parameters”. In: *Astron. Astrophys.* 594 (2016), A13. DOI: `10.1051/0004-6361/201525830`. arXiv: `1502.01589 [astro-ph.CO]`.

[20] H. An, M. B. Wise, and Y. Zhang. “Strong CMB constraint on P-wave annihilating dark matter”. In: *Phys. Lett. B* 773 (2017), pp. 121–124. DOI: `10.1016/j.physletb.2017.08.010`.

[21] E. Izaguirre, G. Krnjaic, and B. Shuve. “Discovering inelastic thermal relic dark matter at colliders”. In: *Phys. Rev. D* 93 (2016), p. 063523. DOI: `10.1103/PhysRevD.93.063523`. arXiv: `1508.03050 [hep-ph]`.

[22] **NA62 Collaboration**, E. Cortina Gil et al. “Measurement of the very rare $\mathrm{K}^+ \to \pi^+ \nu\nu$ decay”. In: *J. High Energy Phys.* 06 (2021), p. 093. DOI: `10.1007/JHEP06(2021)093`. arXiv: `2103.15389 [hep-ex]`.

[23] **NA62 Collaboration**, E. Cortina Gil et al. “Search for π^0 decays to invisible particles”. In: *J. High Energy Phys.* 02 (2021), p. 201. DOI: `10.1007/JHEP02(2021)201`. arXiv: `2010.07644 [hep-ex]`.

[24] **BNL-E949 Collaboration**, A. V. Artamonov et al. “Study of the decay $\mathrm{K}^+ \to \pi^+ \nu\nu$ in the momentum region $140 < P_\pi < 199$ MeV/c”. In: *Phys. Rev. D* 79 (2009), p. 092004. DOI: `10.1103/PhysRevD.79.092004`. arXiv: `0903.0030 [hep-ex]`.

[25] **MicroBooNE Collaboration**, P. Abratenko et al. “Search for a Higgs Portal Scalar Decaying to Electron-Positron Pairs in the MicroBooNE Detector”. In: *Phys. Rev. Lett.* 127 (2021), p. 151803. DOI: `10.1103/PhysRevLett.127.151803`. arXiv: `2106.00568 [hep-ex]`.

[26] **Belle II Collaboration**, I. Adachi et al. “Search for a long-lived spin-0 mediator in $b \to s$ transitions at the Belle II experiment”. In: *Phys. Rev. D* 108 (2023), p. L111104. DOI: `10.1103/PhysRevD.108.L111104`. arXiv: `2306.02830 [hep-ex]`.

[27] **LHCb Collaboration**, R. Aaij et al. “Search for Hidden-Sector Bosons in $\mathrm{B}^0 \to \mathrm{K}^{*0}\mu^+\mu^-$ Decays”. In: *Phys. Rev. Lett.* 115 (2015), p. 161802. DOI: `10.1103/PhysRevLett.115.161802`. arXiv: `1508.04094 [hep-ex]`.

[28] **LHCb Collaboration**, R. Aaij et al. “Search for long-lived scalar particles in $\mathrm{B}^+ \to \mathrm{K}^+\chi(\mu^+\mu^-)$ decays”. In: *Phys. Rev. D* 95 (2017), p. 071101. DOI: `10.1103/PhysRevD.95.071101`. arXiv: `1612.07818 [hep-ex]`.

[29] **CMS Collaboration**, A. Tumasyan et al. “Search for long-lived particles decaying into muon pairs in proton-proton collisions at $\sqrt{s} = 13$ TeV collected with a dedicated high-rate data stream”. In: *J. High Energy Phys.* 04 (2022), p. 062. DOI: `10.1007/JHEP04(2022)062`. arXiv: `2112.13769 [hep-ex]`.

[30] **CHARM Collaboration**, F. Bergsma et al. “Search for axion-like particle production in 400 GeV proton-copper interactions”. In: *Phys. Lett. B* 157 (1985), pp. 458–462. DOI: `10.1016/0370-2693(85)90400-9`.

[31] **KTeV Collaboration**, A. Alavi-Harati et al. “Search for the decay $\mathrm{K_L} \to \pi^0\mu^+\mu^-$”. In: *Phys. Rev. Lett.* 84 (2000), pp. 5279–5282. DOI: `10.1103/PhysRevLett.84.5279`. arXiv: `hep-ex/0001006`.

[32] D. Gorbunov, I. Krasnov, and S. Suvorov. “Constraints on light scalars from PS191 results”. In: *Phys. Lett. B* 820 (2021), p. 136524. DOI: `10.1016/j.physletb.2021.136524`. arXiv: `2105.11102 [hep-ph]`.

[33] **BaBar Collaboration**, J. P. Lees et al. “Search for Long-Lived Particles in $\mathrm{e}^+\mathrm{e}^-$ Collisions”. In: *Phys. Rev. Lett.* 114 (2015), p. 171801. DOI: `10.1103/PhysRevLett.114.171801`. arXiv: `1502.02580 [hep-ex]`.

[34] **L3 Collaboration**, M. Acciarri et al. “Search for neutral Higgs boson production through the process $\mathrm{e}^+\mathrm{e}^- \to \mathrm{Z}^*\mathrm{H}^0$”. In: *Phys. Lett. B* 385 (1996), pp. 454–470. DOI: `10.1016/0370-2693(96)00987-2`.

[35] S. N. Gninenko. “Constraints on sub-GeV hidden sector gauge bosons from a search for heavy neutrino decays”. In: *Phys. Lett. B* 713 (2012), pp. 244–248. DOI: `https://doi.org/10.1016/j.physletb.2012.06.002`. arXiv: `1204.3583 [hep-ph]`.

[36] J. Blümlein and J. Brunner. “New exclusion limits for dark gauge forces from beam-dump data”. In: *Phys. Lett. B* 701 (2011), pp. 155–159. DOI: `https://doi.org/10.1016/j.physletb.2011.05.046`. arXiv: `1104.2747 [hep-ex]`.

[37] J. Blümlein and J. Brunner. “New exclusion limits on dark gauge forces from proton Bremsstrahlung in beam-dump data”. In: *Phys. Lett. B* 731 (2014), pp. 320–326. DOI: `https://doi.org/10.1016/j.physletb.2014.02.029`. arXiv: `1311.3870 [hep-ph]`.

[38] Y.-D. Tsai, P. deNiverville, and M. X. Liu. “Dark Photon and Muon $g-2$ Inspired Inelastic Dark Matter Models at the High-Energy Intensity Frontier”. In: *Phys. Rev. Lett.* 126 (2021), p. 181801. DOI: `10.1103/PhysRevLett.126.181801`.

[39] **BaBar Collaboration**, J. P. Lees et al. “Search for Invisible Decays of a Dark Photon Produced in e^+e^- Collisions at BaBar”. In: *Phys. Rev. Lett.* 119 (2017), p. 131804. DOI: `10.1103/PhysRevLett.119.131804`. arXiv: `1702.03327 [hep-ex]`.

[40] K. Akai, K. Furukawa, and H. Koiso. “SuperKEKB collider”. In: *Nucl. Instrum. Methods Phys. Res. A* 907 (2018), pp. 188–199. DOI: `10.1016/j.nima.2018.08.017`. arXiv: `1809.01958 [physics.acc-ph]`.

[41] T. Abe et al. *Belle II Technical Design Report.* 2010. DOI: `10.48550/arXiv.1011.0352`. arXiv: `1011.0352 [physics.ins-det]`.

[42] H. Aihara et al. *The Belle II Detector Upgrades Framework Conceptual Design Report.* 2024. DOI: `10.48550/arXiv.2406.19421`. arXiv: `2406.19421 [hep-ex]`.

[43] D. Zhou, K. Ohmi, Y. Funakoshi, and Y. Ohnishi. “Luminosity performance of SuperKEKB”. In: *J. Inst.* 19 (2024), T02002. DOI: `10.1088/1748-0221/19/02/T02002`. arXiv: `2306.02692 [physics.acc-ph]`.

[44] M. Bauer. “Measuring the Branching Fraction of $B \to \rho \ell \nu_\ell$ Decays with the Belle II Experiment”. PhD thesis. Karlsruher Institut für Technologie (KIT), 2023. 161 pp. DOI: `10.5445/IR/1000165627`.

[45] H. Ye et al. “Commissioning and performance of the Belle II pixel detector”. In: *Nucl. Instrum. Methods Phys. Res. A* 987 (2021), p. 164875. DOI: `10.1016/j.nima.2020.164875`.

[46] P. Ahlburg et al. “The new and complete Belle II DEPFET pixel detector: Commissioning and previous operational experience”. In: *Nucl. Instrum. Methods Phys. Res. A* 1068 (2024), p. 169763. DOI: `10.1016/j.nima.2024.169763`.

[47] K. Adamczyk et al. “The design, construction, operation and performance of the Belle II silicon vertex detector”. In: *J. Inst.* 17 (2022), P11042. DOI: `10.1088/1748-0221/17/11/P11042`. arXiv: `2201.09824 [physics.ins-det]`.

[48] N. Taniguchi. “Central Drift Chamber for Belle-II”. In: *J. Inst.* 12 (2017), p. C06014. DOI: `10.1088/1748-0221/12/06/C06014`.

[49] T. V. Dong et al. “Calibration and alignment of the Belle II central drift chamber”. In: *Nucl. Instrum. Methods Phys. Res. A* 930 (2019), pp. 132–141. DOI: `10.1016/j.nima.2019.03.072`.

[50] P. Križan. "Particle identification at Belle II". In: *J. Inst.* 9 (2014), p. C07018. DOI: `10.1088/1748-0221/9/07/C07018`.

[51] A. Kuzmin. "Electromagnetic calorimeter of Belle II". In: *Nucl. Instrum. Methods Phys. Res. A* 958 (2020). Proceedings of the Vienna Conference on Instrumentation 2019, p. 162235. DOI: `https://doi.org/10.1016/j.nima.2019.05.076`.

[52] E. Izaguirre, G. Krnjaic, P. Schuster, and N. Toro. "Analyzing the Discovery Potential for Light Dark Matter". In: *Phys. Rev. Lett.* 115 (2015), p. 251301. DOI: `10.1103/PhysRevLett.115.251301`.

[53] **The Belle II Collaboration**, I. Adachi et al. *Measurement of the integrated luminosity of data samples collected during 2019-2022 by the Belle II experiment.* 2024. arXiv: `2407.00965 [hep-ex]`.

[54] S. Agostinelli et al. "Geant4–a simulation toolkit". In: *Nucl. Instrum. Methods Phys. Res. A* 506 (2003), pp. 250–303. DOI: `https://doi.org/10.1016/S0168-9002(03)01368-8`.

[55] **Belle II Framework Software Group**, T. Kuhr et al. "The Belle II Core Software". In: *Comput. Softw. Big Sci.* 3 (2018), p. 1. DOI: `10.1007/s41781-018-0017-9`. arXiv: `1809.04299 [physics.comp-ph]`.

[56] The Belle II Collaboration. *Belle II Analysis Software Framework (basf2).* 2022. DOI: `10.5281/zenodo.5574115`.

[57] J. Alwall et al. "The automated computation of tree-level and next-to-leading order differential cross sections, and their matching to parton shower simulations". In: *J. High Energy Phys.* 07 (2014), p. 079. DOI: `10.1007/JHEP07(2014)079`. arXiv: `1405.0301 [hep-ph]`.

[58] D. J. Lange. "The EvtGen particle decay simulation package". In: *Nucl. Instrum. Methods Phys. Res. A* 462 (2001), pp. 152–155. DOI: `10.1016/S0168-9002(01)00089-4`.

[59] M. Fabbrichesi, E. Gabrielli, and G. Lanfranchi. "Phenomenology of the Massive Dark Photon". In: *The Physics of the Dark Photon: A Primer.* Ed. by M. Fabbrichesi, E. Gabrielli, and G. Lanfranchi. Cham: Springer International Publishing, 2021, pp. 47–67. DOI: `10.1007/978-3-030-62519-1_3`. arXiv: `2005.01515 [hep-ph]`.

[60] E. Kou et al. "The Belle II Physics Book". In: *Prog. Theor. Exp. Phys.* 2019 (2019), p. 123C01. DOI: `10.1093/ptep/ptz106`. arXiv: `1808.10567 [hep-ex]`.

[61] A. Natochii et al. "Measured and projected beam backgrounds in the Belle II experiment at the SuperKEKB collider". In: *Nucl. Instrum. Methods Phys. Res. A* 1055 (2023), p. 168550. DOI: `10.1016/j.nima.2023.168550`. arXiv: `2302.01566 [hep-ex]`.

[62] F. Berends, P. Daverveldt, and R. Kleiss. “Complete lowest-order calculations for four-lepton final states in electron-positron collisions”. In: *Nucl. Phys. B* 253 (1985), pp. 441–463. DOI: `10.1016/0550-3213(85)90541-3`.

[63] N. Davidson et al. “Universal interface of TAUOLA: Technical and physics documentation”. In: *Comput. Phys. Commun.* 183 (2012), pp. 821–843. DOI: `10.1016/j.cpc.2011.12.009`. arXiv: `1002.0543 [hep-ph]`.

[64] S. Uehara. *TREPS: A Monte-Carlo Event Generator for Two-photon Processes at e^+e^- Colliders using an Equivalent Photon Approximation.* 2013. arXiv: `1310.0157 [hep-ph]`.

[65] S. Jadach et al. “The Monte Carlo program KoralW version 1.51 and the concurrent Monte Carlo KoralW&YFSWW3 with all background graphs and first-order corrections to W-pair production”. In: *Comput. Phys. Commun.* 140 (2001), pp. 475–512. DOI: `10.1016/S0010-4655(01)00296-X`. arXiv: `hep-ph/0104049 [hep-ph]`.

[66] G. Balossini et al. “Photon pair production at flavour factories with per mille accuracy”. In: *Phys. Lett. B* 663 (2008), pp. 209–213. DOI: `10.1016/j.physletb.2008.04.007`. arXiv: `0801.3360 [hep-ph]`.

[67] C. M. Carloni Calame et al. “NNLO massive corrections to Bhabha scattering and theoretical precision of BabaYaga@NLO”. In: *Nucl. Phys. B* 225–227 (2012), pp. 293–297. DOI: `10.1016/j.nuclphysbps.2012.02.061`. arXiv: `1112.2851 [hep-ph]`.

[68] S. Jadach, B. F. L. Ward, and Z. Wąs. “The precision Monte Carlo event generator KK for two-fermion final states in $\mathrm{e}^+\mathrm{e}^-$ collisions”. In: *Comput. Phys. Commun.* 130 (2000), pp. 260–325. DOI: `10.1016/S0010-4655(00)00048-5`. arXiv: `hep-ph/9912214 [hep-ph]`.

[69] T. Sjöstrand et al. “An introduction to PYTHIA 8.2”. In: *Comput. Phys. Commun.* 191 (2015), pp. 159–177. DOI: `10.1016/j.cpc.2015.01.024`. arXiv: `1410.3012 [hep-ph]`.

[70] H. CzyŻ, M. Gunia, and J. H. Kühn. “Simulation of electron-positron annihilation into hadrons with the event generator PHOKHARA”. In: *J. High Energy Phys.* 08 (2013), p. 110. DOI: `10.1007/JHEP08(2013)110`. arXiv: `1306.1985 [hep-ph]`.

[71] G. Punzi. *Sensitivity of searches for new signals and its optimization.* 2003. DOI: `10.48550/arXiv.physics/0308063`. arXiv: `physics/0308063 [physics.data-an]`.

[72] **Belle II Tracking Group**, V. Bertacchi et al. “Track Finding at Belle II”. In: *Comput. Phys. Commun.* 259 (2021), p. 107610. DOI: `10.1016/j.cpc.2020.107610`. arXiv: `2003.12466 [physics.ins-det]`.

[73] Jojosito et al. *GenFit/GenFit.* Zenodo. 2023. DOI: `10.5281/zenodo.10301439`.

[74] J.-F. Krohn et al. “Global decay chain vertex fitting at Belle II”. In: *Nucl. Instrum. Methods Phys. Res. A* 976 (2020), p. 164269. DOI: `10.1016/j.nima.2020.164269`. arXiv: `1901.11198 [hep-ex]`.

[75] J. Eschle, A. Puig Navarro, R. Silva Coutinho, and N. Serra. “zfit: Scalable pythonic fitting”. In: *SoftwareX* 11 (2020), p. 100508. DOI: `10.1016/j.softx.2020.100508`. arXiv: `1910.13429 [physics.data-an]`.

[76] J. E. Gaiser. “Charmonium Spectroscopy From Radiative Decays of the J/ψ and ψ'”. PhD thesis. Stanford University, 1982.

[77] T. Skwarnicki. “A study of the radiative CASCADE transitions between the Upsilon-Prime and Upsilon resonances”. PhD thesis. Cracow, INP, 1986.

[78] G. de Marino and G. Casarosa. *K_S^0 efficiency calibration on Run1 data vs MC15.* Internal Note. 2023. URL: `https://docs.belle2.org/record/4020`.

[79] Q.-D. Zhou. *Correction for tracking momentum bias based on invariant mass peak studies.* Internal Note. 2020. URL: `https://docs.belle2.org/record/1947`.

[80] **Belle II Collaboration**, I. Adachi et al. “Measurement of the τ -lepton mass with the Belle II experiment”. In: *Phys. Rev. D* 108 (2023), p. 032006. DOI: `10.1103/PhysRevD.108.032006`. arXiv: `2305.19116 [hep-ex]`.

[81] A. Caldwell, D. Kollár, and K. Kröninger. “BAT – The Bayesian analysis toolkit”. In: *Comput. Phys. Commun.* 180 (2009), pp. 2197–2209. DOI: `10.1016/j.cpc.2009.06.026`. arXiv: `0808.2552 [physics.data-an]`.

[82] G. Cowan. *Statistical data analysis.* Oxford University Press, 1998. DOI: `10.1093/oso/9780198501565.001.0001`.

[83] G. Cowan, K. Cranmer, E. Gross, and O. Vitells. “Asymptotic formulae for likelihood-based tests of new physics”. In: *Eur. Phys. J. C* 71 (2011), p. 1554. DOI: `10.1140/epjc/s10052-011-1554-0`. arXiv: `1007.1727 [physics.data-an]`.

[84] G. Schott. “Hypothesis Testing”. In: *Data Analysis in High Energy Physics.* John Wiley & Sons, Ltd, 2013. Chap. 3, pp. 75–105. DOI: `10.1002/9783527653416.ch3`.

[85] E. Gross and O. Vitells. “Trial factors for the look elsewhere effect in high energy physics”. In: *Eur. Phys. J.* 70 (2010), pp. 525–530. DOI: `10.1140/epjc/s10052-010-1470-8`.

[86] E. Bernreuther et al. “Forecasting dark showers at Belle II”. In: *J. High Energy Phys.* 2022 (2022), p. 5. DOI: `10.1007/JHEP12(2022)005`. arXiv: `2203.08824 [hep-ph]`.

[87] E. Schmidt. “Developing a Displaced Vertex Trigger for Dark Matter Searches at the Belle II Experiment”. MA thesis. Max-Planck-Institute for Physics, 2023. URL: `https://docs.belle2.org/record/3620` Access date: 2024-09-02.

Appendices

Appendix A

Model Parameter Configurations

In Tables A.1 and A.2 I present the model parameter configurations for which simulated samples have been produced. The configurations are divided as they are used for the scans in the $m(\mathrm{h}')$–θ-plane or $m(\chi_1)$–ϵ-plane.

The parameter configurations are chosen to cover a large variety of different scenarios where Belle II is sensitive.

Table A.1: Model parameter variations used for the scans in the $m(\mathrm{h}')$–θ-plane. Equal parameter values share the same colour for better visualisation.

α_D	$m(\chi_1)$	Δm	$c\tau(\chi_2)$	$m(\mathrm{A}')$
0.1	$2.5\,\mathrm{GeV/c^2}$	$0.4\,m(\chi_1)$	0.1 cm	$3\,m(\chi_1)$
0.1	$2.5\,\mathrm{GeV/c^2}$	$0.4\,m(\chi_1)$	0.01 cm	$3\,m(\chi_1)$
0.1	$2.5\,\mathrm{GeV/c^2}$	$0.4\,m(\chi_1)$	1.0 cm	$3\,m(\chi_1)$
0.1	$2.5\,\mathrm{GeV/c^2}$	$0.4\,m(\chi_1)$	100.0 cm	$3\,m(\chi_1)$
0.1	$2.5\,\mathrm{GeV/c^2}$	$0.4\,m(\chi_1)$	0.1 cm	$4\,m(\chi_1)$
0.1	$2.5\,\mathrm{GeV/c^2}$	$0.4\,m(\chi_1)$	1.0 cm	$4\,m(\chi_1)$
0.1	$1.25\,\mathrm{GeV/c^2}$	$0.4\,m(\chi_1)$	0.1 cm	$3\,m(\chi_1)$
0.1	$2.5\,\mathrm{GeV/c^2}$	$0.2\,m(\chi_1)$	0.1 cm	$3\,m(\chi_1)$
0.1	$2.5\,\mathrm{GeV/c^2}$	$0.2\,m(\chi_1)$	0.01 cm	$3\,m(\chi_1)$
0.1	$2.5\,\mathrm{GeV/c^2}$	$0.2\,m(\chi_1)$	1.0 cm	$3\,m(\chi_1)$
0.1	$2.5\,\mathrm{GeV/c^2}$	$0.2\,m(\chi_1)$	100.0 cm	$3\,m(\chi_1)$
0.1	$2.5\,\mathrm{GeV/c^2}$	$0.2\,m(\chi_1)$	0.1 cm	$4\,m(\chi_1)$
0.1	$2.5\,\mathrm{GeV/c^2}$	$0.2\,m(\chi_1)$	1.0 cm	$4\,m(\chi_1)$
0.1	$2.5\,\mathrm{GeV/c^2}$	$1.0\,m(\chi_1)$	0.1 cm	$3\,m(\chi_1)$
0.1	$2.5\,\mathrm{GeV/c^2}$	$1.0\,m(\chi_1)$	0.01 cm	$3\,m(\chi_1)$
0.1	$2.5\,\mathrm{GeV/c^2}$	$1.0\,m(\chi_1)$	1.0 cm	$3\,m(\chi_1)$
0.1	$2.5\,\mathrm{GeV/c^2}$	$1.0\,m(\chi_1)$	100.0 cm	$3\,m(\chi_1)$
0.1	$2.5\,\mathrm{GeV/c^2}$	$1.0\,m(\chi_1)$	0.1 cm	$4\,m(\chi_1)$
0.1	$2.5\,\mathrm{GeV/c^2}$	$1.0\,m(\chi_1)$	1.0 cm	$4\,m(\chi_1)$
0.1	$1.25\,\mathrm{GeV/c^2}$	$1.0\,m(\chi_1)$	0.1 cm	$3\,m(\chi_1)$
0.5	$2.5\,\mathrm{GeV/c^2}$	$0.4\,m(\chi_1)$	0.01 cm	$3\,m(\chi_1)$
0.5	$2.5\,\mathrm{GeV/c^2}$	$0.4\,m(\chi_1)$	1.0 cm	$3\,m(\chi_1)$
0.5	$2.5\,\mathrm{GeV/c^2}$	$0.2\,m(\chi_1)$	0.01 cm	$3\,m(\chi_1)$
0.5	$2.5\,\mathrm{GeV/c^2}$	$0.2\,m(\chi_1)$	1.0 cm	$3\,m(\chi_1)$
0.5	$2.5\,\mathrm{GeV/c^2}$	$1.0\,m(\chi_1)$	0.01 cm	$3\,m(\chi_1)$
0.5	$2.5\,\mathrm{GeV/c^2}$	$1.0\,m(\chi_1)$	1.0 cm	$3\,m(\chi_1)$

Table A.2: Model parameter variations used for the scans in the $m(\chi_1)$–ϵ-plane ($m(\chi_1)$–y-plane). Equal parameter values share the same colour for better visualisation.

α_D	$m(\mathrm{h}')$	$c\tau(\mathrm{h}')$	Δm	$m(\mathrm{A}')$
0.1	$0.4\,\mathrm{GeV/c^2}$	$21.54\,\mathrm{cm}$	$0.4\,m(\chi_1)$	$3\,m(\chi_1)$
0.1	$0.4\,\mathrm{GeV/c^2}$	$21.54\,\mathrm{cm}$	$0.4\,m(\chi_1)$	$4\,m(\chi_1)$
0.1	$0.6\,\mathrm{GeV/c^2}$	$21.54\,\mathrm{cm}$	$0.4\,m(\chi_1)$	$3\,m(\chi_1)$
0.1	$0.6\,\mathrm{GeV/c^2}$	$1.0\,\mathrm{cm}$	$0.4\,m(\chi_1)$	$3\,m(\chi_1)$
0.1	$1.2\,\mathrm{GeV/c^2}$	$21.54\,\mathrm{cm}$	$0.4\,m(\chi_1)$	$3\,m(\chi_1)$
0.1	$0.6\,\mathrm{GeV/c^2}$	$21.54\,\mathrm{cm}$	$0.2\,m(\chi_1)$	$3\,m(\chi_1)$
0.1	$0.6\,\mathrm{GeV/c^2}$	$1.0\,\mathrm{cm}$	$0.2\,m(\chi_1)$	$3\,m(\chi_1)$
0.1	$1.2\,\mathrm{GeV/c^2}$	$21.54\,\mathrm{cm}$	$0.2\,m(\chi_1)$	$3\,m(\chi_1)$

Appendix B

Additional Signal and Background Distributions

In this part of the appendix I present additional signal and SM background distributions of the variables used in the selection. This includes the distributions for the final states that are not already covered in the main part of the thesis.

Fig. B.1 shows the vertex fit probability of the reconstructed χ_2 candidate. The opening angle between the two electrons used to reconstruct the χ_2 vertex for the $\mathrm{e}^+\mathrm{e}^- \to \mathrm{h}'(\to \pi^+\pi^-)\chi_1\chi_2(\to \chi_1\mathrm{e}^+\mathrm{e}^-)$ and $\mathrm{e}^+\mathrm{e}^- \to \mathrm{h}'(\to \mathrm{K}^+\mathrm{K}^-)\chi_1\chi_2(\to \chi_1\mathrm{e}^+\mathrm{e}^-)$ final state is shown in Figs. B.2 and B.3, respectively. The corresponding background distributions are also shown there. The radial vertex position of reconstructed pair conversion processes is shown in Fig. B.4. Figs. B.5 and B.6 show the angle between the h' daughter tracks in the $\mathrm{e}^+\mathrm{e}^- \to \mathrm{h}'(\to \mu^+\mu^-)\chi_1\chi_2(\to \chi_1\mathrm{e}^+\mathrm{e}^-)$ and $\mathrm{e}^+\mathrm{e}^- \to \mathrm{h}'(\to \pi^+\pi^-)\chi_1\chi_2(\to \chi_1\mathrm{e}^+\mathrm{e}^-)$ final state, for both signal and SM background. The signal and background distributions of the pointing angle in the $\mathrm{h}' \to \mu^+\mu^-$ reconstruction channel is shown in Fig. B.7 and the $\mathrm{h}' \to \mathrm{K}^+\mathrm{K}^-$ reconstruction channel is shown in Fig. B.8. Figs. B.9 and B.10 show the missing energy in the $\mathrm{h}' \to \pi^+\pi^-$ and $\mathrm{h}' \to \mathrm{K}^+\mathrm{K}^-$ reconstruction channel, respectively. Furthermore, Figs. B.11 and B.12 show the reconstructed mass of the $\mathrm{e}^+\mathrm{e}^-$pair that forms the χ_2 candidate in the $\mathrm{h}' \to \mu^+\mu^-$ and $\mathrm{h}' \to \mathrm{K}^+\mathrm{K}^-$ reconstruction channel. The ROE distributions of the final states not included in the main part are shown in Figs. B.13 to B.16. Additionally, Figs. B.17 and B.18 show the average event multiplicity after applying all selections for the $\mathrm{e}^+\mathrm{e}^- \to \mathrm{h}'(\to \pi^+\pi^-)\chi_1\chi_2(\to \chi_1\mathrm{e}^+\mathrm{e}^-)$ and $\mathrm{e}^+\mathrm{e}^- \to \mathrm{h}'(\to \mathrm{K}^+\mathrm{K}^-)\chi_1\chi_2(\to \chi_1\mathrm{e}^+\mathrm{e}^-)$ signal process. Lastly, Figs. B.19 and B.20 show the efficiency of the BCS in these two final states.

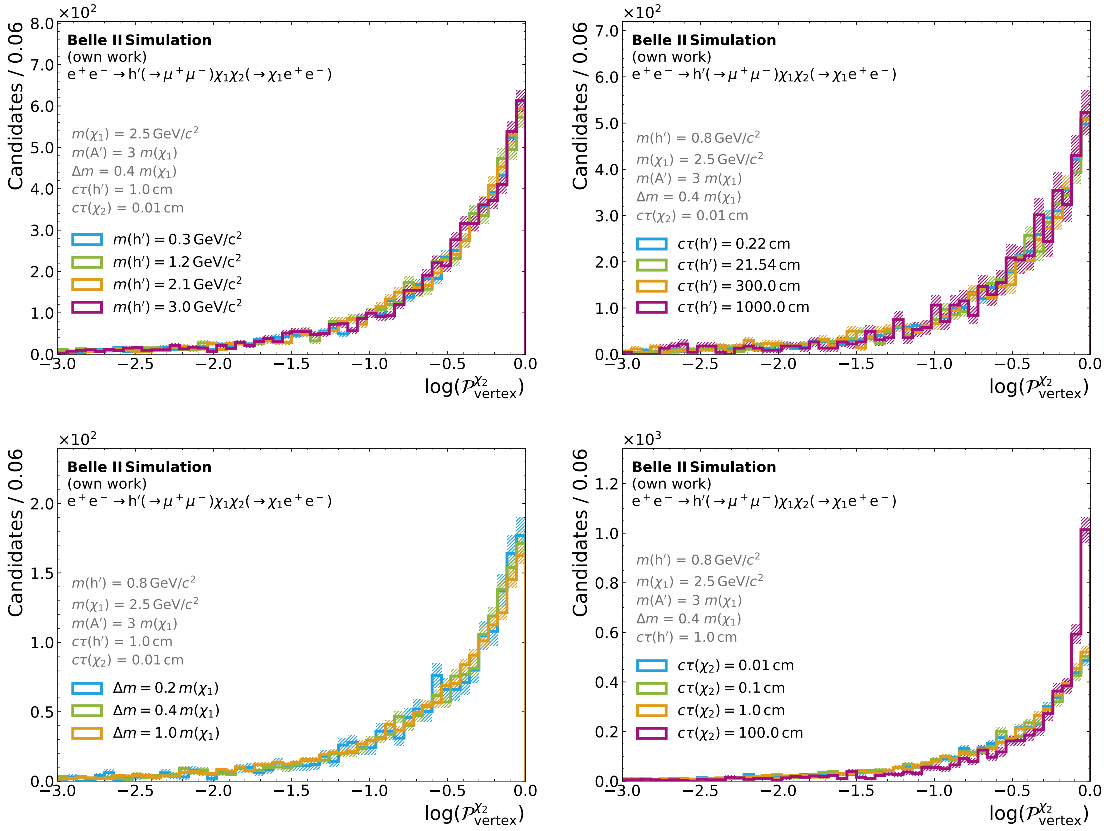

Figure B.1: Signal distributions of vertex fit probability $\mathcal{P}_{\text{vertex}}$ of the χ_2 vertex for the $\mathrm{e}^+\mathrm{e}^- \to \mathrm{h}'(\to \mu^+\mu^-)\chi_1\chi_2(\to \chi_1\mathrm{e}^+\mathrm{e}^-)$ signal process. For better visualisation the vertex fit probability is shown on a logarithmic scale. The distributions are shown for different variations of the model parameters, h' mass (upper left), h' lifetime (upper right), mass splitting Δm(lower left), and χ_2 lifetime (lower right).

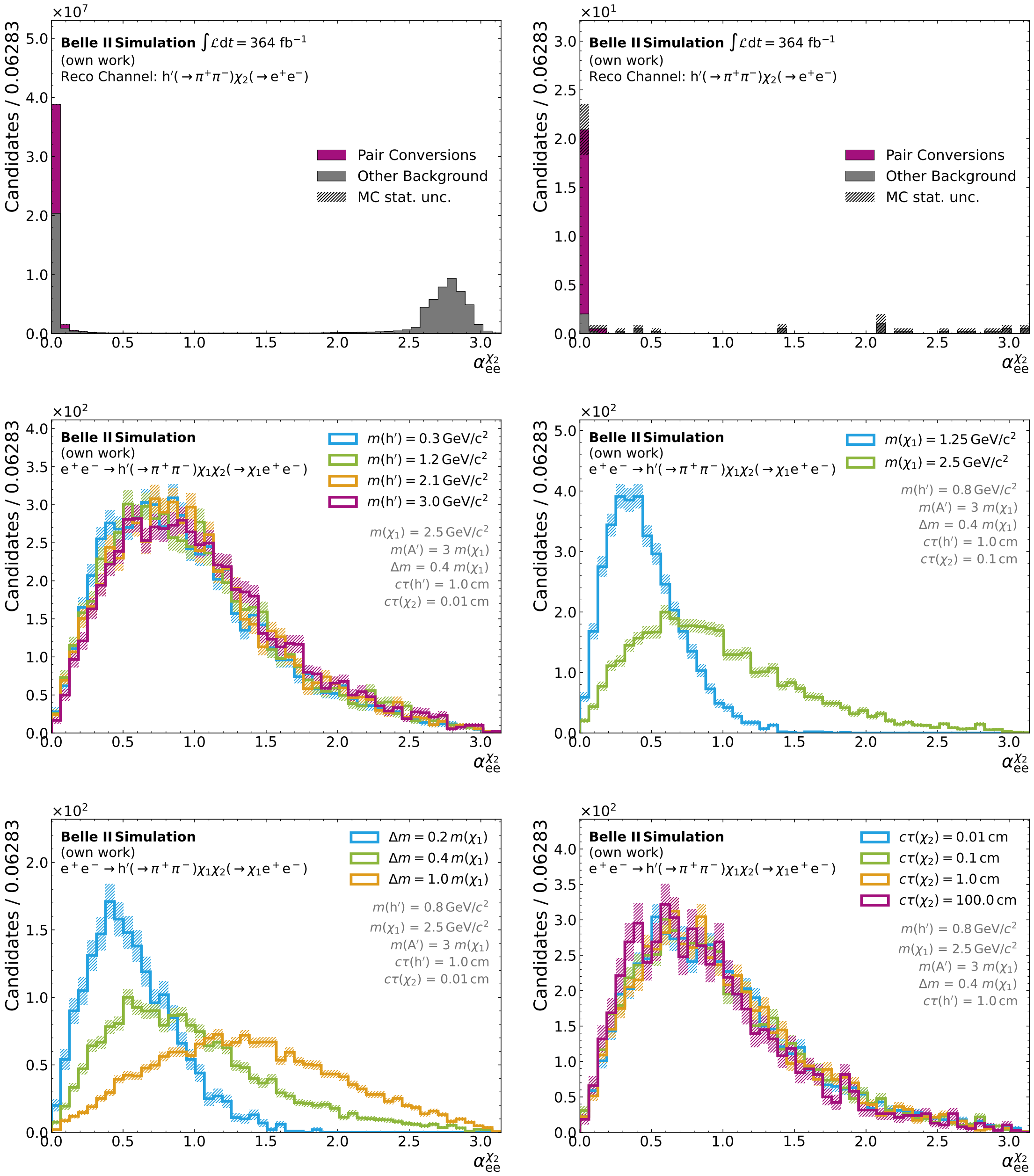

Figure B.2: Background (top) and signal (center and bottom) distributions of the opening angle between the two reconstructed electrons of the χ_2 candidate. For the signal the plots show only the $\mathrm{e}^+\mathrm{e}^- \to \mathrm{h}'(\to \pi^+\pi^-)\chi_1\chi_2(\to \chi_1\mathrm{e}^+\mathrm{e}^-)$ final state in the corresponding $\mathrm{h}' \to \pi^+\pi^-$ reconstruction channel. The background distributions are also only shown in this reconstruction channel. Contributions from truth-matched pair conversions are shown in purple, while the other contributions are shown in grey. The upper left plot shows the background composition with a minimal set of selections applied, while in the right plot all selections from Tables 6.1 and 6.2 besides the opening angle requirement are applied. For signal the plots show different variations of the model parameters: h' mass (center left), $m(\chi_1)$ (center right), mass splitting (lower left), and χ_2 lifetime (lower right).

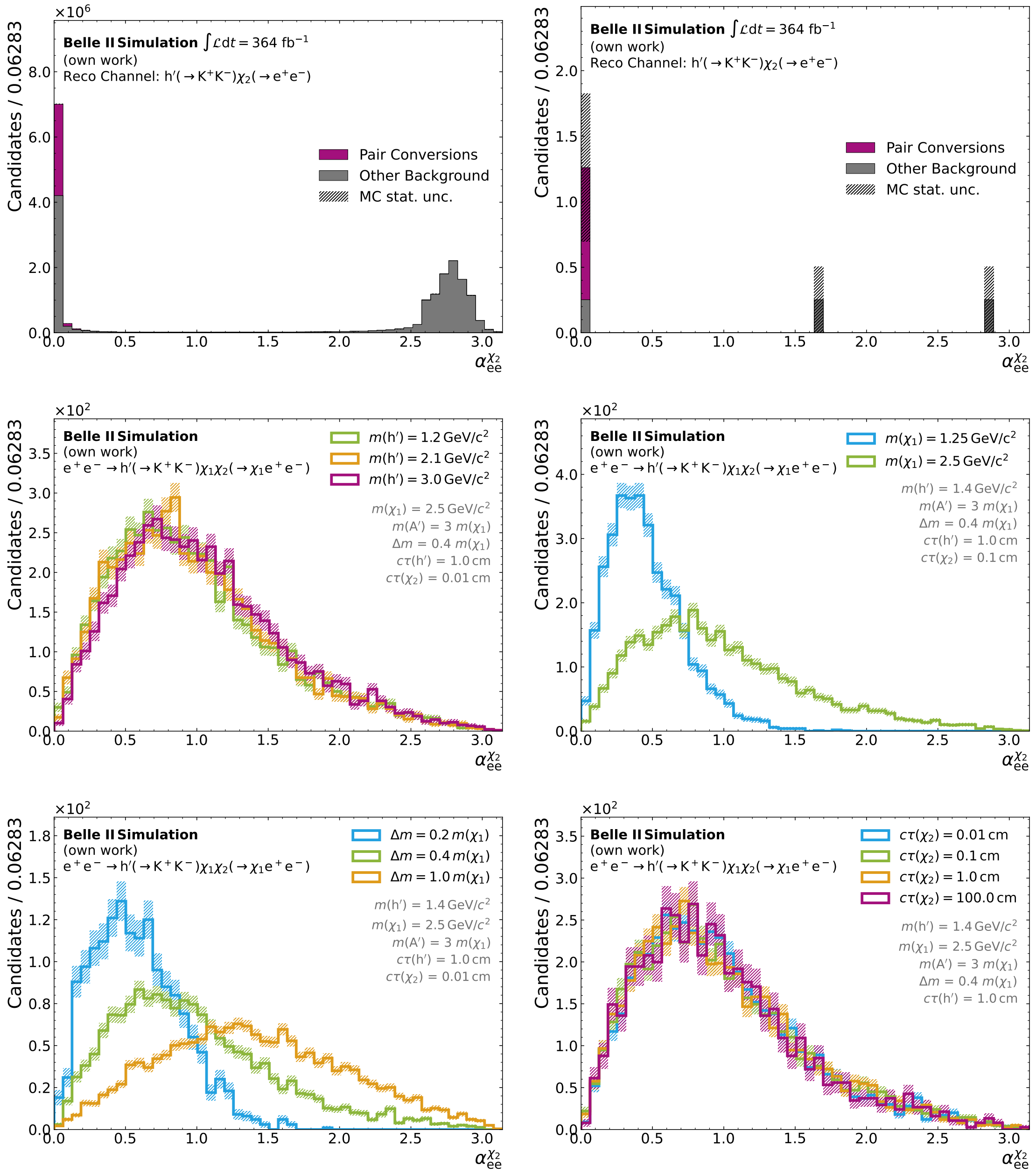

Figure B.3: Background (top) and signal (center and bottom) distributions of the opening angle between the two reconstructed electrons of the χ_2 candidate. For the signal the plots show only the $e^+e^- \to h'(\to K^+K^-)\chi_1\chi_2(\to \chi_1 e^+e^-)$ final state in the corresponding $h' \to K^+K^-$ reconstruction channel. The background distributions are also only shown in this reconstruction channel. Contributions from truth-matched pair conversions are shown in purple, while the other contributions are shown in grey. The upper left plot shows the background composition with a minimal set of selections applied, while in the right plot all selections from Tables 6.1 and 6.2 besides the opening angle requirement are applied. For signal the plots show different variations of the model parameters: h' mass (center left), $m(\chi_1)$ (center right), mass splitting (lower left), and χ_2 lifetime (lower right).

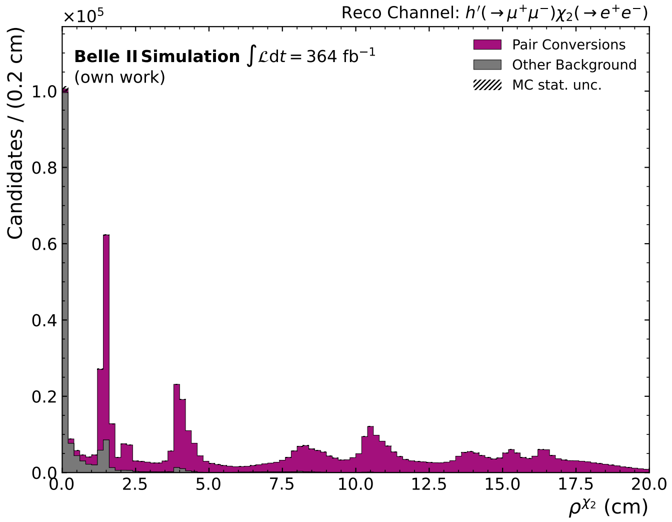

Figure B.4: Distribution of the radial vertex position of the reconstructed χ_2 vertex on simlated SM background samples. The contributions from pair conversions are marked in purple. The plot shows the $h' \to \mu^+\mu^-$ reconstruction channel as an example as the situation is the same for the other two reconstruction channels.

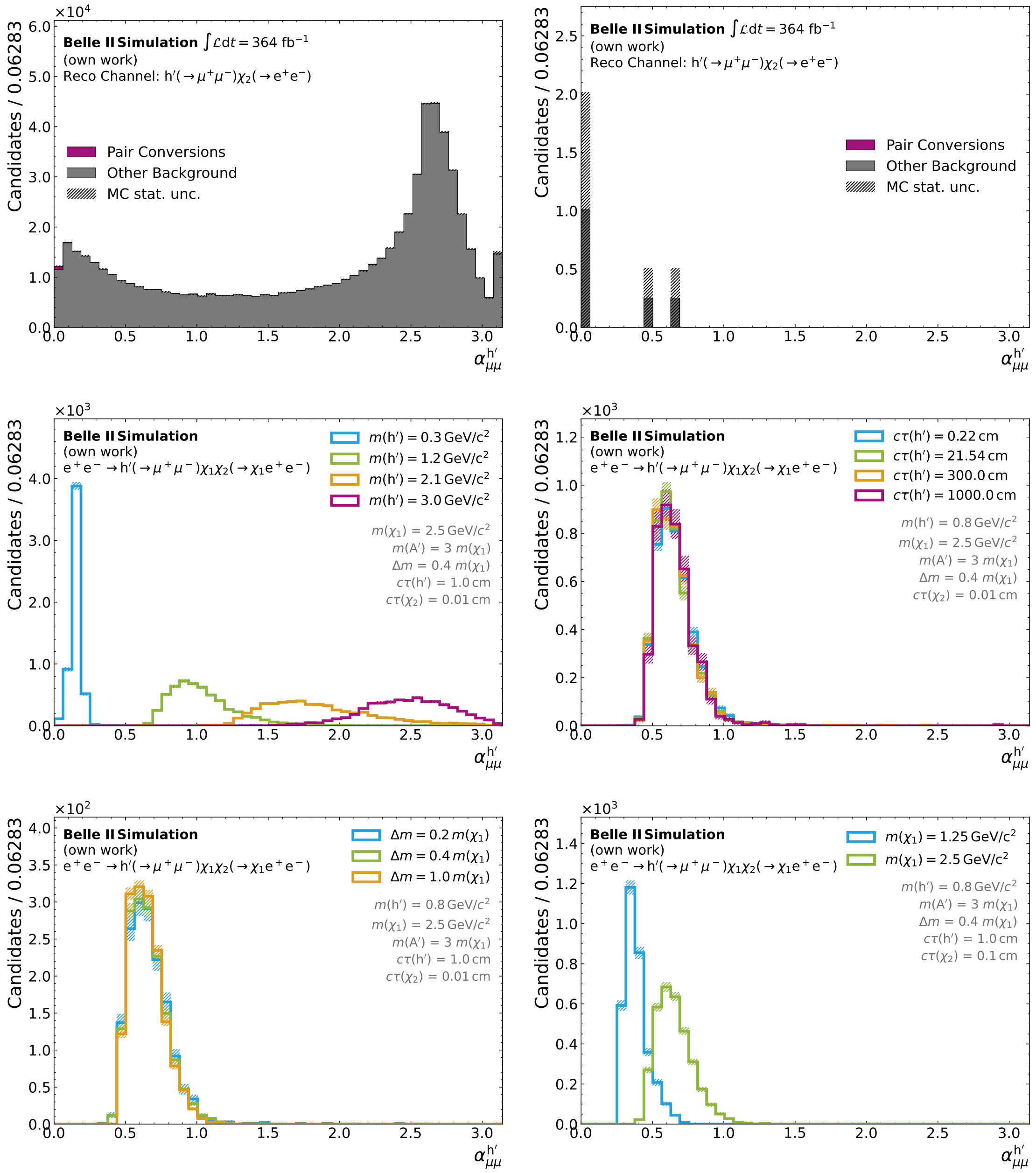

Figure B.5: Background (top) and signal (center and bottom) distributions of the opening angle between the two reconstructed muons of the h' candidate. For the signal the plots show only the $e^+e^- \to h'(\to \mu^+\mu^-)\chi_1\chi_2(\to \chi_1 e^+e^-)$ final state in the corresponding $h' \to \mu^+\mu^-$ reconstruction channel. The background distributions are also only shown in this reconstruction channel. Contributions from truth-matched pair conversions are shown in purple, while the other contributions are shown in grey. The upper left plot shows the background composition with a minimal set of selections applied, while in the right plot all selections from Tables 6.1 and 6.2 besides the opening angle requirement are applied. For signal the plots show different variations of the model parameters: h' mass (center left), h' lifetime (center right), mass splitting (lower left), and $m(\chi_1)$ (lower right).

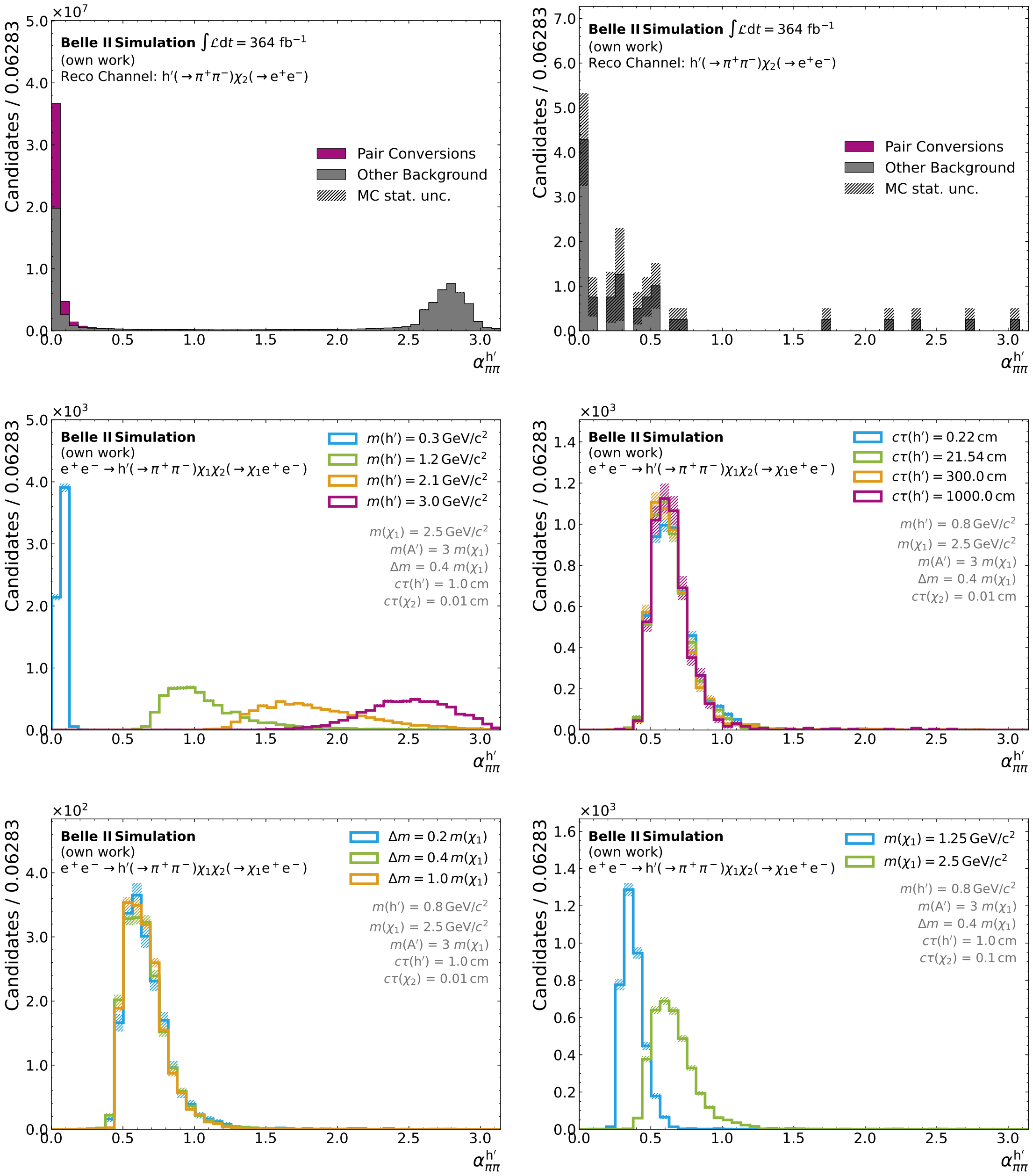

Figure B.6: Background (top) and signal (center and bottom) distributions of the opening angle between the two reconstructed kaons of the h$'$ candidate. For the signal the plots show only the $e^+e^- \to h'(\to \pi^+\pi^-)\chi_1\chi_2(\to \chi_1 e^+e^-)$ final state in the corresponding $h' \to \pi^+\pi^-$ reconstruction channel. The background distributions are also only shown in this reconstruction channel. Contributions from truth-matched pair conversions are shown in purple, while the other contributions are shown in grey. The upper left plot shows the background composition with a minimal set of selections applied, while in the right plot all selections from Tables 6.1 and 6.2 besides the opening angle requirement are applied. For signal the plots show different variations of the model parameters: h$'$ mass (center left), h$'$ lifetime (center right), mass splitting (lower left), and $m(\chi_1)$ (lower right).

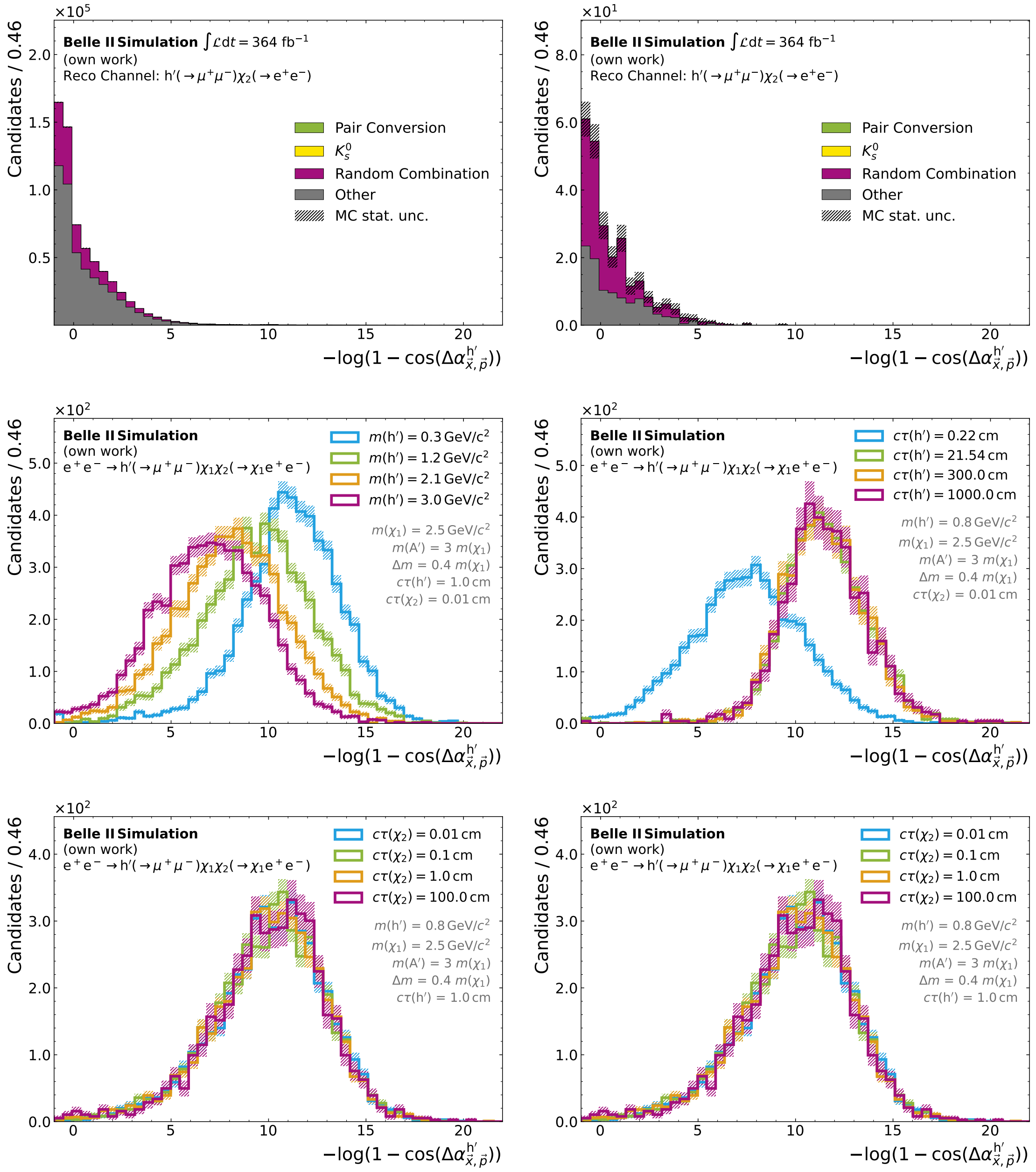

Figure B.7: Background (top) and signal (center and bottom) distributions of the pointing angle $-\log(1-\cos(\Delta\alpha^{\mathrm{h}'}_{\mathbf{x},\mathbf{p}}))$ between momentum and vertex vector of the h' candidate. For the signal the plots show only the $\mathrm{e}^+\mathrm{e}^- \to \mathrm{h}'(\to \mu^+\mu^-)\chi_1\chi_2(\to \chi_1\mathrm{e}^+\mathrm{e}^-)$ final state in the corresponding $\mathrm{h}' \to \mu^+\mu^-$ reconstruction channel. The background distributions are also only shown in this reconstruction channel. Contributions from random track combinations are shown in purple, truth-matched pair conversions in lightgreen and K^0_S decays in yellow, while the other contributions are shown in grey. The upper left plot shows the background composition with a minimal set of selections applied, while in the right plot all selections from Tables 6.1 and 6.2 besides the pointing angle requirement are applied. For signal the plots show different variations of the model parameters: h' mass (center left), h' lifetime (center right), mass splitting (lower left), and χ_2 lifetime (lower right).

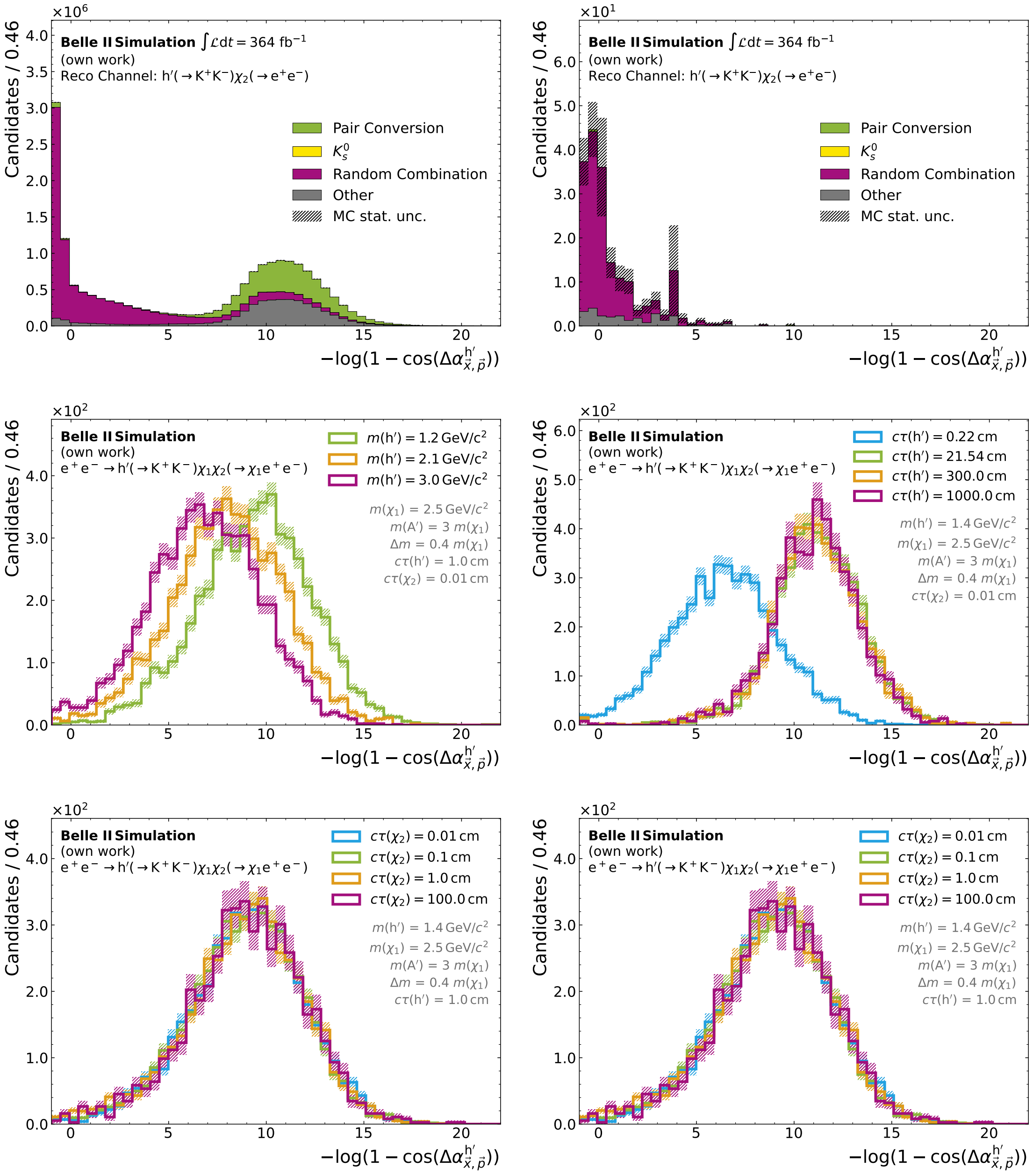

Figure B.8: Background (top) and signal (center and bottom) distributions of the pointing angle $-\log(1-\cos(\Delta\alpha^{h'}_{\mathbf{x},\mathbf{p}}))$ between momentum and vertex vector of the h' candidate. For the signal the plots show only the $e^+e^- \rightarrow h'(\rightarrow K^+K^-)\chi_1\chi_2(\rightarrow \chi_1 e^+e^-)$ final state in the corresponding $h' \rightarrow K^+K^-$ reconstruction channel. The background distributions are also only shown in this reconstruction channel. Contributions from random track combinations are shown in purple, truth-matched pair conversions in lightgreen and K^0_S decays in yellow, while the other contributions are shown in grey. The upper left plot shows the background composition with a minimal set of selections applied, while in the right plot all selections from Tables 6.1 and 6.2 besides the pointing angle requirement are applied. For signal the plots show different variations of the model parameters: h' mass (center left), h' lifetime (center right), mass splitting (lower left), and χ_2 lifetime (lower right).

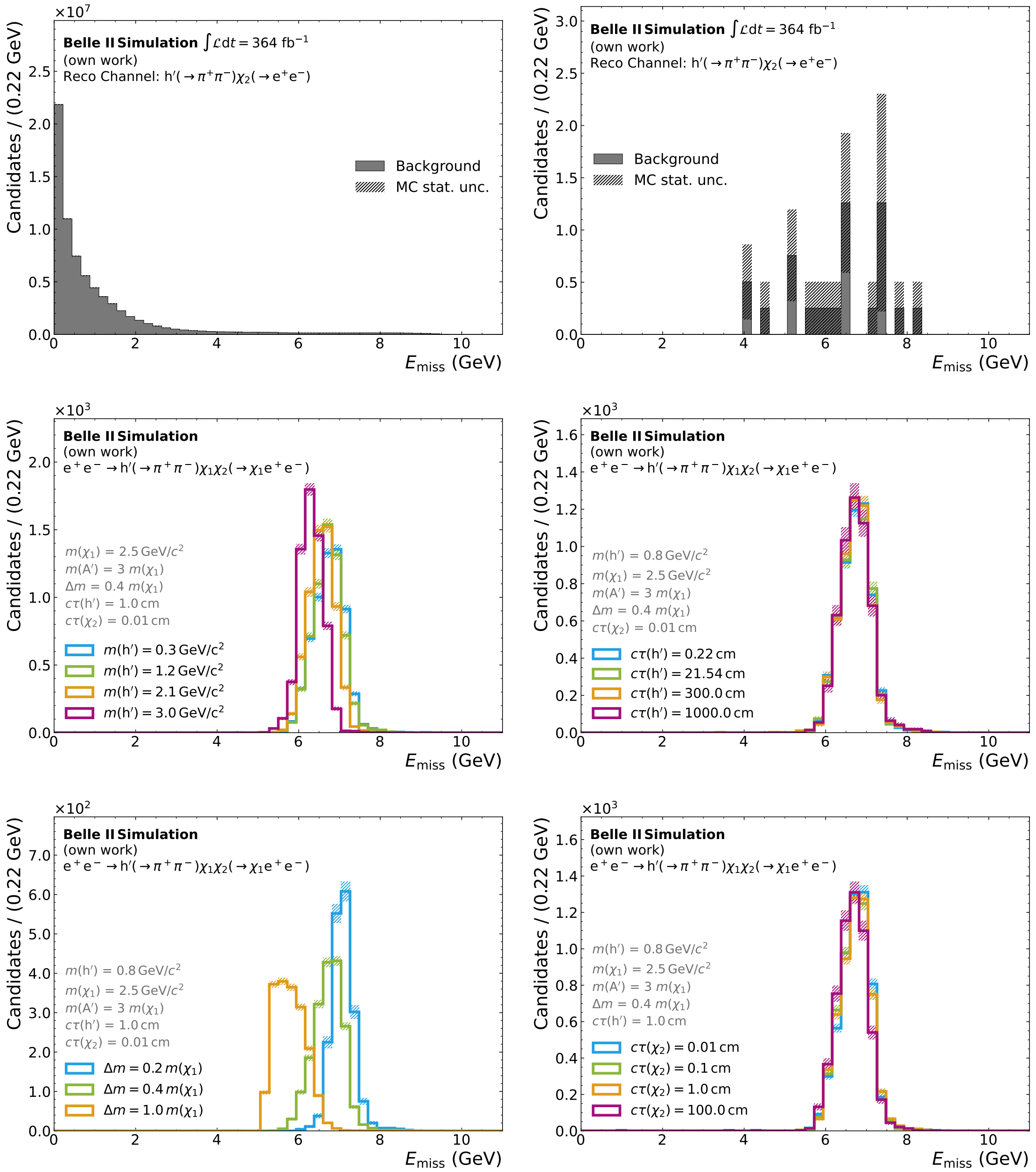

Figure B.9: Background (top) and signal (center and bottom) distributions of the missing energy E_{miss} in the event. For the signal the plots show only the $e^+e^- \to h'(\to \pi^+\pi^-)\chi_1\chi_2(\to \chi_1 e^+e^-)$ final state in the corresponding $h' \to \pi^+\pi^-$ reconstruction channel. The background distributions are also only shown in this reconstruction channel. The upper left plot shows the background composition with a minimal set of selections applied, while in the right plot all selections from Tables 6.1 and 6.2 besides the E_{miss} requirement are applied. For signal the plots show different variations of the model parameters: h' mass (center left), h' lifetime (center right), mass splitting (lower left), and χ_2 lifetime (lower right).

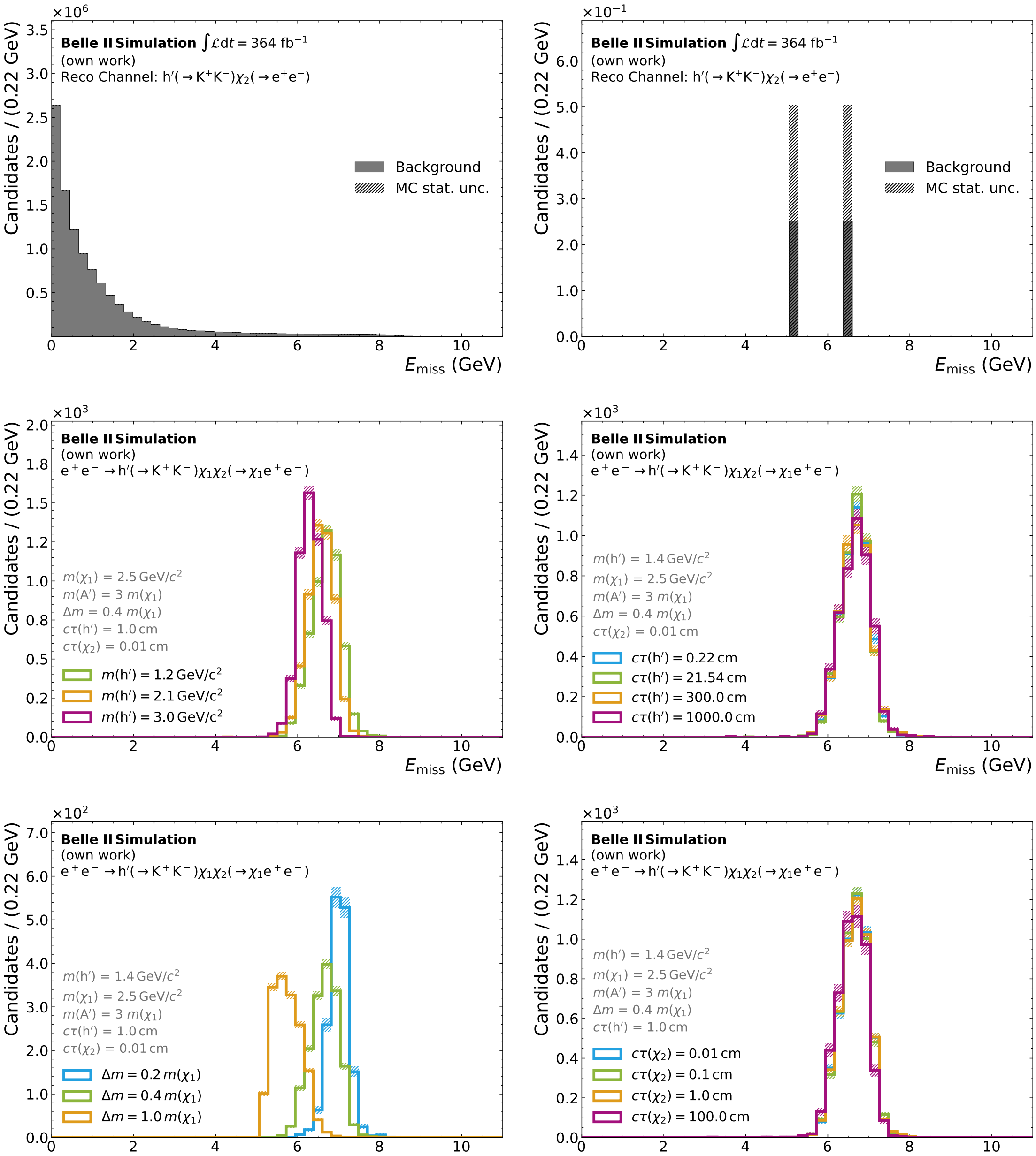

Figure B.10: Background (top) and signal (center and bottom) distributions of the missing energy E_{miss} in the event. For the signal the plots show only the $e^+e^- \rightarrow h'(\rightarrow K^+K^-)\chi_1\chi_2(\rightarrow \chi_1 e^+e^-)$ final state in the corresponding $h' \rightarrow K^+K^-$ reconstruction channel. The background distributions are also only shown in this reconstruction channel. The upper left plot shows the background composition with a minimal set of selections applied, while in the right plot all selections from Tables 6.1 and 6.2 besides the E_{miss} requirement are applied. For signal the plots show different variations of the model parameters: h' mass (center left), h' lifetime (center right), mass splitting (lower left), and χ_2 lifetime (lower right).

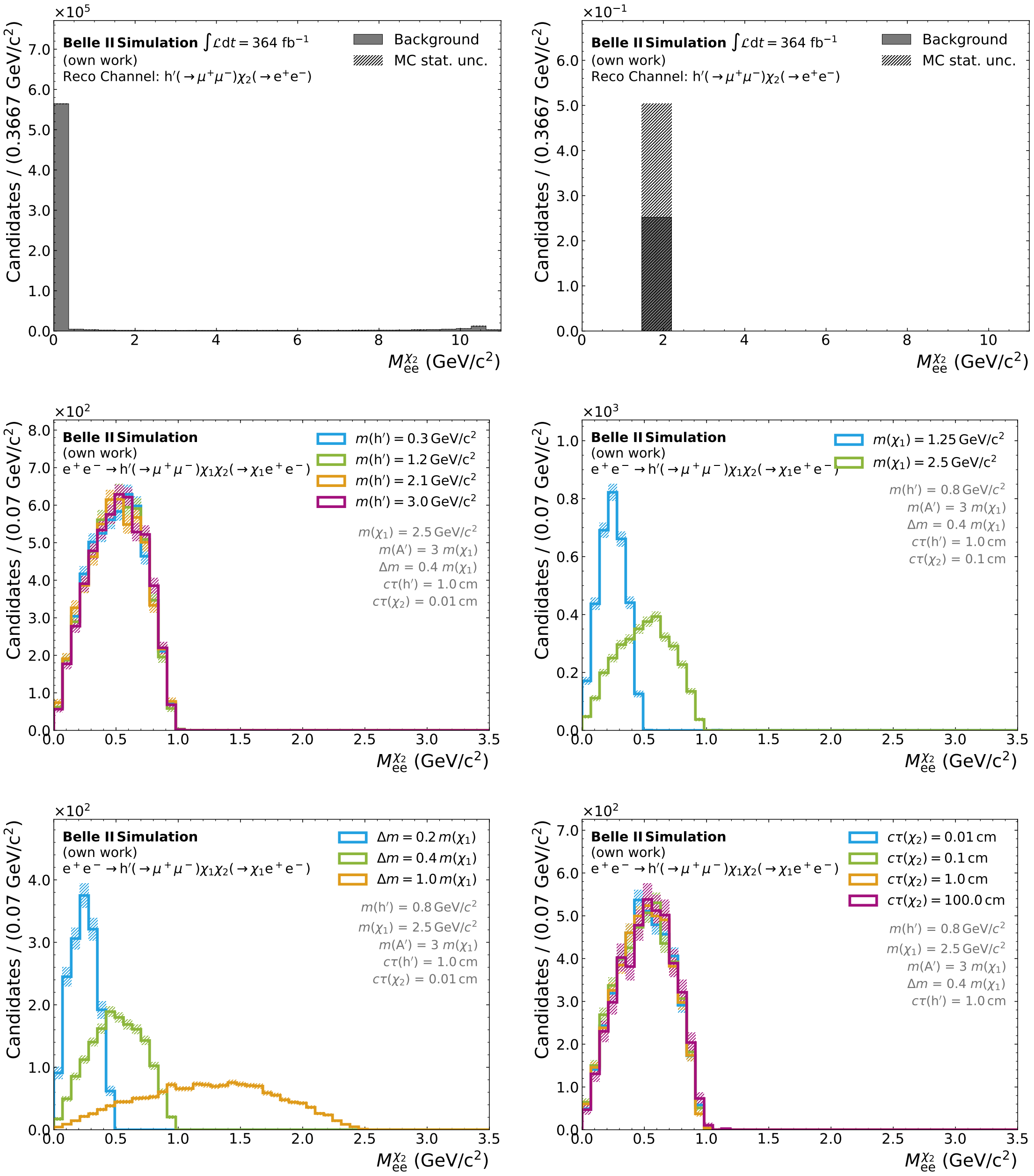

Figure B.11: Background (top) and signal (center and bottom) distributions of the reconstructed mass that forms the χ_2 candidate. For the signal, the plots show only the $e^+e^- \rightarrow h'(\rightarrow \mu^+\mu^-)\chi_1\chi_2(\rightarrow \chi_1 e^+e^-)$ final state in the corresponding $h' \rightarrow \mu^+\mu^-$ reconstruction channel. The background distributions are also only shown in this reconstruction channel. The upper left plot shows the background composition with a minimal set of selections applied, while in the right plot all selections from Tables 6.1 and 6.2 besides the $M_{ee}^{\chi_2}$ requirement are applied. For signal the plots show different variations of the model parameters: h′ mass (center left), χ_1 mass (center right), mass splitting (lower left), and χ_2 lifetime (lower right).

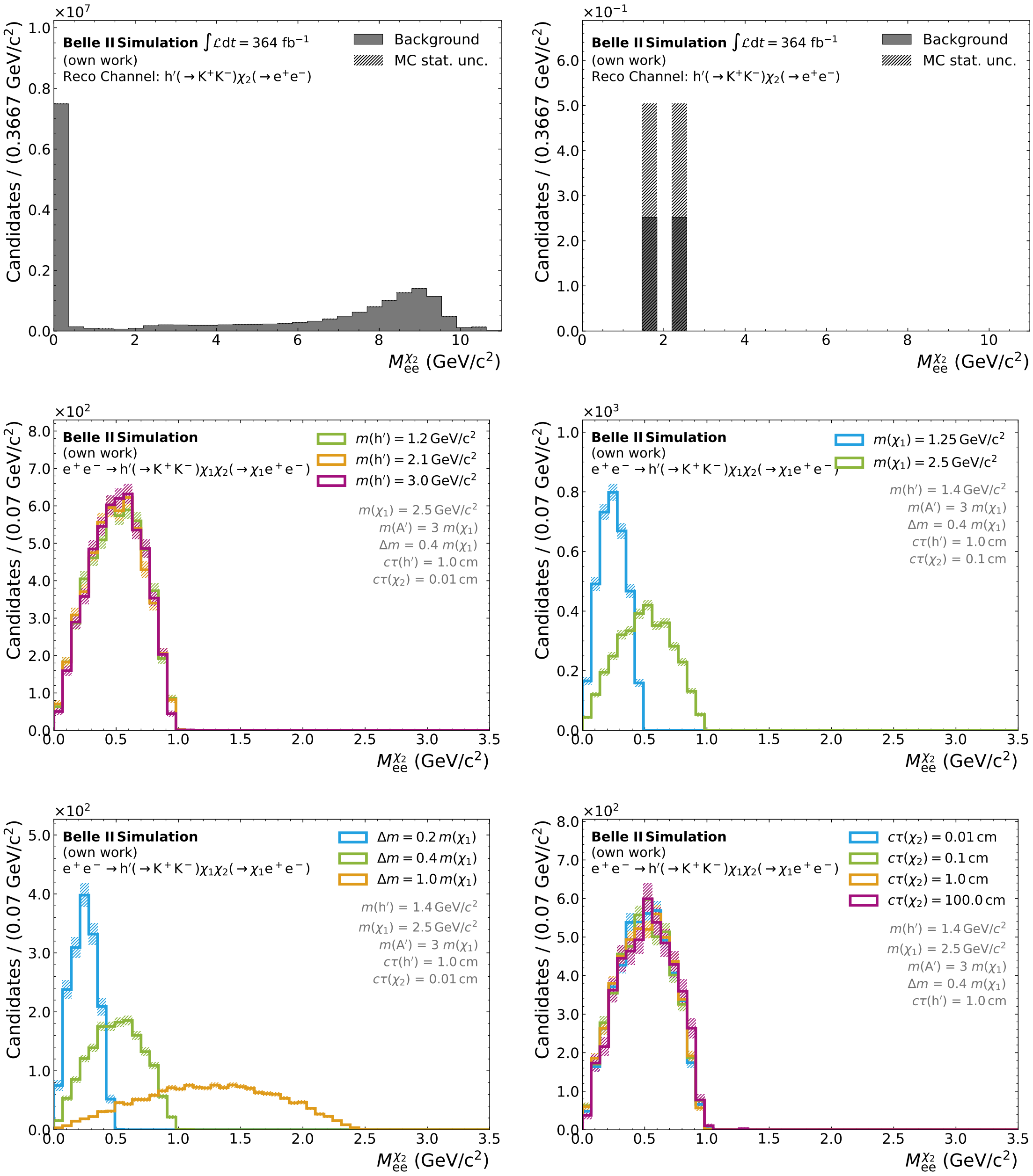

Figure B.12: Background (top) and signal (center and bottom) distributions of the reconstructed mass that forms the χ_2 candidate. For the signal the plots show only the $e^+e^- \to h'(\to K^+K^-)\chi_1\chi_2(\to \chi_1 e^+e^-)$ final state in the corresponding $h' \to K^+K^-$ reconstruction channel. The background distributions are also only shown in this reconstruction channel. The upper left plot shows the background composition with a minimal set of selections applied, while in the right plot all selections from Tables 6.1 and 6.2 besides the $M_{ee}^{\chi_2}$ requirement are applied. For signal the plots show different variations of the model parameters: h' mass (center left), χ_1 mass (center right), mass splitting (lower left), and χ_2 lifetime (lower right).

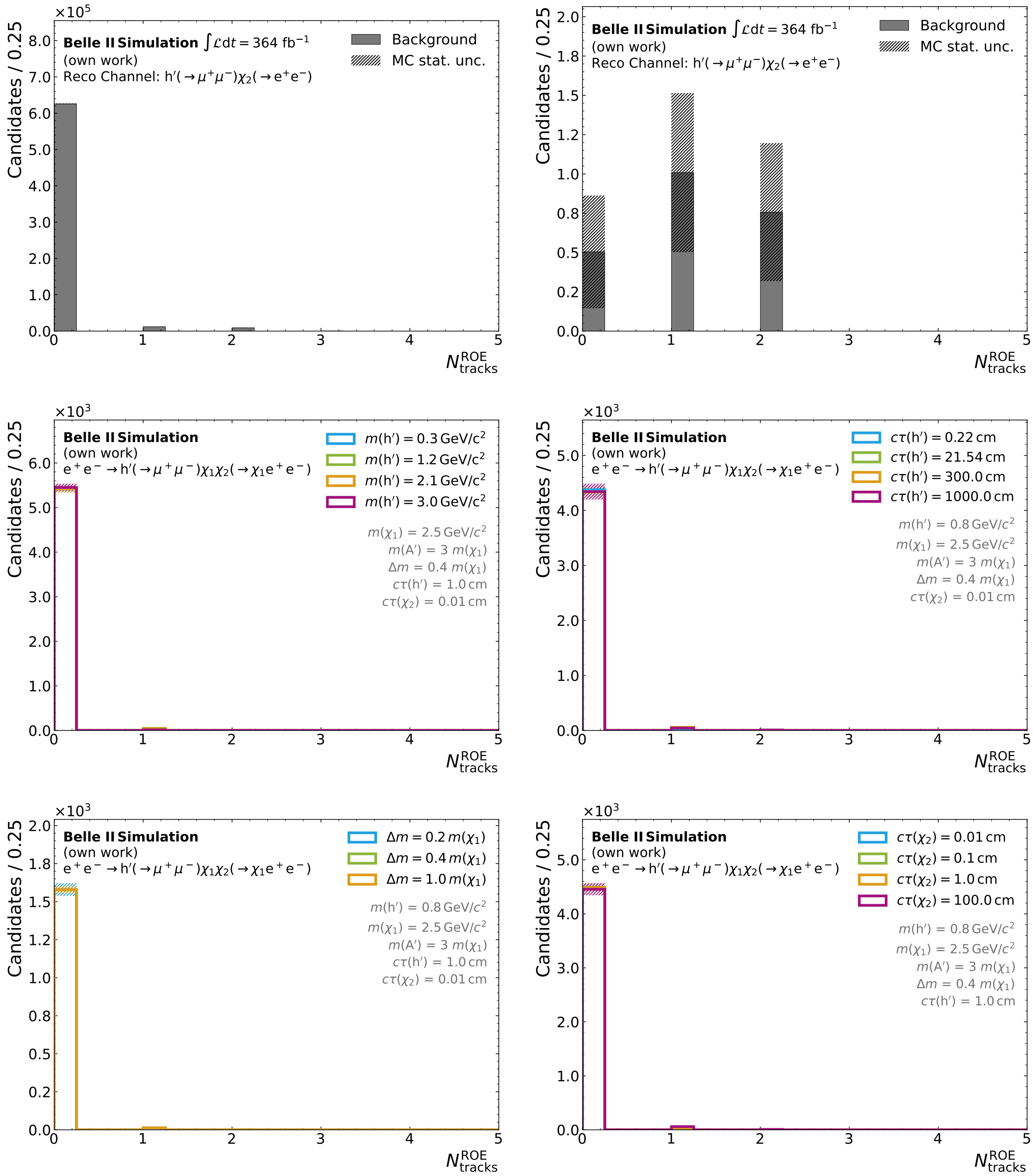

Figure B.13: Background (top) and signal (center and bottom) distributions of the additional tracks in the ROE. For the signal the plots show only the $e^+e^- \to h'(\to \mu^+\mu^-)\chi_1\chi_2(\to \chi_1 e^+e^-)$ final state in the corresponding $h' \to \mu^+\mu^-$ reconstruction channel. The background distributions are also only shown in this reconstruction channel. The upper left plot shows the background composition with a minimal set of cuts applied, while in the right plot all selections from Tables 6.1 and 6.2 besides the $N_{\text{tracks}}^{\text{ROE}}$ requirement are applied. For signal the plots show different variations of the model parameters: h′ mass (center left), h′ lifetime (center right), mass splitting (lower left), and χ_2 lifetime (lower right).

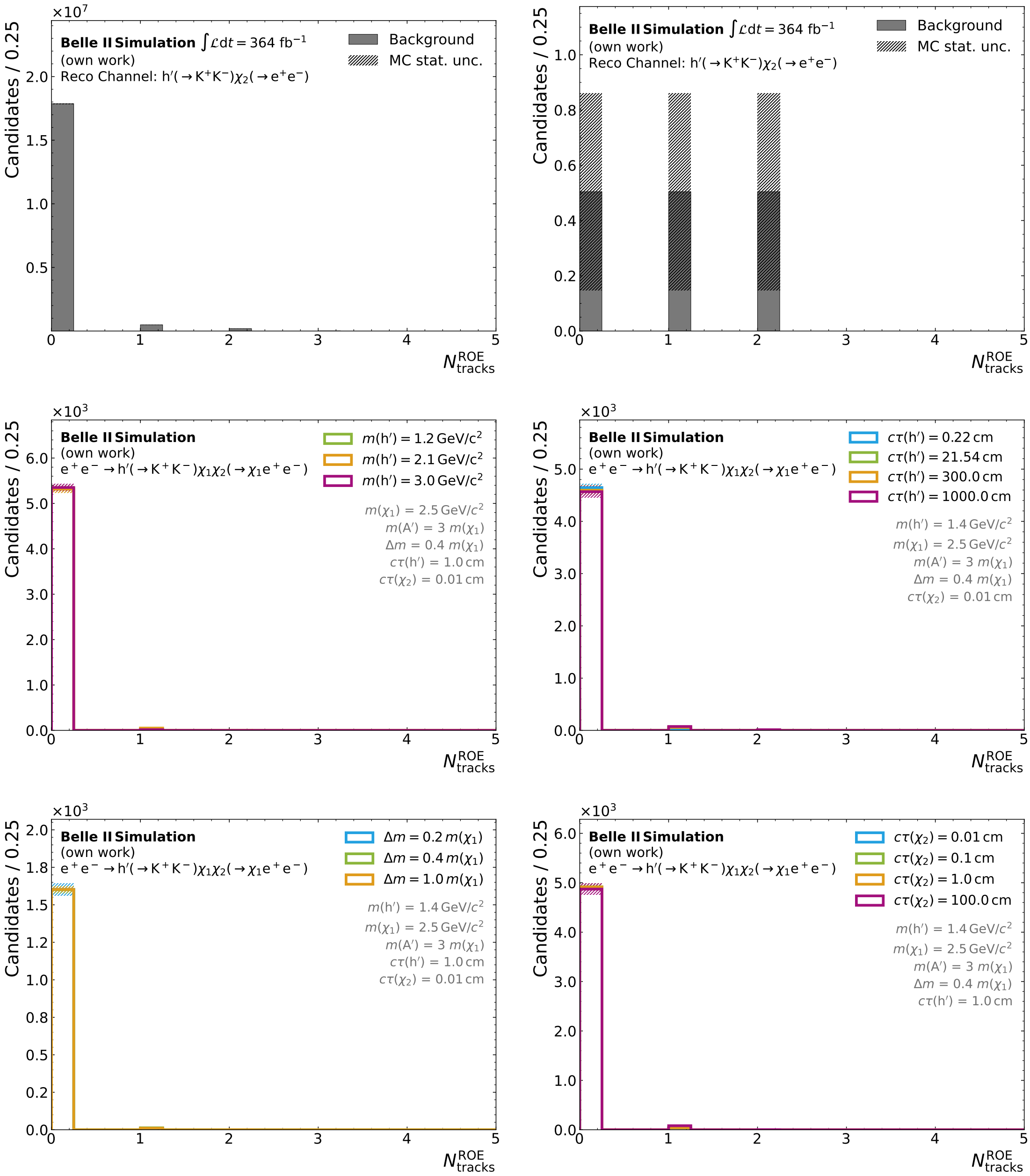

Figure B.14: Background (top) and signal (center and bottom) distributions of the additional tracks in the ROE. For the signal the plots show only the $e^+e^- \rightarrow h'(\rightarrow K^+K^-)\chi_1\chi_2(\rightarrow \chi_1 e^+e^-)$ final state in the corresponding $h' \rightarrow K^+K^-$ reconstruction channel. The background distributions are also only shown in this reconstruction channel. The upper left plot shows the background composition with a minimal set of cuts applied, while in the right plot all selections from Tables 6.1 and 6.2 besides the $N^{\mathrm{ROE}}_{\mathrm{tracks}}$ requirement are applied. For signal the plots show different variations of the model parameters: h' mass (center left), h' lifetime (center right), mass splitting (lower left), and χ_2 lifetime (lower right).

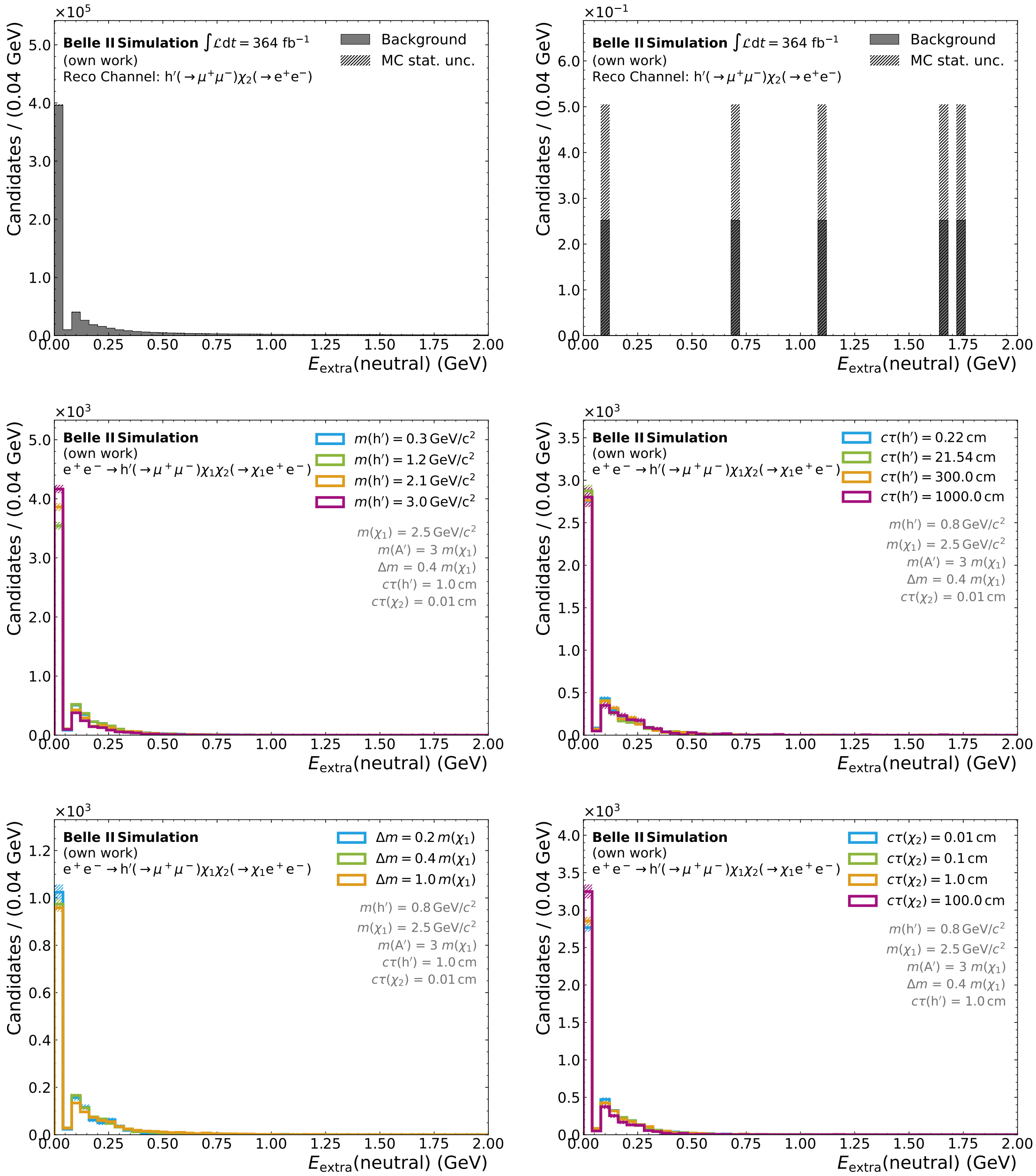

Figure B.15: Background (top) and signal (center and bottom) distributions of the extra energy in the ECL. For the signal the plots show only the $e^+e^- \to h'(\to \mu^+\mu^-)\chi_1\chi_2(\to \chi_1 e^+e^-)$ final state in the corresponding $h' \to \mu^+\mu^-$ reconstruction channel. The background distributions are also only shown in this reconstruction channel. The upper left plot shows the background composition with a minimal set of cuts applied, while in the right plot all selections from Tables 6.1 and 6.2 besides the E_{extra}(neutral) requirement are applied. For signal the plots show different variations of the model parameters: h' mass (center left), h' lifetime (center right), mass splitting (lower left), and χ_2 lifetime (lower right).

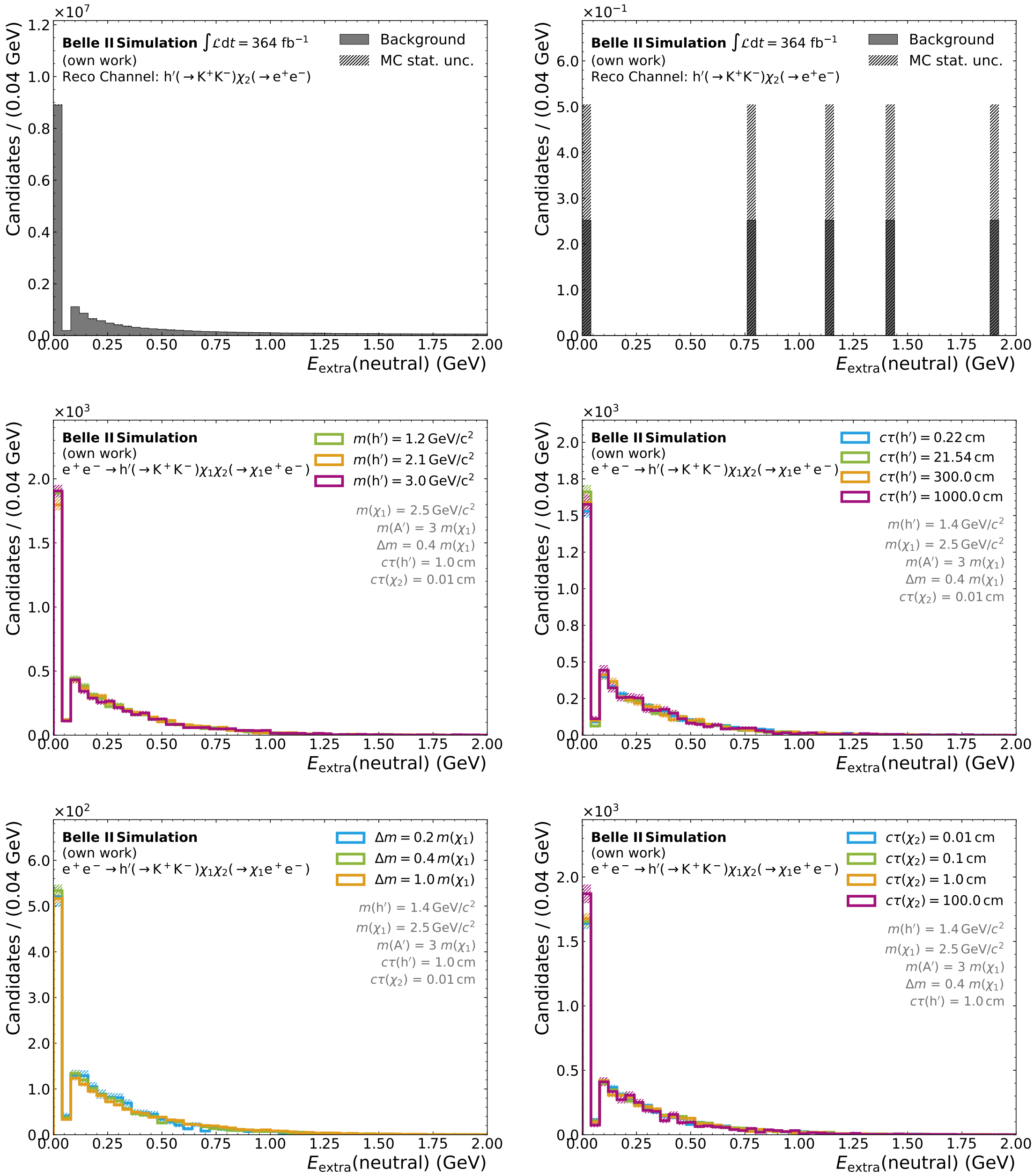

Figure B.16: Background (top) and signal (center and bottom) distributions of the extra energy in the ECL. For the signal the plots show only the $e^+e^- \to h'(\to K^+K^-)\chi_1\chi_2(\to \chi_1 e^+e^-)$ final state in the corresponding $h' \to K^+K^-$ reconstruction channel. The background distributions are also only shown in this reconstruction channel. The upper left plot shows the background composition with a minimal set of cuts applied, while in the right plot all selections from Tables 6.1 and 6.2 besides the E_{extra}(neutral) requirement are applied. For signal the plots show different variations of the model parameters: h' mass (center left), h' lifetime (center right), mass splitting (lower left), and χ_2 lifetime (lower right).

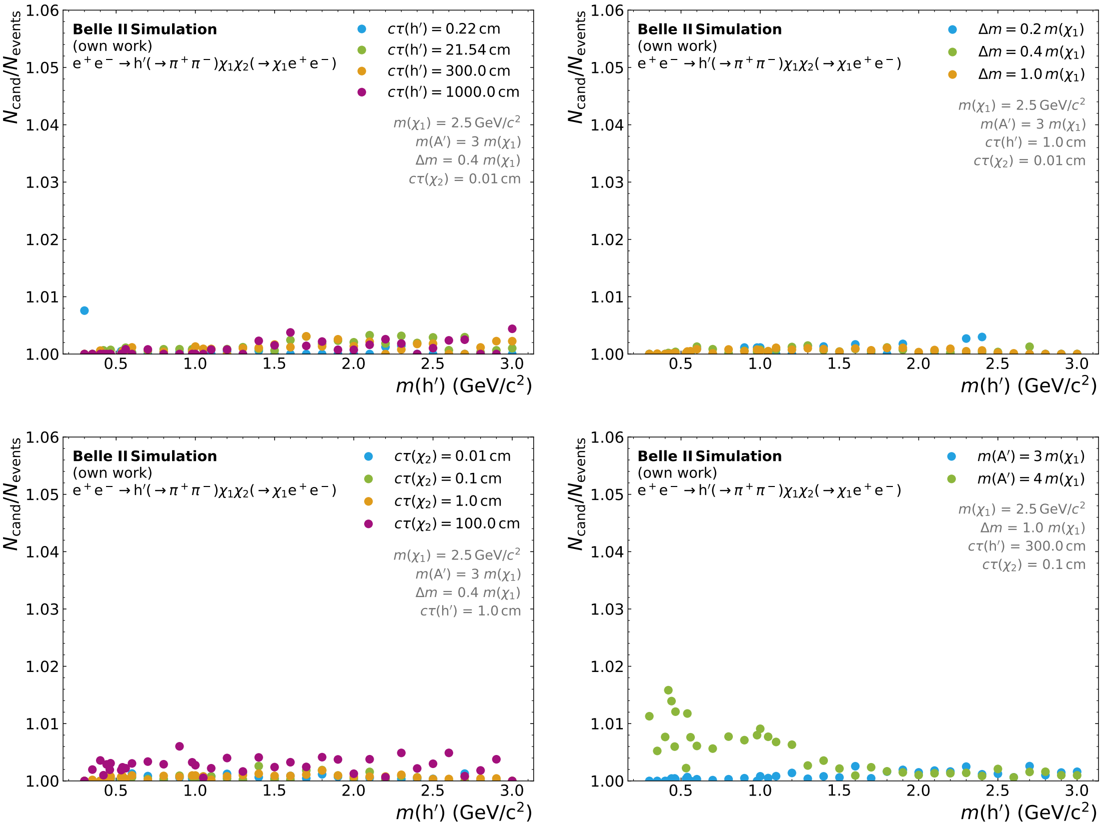

Figure B.17: Average candidate multiplicity as a function of the h' mass for different variations of the model parameters $c\tau(\mathrm{h}')$ (upper left), mass splitting (upper right), $c\tau(\chi_2)$ (lower left), and $m(\mathrm{A}')$ (lower right). The plots are based on $\mathrm{e}^+\mathrm{e}^- \to \mathrm{h}'(\to \pi^+\pi^-)\chi_1\chi_2(\to \chi_1\mathrm{e}^+\mathrm{e}^-)$ signal and show the fraction of correctly reconstructed $\mathrm{h}' \to \pi^+\pi^-$ signal candidates in all three reconstruction channels with respect to the number of reconstructed events.

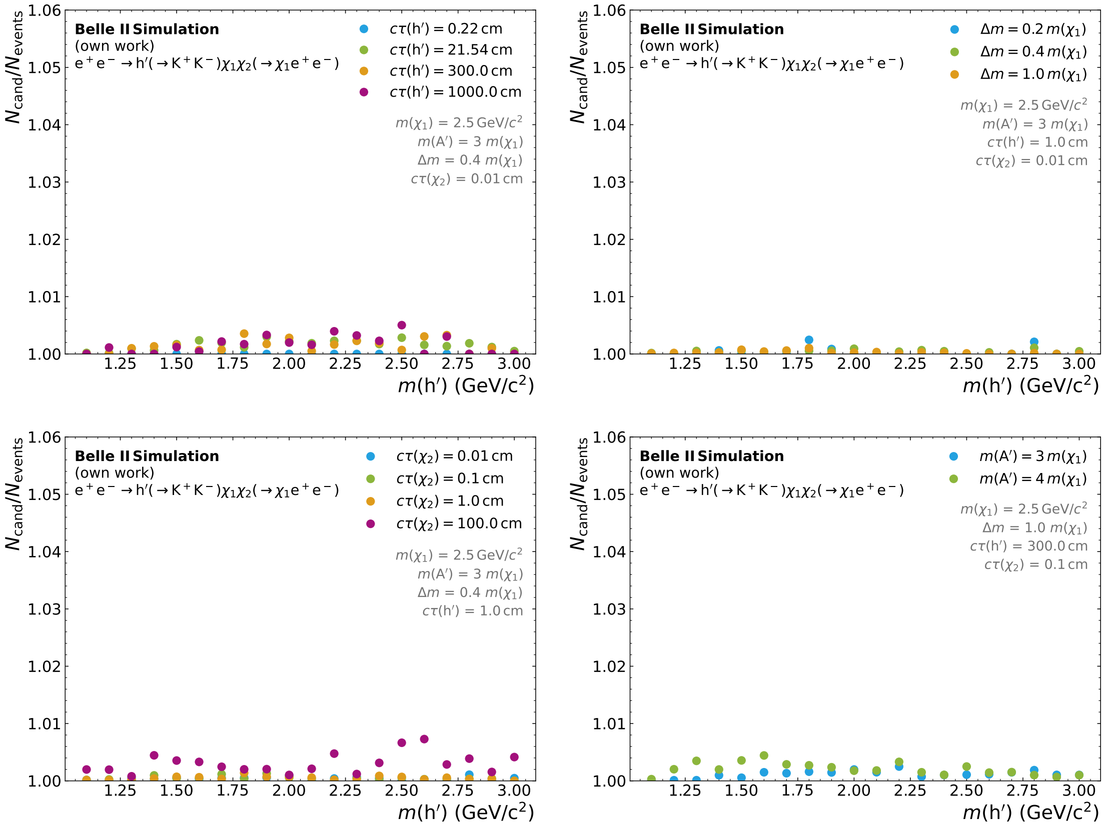

Figure B.18: Average candidate multiplicity as a function of the h' mass for different variations of the model parameters $c\tau(\mathrm{h}')$ (upper left), mass splitting (upper right), $c\tau(\chi_2)$ (lower left), and $m(\mathrm{A}')$ (lower right). The plots are based on $\mathrm{e}^+\mathrm{e}^- \to \mathrm{h}'(\to \mathrm{K}^+\mathrm{K}^-)\chi_1\chi_2(\to \chi_1\mathrm{e}^+\mathrm{e}^-)$ signal and show the fraction of correctly reconstructed $\mathrm{h}' \to \mathrm{K}^+\mathrm{K}^-$ signal candidates in all three reconstruction channels with respect to the number of reconstructed events.

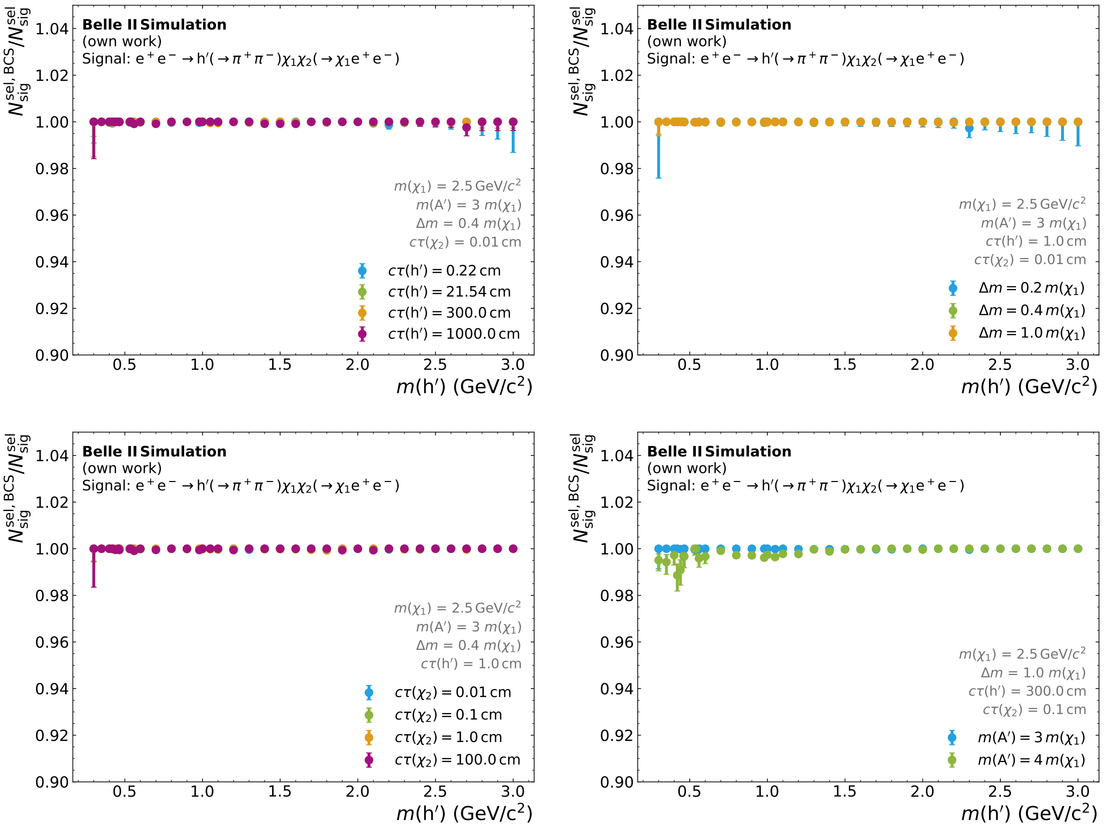

Figure B.19: Performance of the BCS as a function of the h' mass for different variations of the model parameters $c\tau(\mathrm{h}')$ (upper left), mass splitting (upper right), $c\tau(\chi_2)$ (lower left), and $m(\mathrm{A}')$ (lower right). The plots show the fraction of correctly reconstructed $\mathrm{e}^+\mathrm{e}^- \to \mathrm{h}'(\to \pi^+\pi^-)\chi_1\chi_2(\to \chi_1\mathrm{e}^+\mathrm{e}^-)$ signal events that are present after applying the BCS compared to the number of events that pass the selection criteria from Tables 6.1 and 6.2.

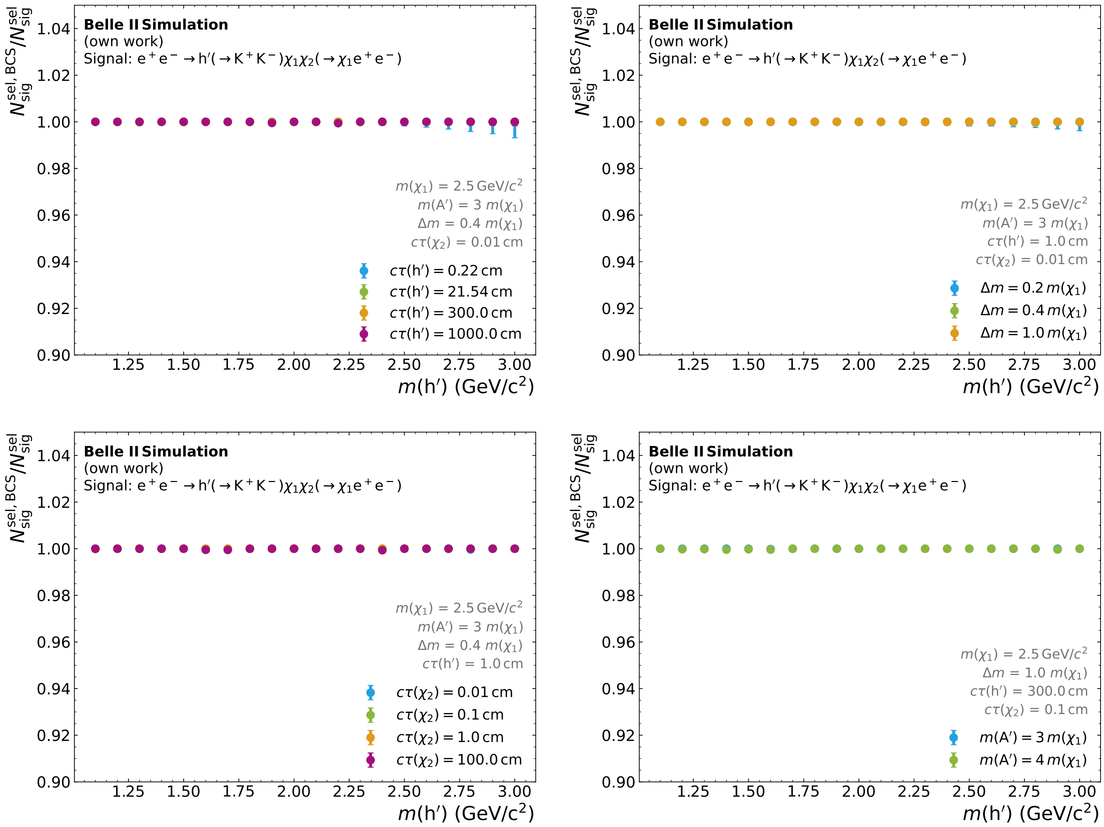

Figure B.20: Performance of the BCS as a function of the h$'$ mass for different variations of the model parameters $c\tau(\mathrm{h}')$ (upper left), mass splitting (upper right), $c\tau(\chi_2)$ (lower left), and $m(\mathrm{A}')$ (lower right). The plots show the fraction of correctly reconstructed $\mathrm{e}^+\mathrm{e}^- \to \mathrm{h}'(\to \mathrm{K}^+\mathrm{K}^-)\chi_1\chi_2(\to \chi_1\mathrm{e}^+\mathrm{e}^-)$ signal events that are present after applying the BCS compared to the number of events that pass the selection criteria from Tables 6.1 and 6.2.

Appendix C

Selection Optimisation

This appendix deals with the optimisation of the selection criteria discussed in Chapter 6. I show plots for the selections that are optimised using the Punzi FOM (Eq. (6.1)). The plots show the last step of the optimisation procedure with and without applying all other selections that are summarised in Tables 6.1 and 6.2 for all three considered final states and several variations of the model parameters.

The optimisation of the selection on the opening angle between the electron pair forming the χ_2 candidate is shown in Figs. C.1 and C.2. Figs. C.3 and C.4 shows the optimisation of the angle between the tracks of the other vertex, the h' candidate. Furthermore, the selection on the pointiness of the h' candidate is optimised in Figs. C.5 and C.6. The outcome of the optimisation of the selection on the neutral extra energy in the ECL is shown in Figs. C.7 and C.8

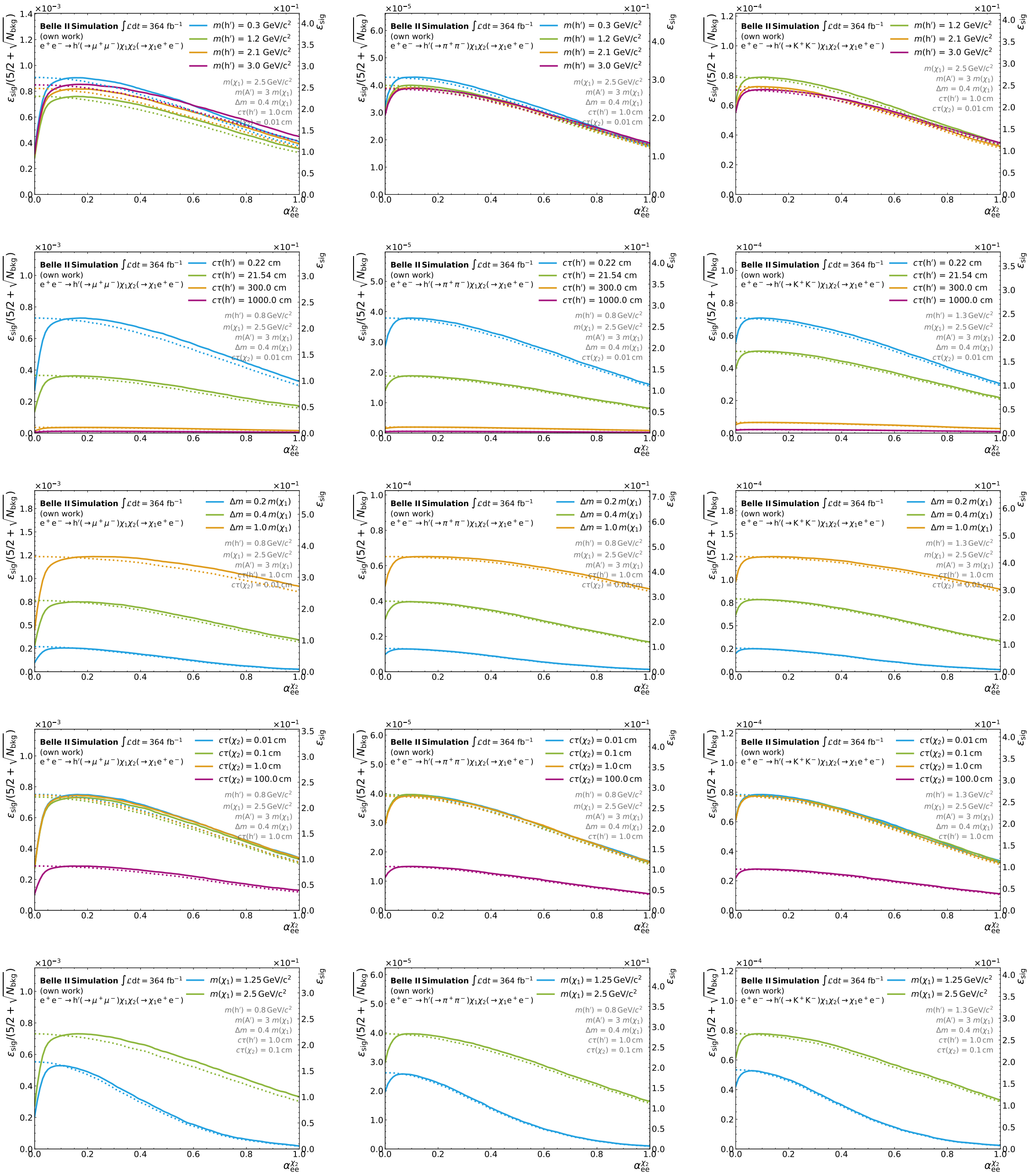

Figure C.1: Optimisation of the selection on the angle between the electrons tracks forming the χ_2 candidate for the $e^+e^- \rightarrow h'(\rightarrow \mu^+\mu^-)\chi_1\chi_2(\rightarrow \chi_1 e^+e^-)$ (left), $e^+e^- \rightarrow h'(\rightarrow \pi^+\pi^-)\chi_1\chi_2(\rightarrow \chi_1 e^+e^-)$ (center), and $e^+e^- \rightarrow h'(\rightarrow K^+K^-)\chi_1\chi_2(\rightarrow \chi_1 e^+e^-)$ signal process. The first row shows variations of the dark Higgs mass and the second row shows the variation of the dark Higgs lifetime. In the third row the mass splitting Δm is varied. The χ_2 lifetime is varied in the fouth row. Variation of the χ_1 mass are shown in the last row. The solid line indicates the Punzi FOM for a discovery while the dashed line shows the corresponding signal efficiency.

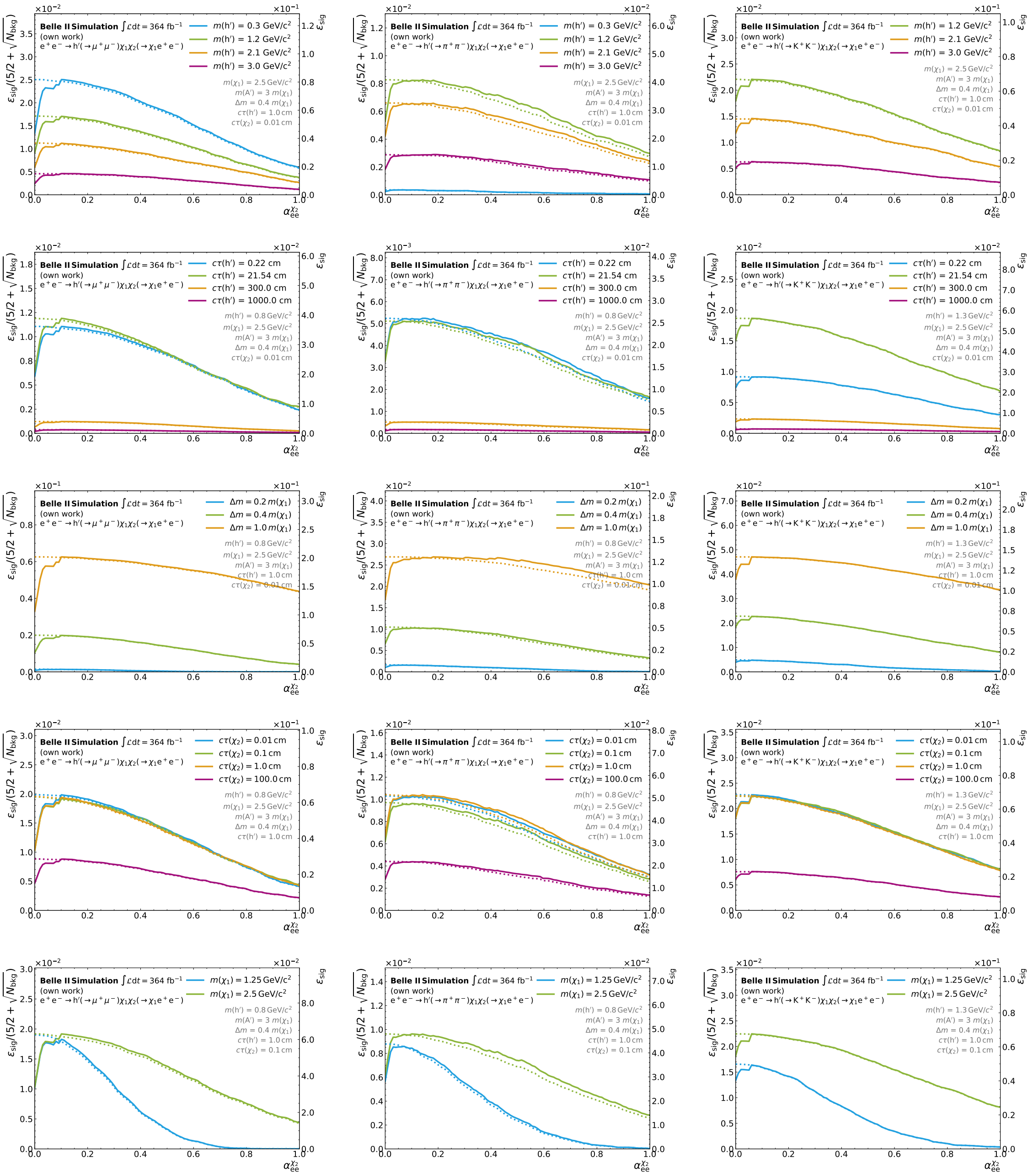

Figure C.2: Optimisation of the selection on the angle between the electrons tracks forming the χ_2 candidate for the $e^+e^- \to h'(\to \mu^+\mu^-)\chi_1\chi_2(\to \chi_1 e^+e^-)$ (left), $e^+e^- \to h'(\to \pi^+\pi^-)\chi_1\chi_2(\to \chi_1 e^+e^-)$ (center), and $e^+e^- \to h'(\to K^+K^-)\chi_1\chi_2(\to \chi_1 e^+e^-)$ signal process. The first row shows variations of the dark Higgs mass and the second row shows the variation of the dark Higgs lifetime. In the third row the mass splitting Δm is varied. The χ_2 lifetime is varied in the fouth row. Variation of the χ_1 mass are shown in the last row. The solid line indicates the Punzi FOM for a discovery while the dashed line shows the corresponding signal efficiency. All selections from Tables 6.1 and 6.2 but the selection on α_{ee} are applied.

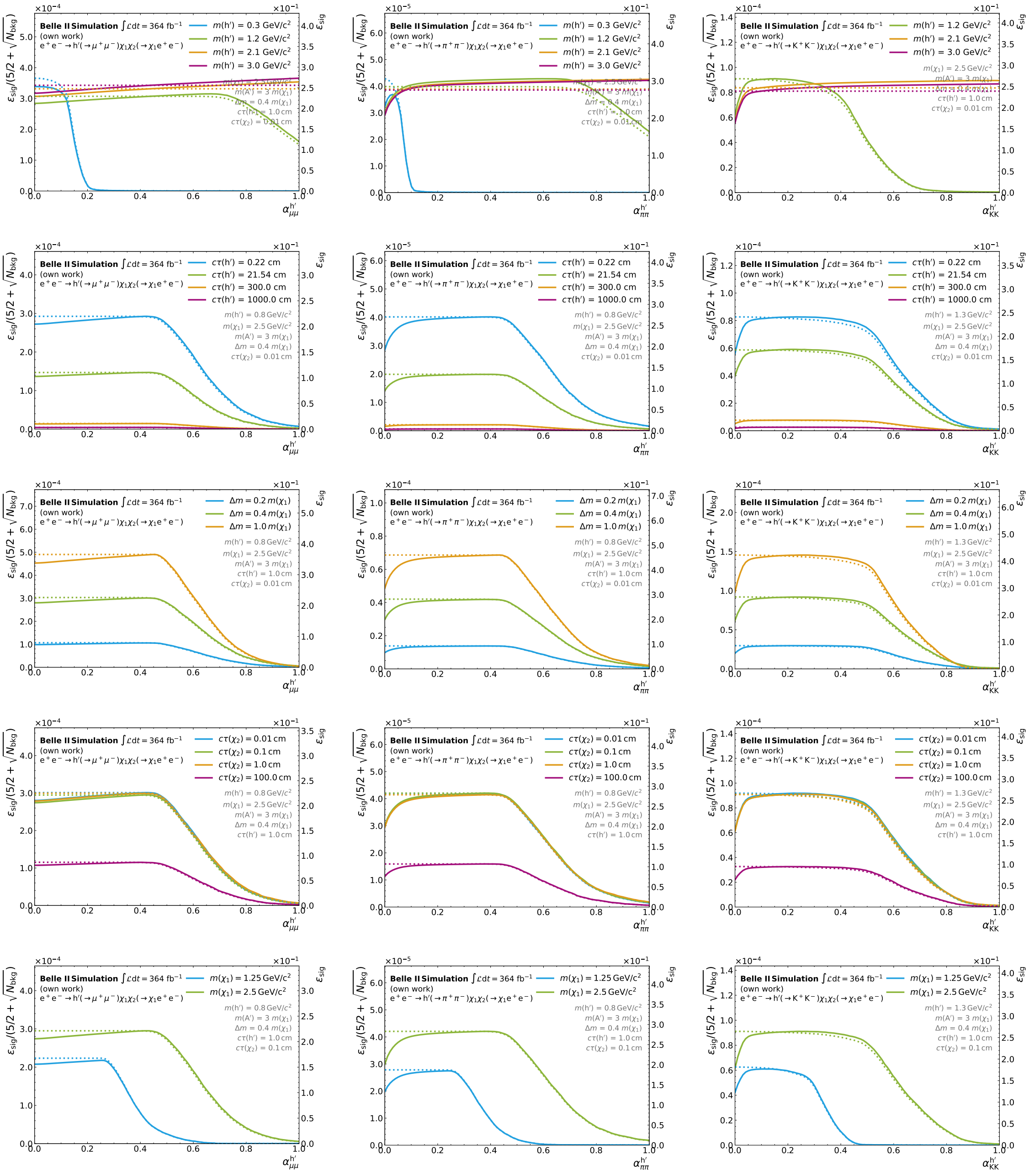

Figure C.3: Optimisation of the selection on the angle between the two tracks forming the h' candidate for the $\mathrm{e^+e^-} \to \mathrm{h}'(\to \mu^+\mu^-)\chi_1\chi_2(\to \chi_1\mathrm{e^+e^-})$ (left), $\mathrm{e^+e^-} \to \mathrm{h}'(\to \pi^+\pi^-)\chi_1\chi_2(\to \chi_1\mathrm{e^+e^-})$ (center), and $\mathrm{e^+e^-} \to \mathrm{h}'(\to \mathrm{K^+K^-})\chi_1\chi_2(\to \chi_1\mathrm{e^+e^-})$ signal process. The first row shows variations of the dark Higgs mass and the second row shows the variation of the dark Higgs lifetime. In the third row the mass splitting Δm is varied. The χ_2 lifetime is varied in the fouth row. Variation of the χ_1 mass are shown in the last row. The solid line indicates the Punzi FOM for a discovery while the dashed line shows the corresponding signal efficiency.

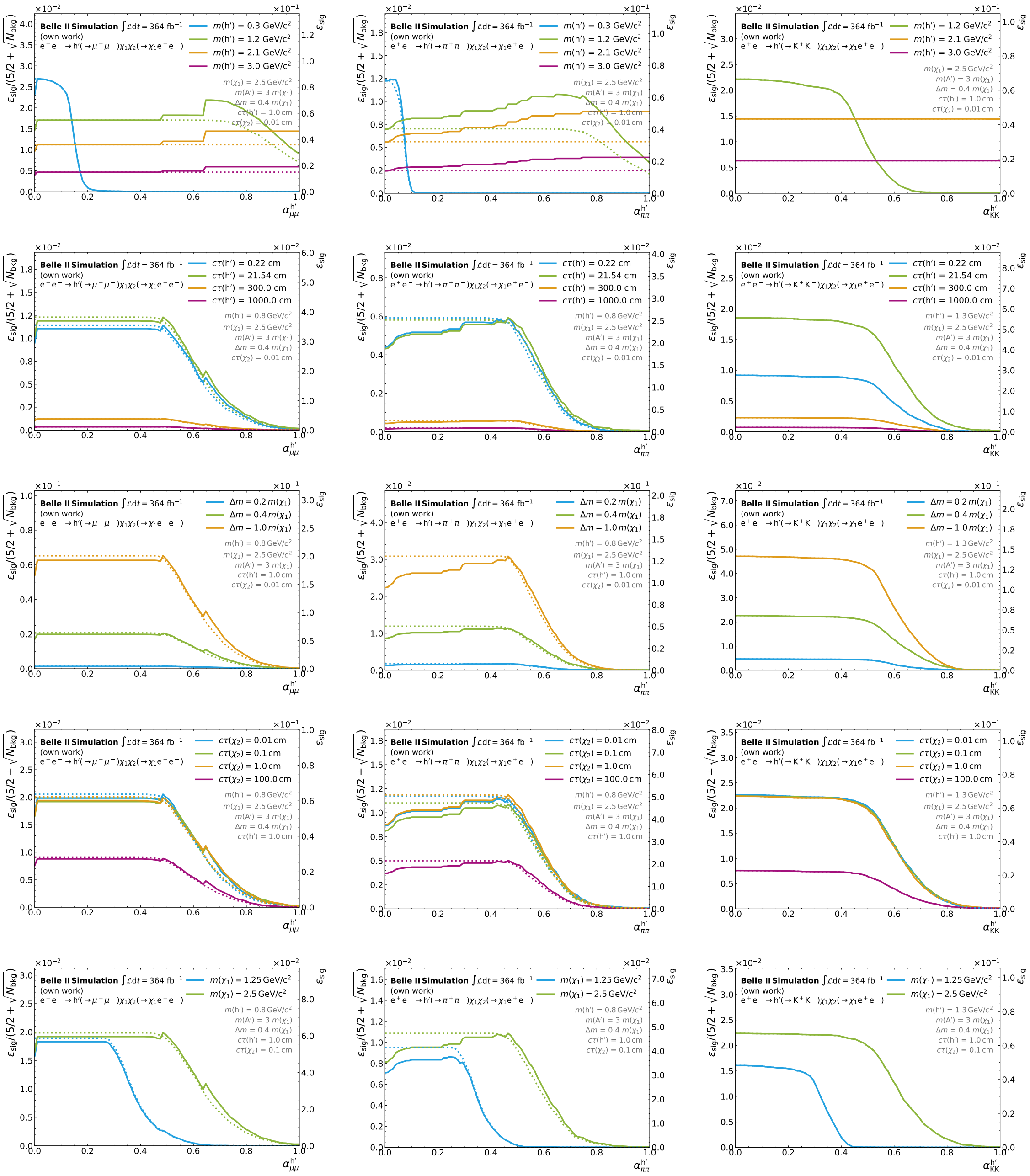

Figure C.4: Optimisation of the selection on the angle between the two tracks forming the h′ candidate for the $e^+e^- \to h'(\to \mu^+\mu^-)\chi_1\chi_2(\to \chi_1 e^+e^-)$ (left), $e^+e^- \to h'(\to \pi^+\pi^-)\chi_1\chi_2(\to \chi_1 e^+e^-)$ (center), and $e^+e^- \to h'(\to K^+K^-)\chi_1\chi_2(\to \chi_1 e^+e^-)$ signal process. The first row shows variations of the dark Higgs mass and the second row shows the variation of the dark Higgs lifetime. In the third row the mass splitting Δm is varied. The χ_2 lifetime is varied in the fouth row. Variation of the χ_1 mass are shown in the last row. The solid line indicates the Punzi FOM for a discovery while the dashed line shows the corresponding signal efficiency. All selections from Tables 6.1 and 6.2 but the selection on $\alpha_{\rm xx}$ are applied.

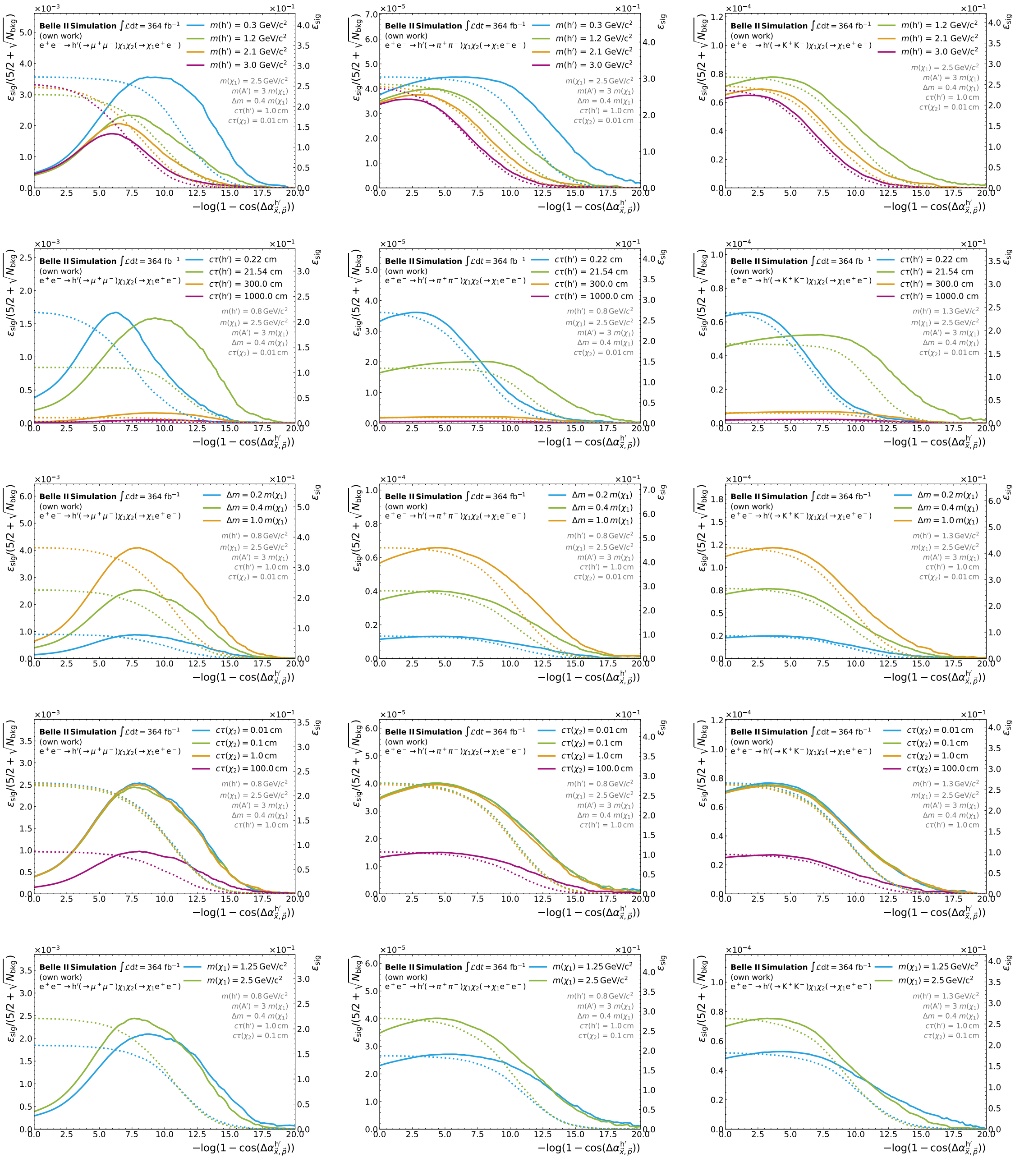

Figure C.5: Optimisation of the selection on the pointiness of the h′ candidate for the $e^+e^- \to h'(\to \mu^+\mu^-)\chi_1\chi_2(\to \chi_1 e^+e^-)$ (left), $e^+e^- \to h'(\to \pi^+\pi^-)\chi_1\chi_2(\to \chi_1 e^+e^-)$ (center), and $e^+e^- \to h'(\to K^+K^-)\chi_1\chi_2(\to \chi_1 e^+e^-)$ signal process. The first row shows variations of the dark Higgs mass and the second row shows the variation of the dark Higgs lifetime. In the third row the mass splitting Δm is varied. The χ_2 lifetime is varied in the fouth row. Variation of the χ_1 mass are shown in the last row. The solid line indicates the Punzi FOM for a discovery while the dashed line shows the corresponding signal efficiency.

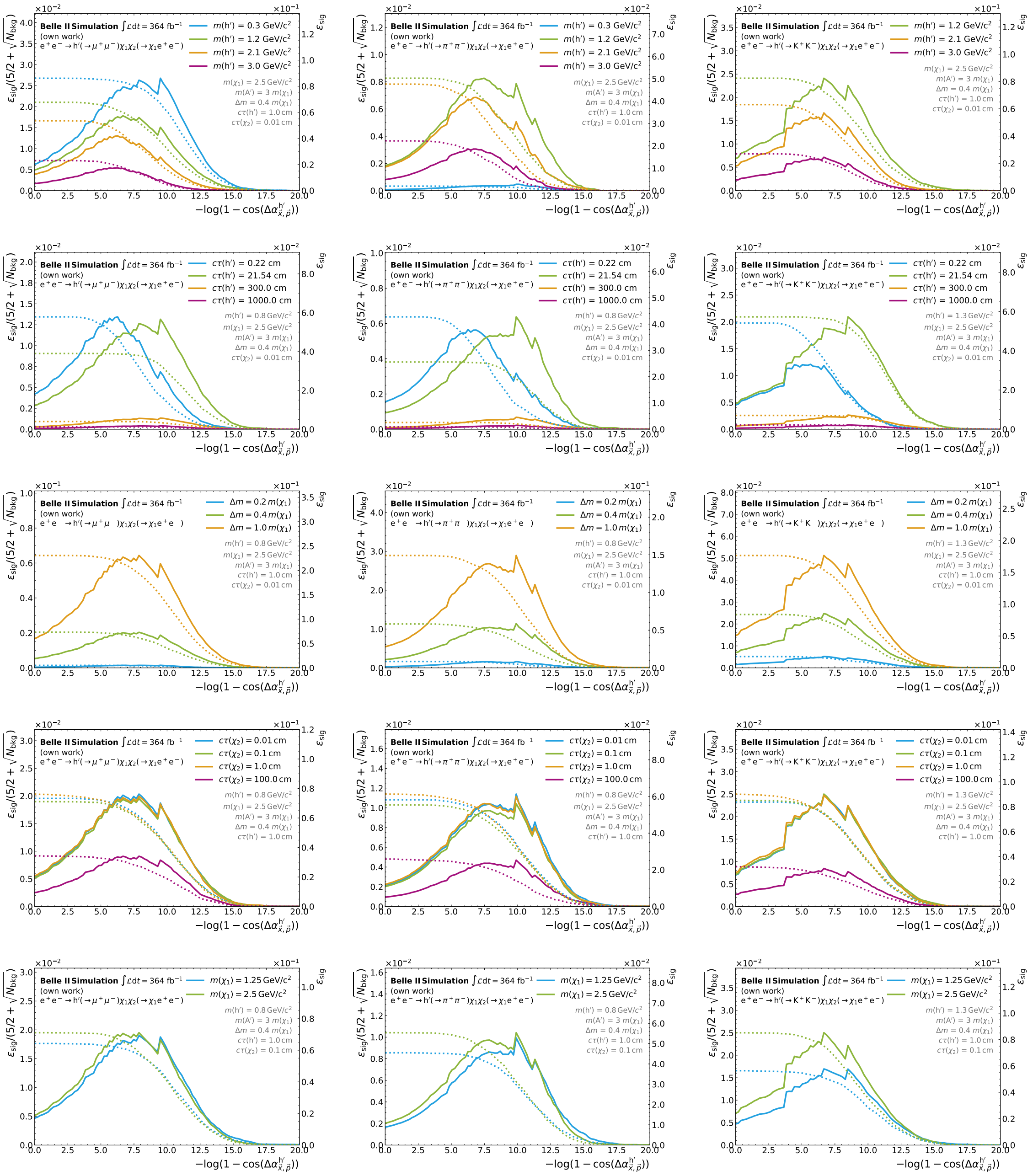

Figure C.6: Optimisation of the selection on the pointiness of the h' candidate for the $\mathrm{e}^+\mathrm{e}^- \rightarrow \mathrm{h}'(\rightarrow \mu^+\mu^-)\chi_1\chi_2(\rightarrow \chi_1\mathrm{e}^+\mathrm{e}^-)$ (left), $\mathrm{e}^+\mathrm{e}^- \rightarrow \mathrm{h}'(\rightarrow \pi^+\pi^-)\chi_1\chi_2(\rightarrow \chi_1\mathrm{e}^+\mathrm{e}^-)$ (center), and $\mathrm{e}^+\mathrm{e}^- \rightarrow \mathrm{h}'(\rightarrow \mathrm{K}^+\mathrm{K}^-)\chi_1\chi_2(\rightarrow \chi_1\mathrm{e}^+\mathrm{e}^-)$ signal process. The first row shows variations of the dark Higgs mass and the second row shows the variation of the dark Higgs lifetime. In the third row the mass splitting Δm is varied. The χ_2 lifetime is varied in the fouth row. Variation of the χ_1 mass are shown in the last row. The solid line indicates the Punzi FOM for a discovery while the dashed line shows the corresponding signal efficiency. All selections from Tables 6.1 and 6.2 but the selection on $-\log(1-\cos(\Delta\alpha^{\mathrm{h}'}_{\mathbf{x,p}}))$ are applied.

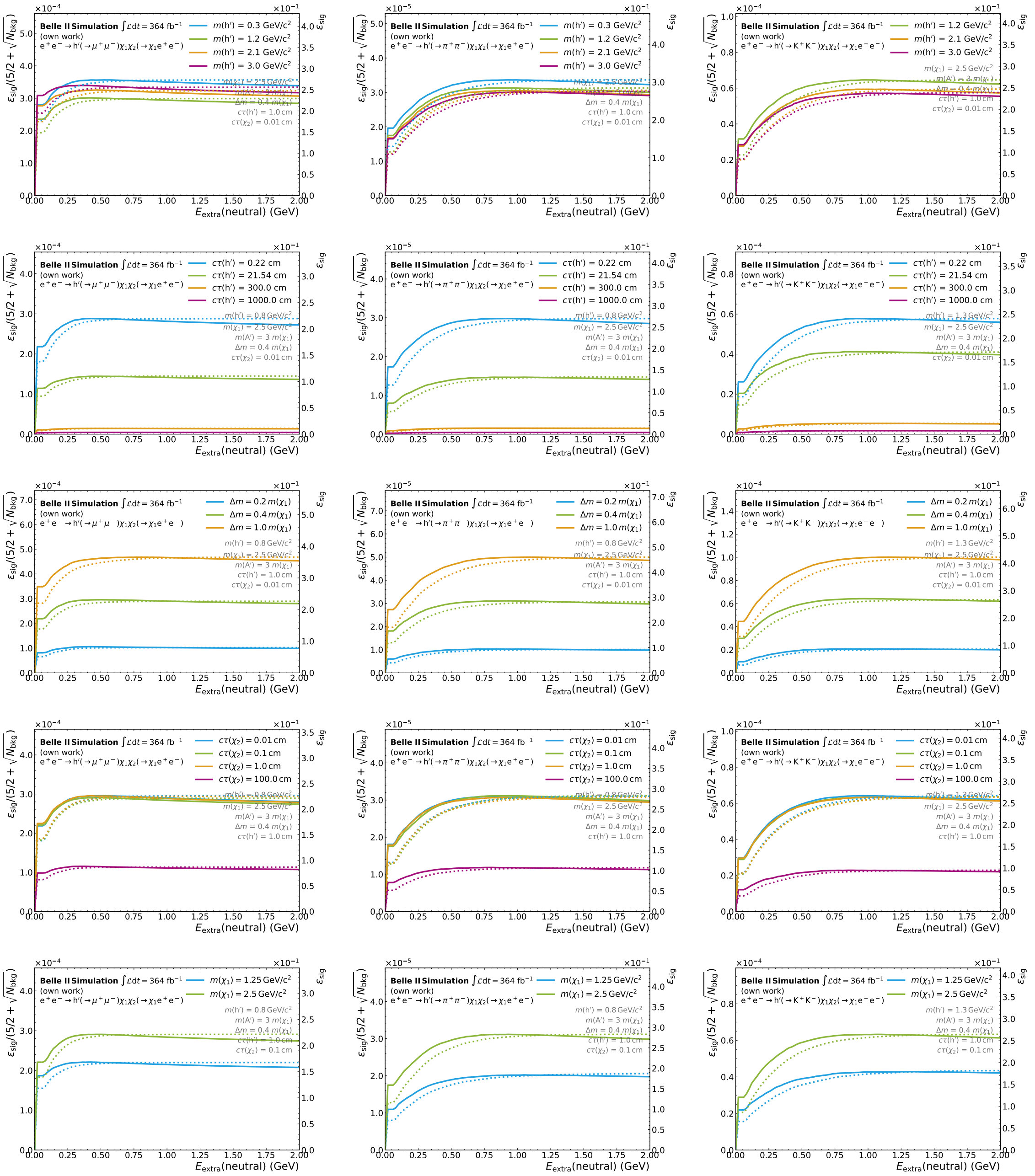

Figure C.7: Optimisation of the selection on the neutral extra energy in the ECL for the $e^+e^- \to h'(\to \mu^+\mu^-)\chi_1\chi_2(\to \chi_1 e^+e^-)$ (left), $e^+e^- \to h'(\to \pi^+\pi^-)\chi_1\chi_2(\to \chi_1 e^+e^-)$ (center), and $e^+e^- \to h'(\to K^+K^-)\chi_1\chi_2(\to \chi_1 e^+e^-)$ signal process. The first row shows variations of the dark Higgs mass and the second row shows the variation of the dark Higgs lifetime. In the third row the mass splitting Δm is varied. The χ_2 lifetime is varied in the fouth row. Variation of the χ_1 mass are shown in the last row. The solid line indicates the Punzi FOM for a discovery while the dashed line shows the corresponding signal efficiency.

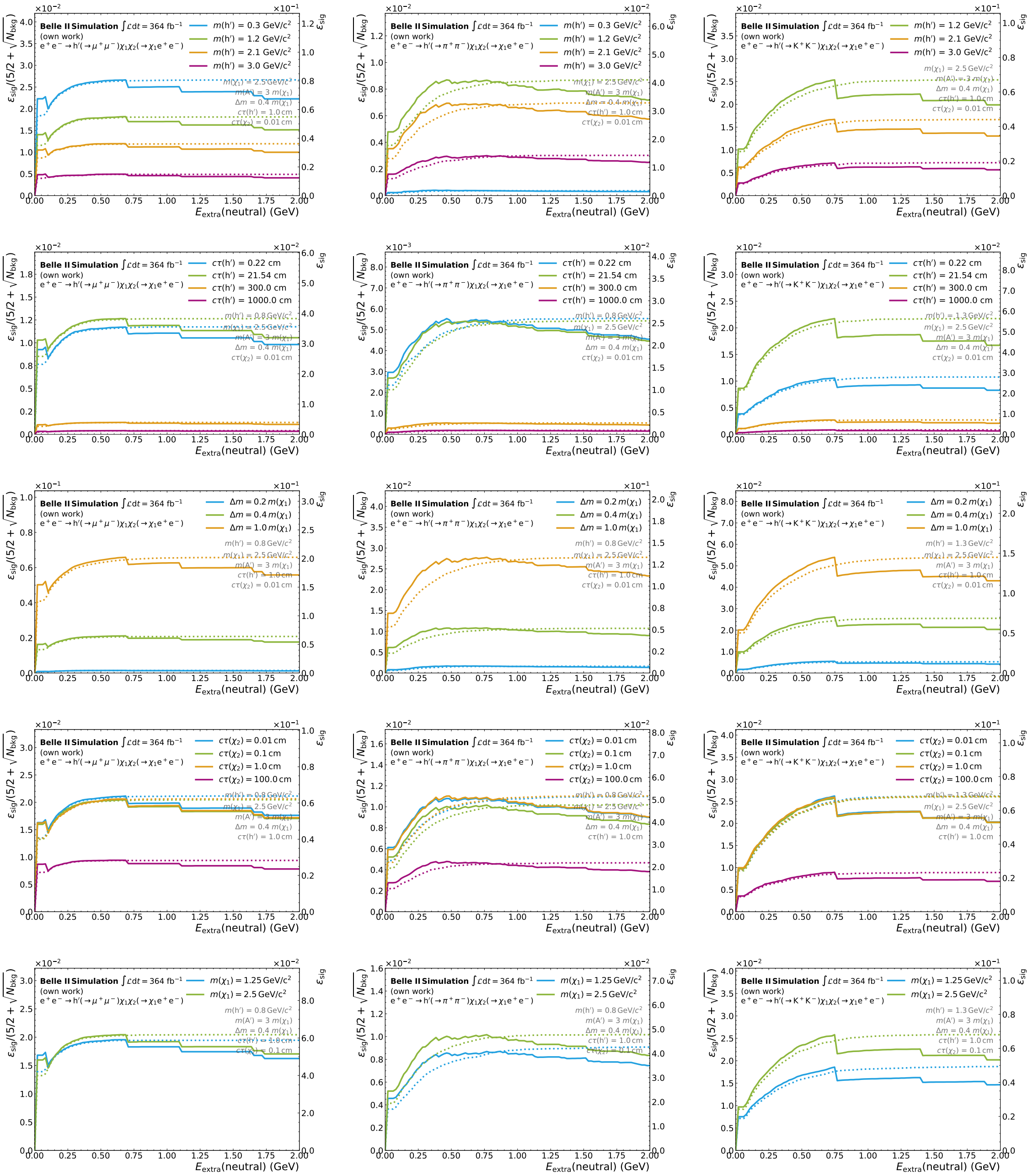

Figure C.8: Optimisation of the selection on the neutral extra energy in the ECL for the $e^+e^- \to h'(\to \mu^+\mu^-)\chi_1\chi_2(\to \chi_1 e^+e^-)$ (left), $e^+e^- \to h'(\to \pi^+\pi^-)\chi_1\chi_2(\to \chi_1 e^+e^-)$ (center), and $e^+e^- \to h'(\to K^+K^-)\chi_1\chi_2(\to \chi_1 e^+e^-)$ signal process. The first row shows variations of the dark Higgs mass and the second row shows the variation of the dark Higgs lifetime. In the third row the mass splitting Δm is varied. The χ_2 lifetime is varied in the fouth row. Variation of the χ_1 mass are shown in the last row. The solid line indicates the Punzi FOM for a discovery while the dashed line shows the corresponding signal efficiency. All selections from Tables 6.1 and 6.2 but the selection on E_{extra}(neutral) are applied.

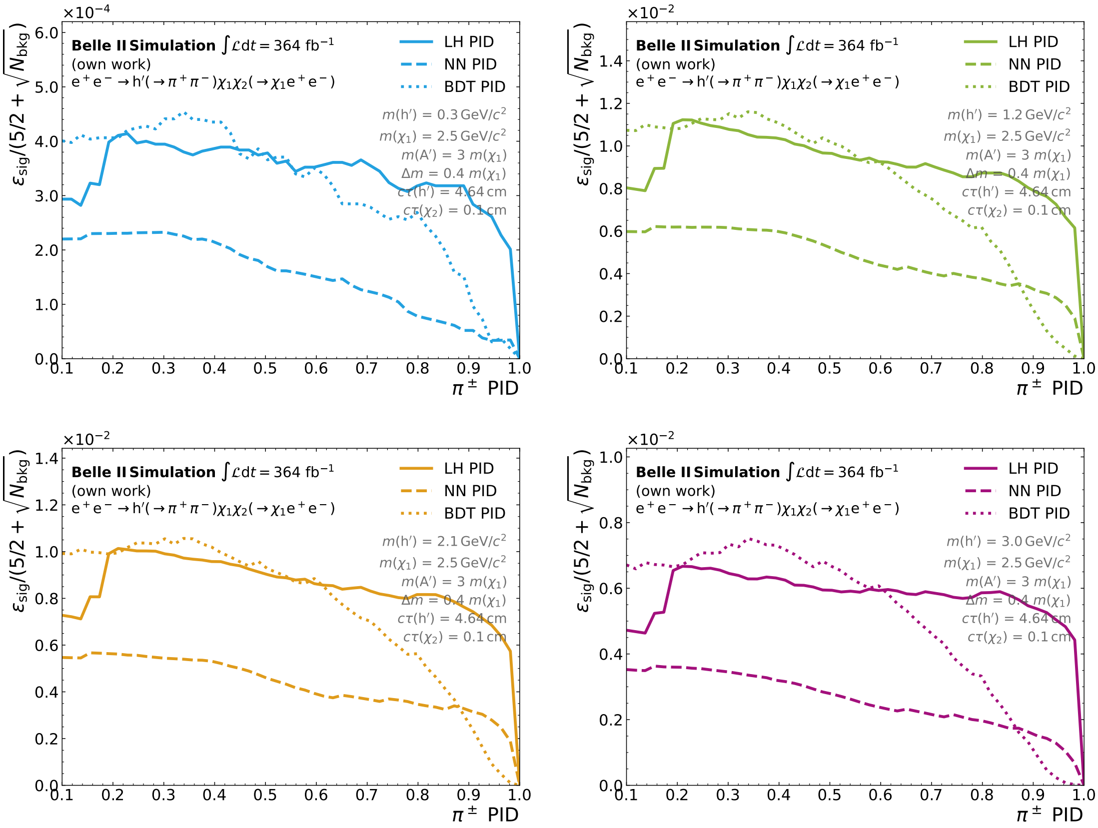

Figure C.9: Punzi FOM for the requirement on the pion PID for the $e^+e^- \to h'(\to \pi^+\pi^-)\chi_1\chi_2(\to \chi_1 e^+e^-)$ signal process in the $h' \to \pi^+\pi^-$ reconstruction channel. The plots show different mass hypotheses for the h' with the remaining model parameters fixed to the values reported in the plots. The different line styles represent the three different PID classifiers: Likelihood (LH), neural network (NN), and boosted decision tree (BDT). Besides the PID requirement all other cuts from Tables 6.1 and 6.2 have been applied beforehand.

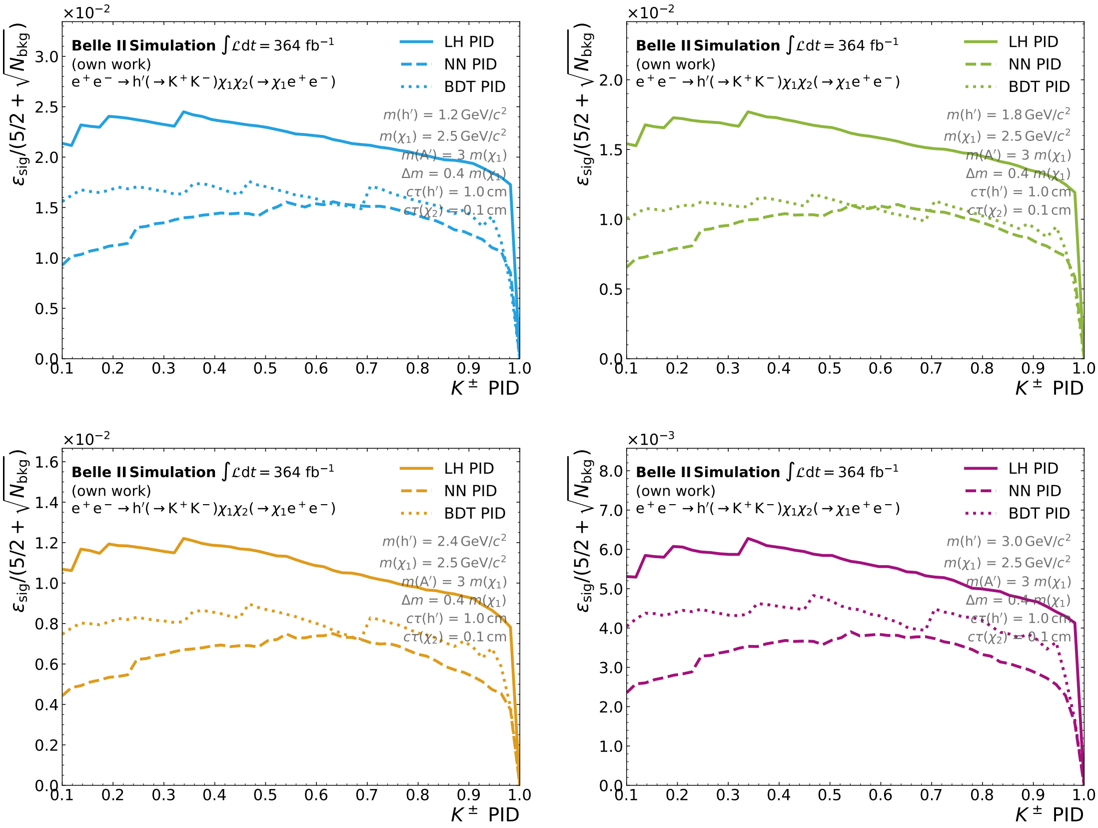

Figure C.10: Punzi FOM for the requirement on the pion PID for the $e^+e^- \to h'(\to K^+K^-)\chi_1\chi_2(\to \chi_1 e^+e^-)$ signal process in the $h' \to K^+K^-$ reconstruction channel. The plots show different mass hypotheses for the h' with the remaining model parameters fixed to the values reported in the plots. Variations of the other model parameters can be found in the appendix. The different line styles represent the three different PID classifiers: Likelihood (LH), neural network (NN), and boosted decision tree (BDT). Besides the PID requirement all other cuts from Tables 6.1 and 6.2 have been applied beforehand.

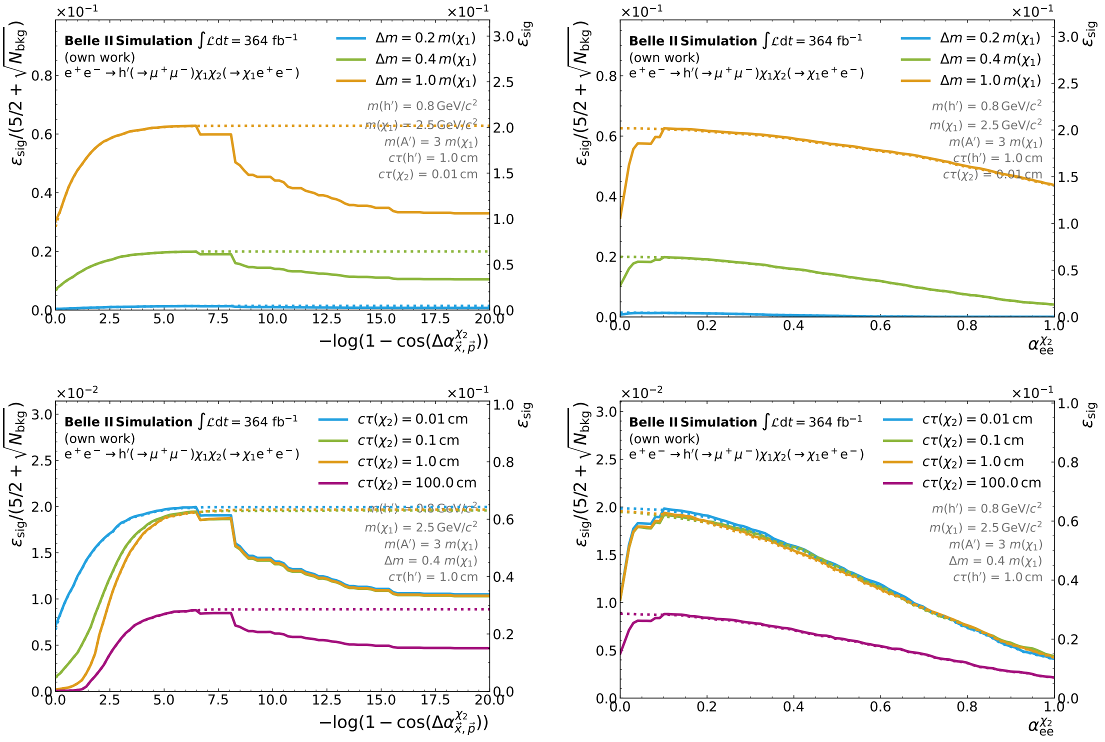

Figure C.11: Punzi figure of merit (solid line) calculated for the threshold on the χ_2 pointing angle (left) and on the χ_2 daughter opening angle (right) in the $h' \to \mu^+\mu^-$ final state with all other cuts shown in Table 6.1 applied. The dashed lines describe the corresponding signal efficiency. The results are shown for different variations of the χ_1 mass and the mass splitting (top) and χ_2 lifetime (bottom) as these are the model parameters where this selection is most sensitive.

Appendix D

Additional Trigger Performance Studies

In this appendix, I present additional studies on the performance of the L1 trigger trigger (see Section 7.2) for the $\mathrm{e}^+\mathrm{e}^- \to \mathrm{h}'(\to \pi^+\pi^-)\chi_1\chi_2(\to \chi_1\mathrm{e}^+\mathrm{e}^-)$ and $\mathrm{e}^+\mathrm{e}^- \to \mathrm{h}'(\to \mu^+\mu^-)\chi_1\chi_2(\to \chi_1\mathrm{e}^+\mathrm{e}^-)$ final state. Both the performance of the HIE trigger and the STT are covered.

Especially for the $\mathrm{e}^+\mathrm{e}^- \to \mathrm{h}'(\to \pi^+\pi^-)\chi_1\chi_2(\to \chi_1\mathrm{e}^+\mathrm{e}^-)$ final state shown in Fig. D.1 the dependence of the performance of the HIE trigger on the mass splitting Δm is less pronounced compared to the $\mathrm{e}^+\mathrm{e}^- \to \mathrm{h}'(\to \mu^+\mu^-)\chi_1\chi_2(\to \chi_1\mathrm{e}^+\mathrm{e}^-)$ final state. For the STT performance drop for larger lifetimes of the h' is independent of the final state.

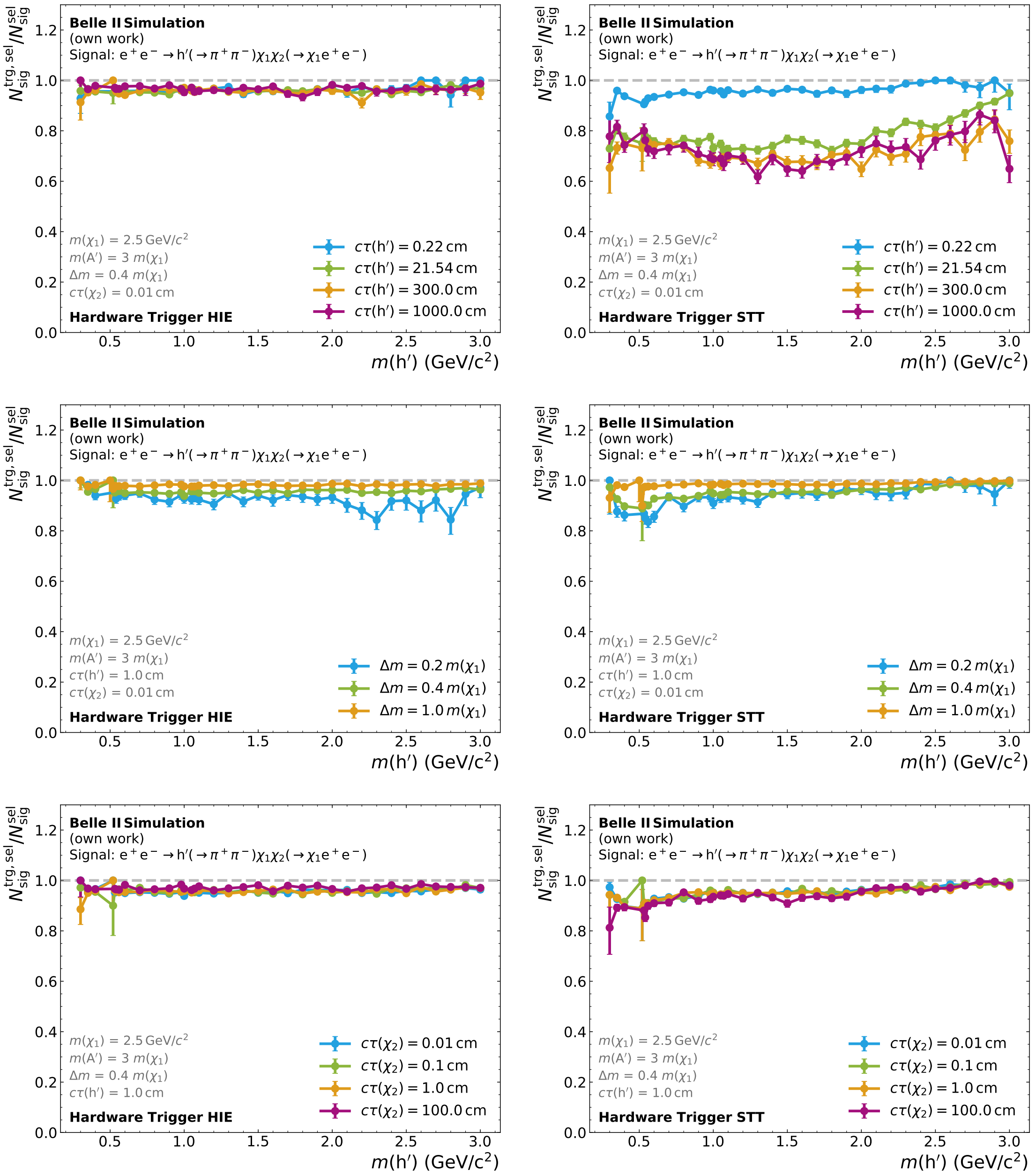

Figure D.1: Fraction of events that are selected and triggered by the HIE (left) and STT L1 trigger line (right) to all selected events. The selected events are selected with the selections from Tables 6.1 and 6.2 (excluding the selection on E_{hie}). The performance is shown as a function of the dark Higgs mass for several variations of the other model parameters: $c\tau(\mathrm{h}')$ (top), Δm (center), and $c\tau(\chi_2)$ (bottom). The plots show the $\mathrm{e}^+\mathrm{e}^- \to \mathrm{h}'(\to \pi^+\pi^-)\chi_1\chi_2(\to \chi_1\mathrm{e}^+\mathrm{e}^-)$ final state. The linear interpolation between the points is added for better visualisation.

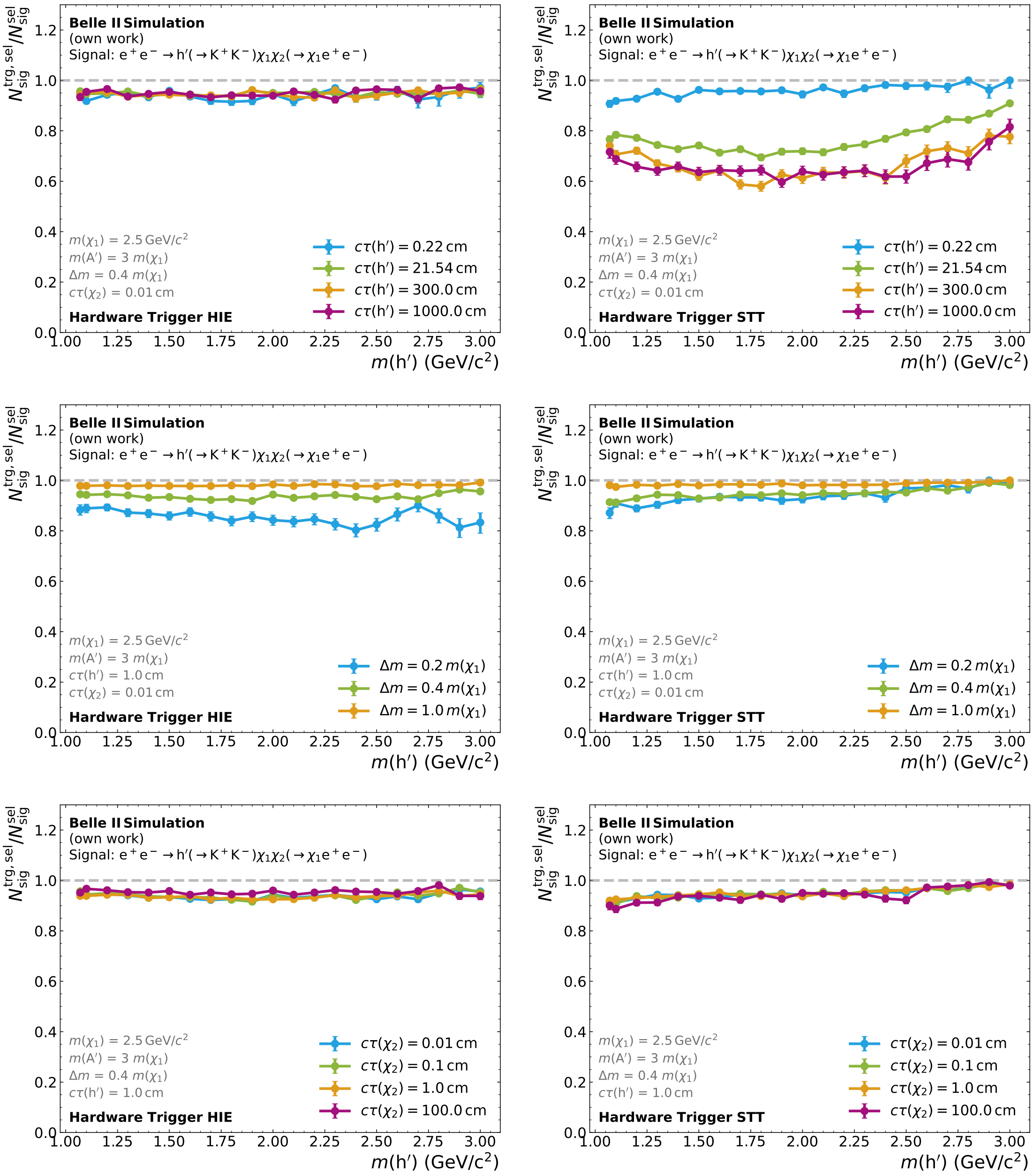

Figure D.2: Fraction of events that are selected and triggered by the HIE (left) and STT L1 trigger line (right) to all selected events. The selected events are selected with the selections from Tables 6.1 and 6.2 (excluding the selection on E_{hie}). The performance is shown as a function of the dark Higgs mass for several variations of the other model parameters: $c\tau(\text{h}')$ (top), Δm (center), and $c\tau(\chi_2)$ (bottom). The plots show the $\text{e}^+\text{e}^- \rightarrow \text{h}'(\rightarrow \text{K}^+\text{K}^-)\chi_1\chi_2(\rightarrow \chi_1\text{e}^+\text{e}^-)$ final state. The linear interpolation between the points is added for better visualisation.

Appendix E

Signal Width Fits

In this part of the appendix, additional material for the parametrization of the signal, described in Section 8.1, is given.

Figs. E.1 and E.2 show for some example model parameter configurations signal shape fits of the $\mathrm{e}^+\mathrm{e}^- \to \mathrm{h}'(\to \pi^+\pi^-)\chi_1\chi_2(\to \chi_1\mathrm{e}^+\mathrm{e}^-)$ and $\mathrm{e}^+\mathrm{e}^- \to \mathrm{h}'(\to \mathrm{K}^+\mathrm{K}^-)\chi_1\chi_2(\to \chi_1\mathrm{e}^+\mathrm{e}^-)$ final state, respectively. The extracted signal width together with a linear fit for the interpolation between the mass points is shown in Figs. E.3 to E.5 for all three considered final states. The plots show the extracted signal width as a function of the h' mass for variations of the dark Higgs lifetime, the mass splitting, the χ_2 lifetime, and the mass of the A'.

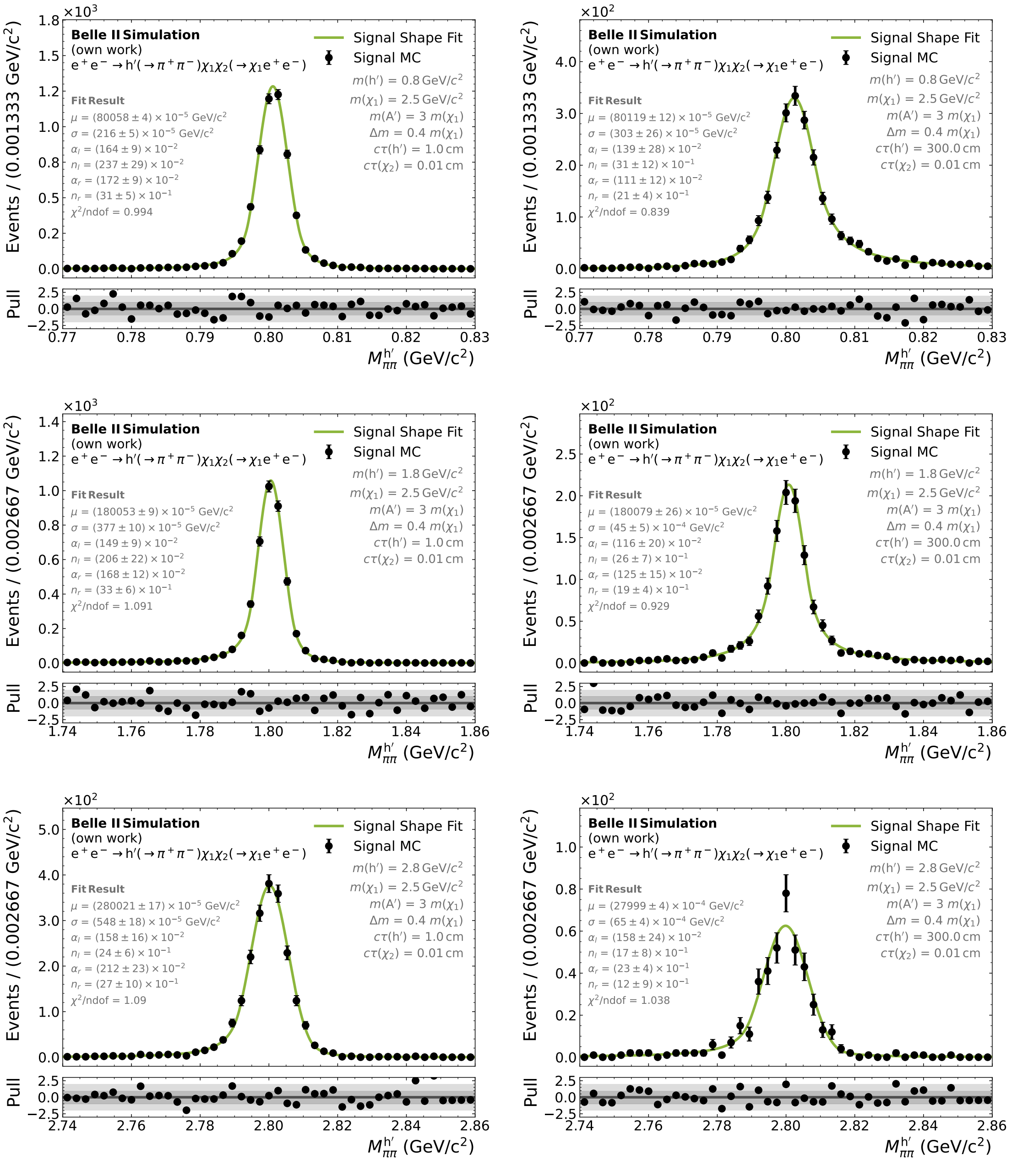

Figure E.1: Signal shape fit examples for the $e^+e^- \to h'(\to \pi^+\pi^-)\chi_1\chi_2(\to \chi_1 e^+e^-)$ final state. The plots show fits on the reconstructed dark Higgs mass using a DSCB function. Plots on the left are produced with a dark Higgs lifetime set to $c\tau(h') = 1.0\,\mathrm{cm}$, while the plots on the right show the corresponding fits for $c\tau(h') = 300.0\,\mathrm{cm}$. The dark Higgs mass is choses as $m(h') = 0.8\,\mathrm{GeV/c^2}$ (top), $m(h') = 1.8\,\mathrm{GeV/c^2}$ (center), and $m(h') = 2.8\,\mathrm{GeV/c^2}$ (bottom). The values of all other model parameters are fixed to the values reported in the plots. The extracted fit parameters and their uncertainty are also shown for each fit in the corresponding plot. All selection requirements from Tables 6.1 and 6.2 are applied.

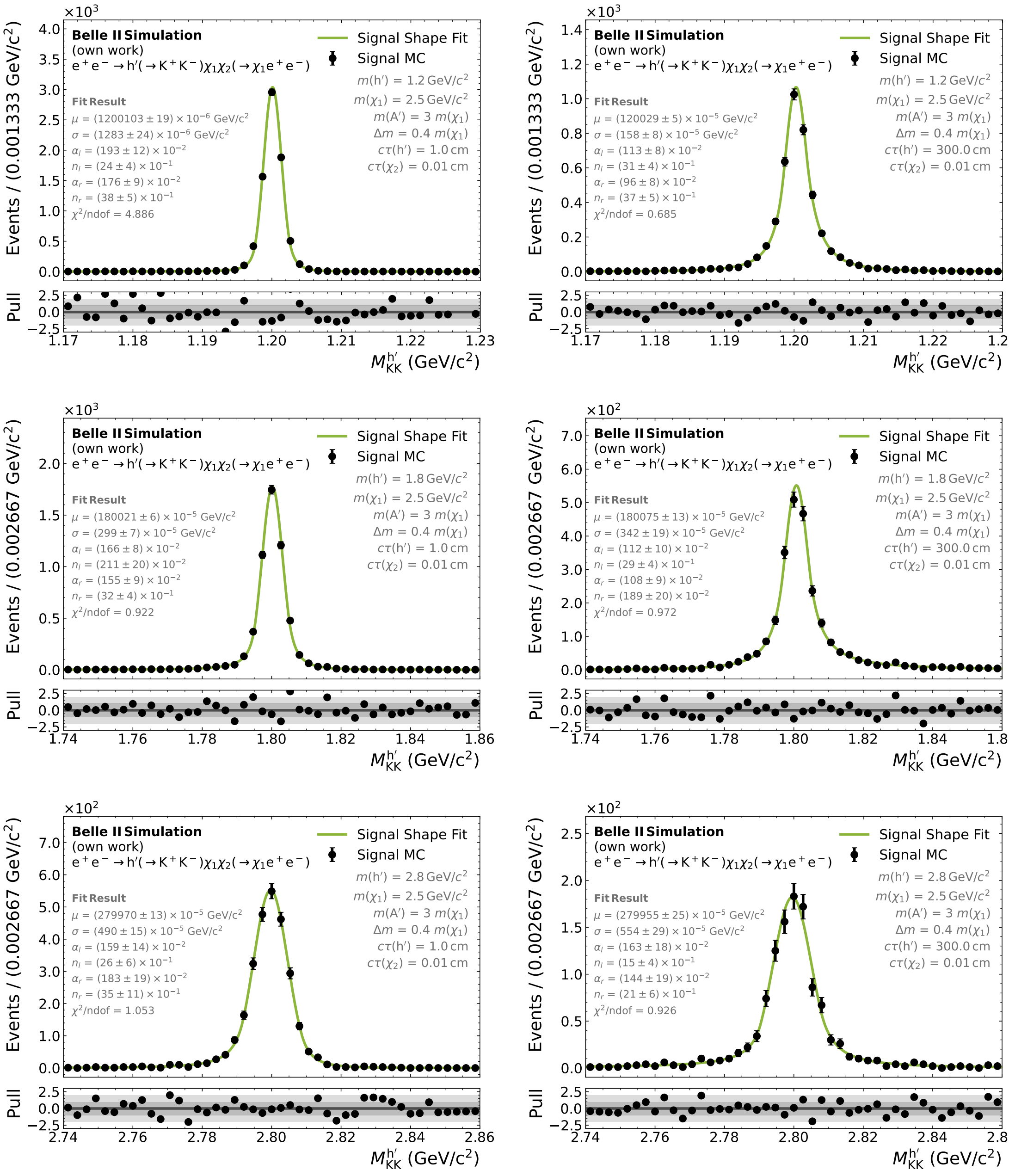

Figure E.2: Signal shape fit examples for the $e^+e^- \to h'(\to K^+K^-)\chi_1\chi_2(\to \chi_1 e^+e^-)$ final state. The plots show fits on the reconstructed dark Higgs mass using a DSCB function. Plots on the left are produced with a dark Higgs lifetime set to $c\tau(h') = 1.0\,\mathrm{cm}$, while the plots on the right show the corresponding fits for $c\tau(h') = 300.0\,\mathrm{cm}$. The dark Higgs mass is choses as $m(h') = 1.2\,\mathrm{GeV/c^2}$ (top), $m(h') = 1.8\,\mathrm{GeV/c^2}$ (center), and $m(h') = 2.8\,\mathrm{GeV/c^2}$ (bottom). The values of all other model parameters are fixed to the values reported in the plots. The extracted fit parameters and their uncertainty are also shown for each fit in the corresponding plot. All selection requirements from Tables 6.1 and 6.2 are applied.

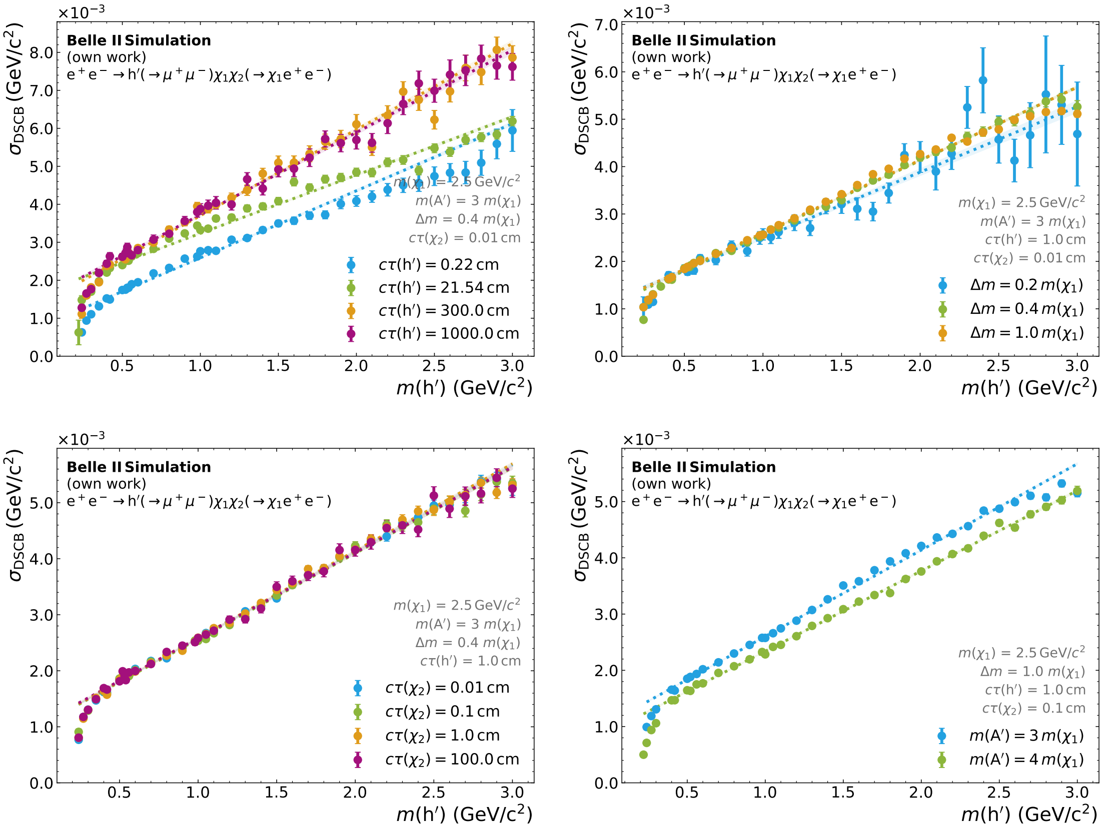

Figure E.3: Extracted width σ_{DSCB} of the DSCB shape fit as a function of the dark Higgs mass. The plots show the $\mathrm{e}^+\mathrm{e}^- \rightarrow \mathrm{h}'(\rightarrow \mu^+\mu^-)\chi_1\chi_2(\rightarrow \chi_1\mathrm{e}^+\mathrm{e}^-)$ final state for several variations of the model parameters $c\tau(\mathrm{h}')$ (upper left), mass splitting Δm (upper right), $c\tau(\chi_2)$ (lower left), and $m(\mathrm{A}')$ (lower right). The linear fit used to interpolate between the mass points is shown in the same colours used for the variation of the model parameters.

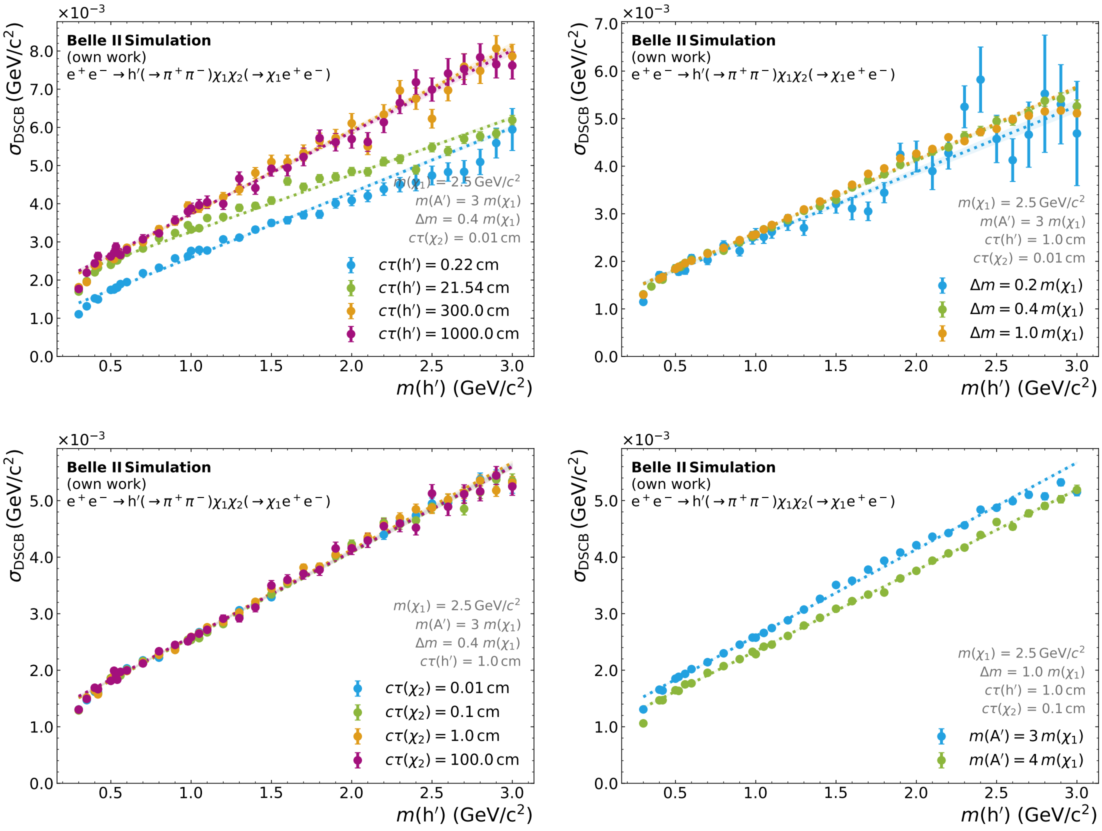

Figure E.4: Extracted width σ_{DSCB} of the DSCB shape fit as a function of the dark Higgs mass. The plots show the $\mathrm{e^+e^-} \to \mathrm{h'}(\to \pi^+\pi^-)\chi_1\chi_2(\to \chi_1\mathrm{e^+e^-})$ final state for several variations of the model parameters $c\tau(\mathrm{h'})$ (upper left), mass splitting Δm (upper right), $c\tau(\chi_2)$ (lower left), and $m(\mathrm{A'})$ (lower right). The linear fit used to interpolate between the mass points is shown in the same colours used for the variation of the model parameters.

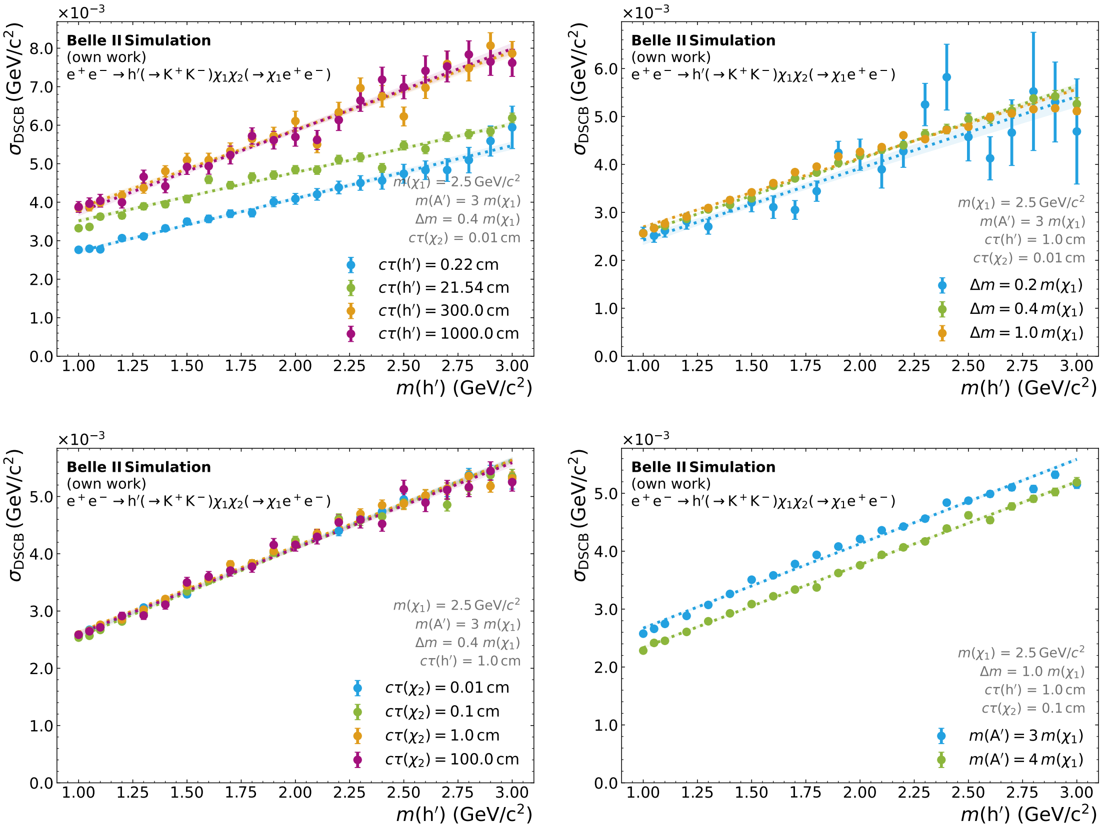

Figure E.5: Extracted width σ_{DSCB} of the DSCB shape fit as a function of the dark Higgs mass. The plots show the $e^+e^- \to h'(\to K^+K^-)\chi_1\chi_2(\to \chi_1 e^+e^-)$ final state for several variations of the model parameters $c\tau(h')$ (upper left), mass splitting Δm (upper right), $c\tau(\chi_2)$ (lower left), and $m(A')$ (lower right). The linear fit used to interpolate between the mass points is shown in the same colours used for the variation of the model parameters.

Appendix F

Additional Control Region Plots

In this appendix I present additional plots from the studies of the control regions. More precisely, further studies on the contribution of cosmic muons in the pointing angle control regions are shown.

In Fig. F.1, I show the comparison of the ϕ distribution of the μ^- track between data and simulation. The correlation between the track momenta of the μ^+ and μ^- track is shown in Fig. F.2. With this study, the assumption that the track-finding algorithm artificially created two tracks out of a single track created by a cosmic muon is substantiated.

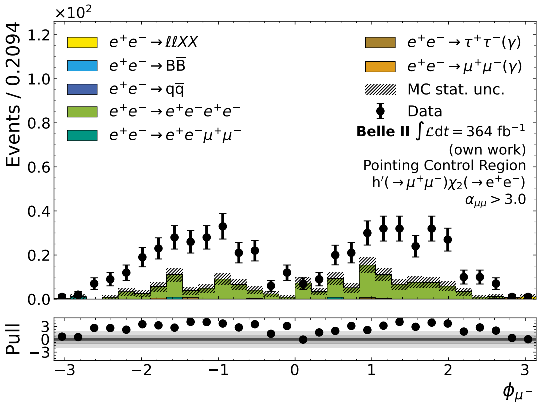

Figure F.1: ϕ distribution of the μ^- track (right) in the $h' \to \mu^+\mu^-$ reconstruction channel of the pointing control region. The plot shows only the region $\alpha^{h'}_{\mu\mu}$ where the huge discrepancy in Fig. 10.6 is observed.

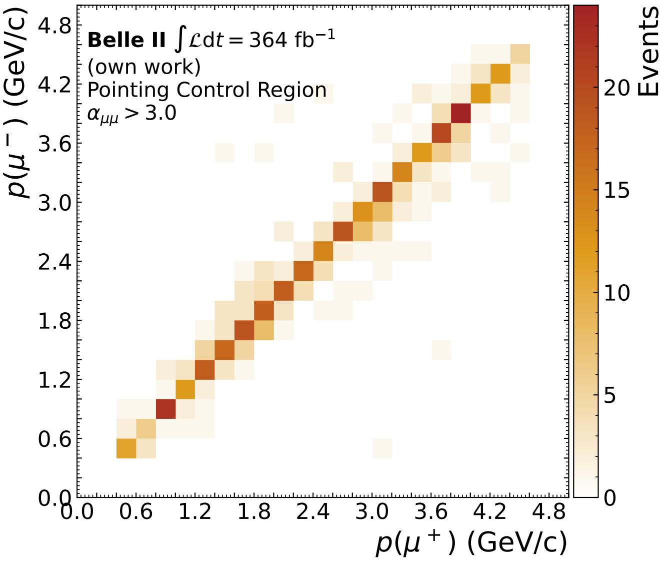

Figure F.2: Momentum of the μ^+ track versus momentum of the μ^- track on data in the pointing control region. The plot only shows the region $\alpha^{h'}_{\mu\mu} > 3.0$ where the huge discrepancy in Fig. 10.6 is observed.

Appendix G

Additional Results

In this part of the appendix, I show the model-independent upper limits on the production cross section $\sigma(\mathrm{e^+e^-} \to \mathrm{h}'\chi_1\chi_2)$ and the branching fractions $\mathcal{B}(\chi_2 \to \chi_1\mathrm{e^+e^-}) \times \mathcal{B}(\mathrm{h}' \to \mathrm{x^+x^-})$ as a function of the dark Higgs mass for different dark Higgs lifetimes. These are shown for all model parameter configurations that are presented in Table A.1. The corresponding plots can be found as Figs. G.1 to G.10. Note that as I chose the mass splitting directly, α_D has no impact on the event kinematics or the displacement of the vertices but only varies the cross section. Therefore the model-independent upper limits for $\alpha_\mathrm{D} = 0.5$ are identical to the corresponding ones with $\alpha_\mathrm{D} = 0.1$ and are therefore not shown explicitly.

Furthermore, I present the additional model-independent upper limits on $\sigma(\mathrm{e^+e^-} \to \mathrm{h}'\chi_1\chi_2) \times \mathcal{B}(\chi_2 \to \chi_1\mathrm{e^+e^-}) \times \mathcal{B}(\mathrm{h}' \to \mathrm{x^+x^-})$ as a function of the χ_1 mass for the model parameter configurations reported in Table A.2. The corresponding plots which show the upper limits for several χ_2 lifetime hypotheses are shown in Figs. G.11 to G.14.

Besides the model-independent upper limit, I show the remaining exclusion limits in the plane of the dark Higgs mass $m(\mathrm{h}')$ and the sine of the mixing angle θ for all model parameter configurations from Table A.1. These can be found as Figs. G.15 to G.19.

The additional exclusions in the plane of the χ_1 mass and the dimensionless variable $y = \epsilon^2\alpha_\mathrm{D}(m(\chi_1)/m(\mathrm{A}'))^4$ for all model parameter configurations from Table A.2 can be founf in Figs. G.20 to G.22.

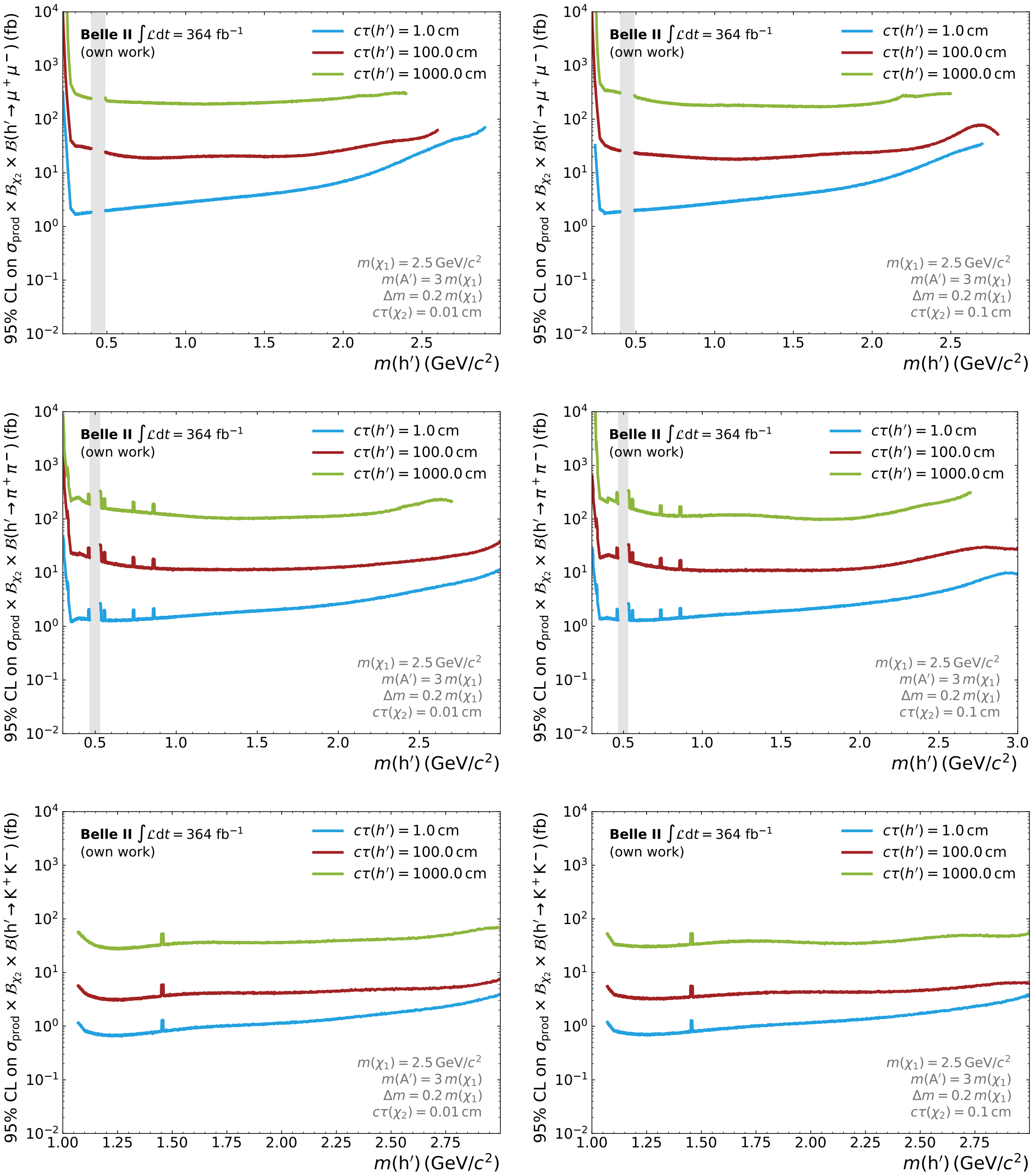

Figure G.1: 95% CL upper limits on the product of the production cross section $\sigma(e^+e^- \to h'\chi_1\chi_2)$ (denoted as σ_{prod}) and the branching fractions $\mathcal{B}(\chi_2 \to \chi_1 e^+e^-) \times \mathcal{B}(h' \to x^+x^-)$ for the different final states $h' \to \mu^+\mu^-$ (top), $h' \to \pi^+\pi^-$ (center), and $h' \to K^+K^-$ (bottom). Different lifetime hypothesis of the h' are indicated with different colours: $c\tau(h') = 1.0\,\text{cm}$ (cyan), $c\tau(h') = 100.0\,\text{cm}$ (red), and $c\tau(h') = 1000.0\,\text{cm}$ (light green). The left side shows a χ_2 lifetime hypothesis of $c\tau(\chi_2) = 0.01\,\text{cm}$ and the right $c\tau(\chi_2) = 0.1\,\text{cm}$. The remaining model parameters are fixed to $m(\chi_1) = 2.5\,\text{GeV/c}^2$, $m(A') = 3\,m(\chi_1)$, and $\Delta m = 0.2\,m(\chi_1)$. The fully vetoed K^0_S region is marked with a grey band.

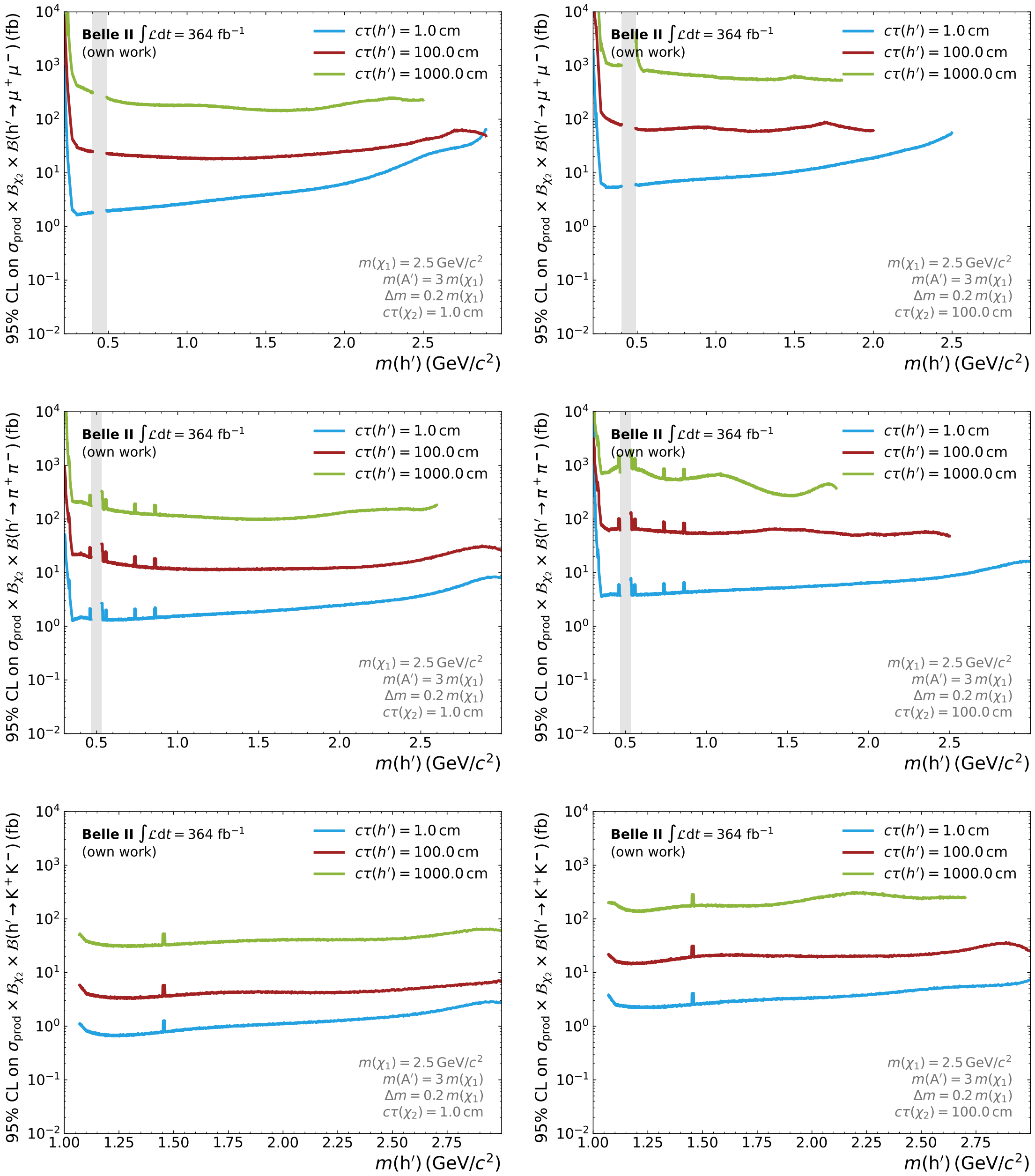

Figure G.2: 95% CL upper limits on the product of the production cross section $\sigma(e^+e^- \to h'\chi_1\chi_2)$ (denoted as σ_{prod}) and the branching fractions $\mathcal{B}(\chi_2 \to \chi_1 e^+e^-) \times \mathcal{B}(h' \to x^+x^-)$ for the different final states $h' \to \mu^+\mu^-$ (top), $h' \to \pi^+\pi^-$ (center), and $h' \to K^+K^-$ (bottom). Different lifetime hypothesis of the h' are indicated with different colours: $c\tau(h') = 1.0\,\mathrm{cm}$ (cyan), $c\tau(h') = 100.0\,\mathrm{cm}$ (red), and $c\tau(h') = 1000.0\,\mathrm{cm}$ (light green). The left side shows a χ_2 lifetime hypothesis of $c\tau(\chi_2) = 1.0\,\mathrm{cm}$ and the right $c\tau(\chi_2) = 100.0\,\mathrm{cm}$. The remaining model parameters are fixed to $m(\chi_1) = 2.5\,\mathrm{GeV/c^2}$, $m(A') = 3\,m(\chi_1)$, and $\Delta m = 0.2\,m(\chi_1)$. The fully vetoed K^0_S region is marked with a grey band.

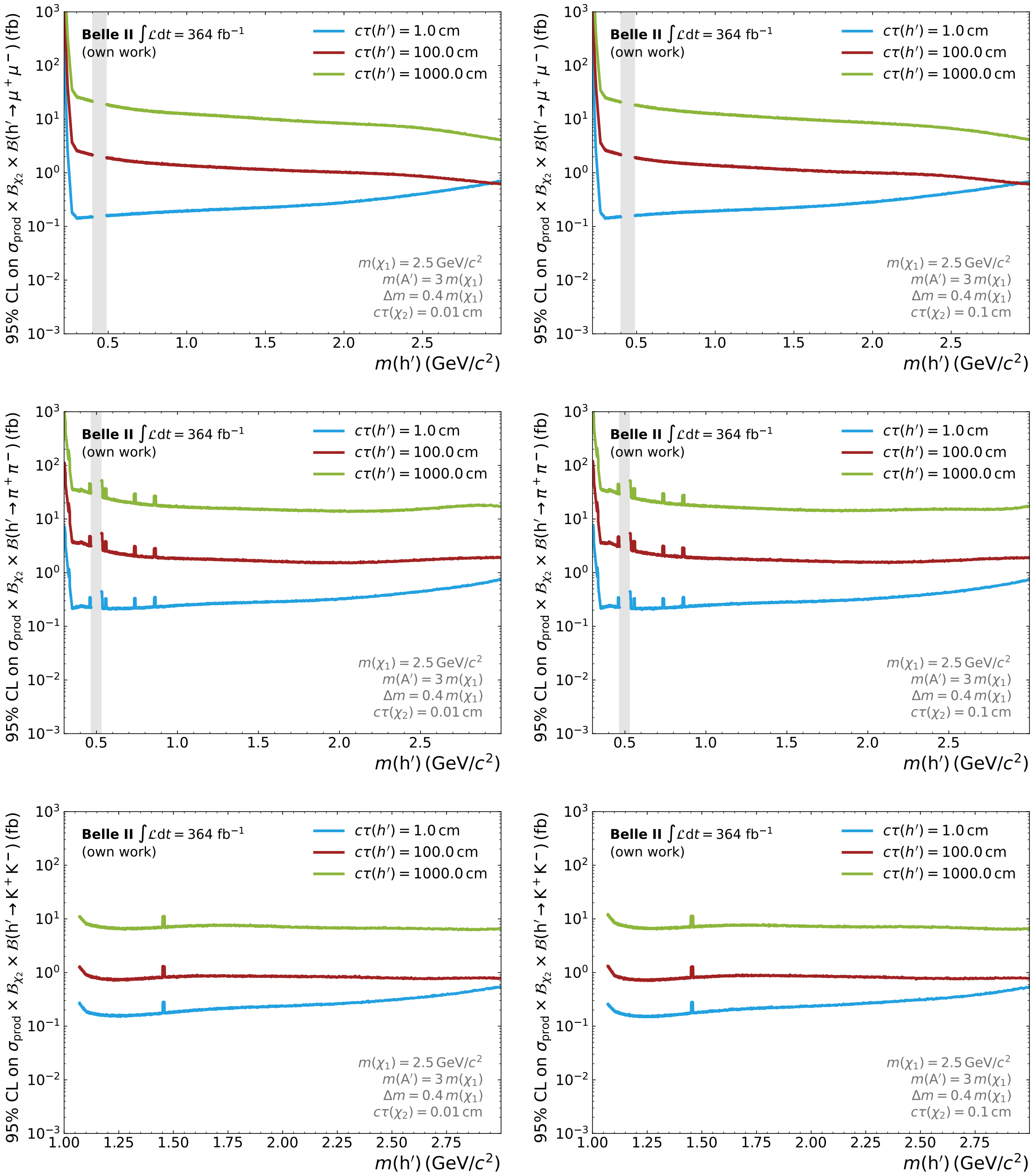

Figure G.3: 95% CL upper limits on the product of the production cross section $\sigma(e^+e^- \to h'\chi_1\chi_2)$ (denoted as σ_{prod}) and the branching fractions $\mathcal{B}(\chi_2 \to \chi_1 e^+e^-) \times \mathcal{B}(h' \to x^+x^-)$ for the different final states $h' \to \mu^+\mu^-$ (top), $h' \to \pi^+\pi^-$ (center), and $h' \to K^+K^-$ (bottom). Different lifetime hypothesis of the h' are indicated with different colours: $c\tau(h') = 1.0\,\text{cm}$ (cyan), $c\tau(h') = 100.0\,\text{cm}$ (red), and $c\tau(h') = 1000.0\,\text{cm}$ (light green). The left side shows a χ_2 lifetime hypothesis of $c\tau(\chi_2) = 0.01\,\text{cm}$ and the right $c\tau(\chi_2) = 0.1\,\text{cm}$. The remaining model parameters are fixed to $m(\chi_1) = 2.5\,\text{GeV/c}^2$, $m(A') = 3\,m(\chi_1)$, and $\Delta m = 0.4\,m(\chi_1)$. The fully vetoed K^0_S region is marked with a grey band.

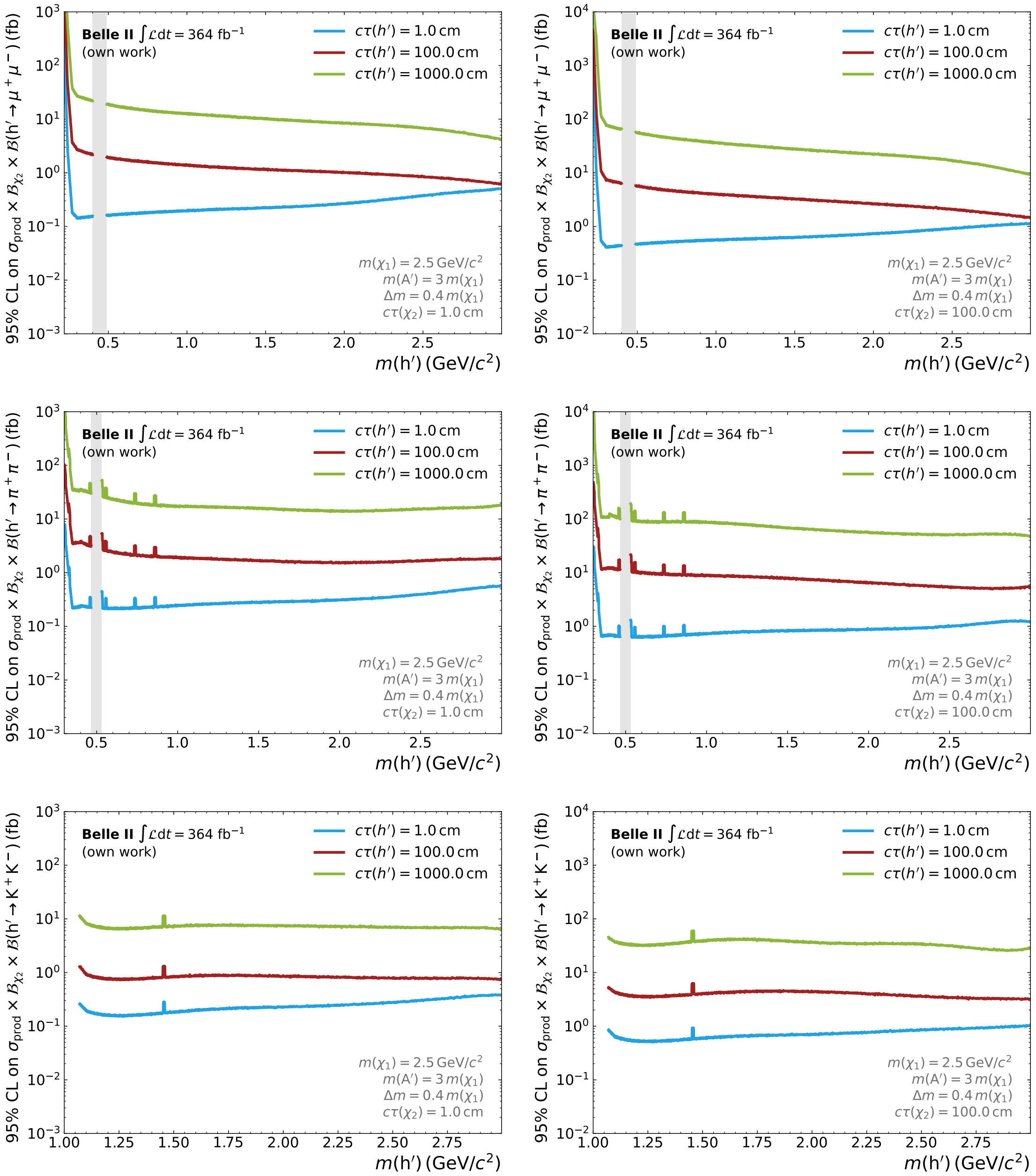

Figure G.4: 95% CL upper limits on the product of the production cross section $\sigma(e^+e^- \to h'\chi_1\chi_2)$ (denoted as σ_{prod}) and the branching fractions $\mathcal{B}(\chi_2 \to \chi_1 e^+e^-) \times \mathcal{B}(h' \to x^+x^-)$ for the different final states $h' \to \mu^+\mu^-$ (top), $h' \to \pi^+\pi^-$ (center), and $h' \to K^+K^-$ (bottom). Different lifetime hypothesis of the h$'$ are indicated with different colours: $c\tau(h') = 1.0$ cm (cyan), $c\tau(h') = 100.0$ cm (red), and $c\tau(h') = 1000.0$ cm (light green). The left side shows a χ_2 lifetime hypothesis of $c\tau(\chi_2) = 1.0$ cm and the right $c\tau(\chi_2) = 100.0$ cm. The remaining model parameters are fixed to $m(\chi_1) = 2.5\,\text{GeV}/c^2$, $m(A') = 3\,m(\chi_1)$, and $\Delta m = 0.4\,m(\chi_1)$. The fully vetoed K^0_S region is marked with a grey band.

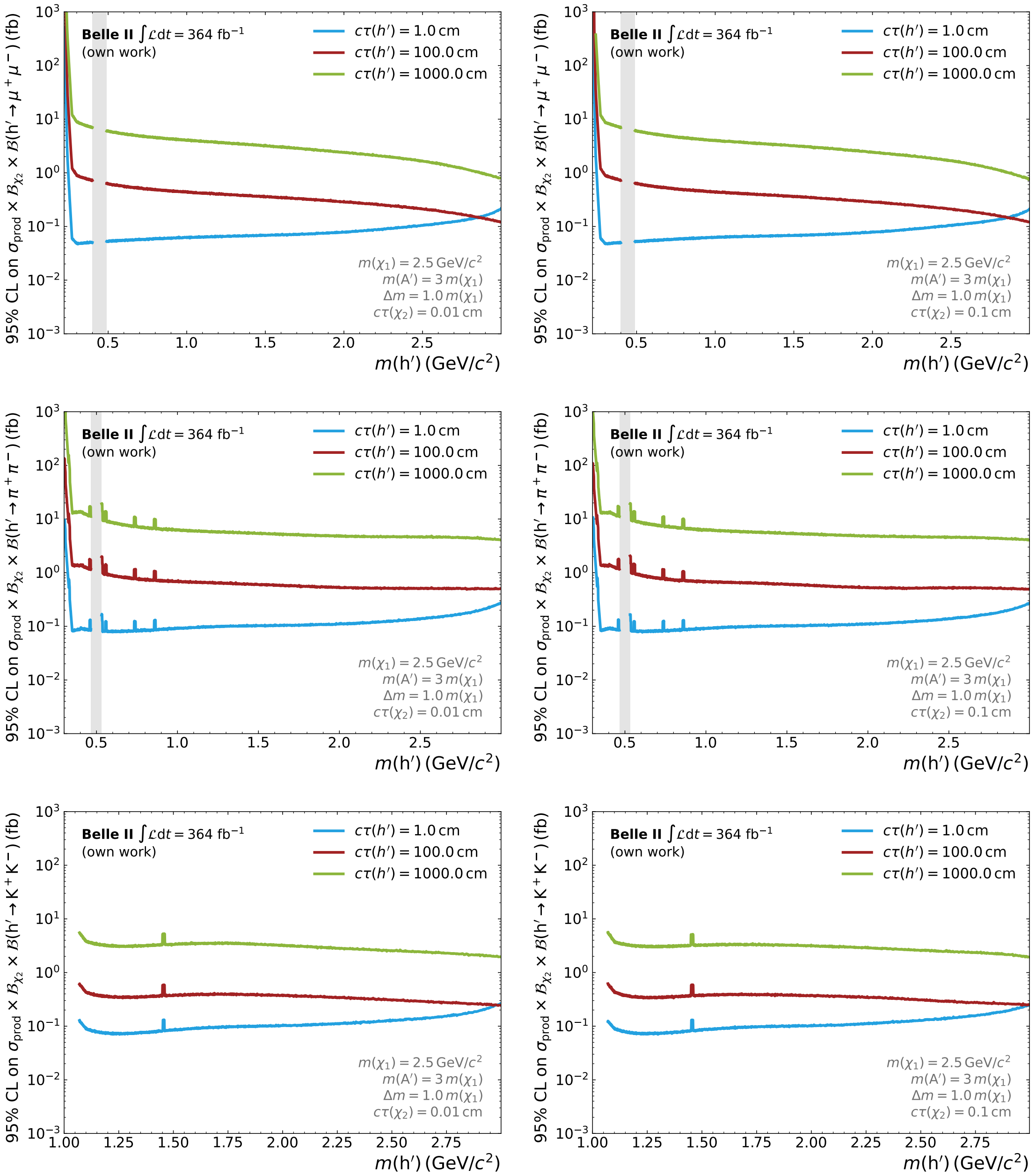

Figure G.5: 95% CL upper limits on the product of the production cross section $\sigma(e^+e^- \to h'\chi_1\chi_2)$ (denoted as σ_{prod}) and the branching fractions $\mathcal{B}(\chi_2 \to \chi_1 e^+e^-) \times \mathcal{B}(h' \to x^+x^-)$ for the different final states $h' \to \mu^+\mu^-$ (top), $h' \to \pi^+\pi^-$ (center), and $h' \to K^+K^-$ (bottom). Different lifetime hypothesis of the h' are indicated with different colours: $c\tau(h') = 1.0\,\text{cm}$ (cyan), $c\tau(h') = 100.0\,\text{cm}$ (red), and $c\tau(h') = 1000.0\,\text{cm}$ (light green). The left side shows a χ_2 lifetime hypothesis of $c\tau(\chi_2) = 0.01\,\text{cm}$ and the right $c\tau(\chi_2) = 0.1\,\text{cm}$. The remaining model parameters are fixed to $m(\chi_1) = 2.5\,\text{GeV/c}^2$, $m(A') = 3\,m(\chi_1)$, and $\Delta m = 1.0\,m(\chi_1)$. The fully vetoed K_S^0 region is marked with a grey band.

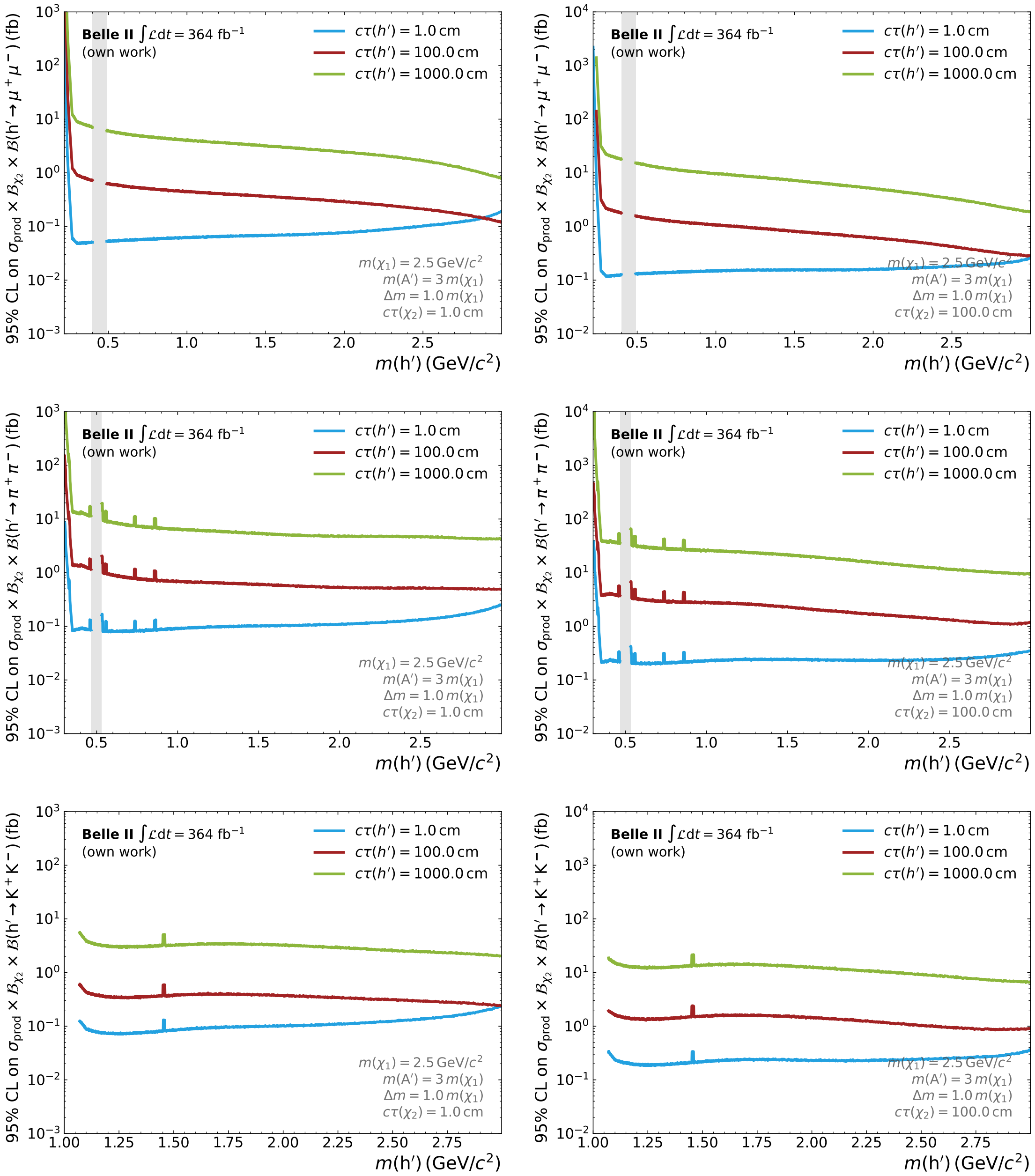

Figure G.6: 95% CL upper limits on the product of the production cross section $\sigma(e^+e^- \to h'\chi_1\chi_2)$ (denoted as σ_{prod}) and the branching fractions $\mathcal{B}(\chi_2 \to \chi_1 e^+e^-) \times \mathcal{B}(h' \to x^+x^-)$ for the different final states $h' \to \mu^+\mu^-$ (top), $h' \to \pi^+\pi^-$ (center), and $h' \to K^+K^-$ (bottom). Different lifetime hypothesis of the h' are indicated with different colours: $c\tau(h') = 1.0\,\text{cm}$ (cyan), $c\tau(h') = 100.0\,\text{cm}$ (red), and $c\tau(h') = 1000.0\,\text{cm}$ (light green). The left side shows a χ_2 lifetime hypothesis of $c\tau(\chi_2) = 1.0\,\text{cm}$ and the right $c\tau(\chi_2) = 100.0\,\text{cm}$. The remaining model parameters are fixed to $m(\chi_1) = 2.5\,\text{GeV/c}^2$, $m(A') = 3\,m(\chi_1)$, and $\Delta m = 1.0\,m(\chi_1)$. The fully vetoed K^0_S region is marked with a grey band.

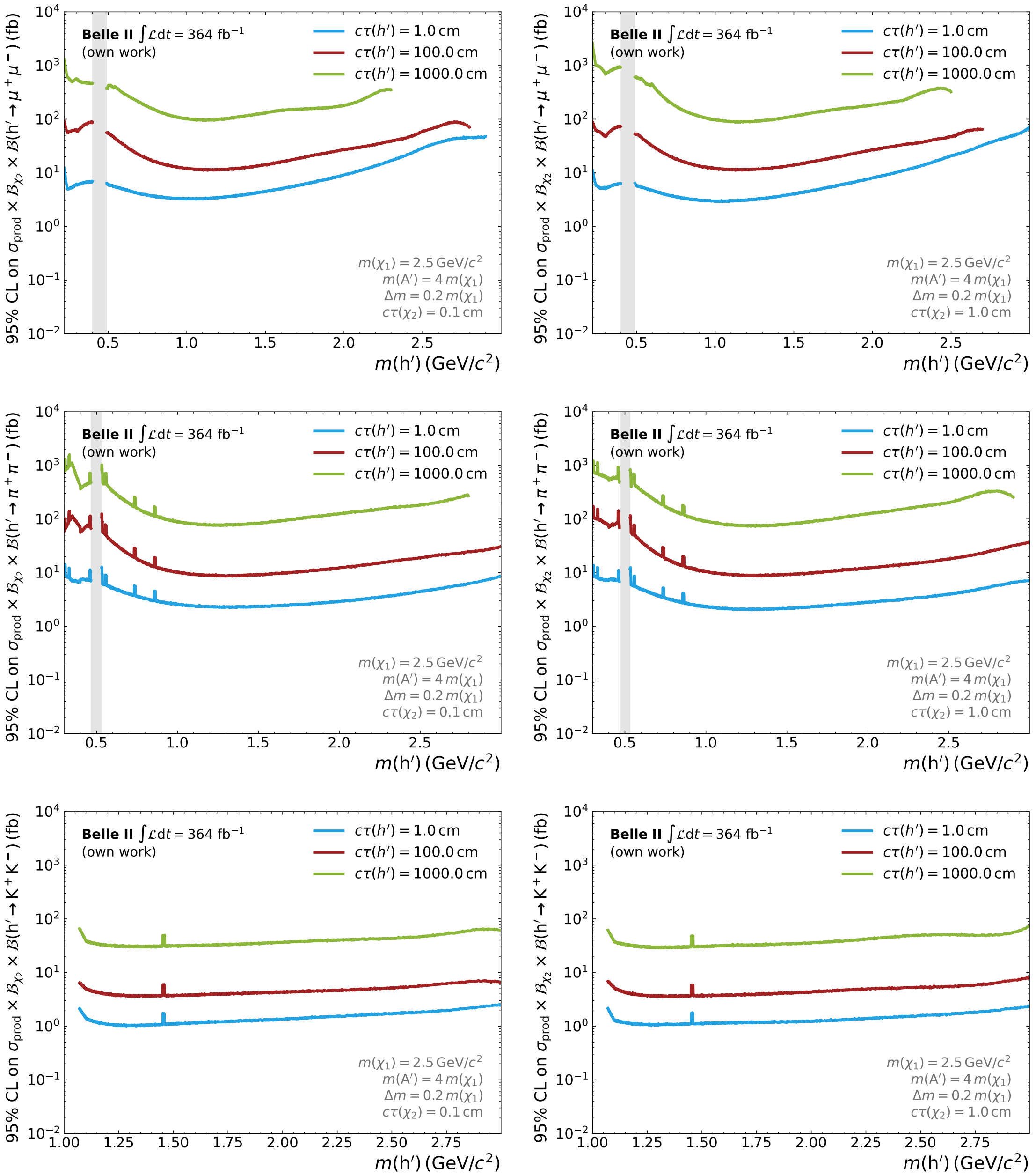

Figure G.7: 95% CL upper limits on the product of the production cross section $\sigma(\mathrm{e^+e^-} \rightarrow \mathrm{h'}\chi_1\chi_2)$ (denoted as σ_{prod}) and the branching fractions $\mathcal{B}(\chi_2 \rightarrow \chi_1\mathrm{e^+e^-}) \times \mathcal{B}(\mathrm{h'} \rightarrow \mathrm{x^+x^-})$ for the different final states $\mathrm{h'} \rightarrow \mu^+\mu^-$ (top), $\mathrm{h'} \rightarrow \pi^+\pi^-$ (center), and $\mathrm{h'} \rightarrow \mathrm{K^+K^-}$ (bottom). Different lifetime hypothesis of the $\mathrm{h'}$ are indicated with different colours: $c\tau(\mathrm{h'}) = 1.0\,\mathrm{cm}$ (cyan), $c\tau(\mathrm{h'}) = 100.0\,\mathrm{cm}$ (red), and $c\tau(\mathrm{h'}) = 1000.0\,\mathrm{cm}$ (light green). The left side shows a χ_2 lifetime hypothesis of $c\tau(\chi_2) = 0.1\,\mathrm{cm}$ and the right $c\tau(\chi_2) = 1.0\,\mathrm{cm}$. The remaining model parameters are fixed to $m(\chi_1) = 2.5\,\mathrm{GeV/c^2}$, $m(\mathrm{A'}) = 4\,m(\chi_1)$, and $\Delta m = 0.2\,m(\chi_1)$. The fully vetoed $\mathrm{K_S^0}$ region is marked with a grey band.

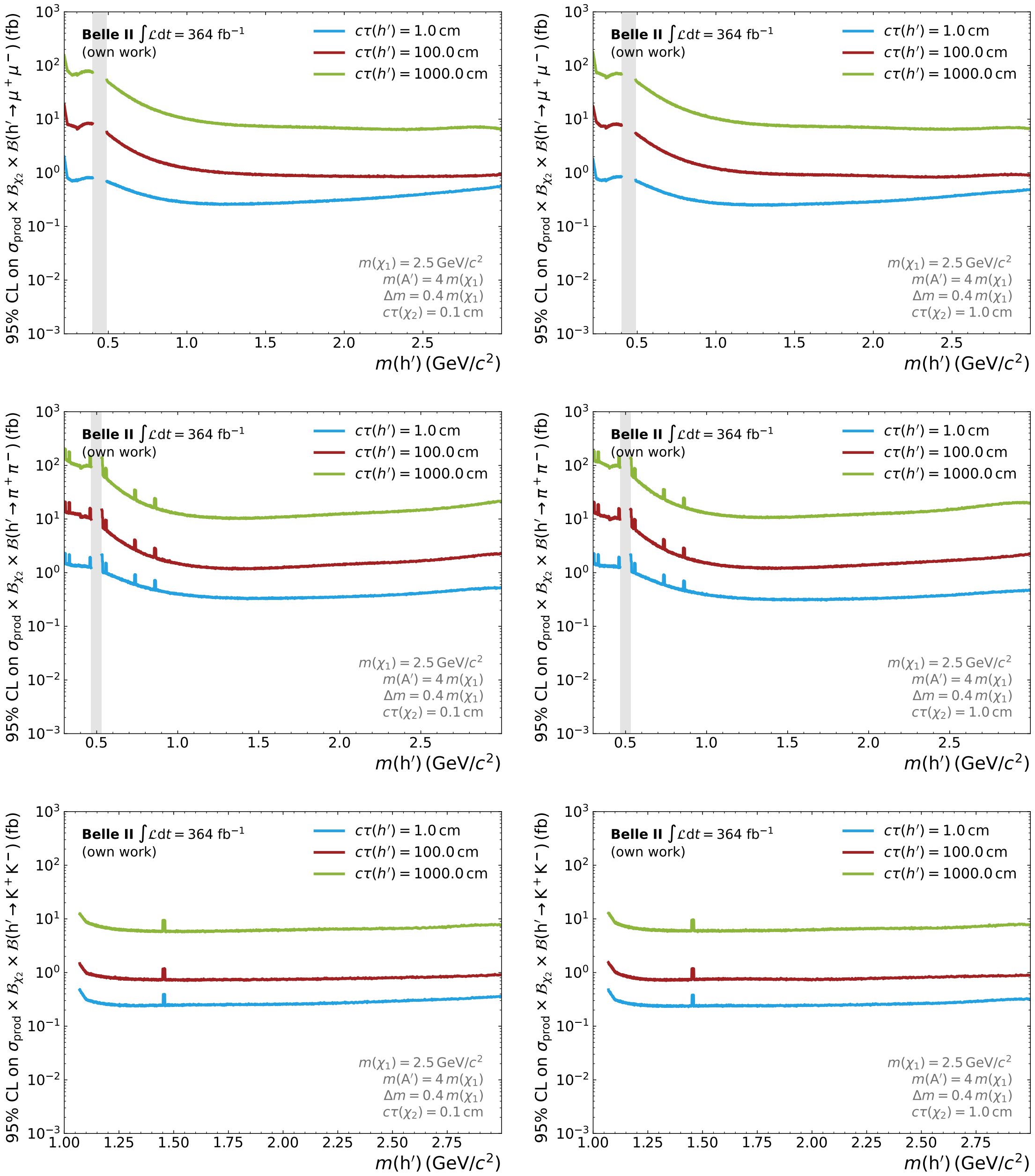

Figure G.8: 95% CL upper limits on the product of the production cross section $\sigma(\mathrm{e^+e^-} \to \mathrm{h}'\chi_1\chi_2)$ (denoted as σ_{prod}) and the branching fractions $\mathcal{B}(\chi_2 \to \chi_1\mathrm{e^+e^-}) \times \mathcal{B}(\mathrm{h}' \to \mathrm{x^+x^-})$ for the different final states $\mathrm{h}' \to \mu^+\mu^-$ (top), $\mathrm{h}' \to \pi^+\pi^-$ (center), and $\mathrm{h}' \to \mathrm{K^+K^-}$ (bottom). Different lifetime hypothesis of the h' are indicated with different colours: $c\tau(\mathrm{h}') = 1.0\,\mathrm{cm}$ (cyan), $c\tau(\mathrm{h}') = 100.0\,\mathrm{cm}$ (red), and $c\tau(\mathrm{h}') = 1000.0\,\mathrm{cm}$ (light green). The left side shows a χ_2 lifetime hypothesis of $c\tau(\chi_2) = 0.1\,\mathrm{cm}$ and the right $c\tau(\chi_2) = 1.0\,\mathrm{cm}$. The remaining model parameters are fixed to $m(\chi_1) = 2.5\,\mathrm{GeV/c^2}$, $m(\mathrm{A}') = 4\,m(\chi_1)$, and $\Delta m = 0.4\,m(\chi_1)$. The fully vetoed $\mathrm{K^0_S}$ region is marked with a grey band.

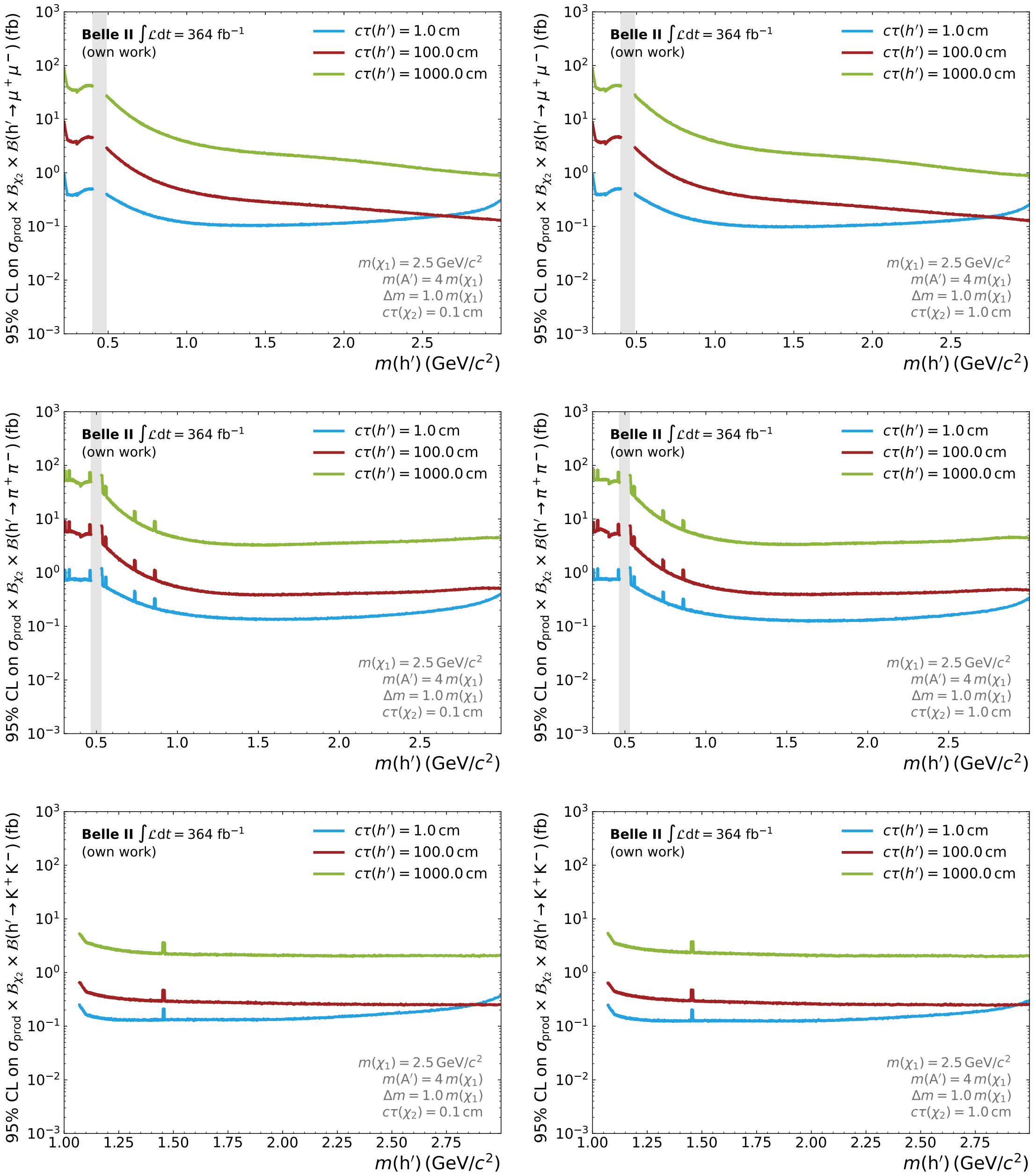

Figure G.9: 95% CL upper limits on the product of the production cross section $\sigma(e^+e^- \to h'\chi_1\chi_2)$ (denoted as σ_{prod}) and the branching fractions $\mathcal{B}(\chi_2 \to \chi_1 e^+e^-) \times \mathcal{B}(h' \to x^+x^-)$ for the different final states $h' \to \mu^+\mu^-$ (top), $h' \to \pi^+\pi^-$ (center), and $h' \to K^+K^-$ (bottom). Different lifetime hypothesis of the h' are indicated with different colours: $c\tau(h') = 1.0\,\text{cm}$ (cyan), $c\tau(h') = 100.0\,\text{cm}$ (red), and $c\tau(h') = 1000.0\,\text{cm}$ (light green). The left side shows a χ_2 lifetime hypothesis of $c\tau(\chi_2) = 0.1\,\text{cm}$ and the right $c\tau(\chi_2) = 1.0\,\text{cm}$. The remaining model parameters are fixed to $m(\chi_1) = 2.5\,\text{GeV/c}^2$, $m(A') = 4\,m(\chi_1)$, and $\Delta m = 1.0\,m(\chi_1)$. The fully vetoed K^0_S region is marked with a grey band.

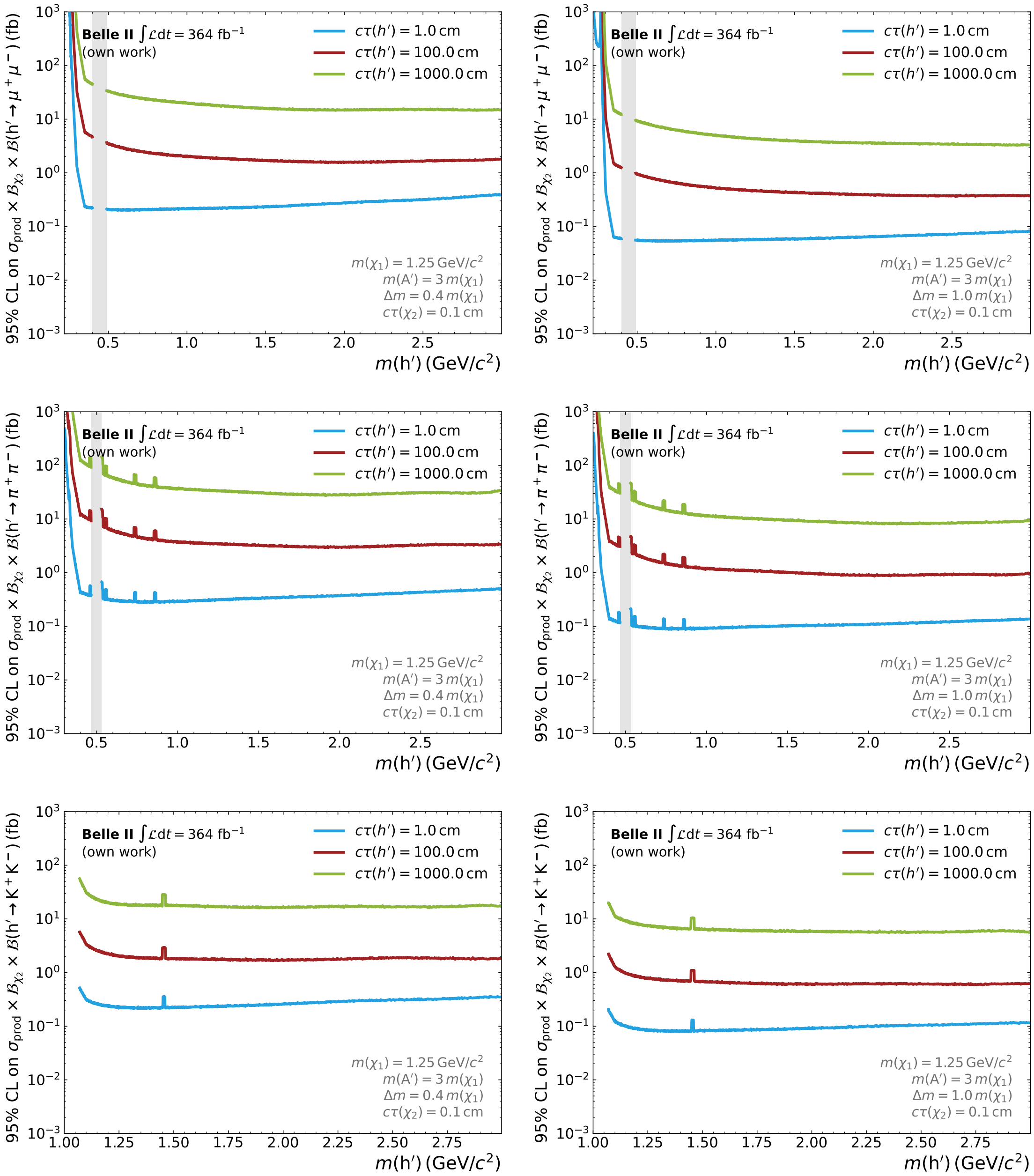

Figure G.10: 95% CL upper limits on the product of the production cross section $\sigma(e^+e^- \to h'\chi_1\chi_2)$ (denoted as σ_{prod}) and the branching fractions $\mathcal{B}(\chi_2 \to \chi_1 e^+e^-) \times \mathcal{B}(h' \to x^+x^-)$ for the different final states $h' \to \mu^+\mu^-$ (top), $h' \to \pi^+\pi^-$ (center), and $h' \to K^+K^-$ (bottom). Different lifetime hypothesis of the h' are indicated with different colours: $c\tau(h') = 1.0\,\text{cm}$ (cyan), $c\tau(h') = 100.0\,\text{cm}$ (red), and $c\tau(h') = 1000.0\,\text{cm}$ (light green). The left side shows a mass splitting of $\Delta m = 0.4\,m(\chi_1)$ and the right $\Delta m = 1.0\,m(\chi_1)$. The remaining model parameters are fixed to $m(\chi_1) = 1.25\,\text{GeV}/c^2$, $m(A') = 3\,m(\chi_1)$, and $c\tau(\chi_2) = 0.1\,\text{cm}$. The fully vetoed K^0_S region is marked with a grey band.

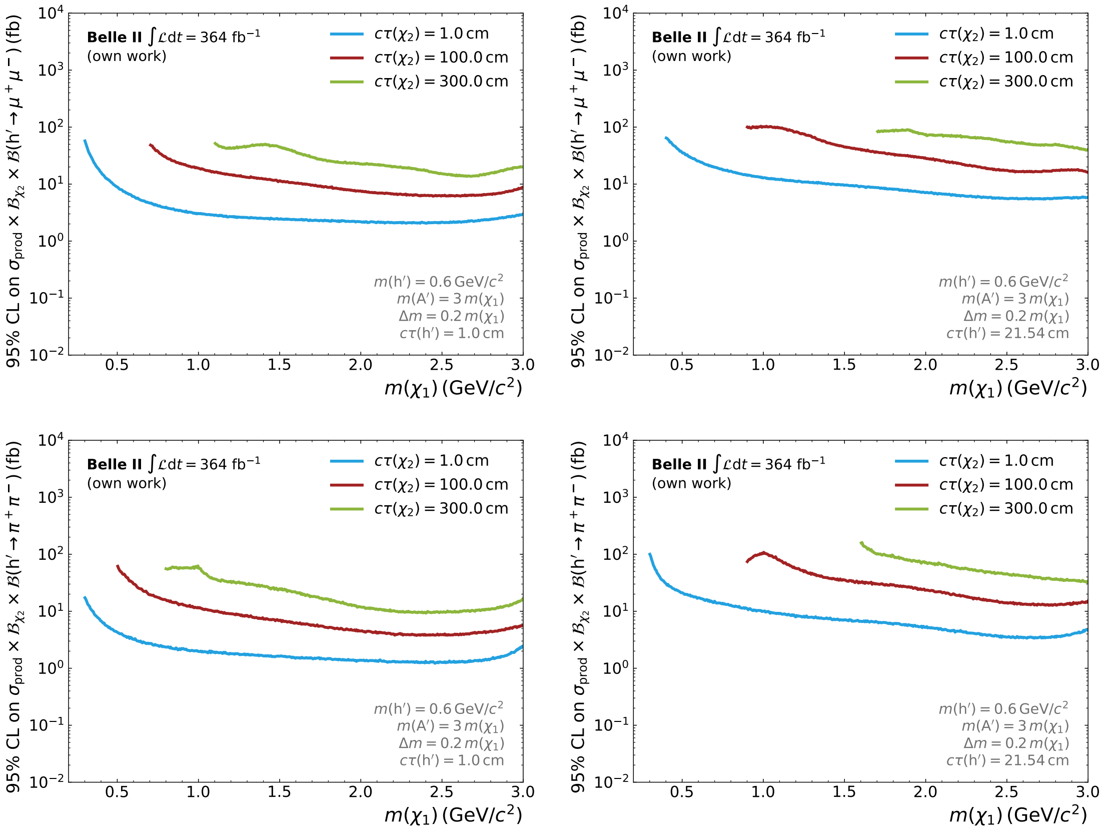

Figure G.11: 95% CL upper limits on the product of the production cross section $\sigma(\mathrm{e}^+\mathrm{e}^- \to \mathrm{h}'\chi_1\chi_2)$ (denoted as σ_{prod}) and the branching fractions $\mathcal{B}(\chi_2 \to \chi_1\mathrm{e}^+\mathrm{e}^-) \times \mathcal{B}(\mathrm{h}' \to \mathrm{x}^+\mathrm{x}^-)$ for the different final states $\mathrm{h}' \to \mu^+\mu^-$ (top) and $\mathrm{h}' \to \pi^+\pi^-$ (bottom). Different lifetime hypothesis of the χ_2 are indicated with different colours: $c\tau(\chi_2) = 1.0\,\mathrm{cm}$ (cyan), $c\tau(\chi_2) = 100.0\,\mathrm{cm}$ (red), and $c\tau(\chi_2) = 300.0\,\mathrm{cm}$ (light green). The left side shows a dark Higgs lifetime hypothesis of $c\tau(\mathrm{h}') = 1.0\,\mathrm{cm}$ and the right side shows $c\tau(\mathrm{h}') = 21.54\,\mathrm{cm}$. The remaining model parameters are fixed to $m(\mathrm{h}') = 0.6\,\mathrm{GeV/c^2}$, $m(\mathrm{A}') = 3\,m(\chi_1)$, and $\Delta m = 0.2\,m(\chi_1)$.

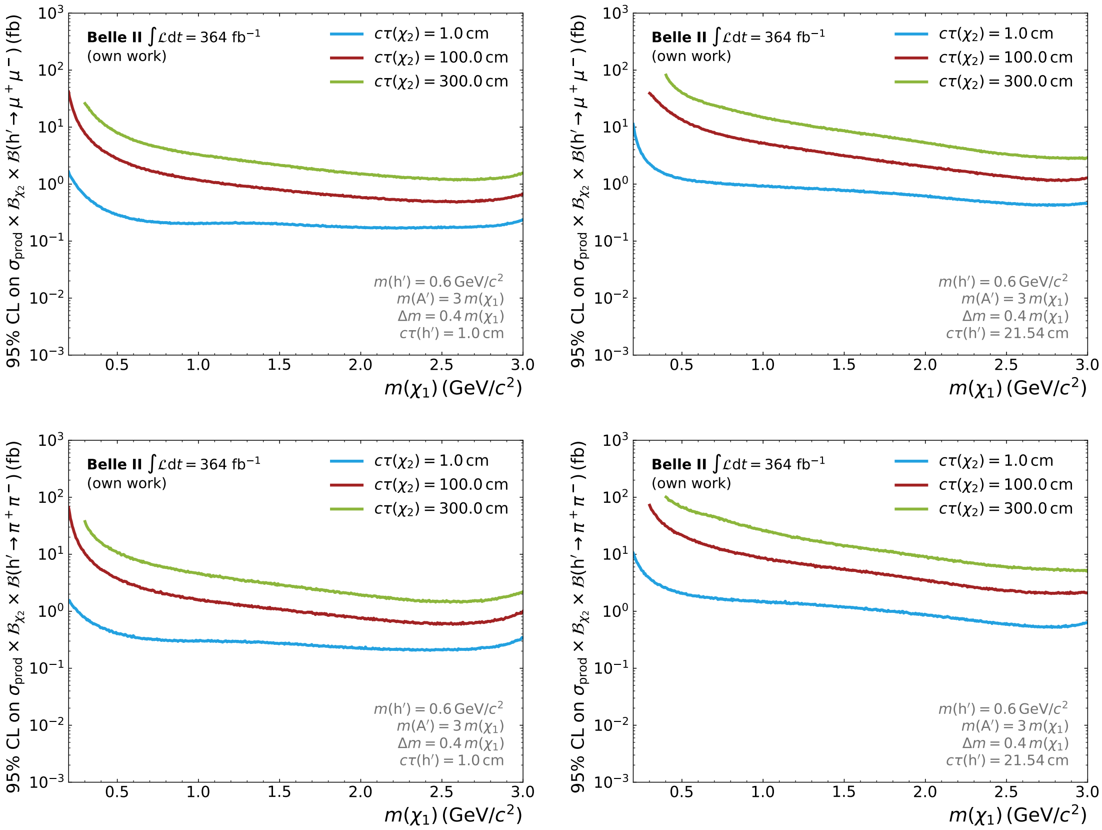

Figure G.12: 95% CL upper limits on the product of the production cross section $\sigma(e^+e^- \to h'\chi_1\chi_2)$ (denoted as σ_{prod}) and the branching fractions $\mathcal{B}(\chi_2 \to \chi_1 e^+e^-) \times \mathcal{B}(h' \to x^+x^-)$ for the different final states $h' \to \mu^+\mu^-$ (top) and $h' \to \pi^+\pi^-$ (bottom). Different lifetime hypothesis of the χ_2 are indicated with different colours: $c\tau(\chi_2) = 1.0$ cm (cyan), $c\tau(\chi_2) = 100.0$ cm (red), and $c\tau(\chi_2) = 300.0$ cm (light green). The left side shows a dark Higgs lifetime hypothesis of $c\tau(h') = 1.0$ cm and the right side shows $c\tau(h') = 21.54$ cm. The remaining model parameters are fixed to $m(h') = 0.6\,\text{GeV/c}^2$, $m(A') = 3\,m(\chi_1)$, and $\Delta m = 0.4\,m(\chi_1)$.

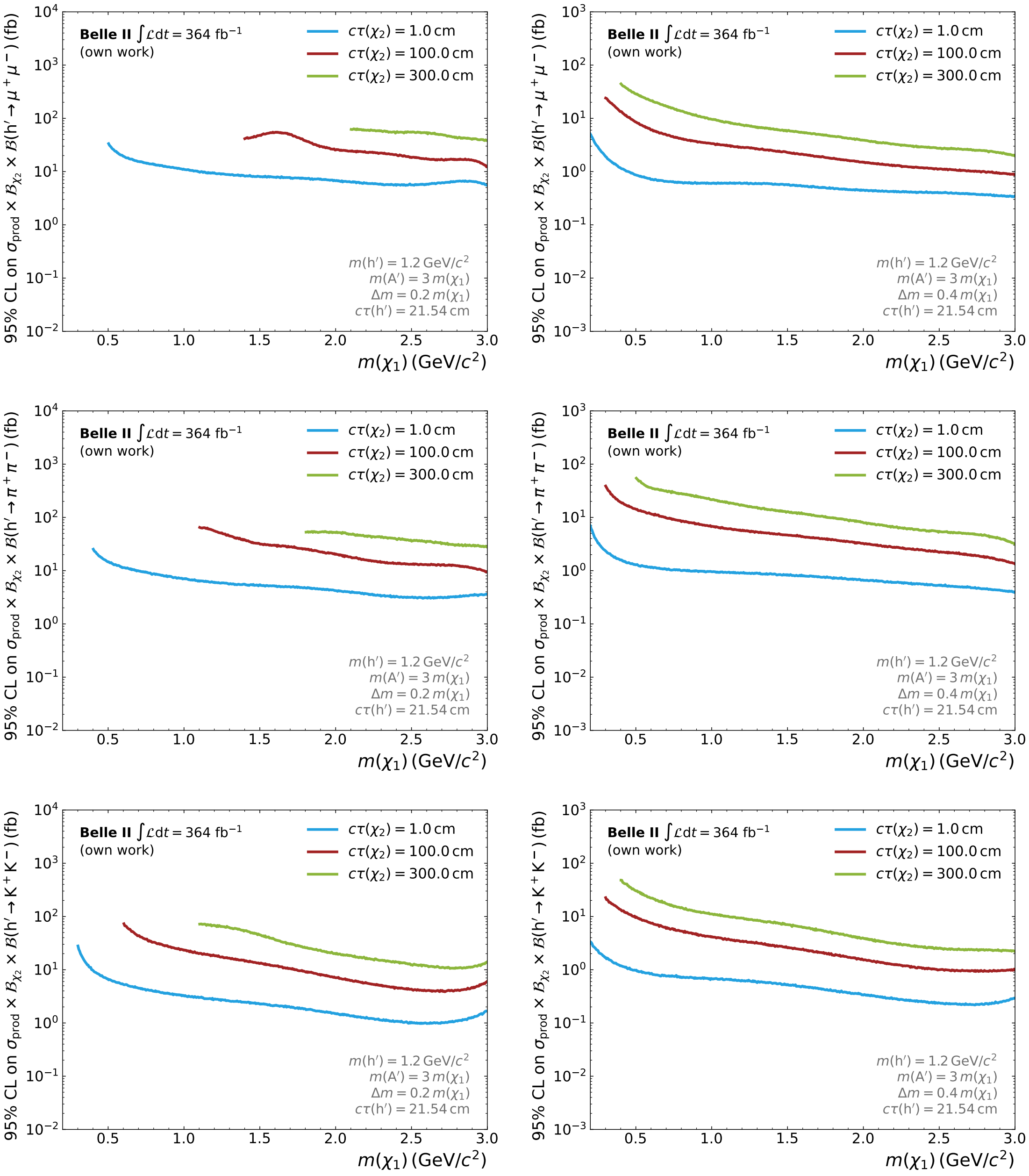

Figure G.13: 95% CL upper limits on the product of the production cross section $\sigma(\mathrm{e}^+\mathrm{e}^- \to \mathrm{h}'\chi_1\chi_2)$ (denoted as σ_{prod}) and the branching fractions $\mathcal{B}(\chi_2 \to \chi_1\mathrm{e}^+\mathrm{e}^-) \times \mathcal{B}(\mathrm{h}' \to \mathrm{x}^+\mathrm{x}^-)$ for the different final states $\mathrm{h}' \to \mu^+\mu^-$ (top), $\mathrm{h}' \to \pi^+\pi^-$ (center) and $\mathrm{h}' \to \mathrm{K}^+\mathrm{K}^-$ (bottom). Different lifetime hypothesis of the χ_2 are indicated with different colours: $c\tau(\chi_2) = 1.0\,\mathrm{cm}$ (cyan), $c\tau(\chi_2) = 100.0\,\mathrm{cm}$ (red), and $c\tau(\chi_2) = 300.0\,\mathrm{cm}$ (light green). The left side shows a mass splitting of $\Delta m = 0.2\,m(\chi_1)$ and the right side shows $\Delta m = 0.4\,m(\chi_1)$. The remaining model parameters are fixed to $m(\mathrm{h}') = 1.2\,\mathrm{GeV/c^2}$, $m(\mathrm{A}') = 3\,m(\chi_1)$, and $c\tau(\mathrm{h}') = 21.54\,\mathrm{cm}$.

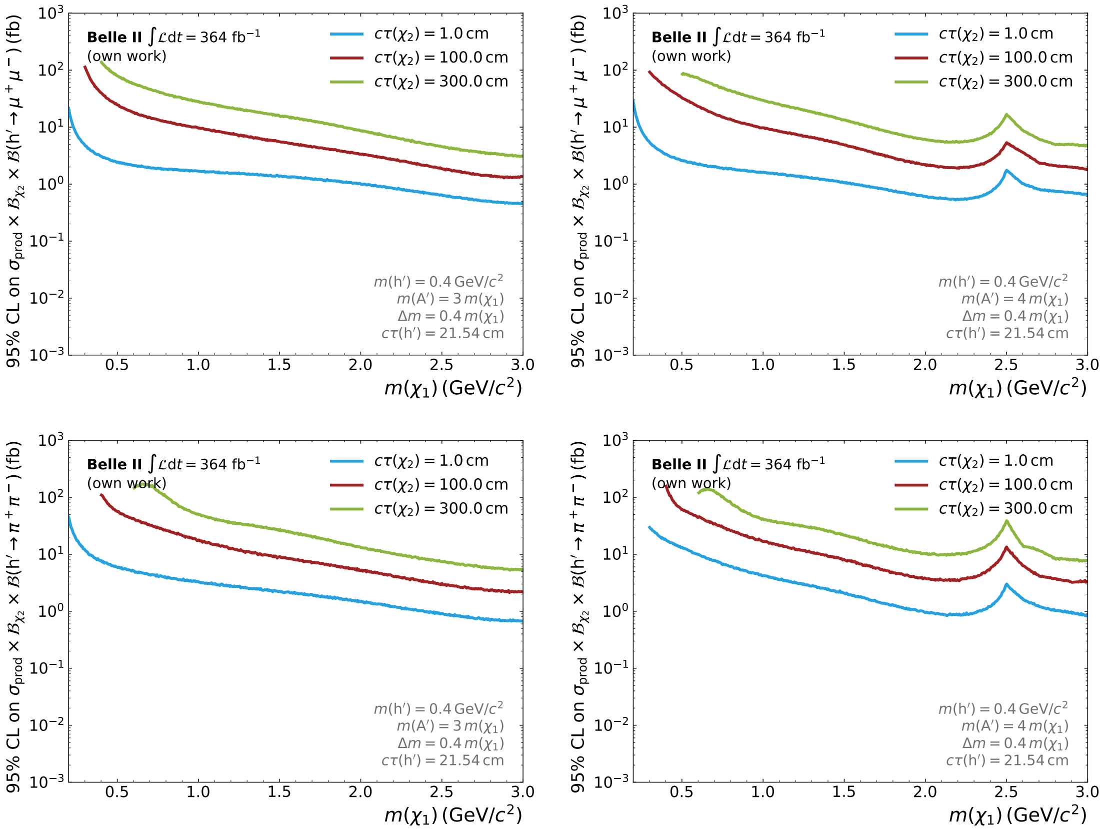

Figure G.14: 95% CL upper limits on the product of the production cross section $\sigma(\mathrm{e}^+\mathrm{e}^- \to \mathrm{h}'\chi_1\chi_2)$ (denoted as σ_{prod}) and the branching fractions $\mathcal{B}(\chi_2 \to \chi_1\mathrm{e}^+\mathrm{e}^-) \times \mathcal{B}(\mathrm{h}' \to \mathrm{x}^+\mathrm{x}^-)$ for the different final states $\mathrm{h}' \to \mu^+\mu^-$ (top) and $\mathrm{h}' \to \pi^+\pi^-$ (bottom). Different lifetime hypothesis of the χ_2 are indicated with different colours: $c\tau(\chi_2) = 1.0\,\mathrm{cm}$ (cyan), $c\tau(\chi_2) = 100.0\,\mathrm{cm}$ (red), and $c\tau(\chi_2) = 300.0\,\mathrm{cm}$ (light green). The left side shows a dark photon mass hypothesis of $m(\mathrm{A}') = 3\,m(\chi_1)$ and the right side shows $m(\mathrm{A}') = 4\,m(\chi_1)$. The remaining model parameters are fixed to $m(\mathrm{h}') = 0.4\,\mathrm{GeV/c^2}$, $c\tau(\mathrm{h}') = 21.54\,\mathrm{cm}$, and $\Delta m = 0.4\,m(\chi_1)$.

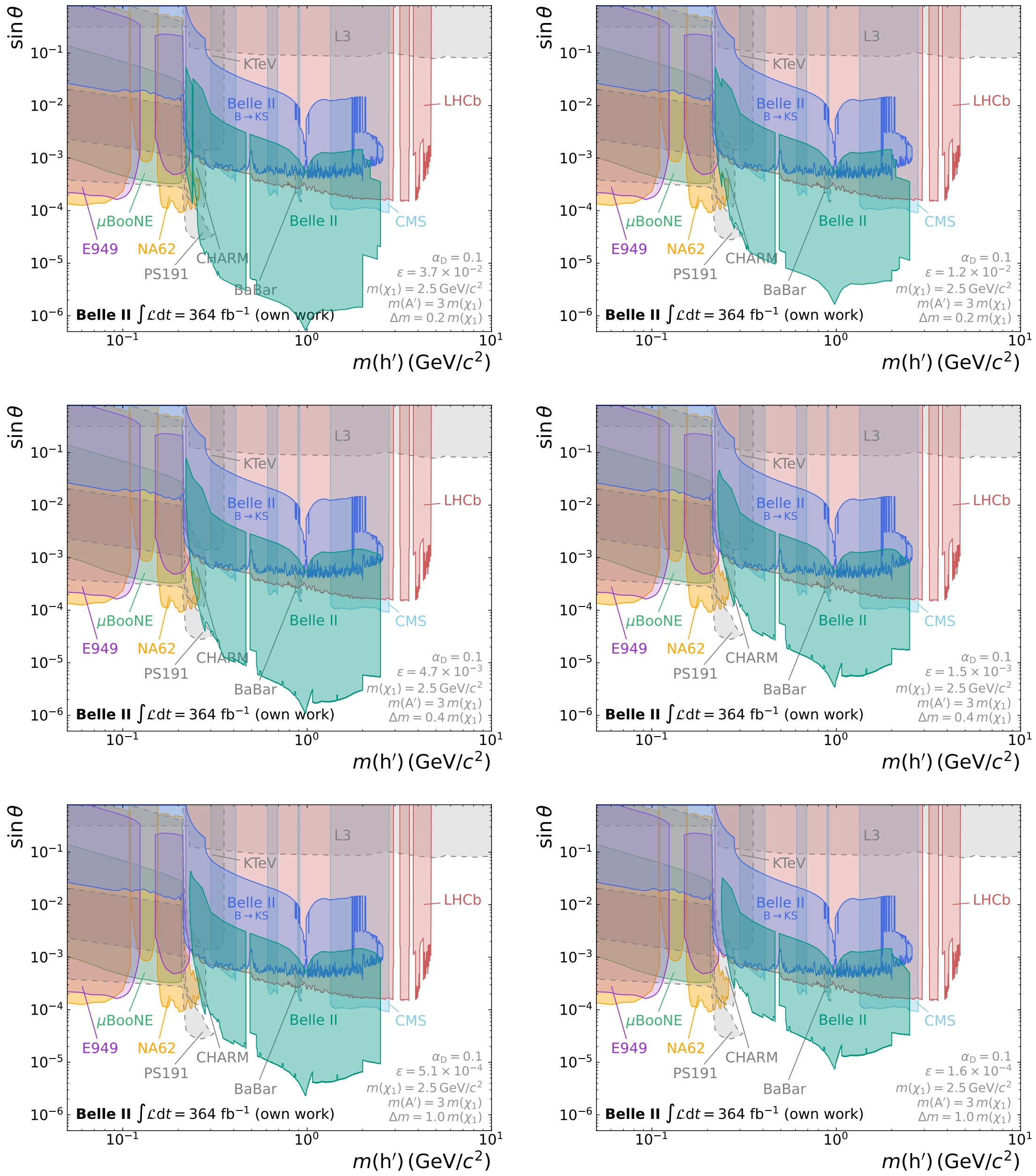

Figure G.15: Exclusions at 95% CL in the plane of the dark Higgs mass $m(\mathrm{h}')$ and the sine of the mixing angle θ of this work (green) together with existing constraints that have been described in Section 2.5. The mass splitting is chosen as $\Delta m = 0.2\,m(\chi_1)$ (top), $\Delta m = 0.4\,m(\chi_1)$ (center), and $\Delta m = 1.0\,m(\chi_1)$ (bottom). Plots on the left show a χ_2 lifetime hypothesis of $c\tau(\chi_2) = 0.01\,\mathrm{cm}$ and the right side shows $c\tau(\chi_2) = 0.1\,\mathrm{cm}$. Depending on the mass splitting this results in different mixing parameters ϵ that are reported in the respective plots. The remaining model parameters are fixed to $\alpha_\mathrm{D} = 0.1$, $m(\chi_1) = 2.5\,\mathrm{GeV/c}^2$, and $m(\mathrm{A}') = 3\,m(\chi_1)$. All other constraints do not depend on the presence of a dark photon or inelastic DM and do consequently not depend on these model parameters.

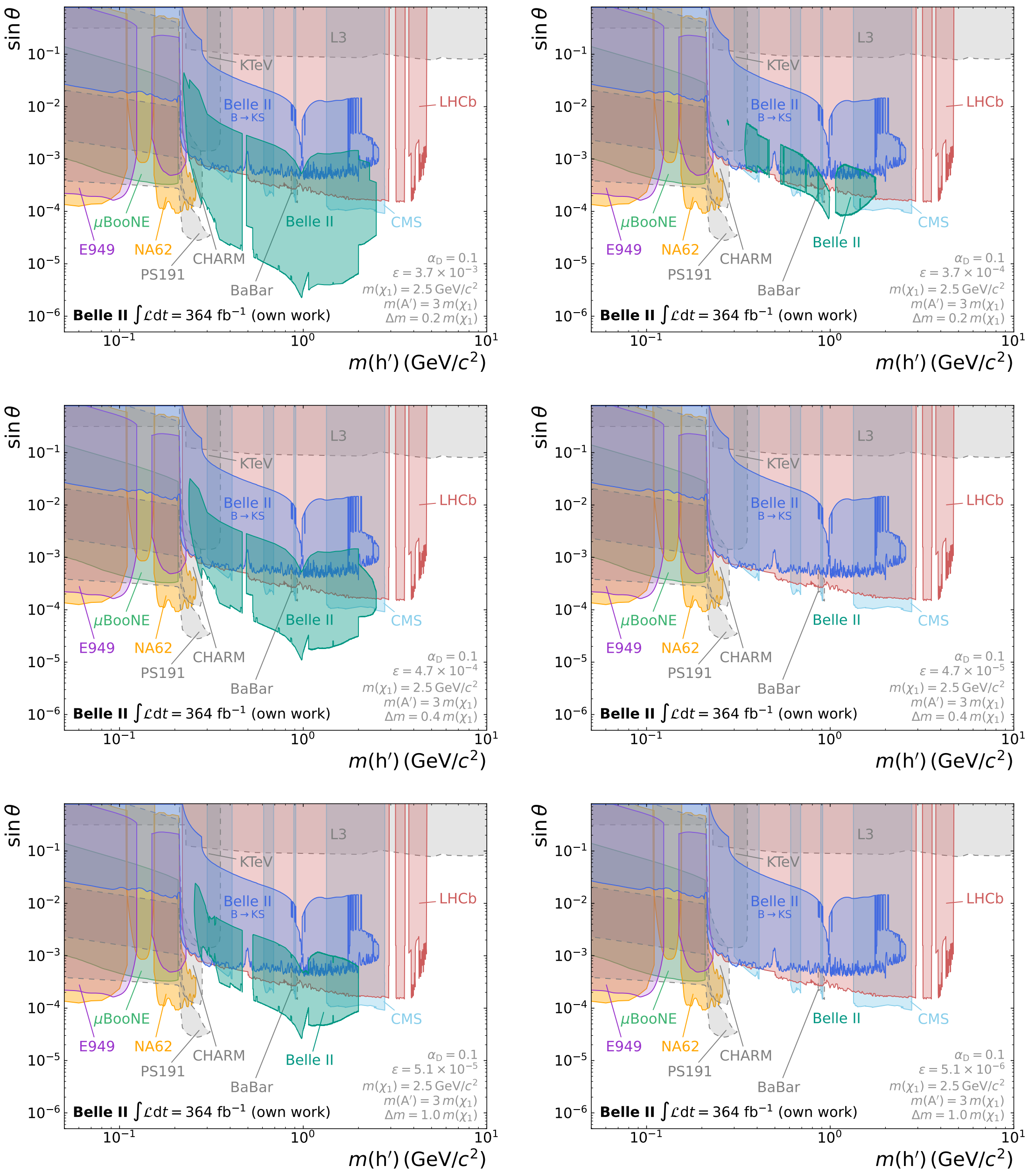

Figure G.16: Exclusions at 95% CL in the plane of the dark Higgs mass $m(\mathrm{h}')$ and the sine of the mixing angle θ of this work (green) together with existing constraints that have been described in Section 2.5. The mass splitting is chosen as $\Delta m = 0.2\,m(\chi_1)$ (top), $\Delta m = 0.4\,m(\chi_1)$ (center), and $\Delta m = 1.0\,m(\chi_1)$ (bottom). Plots on the left show a χ_2 lifetime hypothesis of $c\tau(\chi_2) = 1.0\,\mathrm{cm}$ and the right side shows $c\tau(\chi_2) = 100.0\,\mathrm{cm}$. Depending on the mass splitting this results in different mixing parameters ϵ that are reported in the respective plots. The remaining model parameters are fixed to $\alpha_\mathrm{D} = 0.1$, $m(\chi_1) = 2.5\,\mathrm{GeV/c^2}$, and $m(\mathrm{A}') = 3\,m(\chi_1)$. All other constraints do not depend on the presence of a dark photon or inelastic DM and do consequently not depend on these model parameters. For the two model parameter configurations on the center right and lower right Belle II cannot exclude parts of the parameter space.

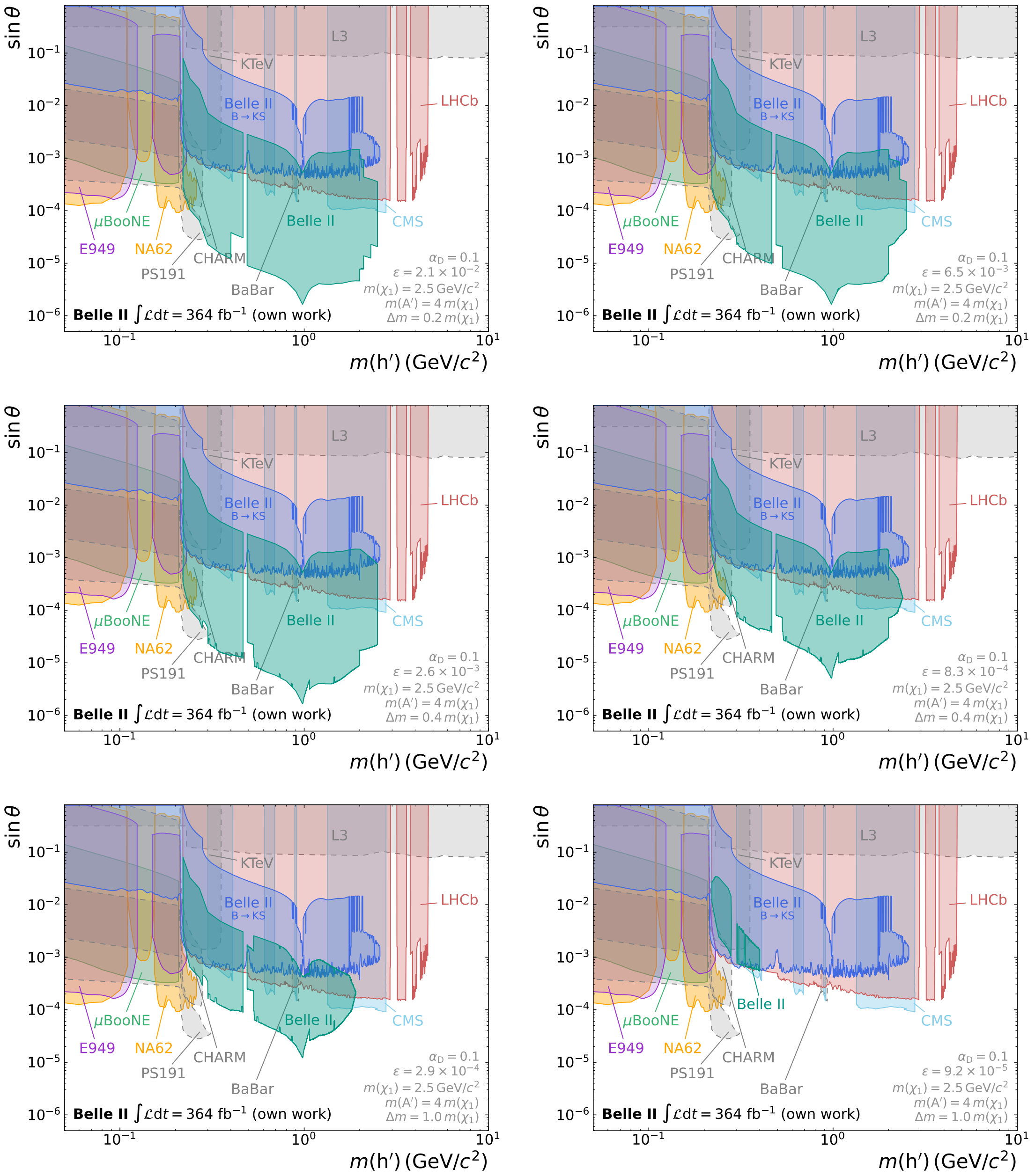

Figure G.17: Exclusions at 95% CL in the plane of the dark Higgs mass $m(\mathrm{h}')$ and the sine of the mixing angle θ of this work (green) together with existing constraints that have been described in Section 2.5. The mass splitting is chosen as $\Delta m = 0.2\,m(\chi_1)$ (top), $\Delta m = 0.4\,m(\chi_1)$ (center), and $\Delta m = 1.0\,m(\chi_1)$ (bottom). Plots on the left show a χ_2 lifetime hypothesis of $c\tau(\chi_2) = 0.1\,\mathrm{cm}$ and the right side shows $c\tau(\chi_2) = 1.0\,\mathrm{cm}$. Depending on the mass splitting this results in different mixing parameters ϵ that are reported in the respective plots. The remaining model parameters are fixed to $\alpha_\mathrm{D} = 0.1$, $m(\chi_1) = 2.5\,\mathrm{GeV/c^2}$, and $m(\mathrm{A}') = 4\,m(\chi_1)$. All other constraints do not depend on the presence of a dark photon or inelastic DM and do consequently not depend on these model parameters.

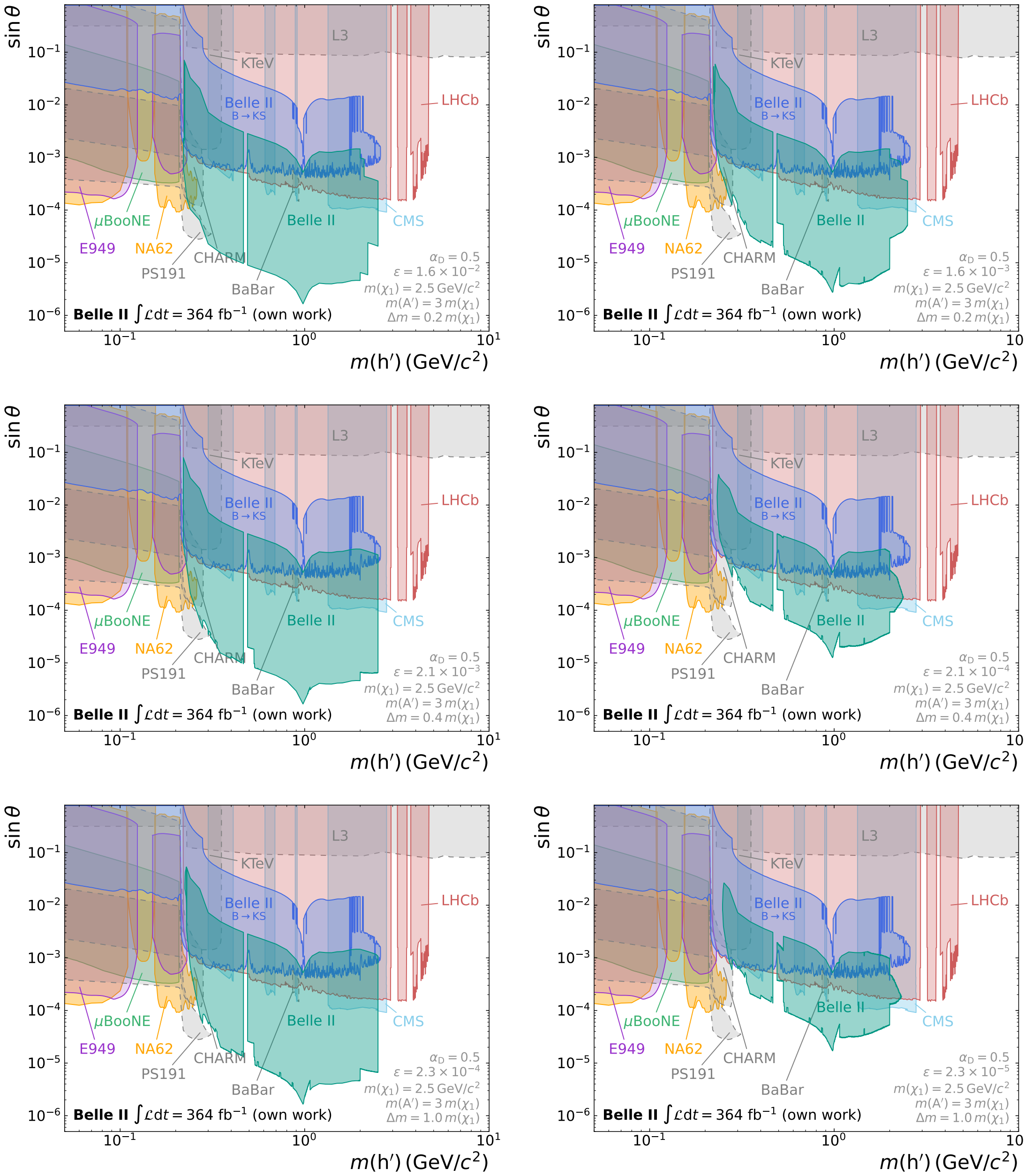

Figure G.18: Exclusions at 95% CL in the plane of the dark Higgs mass $m(\mathrm{h}')$ and the sine of the mixing angle θ of this work (green) together with existing constraints that have been described in Section 2.5. The mass splitting is chosen as $\Delta m = 0.2\,m(\chi_1)$ (top), $\Delta m = 0.4\,m(\chi_1)$ (center), and $\Delta m = 1.0\,m(\chi_1)$ (bottom). Plots on the left show a χ_2 lifetime hypothesis of $c\tau(\chi_2) = 0.01\,\mathrm{cm}$ and the right side shows $c\tau(\chi_2) = 1.0\,\mathrm{cm}$. Depending on the mass splitting this results in different mixing parameters ϵ that are reported in the respective plots. The remaining model parameters are fixed to $\alpha_\mathrm{D} = 0.5$, $m(\chi_1) = 2.5\,\mathrm{GeV/c}^2$, and $m(\mathrm{A}') = 3\,m(\chi_1)$. All other constraints do not depend on the presence of a dark photon or inelastic DM and do consequently not depend on these model parameters.

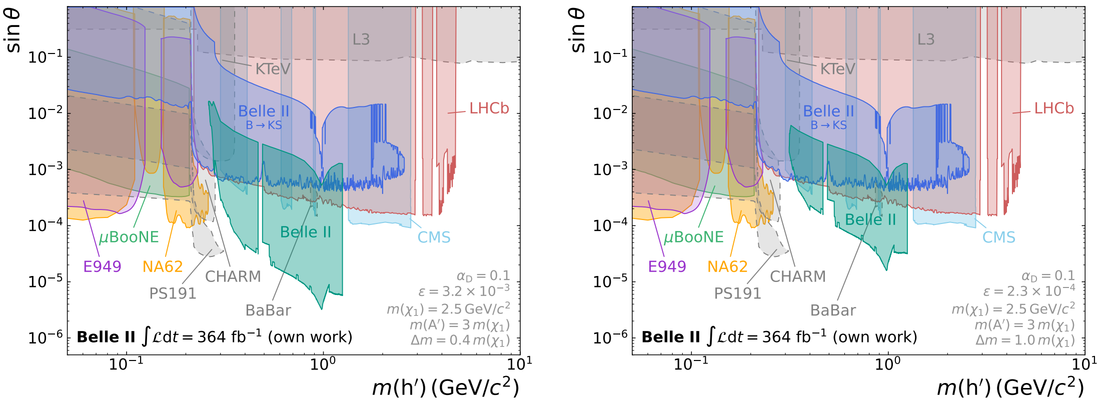

Figure G.19: Exclusions at 95% CL in the plane of the dark Higgs mass $m(\mathrm{h}')$ and the sine of the mixing angle θ of this work (green) together with existing constraints that have been described in Section 2.5. The mass splitting is chosen as $\Delta m = 0.4\, m(\chi_1)$ (left) and $\Delta m = 1.0\, m(\chi_1)$ (right). The lifetime of the χ_2 is set to $c\tau(\chi_2) = 0.1\,\mathrm{cm}$, which results in mixing parameters of $\epsilon = 3.2 \times 10^{-3}$ (left) and $\epsilon = 2.3 \times 10^{-4}$ (right). The remaining model parameters are fixed to $\alpha_\mathrm{D} = 0.1$, $m(\chi_1) = 1.25\,\mathrm{GeV/c^2}$, and $m(\mathrm{A}') = 3\, m(\chi_1)$. All other constraints do not depend on the presence of a dark photon or inelastic DM and do consequently not depend on these model parameters.

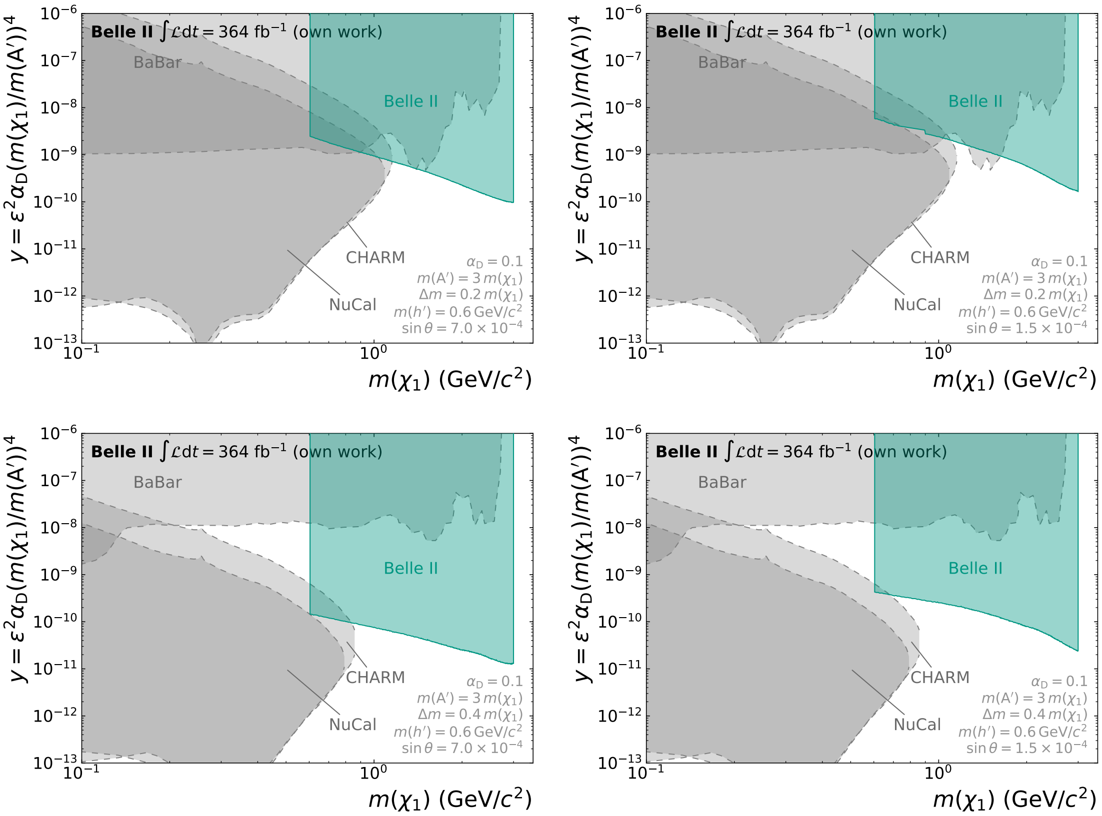

Figure G.20: Exclusions at 95% CL in the plane of the DM mass $m(\chi_1)$ and the dimensionless variable $y = \epsilon^2\alpha_\mathrm{D}(m(\chi_1)/m(\mathrm{A}'))^4$ of this work (green) together with existing constraints from [15, 35–39]. The mass splitting is set to $\Delta m = 0.2\,m(\chi_1)$ (top) and $\Delta m = 0.4\,m(\chi_1)$ (bottom). The lifetime (mixing angle) of the dark Higgs is set to $c\tau(\mathrm{h}') = 1.0\,\mathrm{cm}$ ($\sin\theta = 7.0 \times 10^{-4}$) (left) and $c\tau(\mathrm{h}') = 21.54\,\mathrm{cm}$ ($\sin\theta = 1.5 \times 10^{-4}$) (right). The remaining model parameters are fixed to $\alpha_\mathrm{D} = 0.1$, $m(\mathrm{A}') = 3\,m(\chi_1)$, and $m(\mathrm{h}') = 0.6\,\mathrm{GeV/c^2}$. All other constraints do not depend on the presence of a dark Higgs boson and the model parameters that describe it.

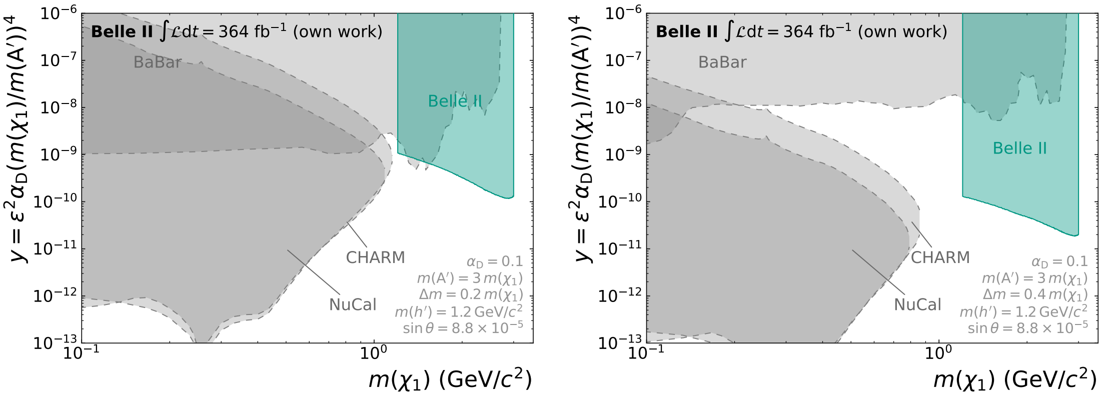

Figure G.21: Exclusions at 95% CL in the plane of the DM mass $m(\chi_1)$ and the dimensionless variable $y = \epsilon^2\alpha_{\mathrm{D}}(m(\chi_1)/m(\mathrm{A}'))^4$ of this work (green) together with existing constraints from [15, 35–39]. The mass splitting is set to $\Delta m = 0.2\,m(\chi_1)$ (left) and $\Delta m = 0.4\,m(\chi_1)$ (right). The lifetime (mixing angle) of the dark Higgs is set to $c\tau(\mathrm{h}') = 21.54\,\mathrm{cm}$ ($\sin\theta = 8.8 \times 10^{-5}$). The remaining model parameters are fixed to $\alpha_{\mathrm{D}} = 0.1$, $m(\mathrm{A}') = 3\,m(\chi_1)$, and $m(\mathrm{h}') = 1.2\,\mathrm{GeV/c^2}$. All other constraints do not depend on the presence of a dark Higgs boson and the model parameters that describe it.

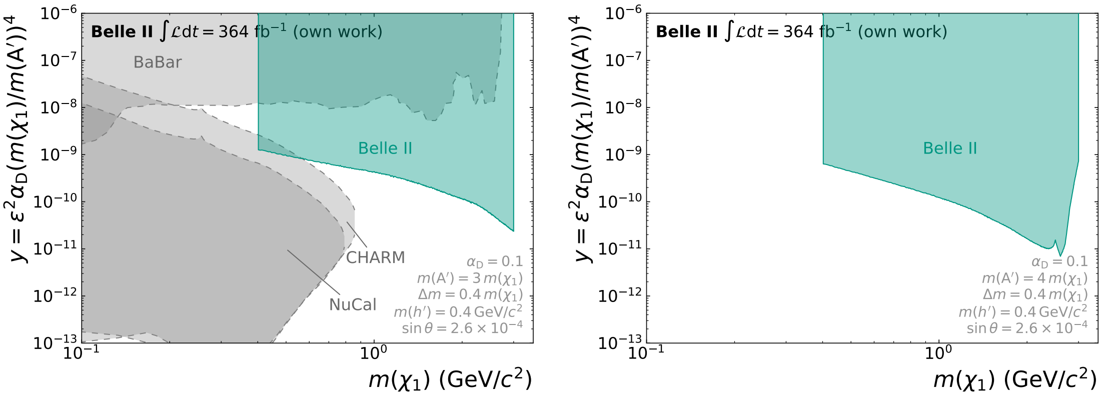

Figure G.22: Exclusions at 95% CL in the plane of the DM mass $m(\chi_1)$ and the dimensionless variable $y = \epsilon^2\alpha_{\mathrm{D}}(m(\chi_1)/m(\mathrm{A}'))^4$ of this work (green) together with existing constraints from [15, 35–39]. The mass splitting is set to $m(\mathrm{A}') = 3\,m(\chi_1)$ (left) and $m(\mathrm{A}') = 4\,m(\chi_1)$ (right). The lifetime (mixing angle) of the dark Higgs is set to $c\tau(\mathrm{h}') = 21.54\,\mathrm{cm}$ ($\sin\theta = 8.8 \times 10^{-5}$). The remaining model parameters are fixed to $\alpha_{\mathrm{D}} = 0.1$, $\Delta m = 0.4\,m(\chi_1)$, and $m(\mathrm{h}') = 0.4\,\mathrm{GeV/c^2}$. For the model parameter configuration on the right no reinterpretations of existing limits are available in the literature. All other constraints do not depend on the presence of a dark Higgs boson and the model parameters that describe it.

Glossary

AAFH A Monte Carlo generator for four-lepton final states in electron-positron collisions. See [62]. 26, 27

BabaYaga@NLO A Monte Carlo generator for Bhabha scattering and photon pair production in electron-positron collisions. See [66, 67]. 26, 27

Bayesian Analysis Toolkit A toolkit for the application of Bayesian inference using Markov Chain Monte Carlo. See [81]. 103, 111

Belle A first-generation B factory and the predecessor of the Belle II experiment. 211

Belle II A second-generation B factory and the successor of the Belle experiment. 1– 3, 7– 11, 13– 16, 18– 20, 25, 31, 64, 72, 79, 84, 87, 92, 114, 117– 119, 121, 122, 127, 128, 139, 205, 211

EvtGen A Monte Carlo Generator suited for the decay of heavy flavour particles. See [58]. 23, 25– 27

GEANT4 A toolkit for simulating the passage of particles through matter using a wide variety of phenomenological models. See [54]. 23, 25

KEKB The electron-positron collider at which the Belle experiment was located. 14

KKMC A Monte Carlo generator specifically for lepton and quark pair production at lepton colliders. See [68]. 26, 27

KoralW A Monte Carlo generator for four-fermion final states in electron-positron collisions. See [65]. 26, 27

MadGraph5_aMC@NLO Framework for the event generation and cross section calculation of SM and physics beyond the SM processes. For further information see [57]. 23

PHOKHARA A Monte Carlo generator for low multiplicity hadronic final states and high energetic photon emissions in electron-positron collisions. See [70]. 26, 27

POCA The point of closest approach (POCA) is a tracks' signed distance to the z axis as determined by the tracking algorithm. 39

PYTHIA8 A general-purpose Monte Carlo generator used to describe hard and soft interactions, parton distributions, initial- and final-state parton showers, multiparton interactions, fragmentation and decay. See [69]. 26, 27

SuperKEKB An upgrade of the KEKB electron-positron collider and the accelerator at which the Belle II experiment is located. 13, 14, 17, 83

Tauola A Monte Carlo generator suited for the decay of τ leptons. See [63]. 26, 27

TREPS A Monte Carlo generator for the production of two-photon processes in electron-positron collisions. See [64]. 26, 27

zfit A python-based model fitting library optimised for simple and direct manipulation of probability density functions. See [75]. 71

Acronyms

ARICH Aerogel Ring-Imaging Cherenkov detector. 16, 17

basf2 Belle II Analysis Software Framework. 23, 25

BCS best candidate selection. 29, 59, 60, 143, 162, 163

BDT Boosted Decision Tree. 32– 34, 99

CDC Central Drift Chamber. 15, 16, 18, 32, 41, 51, 61– 66, 85, 123

CMB cosmic microwave background. 3, 7

cms center-of-mass system. 13, 48

DAF deterministic annealing filter. 31

DEPFET Depleted Field Effect Transistor. 15

DM dark matter. 1– 11, 19, 20, 24, 62, 103, 117– 119, 125– 128, 204– 210

DSCB Double Sided Crystal Ball. 55, 56, 71– 74, 91, 92, 182– 186

ECL Electromagnetic Calorimeter. 17, 18, 31, 37, 39, 48, 51– 53, 61, 63, 66, 68, 84– 86, 92, 97, 98, 114, 158, 159, 165, 172, 173

FPGA field-programmable gate array. 18

FSP Final State Particle. 31– 33, 39, 44, 48, 57, 59, 72, 80, 105, 107

GDL global decision logic. 18

GNN graph neural network. 128

HER High-Energy Ring. 13

HIE high energy. 66– 69, 84– 86, 114, 177– 179

HLT High Level Trigger. 18, 64, 68

IP Interaction Point. 14– 16, 31– 34, 37, 39, 41, 44, 46, 51, 61, 64, 68, 91, 114, 128

ISR Initial State Radiation. 25– 27, 48, 57, 98

KEK High Energy Accelerator Research Organization. 13

KLM K^0_L and muon detector. 17, 31, 33– 36, 92

L1 trigger Level 1 trigger. 18, 25, 37, 39, 64, 66– 69, 85, 86, 114, 177– 179

LER Low-Energy Ring. 13

LHC Large Hadron Collider. 13

LLP long-lived particle. 80, 82, 83, 127

MadGraph5 MadGraph5_aMC@NLO. 23, 25, *Glossary:* MadGraph5_aMC@NLO

NN neural network. 32, 33

PDF probability density function. 72

PID particle identification. 16– 18, 29, 32– 37, 39, 42, 55, 59, 79– 81, 99, 128, 174, 175

POCA Point of closest approach. 39, *Glossary:* POCA

Punzi FOM Punzi figure of merit. 29, 33, 42, 44, 46, 51, 165– 175

PXD Pixel Detector. 15, 16, 18, 32, 44

ROE rest-of-event. 29, 48, 51, 52, 54, 143, 156, 157

RPC resistive plate chamber. 17

SM Standard Model of particle physics. 1– 5, 7, 8, 11, 19, 21, 23– 27, 29, 30, 39, 41, 42, 48, 51, 52, 55, 59, 71, 75, 80, 85, 87, 92– 95, 97– 103, 105, 107, 109, 112, 113, 115, 116, 118, 121– 123, 125, 143, 147, 211

STT single track trigger. 64, 66– 69, 177– 179

SVD Silicon Vertex Detector. 15, 16, 18, 32, 44

TOP Time-Of-Propagation counter. 16, 34, 37

WIMP weakly interactive massive particle. 1